

# **Development and Applications of X-ray Micro-Focusing Optics**

A Thesis Submitted to the

University of London

for the degree of

Doctor of Philosophy

James Michael Ablett

June 2001

# Abstract

The motivation for this thesis is the design and implementation of novel elliptical x-ray reflective micro-focusing optics. The advancement of x-ray micro-beam applications is a primary objective.

Sputtering of a heavy metal onto a spherical substrate can produce the required elliptical profile, and the combination of two mirrors in an orthogonal arrangement can deliver intense x-ray micro-beams at an x-ray synchrotron source. It is believed that this new deposition process offers the best way of obtaining accurate elliptical profiles. Traditionally, reflective x-ray micro-focusing has been achieved by bending a smooth flat substrate, and the new deposition technique renders a much simpler experimental arrangement. Moreover, producing enhanced mirror profiles has the opportunity to provide sub-micron focused x-ray beams with larger apertures and longer working distances. Grazing-incidence rhodium-coated spherical substrates were employed to investigate a variety of systems, using several experimental methods:

- The diamond-anvil cell has provided the opportunity to investigate high-pressure phase-transitions in general. The micro-focused x-ray beam allowed a study of two systems that exhibit abrupt phase-transitions at ultra high-pressures, and a novel x-ray fluorescence spectroscopic measurement was also implemented.
- Micro-focused x-ray fluorescence imaging was used to spatially resolve the calcium content in normal and osteoarthritic bone. This investigation is a unique application of x-ray micro-beams and correlation with infrared micro-spectroscopy is conceivable.
- A process known as ‘SAG’ can control the growth of thin-film semiconductor devices. The material is constrained to within distances that are on the micron length scale, and a micro-focused x-ray beam is essential for growth evaluation.

## Table of Contents

Chapter 1 Introduction and x-ray micro-beam studies.....	5
1.1 X-ray micro-diffraction .....	6
1.2 X-ray photon correlation spectroscopy .....	7
1.3 X-ray microscopy .....	8
1.4 High-pressure x-ray spectroscopy .....	10
1.5 Summary .....	10
Chapter 2 Overview of x-ray micro-focusing optics .....	12
2.1 Kirkpatrick-Baez mirrors .....	12
2.2 Zone plates and Bragg-Fresnel optics .....	15
2.3 Capillary optics .....	22
2.4 Wave-guides .....	26
2.5 Compound refractive lenses .....	28
2.6 Summary .....	34
Chapter 3 Synchrotron radiation and the NSLS X13 straight-section .....	36
3.1 Properties of synchrotron radiation .....	36
3.2 The National Synchrotron Light Source .....	39
3.3 The X13 straight-section and X13B beamline .....	42
3.3.1 IVUN .....	43
3.3.2 EPW .....	46
3.3.3 The X13B beamline .....	47
3.3.4 X13B monochromator characterisation .....	52
3.4 Summary .....	57
Chapter 4 Design and simulations of X13B reflective x-ray optics .....	58
4.1 Fundamental x-ray interactions .....	58
4.2 Grazing incidence x-ray reflectivity .....	62
4.3 Optical Surface errors .....	65
4.3.1 Surface roughness considerations .....	66
4.3.2 Slope error considerations .....	68
4.4 Geometrical description of reflective optics .....	70
4.5 Ray-tracing using SHADOW .....	75
4.5.1 X13 source definition .....	76
4.5.2 Optical configuration .....	76
4.5.3 Mirror parameters .....	78
4.5.4 Simulations .....	80
4.6 Summary .....	82
Chapter 5 Manufacture and characterisation of the NSLS X13B KB optics .....	83
5.1 Optical manufacture and surface profile measurement .....	83
5.2 Experimental set up and control .....	86
5.2.1 Mirror assembly .....	86
5.2.2 Mirror acceptance-slit assembly .....	88
5.2.3 Sample stage assembly .....	88
5.2.4 Optical and x-ray detectors .....	89
5.3 Alignment of the X13B micro-probe .....	90
5.4 Nickel dot fluorescence x-ray beam profile measurements .....	92
5.5 Blade-scan x-ray beam profile measurements and focal considerations .....	94
5.6 Estimation and measurement of photon flux .....	96
5.7 Summary .....	100
Chapter 6 High-pressure x-ray absorption spectroscopy .....	101
6.1 The diamond-anvil cell and high-pressure generation .....	101
6.2 Extended X-ray Absorption Fine Structure ( EXAFS ) .....	103
6.3 Extracting absorption coefficients from thick concentrated samples .....	111
6.3.1 Self-absorption correction of thick nickel sample fluorescence data .....	117
6.4 Summary .....	121

Chapter 7 Electronic and structural changes in thallium-rhenium oxide under high-pressure .....	123
7.1 X-ray transmission experiment and results .....	130
7.2 X-ray fluorescence EXAFS experiment and results .....	133
7.3 Conclusion of XANES and EXAFS measurements .....	137
Chapter 8 High-pressure-induced volume-collapse in praseodymium metal .....	138
8.1 Fluorescence XANES measurement in back-scattering geometry .....	142
8.1.1 Self-absorption correction of XANES spectra .....	145
8.2 Summary .....	151
Chapter 9 X-ray micro-probe fluorescence calcium mapping of normal and diseased bone.....	152
9.1 X-ray micro-probe fluorescence calcium mapping of normal bone .....	155
9.2 X-ray micro-probe fluorescence calcium mapping of osteoarthritic bone.....	158
9.3 Fourier transform infrared micro-spectroscopy .....	161
9.4 Summary .....	162
Chapter 10 Micro-fluorescence investigation of the selective area growth process .....	164
10.1 X-ray micro-probe fluorescence investigation of InGaAsP quantum-wells .....	165
10.2 Summary .....	168
Chapter 11 Conclusion and Outlook.....	169
Appendix A: List of abbreviations.....	172
Appendix B: List of frequently used symbols .....	173
Appendix C: SHADOW ray-tracing input parameters - X13B x-ray micro-probe design .....	174
Appendix D: List of manufacturers - X13B x-ray micro-probe .....	175
Bibliography .....	176
Acknowledgement .....	185



## Chapter 1 Introduction and x-ray micro-beam studies

The large x-ray absorption resonances of the elements make x-rays an ideal source for investigating the electronic structure of materials.<sup>1</sup> X-ray wavelengths are of the same order as inter-atomic distances and are an excellent probe for structure determination. High signal-to-background ratios are beneficial in x-ray fluorescence trace-element analysis,<sup>2</sup> and the large photoabsorption lengths allow for bulk studies and investigation of buried structures to be performed. As detailed in Chapter 3, synchrotron x-ray sources are the brightest of x-ray generators to-date (Figure 1-1), and the development of micron-sized x-ray beams offers enormous potential to a wide-range of investigations and provides the motivation for this thesis.

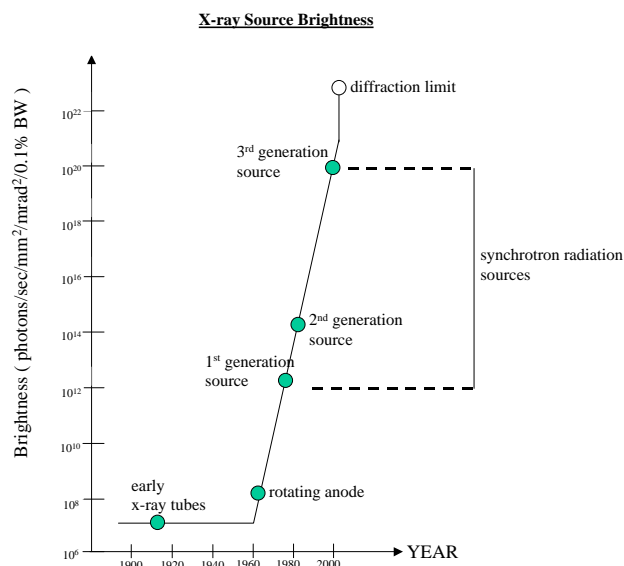


Figure 1-1: Chronological progress towards more powerful x-ray sources.

In addition to the greater number of photons being delivered to the sample than compared with conventional x-ray sources, the spectral distribution of synchrotron radiation is very broad (Figure 3-2, Figure 3-3) and crystal monochromators are able to select a narrow range of x-ray wavelengths.<sup>3</sup> For example, the energy resolution of the silicon (111) reflection is  $\frac{\Delta E}{E} \sim 10^{-4}$ . X-rays are sensitive to elemental, chemical and structural content, and a micro-focused x-ray beam can provide microscopic maps of sample composition and structure.

There are several types of optics that can be used to focus x-rays. These are discussed in Chapter 2, and all have the potential for delivering sub-micron x-ray beams. A selection of applications that are suited to x-ray micro-probes, and recent experimental results, are described in the remaining sections of this chapter.

## **1.1 X-ray micro-diffraction**

Diffraction studies can reveal a wealth of information on the structure of materials.<sup>3</sup> Diffraction utilising micron-sized x-ray beams (micro-diffraction) is extremely important when one considers the technological importance of micro-fabrication and its role in micro-electronic device production. By manufacturing smaller devices, they become more powerful, but the building processes become drastically more challenging. Stresses and strains develop in electronic devices through a combination of electromigration and lattice mismatch between the substrate and material.<sup>4-6</sup> When small interconnect wires are patterned on a substrate, these forces can lead to under-performance and eventual collapse of the micro-structure. By trying to understand the underlying physics of such failures, one could perhaps develop a more robust structure.

In diffraction experiments, the lattice spacing is measured according to Bragg's law.<sup>3</sup> For monochromatic x-rays, the x-ray energy and angle between the incident and diffracted rays determine the lattice spacing, and the sample is rotated to satisfy the Bragg condition. This arrangement is shown in Figure 1-2. Angular deviations of the diffracted rays with respect to a reference sample, indicate lattice parameter differences and inherent strains. Such measurements are popular where there is a strong preferred crystal orientation and x-ray micro-beams are not required.

For studying strain in polycrystalline materials, an x-ray micro-beam is essential in resolving individual micro-grains. However, exposing the crystal to monochromatic x-rays and rotating the sample to satisfy Bragg's law is undesirable. This is because a varying number of micron-sized grains are illuminated as the sample is turned about the incident x-ray beam (Figure 1-3) and small displacement errors are also introduced as the sample is rotated.<sup>7</sup>

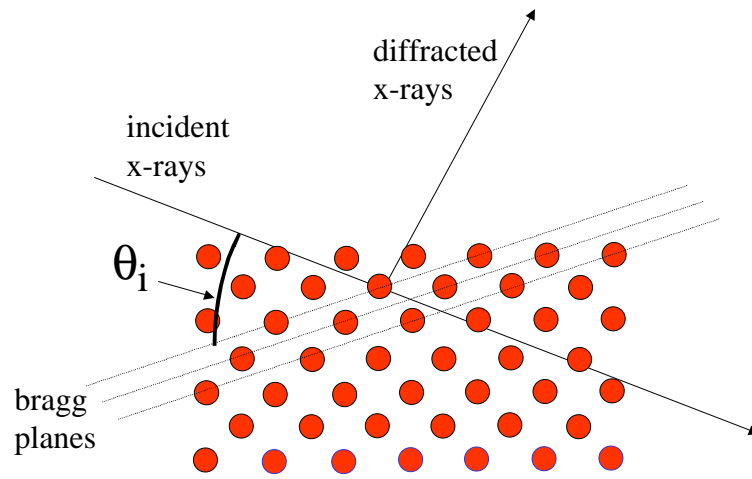


Figure 1-2: X-ray diffraction from a single crystal.  $\theta_i$  is the angle satisfying Bragg's law.

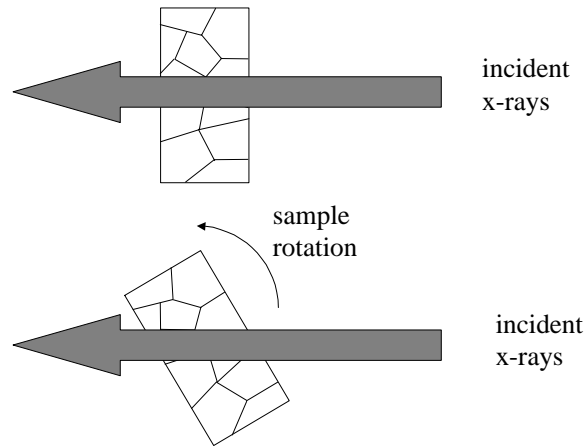


Figure 1-3: The disadvantage of sample rotation for studying polycrystalline materials.

It is therefore impossible to determine the orientation and lattice parameters of individual grains from such a measurement. However, by using broad band-pass or tuneable monochromatic x-rays, it is possible to index the overlapping Laue diffraction patterns and determine the orientation and strain of individual micro-grains in a static experimental set up.<sup>8,9</sup>

## 1.2 X-ray photon correlation spectroscopy

Investigation of particle dynamics with laser light<sup>10</sup> is a well established tool for probing the long wavelength hydrodynamics of fluids, polymers and colloids, and x-rays have the potential to probe the short-wavelength dynamics of opaque systems. The

relatively new experimental technique of “x-ray photon correlation spectroscopy” (or “speckle”) measures the x-ray intensity variations from disordered systems with respect to the x-ray scattering vector.<sup>11-13</sup> The speckle pattern is formed from the interference between scattered x-rays from different parts of the material and can provide information on the spatial arrangement of the disorder. A highly-coherent x-ray source is mandatory in these experiments, which are well-suited to zone-plate optics. Zone plates also deliver a higher photon flux than can be obtained using small pin-hole apertures (Section 2.2).

Speckle patterns have been investigated on a variety of disordered systems: Structure factors and the dynamics of gold particles immersed in glycerol fluid have been measured<sup>12</sup> and speckle patterns from randomly orientated islands in thin polymer films have also revealed the potential power of this technique.<sup>13</sup>

### **1.3 X-ray microscopy**

A natural use of the x-ray micro-probe is in the elemental/chemical imaging of materials. By tuning the incident x-ray energy above the elemental absorption edges, material composition can be obtained by recording the energy and intensity of the fluorescence photons. Fluorescence near-edge x-ray absorption spectroscopy, where the incident x-ray energy is scanned across an absorption edge, can also reveal chemical changes within the material.<sup>14</sup>

An interesting area of research is in the geological sciences: The Earth is continuously bombarded by interplanetary dust particles (IDPs).<sup>15</sup> IDPs of diameters greater than  $\sim 100\mu\text{m}$  vaporise when they enter the Earth’s atmosphere producing smaller particles ranging from  $\sim 5\mu\text{m} \rightarrow 35\mu\text{m}$ , which have been collected in the stratosphere by NASA sampling aircraft for more than two decades. These IDPs originate from asteroids and comets, and their composition provides information on the physical, chemical and mineralogical properties of their parent body. Investigation of IDPs are well suited to x-ray micro-focusing optics at synchrotron sources, which can deliver enough photons to these tiny samples to provide adequate analysis. Kirkpatrick-

Baez x-ray micro-focusing optics (Section 2.1) have been employed to perform trace elemental analysis on IDPs at the copper-through-to-strontium absorption edges.<sup>15</sup> This information can provide clues as to the nature of the asteroids or comets from which these small particles had originated.

The imaging of sub-micron domain patterns in magnetic materials is an exciting area of research that can directly reveal the magnetic anisotropy. The contrast in such experiments utilises the difference in the absorption coefficient between right and left circular-polarised x-rays.<sup>16</sup> Fluorescence imaging of micron-sized magnetic domains in a  $\text{HoFe}_2$  crystal has been performed,<sup>17</sup> and magnetic-contrast transmission spectra have been recorded on FeGd multilayer materials.<sup>18,19</sup>

X-ray microscopy is usually performed by measuring the absorption coefficient of materials in a transmission geometry. However, for the lighter elements, absorption contrast is low and the experiment is unfeasible. However, by using coherent micro-beams, it is possible to image systems by phase-contrast techniques.

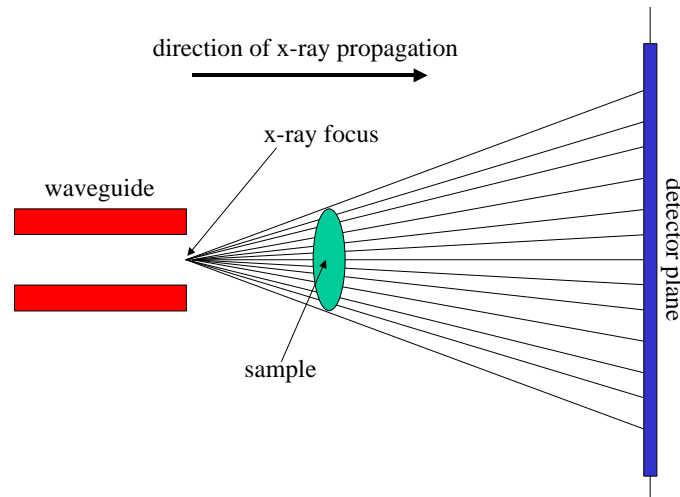


Figure 1-4: An example of an arrangement used for performing phase-contrast experiments.<sup>20</sup>

An example of the set up for phase-contrast imaging is shown in Figure 1-4. In this arrangement, a wave-guide (Section 2.4) is used to focus x-rays into a highly-coherent

sub-micron spot. The sample is placed downstream of the focal point, and the divergent x-rays produce a magnified image at the detector position. This interference pattern is formed from the optical-path differences between the scattered and transmitted rays, and the image can be reconstructed to provide valuable structural information.<sup>20,21</sup>

#### **1.4 High-pressure x-ray spectroscopy**

Pressure is the least used of the thermodynamic variables to investigate changes in materials. Matter at high pressures exhibit phenomena such as insulator-to-metal transitions,<sup>22</sup> loss of magnetic moments<sup>23,24</sup> and enhanced superconductivity.<sup>25,26</sup> Pressure can also be used to synthesise new materials.<sup>27</sup> High-pressure x-ray spectroscopy has been made possible with the advent of the diamond-anvil cell (Section 6.1). This device provides the pressure generation and x-ray micro-probe optics are required to deliver a large number of photons to the inherently small sample.

Theoretical predictions as to how materials are expected to perform under high pressures are important as they can identify new areas of research. An interesting system that has been postulated to turn into a conductor at ultra-high pressures is hydrogen.<sup>28,29</sup> Hydrogen is a diatomic molecule in its natural state and an insulator due to the strong covalent bond. It exists as a liquid below temperatures of 20 K, and finally becomes a solid below 14 K. However, in the solid state, hydrogen remains an insulator as the diatomic molecular structure still exists. It has been postulated that by subjecting hydrogen to ultra high-pressures, this would eventually break apart the strong bonds of the substance and turn it into a conductor. Superconductivity has been postulated to occur at pressures exceeding 400 GPa, with the possibility that when the pressure is released, it can remain in this state to form the first room-temperature superconductor.<sup>29</sup>

#### **1.5 Summary**

There are many areas of research which require intense x-ray micro-beams. Progress in these areas will continue as improvements in optical manufacture, x-ray detector development and data analysis advance. Until only recently, high-pressure experiments were carried out in the optical regime using Raman spectroscopy. With the advent of

pressure-generating diamond-anvil cells and x-ray micro-focusing optics, investigations using synchrotron radiation have been realised. When materials are subjected to pressures, they deform and phase transitions can occur. Some of these phase transitions are abrupt. For example at ultra high-pressures, thallium-rhenium-oxide transforms from a light-grey to black colour (Chapter 7), and praseodymium metal exhibits a large volume-collapse (Chapter 8). Micro-beam x-ray investigations have been performed on these materials using the optics designed in this thesis.

X-ray micro-focussing optics are ideally suited to elemental specific mapping. Micro-imaging of the calcium content of regions in an osteoarthritic knee joint (Chapter 9) have been performed by collecting the calcium fluorescence photons. Results indicate that such x-ray micro-probe studies are a powerful tool in this field of research.

Controlling the manufacturing processes of micro-optoelectronic devices is an important area of research and development. “Selective Area Growth” (or “SAG”) is a powerful technique for controlling the growth of semiconductor materials, and is used to build laser modulators, multi-quantum wells and optical wave-guides. These devices have dimensions of the order of microns, and x-ray micro-beams are required to investigate these materials. Models for controlling the growth process have recently been developed and experimental data are needed to test the theory. Chapter 10 describes a preliminary study on InGaAsP quantum-well structures, and further uses of x-ray micro-beams in this field are envisaged.

## Chapter 2 Overview of x-ray micro-focusing optics

This chapter will introduce the optics which are capable of delivering intense micro-focused x-ray beams from synchrotron radiation sources.<sup>30,31</sup> The basic aim of micro-focusing is to concentrate more photons into a smaller area than a slit of the same dimensions could render, and gains approaching  $10^4$  can be realised.<sup>32</sup> Focusing can be achieved by reflection, refraction or diffraction of the incident x-ray beam, and each variety of micro-focusing optic has potential advantages and disadvantages, dependent upon experimental requirements.

Focusing of x-rays by bending perfect crystals is a standard method implemented at many x-ray synchrotron source beamlines. This is often incorporated into the monochromator assembly to provide beams with dimensions of a few hundred microns.<sup>33,34</sup> Smaller spot sizes are possible using carefully chosen geometrical arrangements and intricate crystal design. Focusing to  $\sim 10\text{ }\mu\text{m}$  has been demonstrated using perfect crystals in the high-energy asymmetric Laue geometry,<sup>35</sup> and beam sizes of  $\sim 20\text{ }\mu\text{m} \rightarrow 40\text{ }\mu\text{m}$  have been demonstrated using Bragg reflection.<sup>36</sup> Due to the large aberrations inherent in bent crystal-optics, and one-dimensional focusing, these perfect-crystal 'micro-probes' will not be discussed. Instead, this chapter will concentrate on devices that can produce beams of at least an order of magnitude smaller than those obtained through crystal bending.

### 2.1 Kirkpatrick-Baez mirrors

Kirkpatrick-Baez (KB) mirrors offer one of the most versatile ways of producing sub-micron x-ray beams. They were first proposed in 1948<sup>37</sup> to remove astigmatism by the use of two concave mirrors positioned at right-angles to one another, and were the optics chosen for this thesis. This section will be relatively brief, with a more detailed explanation of the optical design given in Chapter 4. The general set-up of a single KB optic is shown in Figure 2-1.



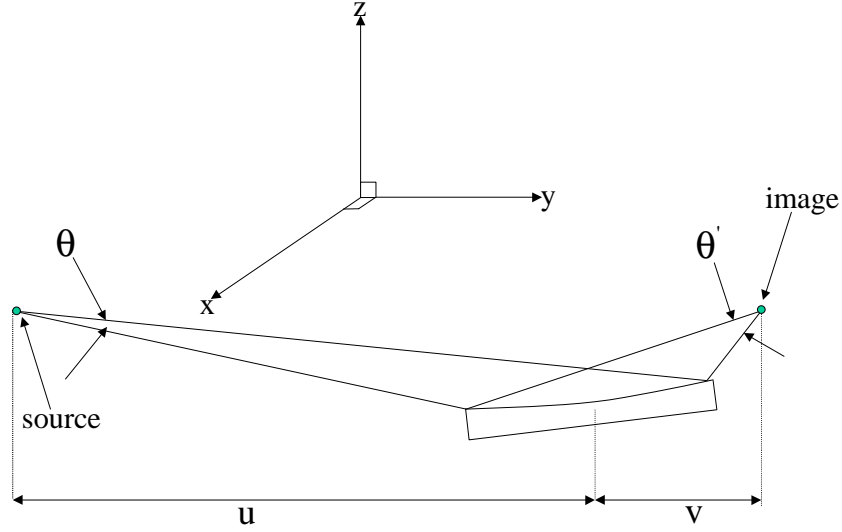


Figure 2-1: Geometry of a reflective focusing optic.

In the above figure,  $\theta$  and  $\theta'$  are the angles subtended from the source-to-mirror and from the mirror-to-image respectively.  $u$  is the source-to-optic distance<sup>†</sup>, and  $v$  is the optic-to-image distance.<sup>†</sup> It is assumed that reflection occurs in the y-z plane only, and the mirror is elliptical along the y-direction and planar along the sagittal x-direction. This arrangement achieves focusing in one plane, and the KB configuration of two mirrors in an orthogonal set up provides a point focus.<sup>37</sup> If  $\sigma$  and  $\sigma'$  are the respective source and image sizes in the z-direction, then conservation of phase space specifies the relationship:

$$\theta \sigma = \theta' \sigma' \quad \{2.1\}$$

and the demagnification is simply given by the ratio,

$$M = \frac{\sigma'}{\sigma} = \frac{\theta}{\theta'} \quad \{2.2\}$$

At an x-ray synchrotron source,  $u \gg v$  and the demagnification of the optics is given to very good approximation by,

---

<sup>†</sup> With respect to the mirror pole.

$$M = \frac{v}{u} \quad \{2.3\}$$

In the x-ray region, grazing angles of incidence are required to reflect the incident radiation, and high-Z materials such as platinum, rhodium or gold can be used to coat the mirror substrates (Section 4.2). Long mirrors ( $\sim > 10$  cm) are required to collect a large proportion of the synchrotron radiation, and this necessitates rigorous optical manufacturing processes to maintain good roughness and slope errors over the whole surface area (Section 4.3). Reflective optics are wavelength independent (achromatic) and an elliptical surface provides point-to-point focusing. Several methods have been employed in the past to form the elliptical shape. Until only recently, there were no methods of forming the mirror surface directly. Flat surfaces and figures with high degrees of revolution such as spheres and toroids were the only surfaces that could be polished to the required shape. However, these profiles cannot provide sub-micron focusing due to large geometrical aberrations inherent in these systems (Section 4.3.2).

By bending a flat surface, an elliptical shape can be approximated.<sup>32,38-40</sup> The flat mirror surface is typically formed by depositing a thin coating of the mirror material onto a low-roughness variable-width substrate such as float-glass or silicon.<sup>38</sup> Then, by a suitable mechanical design, the forces are applied and the elliptical shape is formed. This method has produced some very encouraging results with reported beam sizes ranging from  $0.8 \mu\text{m}$  and upwards.<sup>32,38</sup> However, these beam dimensions are difficult to reproduce and surface profiles tend to deteriorate after they have been bent a number of times. A typical beam dimension of  $\sim 10 \mu\text{m}$  is regularly achieved at the National Synchrotron Light Source (NSLS) bending magnet X26A.<sup>14</sup> Also, the complication of motors, that are needed to apply the bending forces, makes the system rather bulky and expensive.<sup>†</sup>

Recently, the idea of coating a spherical substrate to form an elliptical shape has been proposed (differential coating), with an anticipated improvement in slope error

---

<sup>†</sup> Bent multilayer mirrors can also be used to focus x-rays from synchrotron radiation sources.<sup>41</sup>

(Section 4.3.2).<sup>42</sup> Although the mirror parameters are fixed in this configuration, the absence of bending mechanisms make this system highly desirable. This was the optical design developed for this dissertation and has also been recently demonstrated.<sup>42</sup>

### **Advantages**

The major advantage of KB mirrors are their achromatic point-to-point focusing properties, and are the optics most suited to conserving source brightness. The elliptical shape minimises aberrations, and the ability to achieve sub-micron focusing has been demonstrated.<sup>32,38,40,42</sup> The recent development of differentially coated optics<sup>42</sup> has stimulated the quest for smaller beam dimensions and placed added emphasis on mirror manufacturers to achieve lower slope errors (Section 4.3.2). Although these reflective optics require grazing angles of incidence, they still offer the largest collection apertures compared with other x-ray micro-focusing devices. Mirror manufacture has improved greatly over the years, and differentially coated optics are relatively inexpensive and robust.

### **Disadvantages**

The disadvantages associated with KB mirrors are dependent on the type of experiment that is to be performed. When resolution on the micron scale needs to be accomplished, then this type of optic should be chosen. Reduction in beam size significantly less than a fraction of a micron has not yet been demonstrated (best  $\sim 0.46 \mu\text{m}$ <sup>42</sup>). Differentially coated KB mirrors are fixed focal-length optics, and bendable KB mirrors may seem more flexible. However, bendable optics are relatively expensive and bulky, and forming the exact elliptical shape is difficult.<sup>40</sup>

## **2.2 Zone plates and Bragg-Fresnel optics**

Zone plates and Bragg-Fresnel optics are diffractive elements that utilise the enhancement in optical path differences to form the image. Before discussing Bragg-Fresnel optics, a simple discussion on the properties of zone plates will be given, and

the reader should consult an excellent review of their properties by Michette *et al.*<sup>43</sup> A schematic of a circular zone plate is shown in Figure 2-2.

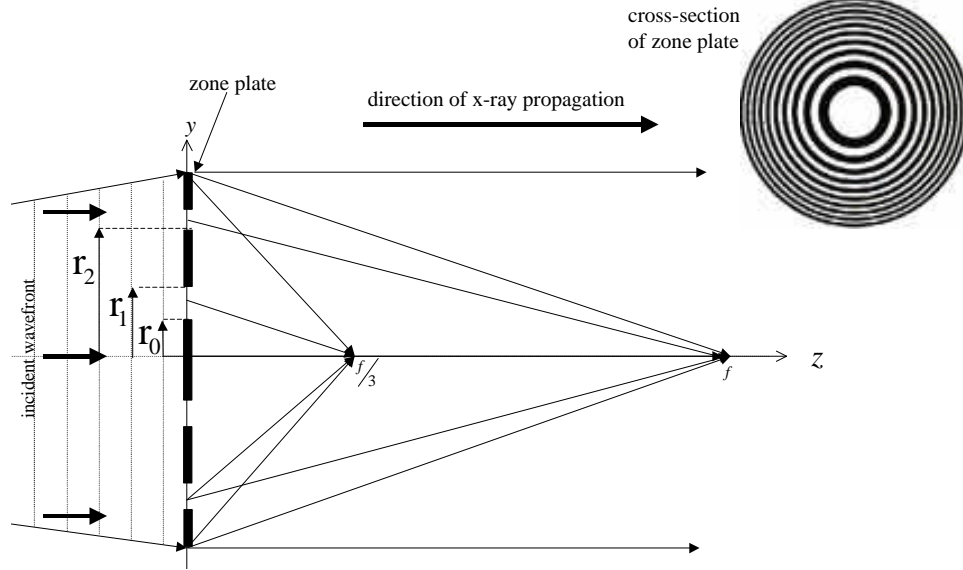


Figure 2-2: Fresnel zone plate schematic.

Coherent monochromatic x-rays are diffracted by the zone plate which results in odd orders being axially focused, negative odd orders resulting in diverging beams (not shown) and a non-diffracted zero order. Due to the requirement of coherency, these optics are ideally suited to undulator beamlines at synchrotron radiation sources.<sup>44</sup> The diffracted rays are selected on-axis by a small pin-hole called an 'order-sorting aperture', and if the zone plate is exposed to polychromatic light, then it can function as an x-ray monochromator. In a conventional Fresnel zone plate (FZP), the opaque regions completely absorb the incoming wave, and can be thought of as blocking those wavelengths that would destructively interfere at the focal point.

The radius of the  $n^{\text{th}}$  zone is given by,

$$r_n = \sqrt{n \lambda f + r_0^2} \quad \{2.4\}$$

where  $f$  is the focal length of the zone plate,  $r_0$  is the radius of the central zone and  $\lambda$  is the x-ray wavelength.

From Equation {2.4}, the line density grows as the number of zones increase, the pattern is periodic in  $r^2$  and the area of each zone is constant. The efficiency of even orders are zero,<sup>43</sup> and the real on-axis foci are given by,

$$f_m = \frac{f}{m}, \quad m = 1, 3, 5, \dots \quad \{2.5\}$$

where  $m$  is the order of diffraction.

For a large number of zones it can be shown that the zone width and focal length are given by,

$$d_n \sim \frac{\lambda f}{2r_n} \sim \frac{r_n}{2n} \quad \{2.6\}$$

$$f \sim \frac{2 r_n d_n}{\lambda} \sim \frac{D_n d_n}{\lambda} \quad \{2.7\}$$

where  $D_n$  is the diameter of the  $n^{\text{th}}$  zone.

The efficiency of a Fresnel zone plate (rectangular diffracting profile)<sup>45,46</sup> into the focused on-axis orders is given by,<sup>†</sup>

$$\varepsilon(m) = \frac{1}{m^2 \pi^2} \left( 1 + e^{-2\phi \frac{\beta}{\delta}} - 2e^{-\phi \frac{\beta}{\delta}} \cos \phi \right), \quad m = 1, 3, 5, \dots \quad \{2.8\}$$

where  $\phi$  is the phase-shift induced by the absorbing material, and the optical constants are represented by  $\delta$  and  $\beta$  (Chapter 4).

For a pure FZP, the absorption index  $\beta$  is large and the opaque material is thick enough to absorb the entire incident x-rays. The theoretical efficiency into the first-

---

<sup>†</sup> The zeroth undiffracted order contributes to 25 % of the transmitted intensity.

order is 10% , and by manufacturing alternative zone profiles, the efficiency into the various orders can be increased. This can be accomplished by replacing the opaque regions of the standard FZP with transparent phase-shifting areas so that all diffracted rays interfere constructively at the focal point. This optic is called a Fresnel phase zone plate (FPZP). For the ideal case,  $\frac{\beta}{\delta}$  is small and a  $\pi$  phase-shift is induced between neighbouring regions. In this case, the maximum theoretical efficiency into the first-order is 40% . In practice, there is some absorption, and efficiencies around 35% are more realistic. Moreover, using a parabolic profile for the phase-shifting region can further increase the efficiency. However, present lithographic techniques are incapable of producing such structures, but blazed profiles can deliver higher photon throughputs.<sup>47</sup>

Zone plates possess excellent focusing properties, and it is commonplace in the soft x-ray region to reach a resolution of  $< 50 \text{ nm}$ .<sup>48</sup> It can be shown that the transverse resolution is given by the Rayleigh criterion,

$$\rho_R = \frac{1.22 \lambda f_m}{D_N} = \frac{1.22 d_N}{m} \quad \{2.9\}$$

where  $D_N$  and  $d_N$  are the diameter and outer-zone width of the zone plate respectively, and the resolution corresponds to the distance between the intensity maxima and neighbouring minima.

The axial resolution is defined as the distance between the two intensity minima that lie to either side of the intensity maximum<sup>†</sup> and is given by,

$$\frac{\Delta f_m}{f_m} = \frac{2}{m N} \quad \{2.10\}$$

---

<sup>†</sup> The depth of focus is half of this value.<sup>43</sup>

At the NSLS X1A soft x-ray undulator beamline, nickel and germanium Fresnel zone plates deposited on  $\text{Si}_3\text{N}_4$  membranes have been used in a scanning transmission microscope set up, with outer zone-widths of  $20\text{ nm} \rightarrow 80\text{ nm}$  and apertures of  $80\text{ }\mu\text{m} \rightarrow 160\text{ }\mu\text{m}$ , functioning in the wavelength range of  $1.2\text{ nm} \rightarrow 5.5\text{ nm}$  ( $1\text{ keV} \rightarrow 225\text{ eV}$ ).<sup>49</sup> The source-to-optics distance is  $\sim 22\text{ m}$  here, and the source size is  $\sigma_x \times \sigma_z \sim 430\text{ }\mu\text{m} \times 13\text{ }\mu\text{m}$  (standard deviation). Using the above equations, the operating values are shown in Table 2-1.  $\sigma'_x$ ,  $\sigma'_z$  are the geometrically demagnified images (standard deviation) and are dependent on the focal position. The overall resolution can be closely approximated by adding the geometrical and diffraction-limited image sizes in quadrature.

$d_N$ (nm)	$\lambda$ (nm)	$D_N$ ( $\mu\text{m}$ )	$f$ (mm)	$n^0$ zones (n)	$\sigma'_x$ (nm)	$\sigma'_z$ (nm)	$\rho_R$ (nm)	Depth. Focus ( $\mu\text{m}$ )
20	1.2	80	1.3	1000	25.4	0.8	24.4	1.3
"	"	160	2.6	2000	52.8	1.6	"	"
"	5.5	80	0.3	1000	5.9	0.2	"	0.3
"	"	160	0.6	2000	11.7	0.4	"	"
80	1.2	80	5.3	250	103.6	3.1	97.6	21.2
"	"	160	10.6	500	207.2	6.3	"	"
"	5.5	80	1.2	250	23.5	0.7	"	4.8
"	"	160	2.4	500	46.9	1.4	"	"

Table 2-1: Design specifications of NSLS X1A Fresnel zone plates, using first-order diffraction.

In the soft x-ray region, electron-beam lithography<sup>49,50</sup> is the state-of-the-art method used to produce the most accurate and narrowest zone plate structures. This method has resulted in the smallest outer zone width of  $20\text{ nm}$  to-date.<sup>49</sup> However, zone plates in the hard x-ray region require more sophisticated manufacturing procedures due

to the thicker zone plate profiles that are required to block or phase-shift this shorter wavelength radiation correctly. As electron-beam lithography cannot produce the high aspect ratios that hard x-ray zone plates dictate, other manufacturing techniques are used:

Sputtered-sliced techniques were the first methods for manufacturing hard x-ray zone plates. This process involves starting with a very thin central absorbing wire onto which alternating low-Z and high-Z materials are transferred. After the required number of layers have been deposited, the structure is sliced to the correct thickness and then polished. A sputtered-slice FPZP has been tested at a Japanese synchrotron source.<sup>51</sup> This zone plate consisted of 50 zones of silver and carbon that were deposited onto a gold wire of radius  $23.5\text{ }\mu\text{m}$ . The outer zone width was  $d_N \sim 0.25\text{ }\mu\text{m}$ , and the thickness of the silver zones was  $\sim 8\text{ }\mu\text{m}$ , that induced a  $3\pi$  phase-shift of the incident wave-front. This achieved a first-order resolution of  $0.5\text{ }\mu\text{m}$  and an efficiency of 11% at  $\sim 8\text{ keV}$ .

However, the reasons why sputtered-sliced zone plates have never ultimately achieved diffraction-limited resolution is due to the inherent roughness which is accumulated with each additional zone layer. Thankfully, it is possible to use electron-beam lithography (as used for soft x-rays), together with x-ray lithography to produce a smooth-accurate diffractive optic: In the first demonstration of this technique,<sup>46</sup> a zone-plate mask was wrote by electron beam lithography and then transferred, using x-ray lithography, into a thick photo-resist. Development of the resist created an aspect ratio of 6 in the membrane, which was then electroplated with a  $3.1\text{ }\mu\text{m}$  nickel layer to form the final zone plate structure. This produced a relatively large first-order efficiency of 33% for 8 keV x-rays, an aperture of  $60\text{ }\mu\text{m}$  and an outer zone width of  $0.2\text{ }\mu\text{m}$  with sub-micron resolution.<sup>52</sup> Recently, to increase the aspect ratio further to obtain sub-0.1 micron resolution, several novel ways of improving x-ray lithographic techniques have been devised. These have produced zone plates with virtually diffraction-limited 150 nm first-order and 90 nm third-order image sizes at 8 keV.<sup>53</sup>



The major disadvantage of zone-plates is that they can only operate in a very narrow energy range, as dictated by the thickness of the phase-shifting regions. Subsequently, a better method of creating zone-plates that can operate over a wider energy range, and in particular in the high-energy x-ray regime, have recently been developed: The zone-plate structure is transferred into a crystal or multilayer, thus creating a true phase-shifting optic that operates in reflection. These Bragg-Fresnel lenses (BFLs) have phase-shifts that are independent of energy and dependent only on the zone structure height and order of Bragg reflection. They have maximum efficiencies of 40% and were first proposed<sup>54</sup> and realised by Aristov *et al.*<sup>55,56</sup> The simplest BFL optic is the linear type that is depicted in Figure 2-3.

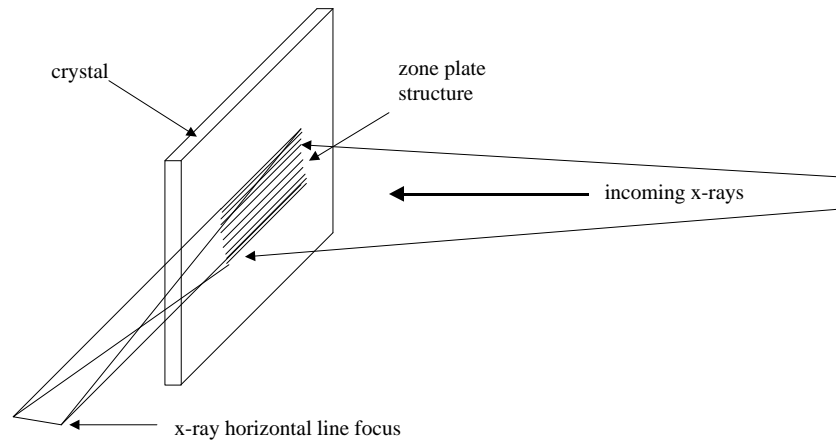


Figure 2-3: Linear Bragg-Fresnel lens schematic.

In this geometry, the zone-plate structure will sagittally focus x-rays in the plane perpendicular to the grooves, and these lenses could be placed orthogonal to one another to produce an intense focal spot.<sup>57</sup>

It is possible to use BFLs with circular patterns to form a focused beam in both directions from one singular optic: Focusing of hard x-rays ( $\sim 6$  keV) with a circular BFL was performed by Basov *et al.*<sup>58</sup> and reported efficiencies very close to the theoretical 40 % value. An attractive use for a circular BFL is to focus hard x-rays into a small spot with high energy resolution. A demonstration of this technique using a germanium circular BFL was performed at the ESRF micro-focus undulator beamline, and obtained a spot size of  $0.7 \mu\text{m}$  at 7.6 keV, with an efficiency of 35 %.<sup>59,60</sup>

## **Advantages**

Zone plates operating in the soft x-ray region have produced the smallest x-ray beams to-date.<sup>49</sup> However, in the hard x-ray region, they are difficult to fabricate due to the large aspect ratios that are required, and Bragg-Fresnel optics maybe the best option. A FPZP hard x-ray zone-plate has produced excellent results with first and third order foci of 150 nm and 90 nm respectively.<sup>53</sup> Zone plates have focal lengths of  $> \sim 10$  cm in the hard x-ray region and sample manipulation is relatively easy.

## **Disadvantages**

Zone plate optics require a highly coherent beam, which are suited to undulators but not bending magnet sources. They are chromatic, which can make spectroscopic measurements cumbersome. Typical diameters are of the order of  $200\text{ }\mu\text{m}$ , and greater photon collection can be gained by using reflective mirrors. FZPs are only able to operate within a discrete range of wavelengths due to the wavelength-dependence of the phase-shift material, although this constraint can be relieved using Bragg-Fresnel optics. Linear BFLs allow a greater degree of freedom in energy selection, but they can only successfully focus in one direction. Circular BFLs also have a limited range of operation due to the geometry, but have the advantage of being able to focus in both horizontal and vertical directions.

## **2.3 Capillary optics**

Through total external reflection within the walls of a glass capillary, x-rays can be guided to provide a more concentrated beam at the exit aperture. Mono-capillary optics, similarly employed in fibre-optical technology and also applicable to neutron sources,<sup>61</sup> are currently used to provide 'focusing' in the micron region and below. Initial experiments performed by Stern *et al.*<sup>62</sup> demonstrated their ability to concentrate x-rays from a synchrotron radiation source. Strictly speaking, the term 'focusing' should not be applied to these optics as they often rely on multiple reflections to compress the x-ray beam, and therefore do not directly reimage the source. However, single-bounce

capillaries<sup>63</sup> with parabolic or elliptical profiles<sup>64</sup> are true focusing optics. Figure 2-4 shows a schematic of a tapered glass capillary.

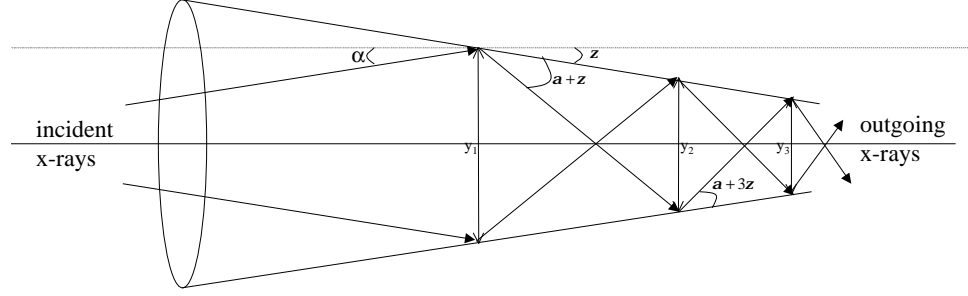


Figure 2-4: The tapered glass capillary.

The tapered capillary is a multi-bounce concentrating optic, and for an x-ray entering the capillary at an angle  $\alpha$  to the optical axis, it will be reflected at an angle  $\alpha + 2\zeta$  to this axis. By ensuring that the reflected rays meet the interface at angles less than the critical angle of the material (Equation {4.20}), the x-rays will exit the capillary with minimal intensity loss. Referring to Figure 2-4, if the capillary was extended to meet at the optical axis, then the total length would be given by,

$$L \sim \frac{d}{2\zeta} \quad \{2.11\}$$

where  $d$  is the entrance diameter of the capillary and  $\zeta$  is the taper angle.

In reality, the capillary is cut so that the x-ray beam can escape, with a length given by,

$$L_{\text{cut}} \sim L \left( 1 - \frac{x}{d} \right) \quad \{2.12\}$$

where  $x$  is the exit diameter.

Through simple geometry (Figure 2-4), the ray impinging at a point with diameter  $y_1$  is reflected to a point with diameter  $y_2$  where,

$$\frac{y_2}{y_1} = \frac{\sin(\alpha + \zeta)}{\sin(\alpha + 3\zeta)} \quad \{2.13\}$$

and the demagnification for  $(n+1)$  reflections is simply,

$$\frac{y_{n+1}}{y_1} = M_{n+1} \sim \frac{\alpha + \zeta}{\alpha + (2n+1)\zeta} \quad \{2.14\}$$

For total external reflection,  $\alpha + (2n+1)\zeta \leq \theta_c$ , hence the highest demagnification achievable with a capillary is given by,

$$M_{\max} = \frac{\alpha + \zeta}{\theta_c} \quad \{2.15\}$$

where  $\theta_c$  is the critical angle of the capillary material.

The theoretical gain of the capillary optic is given by,

$$\frac{I_{\text{out}}}{I_{\text{in}}} \sim R_{\text{total}} \frac{D_{\text{exit}}^2}{D_{\text{entrance}}^2} \quad \{2.16\}$$

where  $R_{\text{total}}$  is the integrated reflectivity over all reflections and,  $D_{\text{exit}}$  and  $D_{\text{entrance}}$  are the exit and entrance apertures of the capillary respectively.

Assuming a  $100\text{ }\mu\text{m}$  capillary aperture and a desired  $1\text{ }\mu\text{m}$  concentrated beam, a demagnification of  $\frac{1}{100}$  is required, resulting in a taper angle,  $30\text{ rad } (\zeta \rightarrow 0)$ . At the NSLS, the beam divergence from a bending magnet is  $\sim 0.2\text{ mrad}$  (Equation {3.1}) and only a small amount of flux can be accepted. Conversely, a third-generation insertion-device undulator with a photon central-cone divergence of  $\sim 25\text{ }\mu\text{rad}$ <sup>31</sup> is ideally suited to these optics.

Capillaries are usually drawn from borosilicate, quartz or high-density lead glass. To maximise the overall efficiency, the number of internal reflections should be minimised. Unfortunately, reducing the number of reflections in a linear tapered

capillary also decreases the demagnification (Equation {2.14}).<sup>62</sup> However, by gradually increasing the taper angle so that the reflected rays impinge the glass walls at continually steeper angles (still below  $\theta_c$ ), demagnification can be increased.<sup>62</sup> Intuitively, completely optimised capillaries would be elliptical, and all rays striking the surface would incur only one reflection before being brought to a focus.<sup>64</sup>

A group at the Cornell (CHESS) 5.3 GeV synchrotron radiation source first demonstrated sub-micron focusing with a 35  $\mu\text{m}$  diameter leaded glass capillary. This resulted in a beam-size of less than 300 nm<sup>65</sup> and later improvements to the manufacturing process resulted in a compressed x-ray beam diameter of only 95 nm.<sup>66</sup>

### **Advantages**

The major advantage of capillary optics is that they are relatively inexpensive to produce and can operate effectively for energies below  $\sim 10$  keV, above which the critical angle for glass falls drastically. They have also obtained one of the smallest x-ray beams of  $\sim 95$  nm in the hard x-ray region.<sup>66</sup> Overall, their modest demagnifications could be beneficial for a final concentrating stage in an optical configuration where pin-holes are often used.

### **Disadvantages**

The major disadvantage with capillary optics is that they are small-aperture devices. As these optics are relatively long (typically  $< 50$  cm) and light, exceptional vibration-damping measures have to be incorporated into the system for stable use. Even though they can operate using polychromatic x-rays, they are often used in monochromatic mode due to the low melting temperatures of glass, which can be exasperated on focused beamlines. Also, slope error and roughness play an important role in the spatial beam profile at the capillary exit<sup>67</sup> and it is impossible to polish them. Due to diffraction effects and high beam-divergence, the sample has to be placed extremely close to the exit aperture.<sup>67</sup> Finally, because capillaries are composed from insulating materials, this makes them suspect to radiation damage.

## 2.4 Wave-guides

There have been a number of experiments that have demonstrated the focusing properties of thin-film wave-guides in the hard x-ray region<sup>20,68-72</sup> although they have yet to be used widely as an x-ray collimating optic. Wave-guides operating in the x-ray region are analogous to those used at microwave, infrared and optical frequencies.<sup>73,74</sup> These optics are also applicable to particle sources such as neutrons.<sup>75</sup>

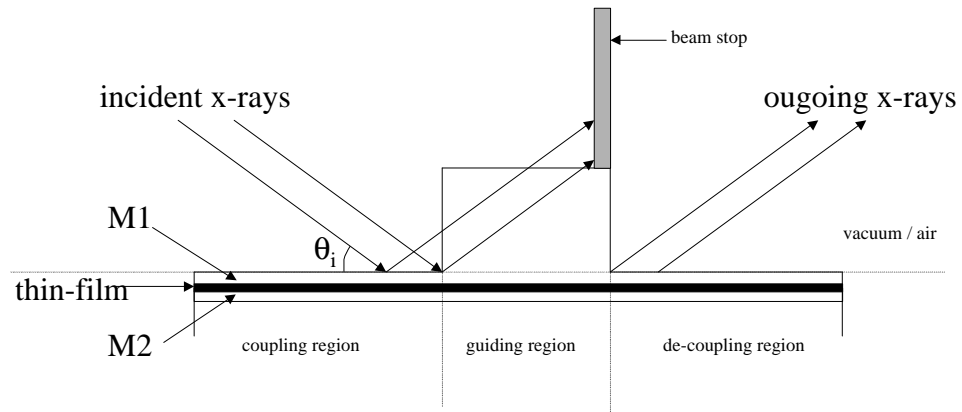


Figure 2-5: Thin-film wave-guide schematic.

A wave-guide is a thin-film sandwiched between two materials, M1 and M2, which have lower refractive indices than the film itself. If the incident wave impinges on M1 at an angle less than the critical angle for the air/vacuum - material interface, then the majority of the incoming x-rays will be totally externally reflected. However, there is also an exponentially decreasing wave that propagates through the material. Inside the thin-film, there are a number of resonant modes that can be excited by this evanescent wave. This coupling can be significantly enhanced if the incident beam has a small angular divergence and a high degree of coherence. Once this coupling is complete, the initially decreasing wave travelling through M1 becomes exponentially increasing and sharp dips in the reflectivity spectrum are measured that correspond to these excited modes. A propagating wave is then set up in the thin-film region, which is constrained there by total internal reflection from the outer walls and the thicker-guiding region. This propagating wave can then be extracted through a decoupling region<sup>69,71</sup> or by terminating the periodic structure,<sup>20,68,70,72</sup> and the emerging beam is highly coherent. By terminating the wave-guide, the out-going beam has dimensions equal to the film

thickness, and the production of sub-micron beams is possible. Recently, there have been a small number of experiments that have demonstrated the use of x-ray planar wave-guides.

Jark *et al.* used the third-generation undulator at beamline ID-13 (ESRF) to investigate a  $\sim 1$  cm long terminated chromium-carbon-chromium wave-guide for producing sub-micron beams.<sup>70</sup> A vertical beam spot of  $0.4\text{ }\mu\text{m}$  was measured at a distance of  $100\text{ }\mu\text{m}$  from the wave-guide exit with an overall efficiency of 1% at 13 keV. A practical use of the wave-guide, for phase-contrast imaging, was subsequently performed in a projection set up:<sup>20</sup> A nylon fibre and a gold-strip test pattern were magnified by the divergent x-rays emerging from the structure and interference between the transmitted and refracted rays provided the phase-contrast. A further experiment,<sup>72</sup> in conjunction with an elliptical mirror to provide horizontal focusing, was performed to illustrate the effectiveness of the wave-guide in micro-diffraction studies in the energy range  $\sim 13\text{ keV} \rightarrow 15\text{ keV}$ . Powder diffraction patterns on aluminium-oxide and paraffin samples, placed less than  $100\text{ }\mu\text{m}$  from the wave-guide exit, were subsequently recorded.

### **Advantages**

Synchrotron radiation is well matched to the operation of wave-guides. The primary attraction of wave-guide ‘focusing’ is that they can produce a coherent line focus,<sup>20</sup> and can be manufactured to deliver very small x-ray beams, approximately equal to the thin-film thickness. Film thicknesses are typically of the order of a few hundred nanometres, and vertical beam sizes of less than  $0.4\text{ }\mu\text{m}$  have been recorded.<sup>70</sup> Wave-guides could also be illuminated by the white-beam from a synchrotron radiation source, and used as a broad band-pass monochromator.<sup>69</sup> Another advantage is that they can provide sub-micron beam sizes at very high energies, where reflective optics are redundant.

## Disadvantages

Wave-guides have not found general favour in x-ray micro-beam development as they have only demonstrated collimation in one direction. Another reason for their unpopularity is that the beam exits the optic through a small opening, which produces diffraction effects.<sup>68,70</sup> This specifies that the sample should be placed extremely close to the wave-guide exit to minimise beam spread. They are also extremely inefficient when one considers the need for a highly coherent source, and overall efficiencies are less than 2 %. Also, x-rays of energies of less than  $\sim 10$  keV can not be accommodated due to the absorption through and along the wave-guide.

## 2.5 Compound refractive lenses

Just as optical light can be successfully focused by refractive lenses, this method can also be used to focus x-rays. The final optical system capable of forming small x-ray beams to be discussed in this chapter, is the compound refractive lens (CRL). A schematic of the device is shown in Figure 2-6, and the first demonstration of this optic was in the focusing of neutrons.<sup>76</sup>

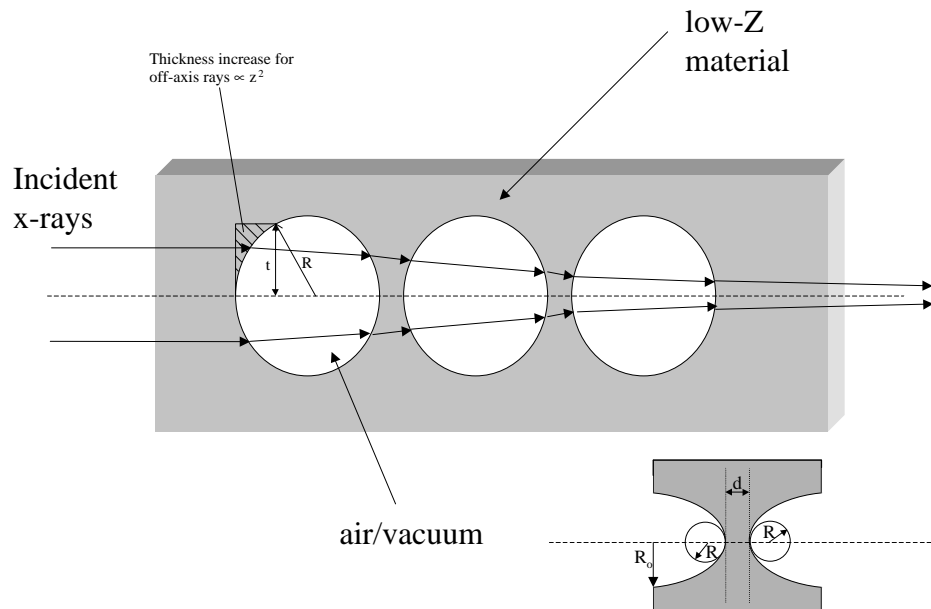


Figure 2-6: The Compound Refractive Lens.



To focus the x-rays, a series of holes are drilled into a material to refract the incident rays towards the optical axis. Since the refractive index decrement,  $\delta$  ranges from  $\sim 10^{-4} \rightarrow 10^{-7}$  in the x-ray region and the complex refractive index,  $\tilde{n}_{\text{air}} \sim 1 - \delta_{\text{air}} < 1$ , a concave lens is required.

The focal length of a single cylindrical lens of radius  $R$  is given by,

$$f = \frac{R}{2\delta} \quad \{2.17\}$$

and since  $\delta$  is small,  $f$  is relatively long. For example, beryllium at 10 keV and a lens radius of  $300 \mu\text{m}$ , would produce a focal length of 44 m. Snigirev *et al.*<sup>77</sup> proposed that it would be possible to reduce this obtrusive long focal length by combining many of these lenses in series to give ,

$$f = \frac{R}{2 N \delta} \quad \{2.18\}$$

where  $N$  is the number of lenses that form the CRL.

Although beryllium is thought to be the best material for manufacturing a CRL, it is a very difficult material to machine and is highly toxic, although some success has been recently demonstrated.<sup>78</sup> Subsequently, other materials have been tested to try to obtain the best functioning CRL such as a variety of plastics, polymers and aluminium compounds.<sup>78-81</sup>

Cylindrical holes suffer from spherical aberration and provide focusing in only one direction, and crossed lenses are required to focus in both planes. However, it is possible to manufacture rotationally symmetric parabolic profiles to focus the incident x-rays.<sup>78,82,83</sup> In this set up, the need for a crossed geometry is absent and the CRL is shorter, thereby increasing transmission. However, the experimentally measured gains are much smaller than the calculated values, and the focal spot is blurred due to lens imperfections and scattering effects. To maximise transmission, the mass absorption coefficient of the lens material should be minimised, which dictates low-Z materials.

It can be shown that the total length of a parabolic focusing lens is given by,

$$L_p = N \left( \frac{R_o^2}{R} + d \right) \quad \{2.19\}$$

where  $R_o$  is the radial aperture,  $R$  is the radius of the best-fit circle to the parabola vertex and  $d$  is the distance between adjacent parabola vertices (Figure 2-6). This distance must be small enough to provide good transmission but large enough to give inherent strength to the structure.

Figure 2-7 shows the calculated optical constants that govern refraction and absorption for two types of proposed compound refractive lens material (beryllium and aluminium) and the inter-lying air-void. As can be seen, the refractive index decrement falls sharply as the inverse square of the energy, and the optic is highly chromatic.

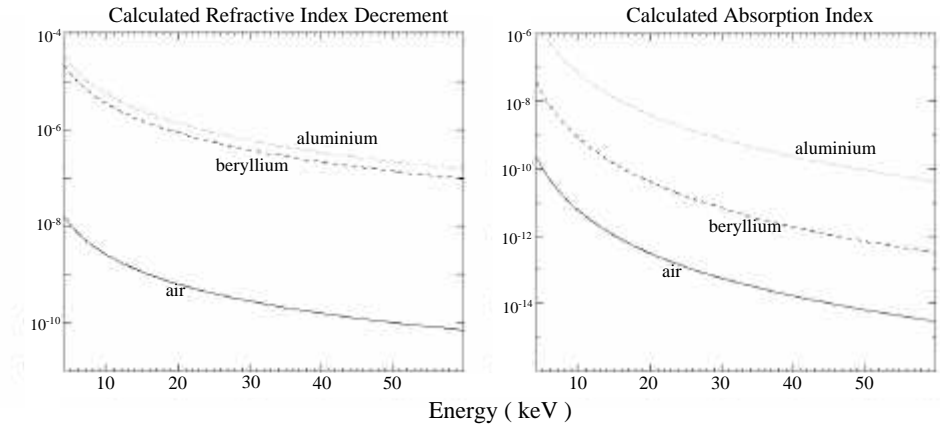


Figure 2-7: Optical constants for various CRL media. Data obtained from the Henke tables,<sup>1</sup> which can be found within the XOP computer package.<sup>84</sup>

With increasing incident x-ray energy, scattering effects can become a major contribution to the focal-spot blur. For example, the photoelectric cross-section is equal to the sum of the incoherent and coherent scattering cross-sections at  $\sim 12.2$  keV for beryllium.<sup>85</sup>

An excellent criterion for selecting a lens material is found by maximising the  $\frac{\delta}{\beta}$  ratio.<sup>79</sup> The transmission  $T_p$  and gain  $g_p$  for a parabolic lens have previously been reported<sup>78</sup> and are given by,

$$T_p = \frac{1}{a_p} \left[ 1 - e^{-a_p} \right] \left[ e^{-\mu N d} \right] \quad \{2.20\}$$

$$a_p = \mu N \frac{R_o^2}{R} \sim \left( \frac{\mu}{\rho} \right) \pi R_o^2 \left( N_A r_e \frac{Z}{A} \lambda^2 f \right)^{-1}$$

$$g_p \sim \frac{R_o^2 T_p}{\sigma_x \sigma_z} \left( \frac{u-f}{f} \right)^2 \quad \{2.21\}$$

where  $\frac{\mu}{\rho}$  is the mass absorption coefficient  $r_e$  is the classical electron radius,  $\sigma_x$  and  $\sigma_z$  are the horizontal and vertical source size (standard deviation), and  $u$  is the source-to-CRL distance. The gain is defined as the photon flux that would be measured through a pin-hole of dimensions equal to the CRL focused beam, when no lens is present.

Referring to Equation {2.20}, the transmission  $T_p$  is governed by the factor  $a_p$ , which is independent of the radius of curvature,  $R$ . This can be recognised by the following argument: for any given radial aperture  $R_o$ , a larger radius of curvature reduces the lens absorption but a greater number of lenses are needed to achieve the same focusing properties and these contributions cancel. Also,  $a_p$  is independent of the density of the lens material which can be understood from the larger refractive index of the heavier elements, which reduces the number of lenses needed, and the effects cancel. This also has the added benefit of reducing lens imperfections that tend to increase with a larger number of optical elements.

Another important parameter is the effective aperture, and is defined to be twice the radial distance at which the transmission falls by a factor of  $\frac{1}{e}$  through the system. Absorption increases as approximately the square of the distance from the lens axis and the effective aperture is given by,

$$A_{\text{eff}} = 2 \sqrt{\frac{R}{\mu N} \left( 1 - e^{-a_p} \right)} \quad \{2.22\}$$

Thus, as the focal length increases  $a_p$  decreases, the numerical aperture can be made larger and transmission is maximised (Equation {2.20}).

To give the reader an introduction to the theoretical predictions for CRLs, some calculations have been computed for two lens media, beryllium and aluminium at x-ray energies of 5 keV , 10 keV , 20 keV and 30 keV . The expected gain and demagnified source size for two insertion devices at the ESRF-ID22 (experimental hutch 1) and NSLS-X13B are presented: The FWHM source sizes in the vertical and horizontal directions are  $30 \mu\text{m} \times 700 \mu\text{m}$  and  $14 \mu\text{m} \times 950 \mu\text{m}$  for ID22 and X13 respectively. The source-to-lens distance  $u$  is taken to be inside the experimental hutches, which are 40 m (ID-22) and 25 m (X13B). For a 1 m long focal length, the corresponding FWHM demagnified image sizes for ID-22 and X13 are  $0.75 \mu\text{m} \times 17.5 \mu\text{m}$  and  $0.56 \mu\text{m} \times 38 \mu\text{m}$  respectively. The following parameters for the compound refractive lens are kept constant;  $R = 250 \mu\text{m}$ ,  $R_o = 500 \mu\text{m}$ ,  $d = 5 \mu\text{m}$ , and the length of the CRL is approximately equally to the number of holes in millimetres. The results are shown in Table 2-2, where  $g_{\text{ESRF}}$  and  $g_{\text{NSLS}}$  represent the calculated gains for these sources.

From Table 2-2, beryllium is the ideal candidate for CRL manufacture although the difficulty of machining and toxicity are prohibitive. Alternatively, aluminium is easy to machine and inexpensive. Although aluminium CRL transmission values of  $\sim 1\%$  seem small, they may offer the best hope of diffraction-limited resolution and can withstand the high-brightness of third-generation insertion-device sources. There are currently a number of plastic lenses that are being tested by Adelphi Technology Inc. (Palo Alto, California, U.S.A.), but their resistance to radiation damage has not yet been verified. Such lenses have been tested recently at the NSLS-X13B beamline and have performed poorly.<sup>86</sup> Aluminium CRL lenses have recently been shown to provide a focused x-ray beam with a vertical resolution of  $1.6 \mu\text{m}$  at the ESRF.<sup>82</sup>

Material	E (keV)	$\lambda$ (Å)	$\mu$ (m <sup>-1</sup> )	$\delta$ ( $\times 10^{-6}$ )	N	T <sub>p</sub> (%)	A <sub>eff</sub> ( $\mu$ m)	$\xi_{\text{ESRF}}$	$\xi_{\text{NSLS}}$
Al	5	2.480	51387	22.185	6	0.07	57	70	40
	10	1.240	6938	5.464	23	0.28	79	280	170
	20	0.620	924	1.348	93	0.76	108	760	460
	30	0.413	304	0.601	208	1.16	126	1170	700
Be	5	2.480	741	13.657	10	13.75	367	13910	8250
	10	1.240	113	3.408	37	24.03	485	24310	14420
	20	0.620	41	0.851	147	16.13	407	16315	9680
	30	0.413	33	0.378	331	8.61	303	8710	5170

Table 2-2: Design specifications of aluminium and beryllium CRLs that could be used at the NSLS X13B or ESRF ID-22 x-ray beamlines. Absorption coefficients are obtained from the Henke tables,<sup>1</sup> which can be found within the XOP computer package.<sup>84</sup>

A novel idea for using the lens as a collimator, and not a focusing device has been demonstrated by Baron *et al.*<sup>87-89</sup> In this set up, the synchrotron radiation source is placed at the focal position of the lens so that emerging rays exit approximately parallel to the optical axis, which has potential benefits for increasing the energy resolution and intensity of crystal monochromators.

### Advantages

Since the proposal that these devices could be useful in the hard x-ray region,<sup>77</sup> interest began to increase due to the simplicity and low cost of such an optic. Focusing on the micron-scale and below would readily make available micro-beam technology to every synchrotron radiation beamline at minimal cost. These optics are less sensitive to deviations in surface error than reflective devices as they operate at nearly normal-incidence, and can also be used at much higher energies. They are light, compact and

are relatively easy to align.<sup>90</sup> CRLs do not alter the optical axis of the system, unlike grazing incidence mirrors. Previous testing of parabolic aluminium refractive lenses have shown promising focusing properties with spot-sizes extremely close to their theoretical values<sup>78</sup> and in theory, should be able to approach diffraction-limited resolution.

### **Disadvantages**

The major disadvantage of CRLs is they have not yet been shown to focus to their specifications, and measured gains are much less than the calculated values.<sup>78</sup> This is most probably due to deviations from the parabolic shape, inherent in the manufacturing process. They are also very inefficient, due to absorption through the CRL material. These devices are extremely chromatic, as the focal length is proportional to the inverse of the wavelength squared, and spectroscopy experiments would prove cumbersome. Also, previously cited papers reveal large excess scattering around the focal position that would produce a significant background for many experiments.

## **2.6 Summary**

All of the aforementioned optics have benefits and disadvantages in their use. The most appealing optics for producing x-ray beam dimensions on the micron scale and below are those utilising grazing incidence reflective optics in the Kirkpatrick-Baez arrangement. Due to the new technology of differentially coating a spherical substrate to create an elliptical surface (Chapter 4, Chapter 5), sub-micron beams should be readily achieved. KB mirrors are relatively inexpensive to produce and an achromatic focus is one of their major benefits. To summarise this chapter, the properties of the various optics are reviewed in Table 2-3:

OPTIC	ENERGY RANGE (APPROX.)	ADVANTAGES	DISADVANTAGES	STANDARD RESOLUTION	BEST RESOLUTION
Kirkpatrick-Baez Elliptical Mirrors	< 25 keV	Achromatic, efficient, large aperture, point-to-point focusing, wide-energy range, long focal length (~1cm to 50 cm) i) bendable- flexible focal length. ii) differentially deposited-accurate figure possible.	High-energy cut-off of mirror material, differentially deposited-fixed focal length and ~ fixed source-to-optic distance.	1 $\mu\text{m}$ $\rightarrow$ 10 $\mu\text{m}$	0.46 $\mu\text{m}$ <sup>42</sup>
Zone Plates (Phase-Shifting)	< 8 keV	Phase-contrast experiments possible, long focal length.	Monochromatic and coherent beam required, chromatic, small aperture, demagnification decreases with energy, inefficient, difficult to manufacture-large aspect ratios.	< 0.5 $\mu\text{m}$	90 nm <sup>53</sup>
Bragg-Fresnel Optics	~ Unlimited	Phase-contrast experiments possible, long focal length.	Monochromatic and coherent beam required, chromatic, limited energy range for each optic, demagnification decrease with energy, inefficient. i) linear type - more energy range but one-dimensional focusing. ii) circular - two dimensional focusing but very limited energy range.	1 $\mu\text{m}$ $\rightarrow$ 2 $\mu\text{m}$	0.7 $\mu\text{m}$ <sup>60</sup>
Capillaries	< 10 keV	Inexpensive, could replace pin-holes as a final concentrating stage.	Small aperture, impossible to polish, energy-dependent beam-profile, sample placement very close to aperture, limited lifetime (radiation damage).	< 10 $\mu\text{m}$	95 nm <sup>66</sup>
Wave-guides	> 10 keV	Phase-contrast experiments possible, good for projection microscopy.	Inefficient, very small aperture, one-dimensional focusing, sample placement very close to aperture.	< 0.5 $\mu\text{m}$	0.4 $\mu\text{m}$ <sup>70</sup>
CRL	> 10 keV	Inexpensive, large energy-range (few keV) for each lens system.	Small aperture, inefficient, lens imperfections, chromatic, demagnification decreases with energy, limited lifetime for plastic and polymer lenses (radiation damage).	< 5 $\mu\text{m}$	1.58 $\mu\text{m}$ <sup>82</sup>

Table 2-3: Hard x-ray micro-probe optic review.

## **Chapter 3 Synchrotron radiation and the NSLS X13 straight-section**

This chapter will introduce the basic concepts needed to understand the usefulness of synchrotron radiation, and will proceed with a brief overview of the National Synchrotron Light Source facility (NSLS).<sup>†</sup> The NSLS X13B x-ray beamline and operation will then be described fully, at which the experiments that constitute this thesis were performed. A well-grounded knowledge of synchrotron radiation is an essential step towards the successful completion of an experiment. Each storage ring facility around the world has a unique design, the most important being the energy of the electron beam, and the researcher may benefit by performing experiments at a particular location. There are numerous texts that give excellent in-depth descriptions of synchrotron radiation, and the reader should consult these for more rigorous explanations.<sup>43,91,92</sup>

### **3.1 Properties of synchrotron radiation**

Synchrotron radiation are the electromagnetic waves originating from accelerated charged particles and were initially thought of as a parasitic phenomena in the early years of high energy accelerators. The first reported observation of synchrotron radiation was at the General Electric Company's electron accelerator in 1947.<sup>93</sup>

Synchrotron radiation is chiefly associated with electron storage rings that are specifically designed to enhance the qualities of this radiation. These facilities circulate electrons in bunches within a vacuum environment, and the radiation which is emitted tangentially to the electron orbit, is collected several metres away in various experimental enclosures. However, before the experimentalist uses this radiation, it is usually modified in some way. For example, a narrow-band of wavelengths may be selected by a silicon monochromator or the light could be focused by a toroidal mirror, depending upon experimental requirements.

---

<sup>†</sup> The National Synchrotron Light Source is situated within the Brookhaven National Laboratory, Upton, New York, USA.



Returning to the basics of synchrotron radiation, the electrons are made to orbit in a circular path by applying a magnetic field using dipole-bending magnets that are situated at various locations within the storage ring. When the electron trajectory is altered by these dipole magnets, the electrons are accelerated and synchrotron radiation is emitted. As the electron energy of a typical storage ring is in the GeV range, the electrons are travelling relativistically and the radiation is strongly peaked in the forward direction of the electron motion. The energy that the electrons lose due to the emission of synchrotron radiation must be replaced for them to maintain their circular orbit. This is achieved by radio-frequency (RF) cavities that use time-varying electric fields to accelerate the electrons back to their original energy. Some important equations that describe the properties of synchrotron radiation are set out below.<sup>†</sup>

$$\text{Synchrotron opening angle, } \theta \sim \frac{1}{\gamma} \quad \{3.1\}$$

$$\text{Relativistic factor, } \gamma = \frac{E^*}{m_e c^2} = \frac{1}{\sqrt{1 - \frac{v^2}{c^2}}} \sim 1957 E^* [\text{GeV}] \quad \{3.2\}$$

$$\text{Bending magnet radius, } R[\text{m}] \sim \frac{3.33 E^* [\text{GeV}]}{B[\text{T}]} \quad \{3.3\}$$

$$\text{Critical wavelength, } \lambda_c [\text{\AA}] \sim \frac{5.59 R[\text{m}]}{E^{*3} [\text{GeV}]} \sim \frac{18.64}{B[\text{T}] E^{*2} [\text{GeV}]} \quad \{3.4\}$$

$$\text{Critical Energy, } E_c (\text{keV}) \sim \frac{2.22 E^{*3} [\text{GeV}]}{R[\text{m}]} \sim 0.665 E^{*2} [\text{GeV}] B[\text{T}] \quad \{3.5\}$$

where  $E^*$  and  $v$  are the energy and speed of the electrons which travel in an arc of radius  $R$  due to the magnetic field  $B$ . The rest mass and speed of light in a vacuum are represented by the symbols,  $m_e$  and  $c$ .  $E_c$  and  $\lambda_c$  are the critical energy and critical

---

<sup>†</sup> These parameters can also be changed locally within sections of the storage ring by ‘insertion devices’ such as wigglers and undulators (Section 3.3.1 and Section 3.3.2).

wavelength of the x-ray photon beam which divide the synchrotron power spectrum in half.

The energy and wavelength of the photons are related by the expression,

$$E = \frac{hc}{\lambda} \rightarrow E[\text{keV}] \sim \frac{12.398}{\lambda[\text{\AA}]} \quad \{3.6\}$$

To compare the various synchrotron radiation facilities around the world, a number of terms have been devised so that comparisons can be made:<sup>†</sup>

**Flux** - The number of photons emitted per second per 0.1% bandwidth.

**Brilliance** - The number of photons emitted per second per 0.1% bandwidth into a solid angle of 1 mrad<sup>2</sup>.

**Brightness** - The number of photons emitted per second per 0.1% bandwidth into a solid angle of 1 mrad<sup>2</sup> from a source size of 1 mm<sup>2</sup>.

These definitions are quoted in terms of ‘0.1% bandwidth’ because the broad-band synchrotron radiation is often monochromated to select a narrow wavelength range. For example, a silicon double-crystal monochromator set to select an energy of 10 keV has an intrinsic bandwidth of approximately 0.01 % .

---

<sup>†</sup> The definitions, brilliance and brightness are those used in the United States. In the European Union, these definitions are interchanged.

### 3.2 The National Synchrotron Light Source

The NSLS is a unique facility in that it operates two separate electron storage rings. One delivers photons in the x-ray region ranging from around 1 keV and upwards, and the other operates in the vacuum ultra-violet (VUV) part of the electromagnetic spectrum. A 100 keV triode electron gun is the source of electrons that are accelerated to an energy of 120 keV by a linear accelerator (LINAC). These electrons are then fed into a booster synchrotron that accelerates them to an energy of 750 MeV before delivering them either to the x-ray or VUV rings for further acceleration. To-date, the x-ray ring has two modes of electron energy use, one at 2.584 GeV and the other at 2.8 GeV, while the VUV ring operates at 800 MeV. The circumference of the storage ring is 170.1 m,<sup>†</sup> and there are 16 dipole bending magnets of field strength 1.25 T ( $E^* = 2.584 \text{ GeV}$ ). The electron energies of 2.584 GeV and 2.8 GeV correspond to critical photon energies (Equation {3.5}) of 5.6 keV and 7.1 keV. The storage ring can be operated in either single bunch or 30 bunch mode, with a maximum beam current of ~280 mA for 30 bunch operations. A diagram of the storage ring is shown in Figure 3-1.

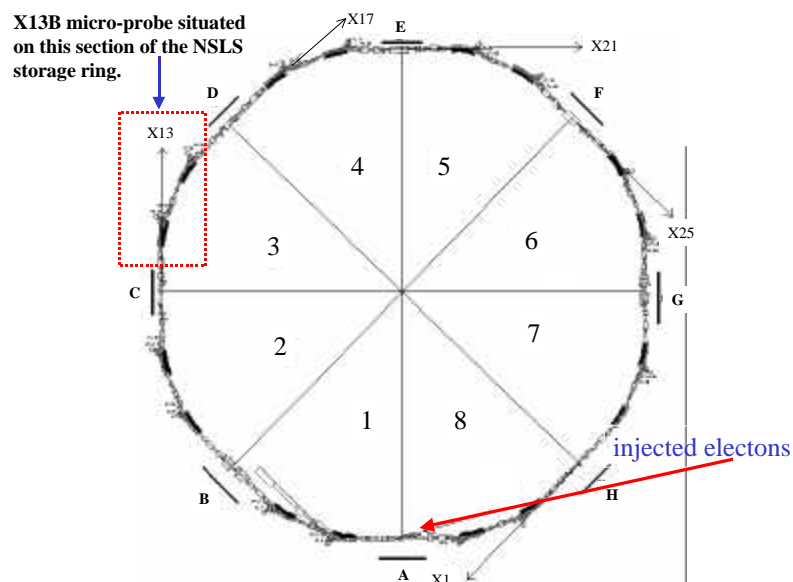


Figure 3-1: NSLS X-ray Storage ring: 1-8=super periods A) Injection Straight B) RF Cavity C) X13 Straight-Section (S.S) D) X17 Superconducting Wiggler S.S. E) X21 Hybrid Wiggler S.S. F) X25 Hybrid S.S. G) RF Cavity H) X1 Soft X-ray Undulator S.S.

<sup>†</sup> All subsequent references to the word 'storage ring' will refer to the NSLS x-ray storage ring.

The magnetic design of the storage ring is that of the Chasman-Green lattice which was developed at the NSLS and is implemented at many synchrotron sources worldwide.<sup>94</sup> Each magnetic section of the ring is divided into 8 super-periods, which consist of 2 dipole bending magnets. Also, several focusing magnets are located in these super-periods to maintain the electron trajectory.

The electron beam parameters are given by the following equations and detailed in Table 3-1 for two sources at the NSLS.

$$\sigma_x \sim \left[ \epsilon_x \beta_x + (\eta \sigma_E)^2 \right]^{\frac{1}{2}} \quad \{3.7\}$$

$$\sigma_z \sim \left[ \epsilon_z \beta_z \right]^{\frac{1}{2}} \quad \{3.8\}$$

$$\Sigma_x' = \left[ \epsilon_x \frac{1 + \alpha_x^2}{\beta_x} + (\sigma_E \eta_x')^2 \right]^{\frac{1}{2}} \quad \{3.9\}$$

$$\Sigma_z' = \left[ \epsilon_z \frac{1 + \alpha_z^2}{\beta_z} \right]^{\frac{1}{2}} \quad \{3.10\}$$

	NSLS X13 Straight Section		NSLS Dipole Bending Magnet	
Electron Energy , E <sup>*</sup>	2.584 GeV	2.8 GeV	2.584 GeV	2.8 GeV
H. Emittance, $\epsilon_x$	94 nm rad	111 nm rad	94 nm rad	111 nm rad
V. Emittance, $\epsilon_y$	0.10 nm rad	0.12 nm rad	0.10 nm rad	0.12 nm rad
H. Beta Function, $\beta_x$	1.7 m	1.7 m	1.5 m	1.5 m
V. Beta Function, $\beta_z$	0.37m	0.37m	15.7 m	15.7 m
H. Momentum Compaction Factor, $\alpha_x$	0.23	0.23	0.0	0.0
V. Momentum Compaction Factor, $\alpha_z$	-0.017	-0.017	2.5	2.5
Dispersion Function, $\eta$	-0.057 m	-0.057 m	0.25 m	0.25 m
Dispersion Slope, $\eta'$	0.031	0.031	0.2	0.2
Energy Spread, $\sigma_E$	8.6x10 <sup>-4</sup>	9.3x10 <sup>-4</sup>	8.6x10 <sup>-4</sup>	9.3x10 <sup>-4</sup>
H. Source Size, $\sigma_x$	404 m	437 m	433 m	470 m
V. Source Size, $\sigma_z$	6.1 m	6.6 m	39.6 m	42.9 m
H. Source Divergence, $\Sigma_x'$	243 rad	263 rad	304 rad	330 rad
V. Source Divergence, $\Sigma_z'$	16.4 rad	17.7 rad	6.8 rad	7.4 rad

Table 3-1: NSLS Source Characteristics for the X13 straight-section and dipole bending magnet sections. H.=horizontal, V.=vertical. All values are quoted in terms of the standard deviation.

As defined previously, brightness and flux are important measures of the synchrotron radiation quality at electron storage rings and some calculated values are presented for three synchrotron sources in Figure 3-2 and Figure 3-3. These two graphs are extremely important to the experimentalist as the number of photons delivered to the sample can be estimated from these curves. The graphs may at first appear somewhat confusing but they should give the reader an insight to the potential power of synchrotron radiation. The seven smooth curves represent radiation from dipole bending magnets and wiggler devices, whereas the curves which show a degree of structure emanate from undulator devices that exhibit coherence effects. It should be emphasised that the radiation properties measured at a beamline will not follow these curves as objects placed in the path of the photon beam will affect them. However, corrections can be made to retrieve the calculated values.

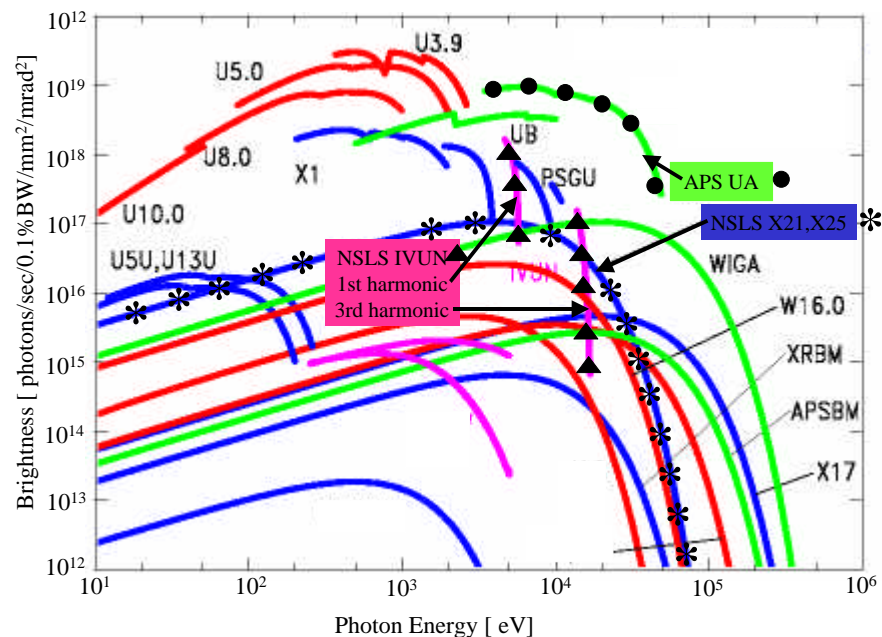


Figure 3-2: Brightness comparisons between the various x-ray sources located at several United States synchrotron radiation facilities: NSLS=National Synchrotron Light Source (at 400 mA). APS=Advanced Photon Source (at 200 mA).

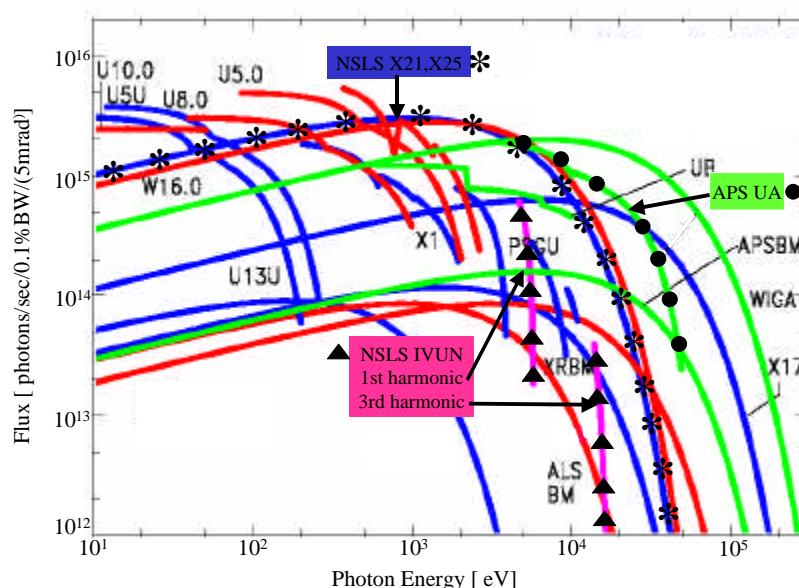


Figure 3-3: Flux comparisons between the various synchrotron radiation facilities: NSLS=National Synchrotron Light Source (at 400 mA). APS=Advanced Photon Source (at 200 mA).

To highlight the difference between the terms ‘brightness’ and ‘flux’, I draw the attention of the reader to the curves representing the insertion device UA (APS) and the curve representing the insertion devices, X21 and X25 (NSLS). In the graph representing brightness, the peaks of these curves are approximately two orders of magnitude apart whereas in the graph representing flux, they are approximately equal. The reason behind this apparent discrepancy is that UA is an undulator source which can concentrate the synchrotron radiation into a much narrower cone than that of a dipole bending magnet or wiggler source (Section 3.3.1). Hence, if the intensity of the photon beam is measured with a 100  $\mu\text{m}$  pinhole, a higher value will be obtained at UA than either at the X21 or X25 wiggler beamlines. However, if the entire number of photons are detected, then the overall intensity will be comparable. X-ray micro-focusing optics have apertures of only a few hundred microns and brightness is the best parameter to use to estimate the number of photons delivered to the sample.

### 3.3 The X13 straight-section and X13B beamline

The X13 straight section is a dedicated research beamline that is used to test and develop small-gap insertion devices. The small betatron function within the X13 straight section allows for small gap devices such as IVUN<sup>95,96</sup> to be located there with

negligible effect on the x-ray ring current. It currently houses two insertion devices, namely an In-Vacuum undulator (IVUN), and a time-varying elliptically polarised wiggler (EPW).<sup>97-100</sup>

### 3.3.1 IVUN

An undulator is a magnetic array that is located in a straight section of a storage ring. The magnetic field forces the electrons into a periodic motion about their mean value and thus synchrotron radiation is emitted. Undulators differ from wiggler devices in that interference effects are important.<sup>†</sup> IVUN is situated in the X13 straight section at a distance of 25.631 m from the centre of the X13B experimental hutch (Figure 3-7). A schematic of an undulator is shown in Figure 3-4, and the IVUN parameters are summarised in Table 3-2.<sup>95,96</sup>

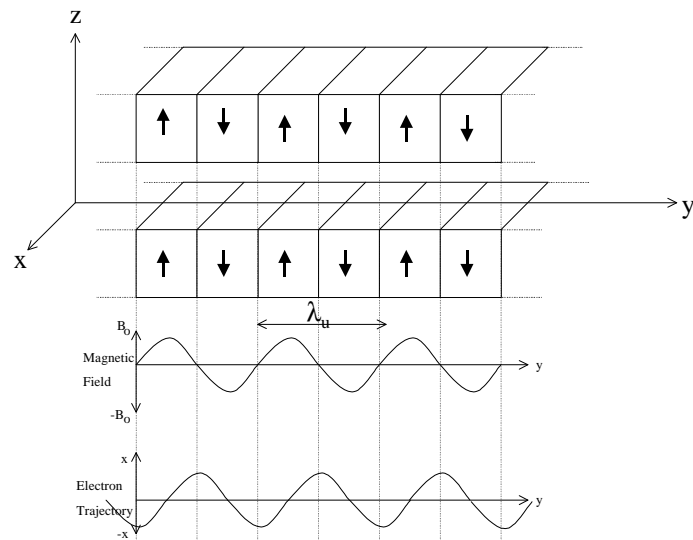


Figure 3-4: Basic undulator design: The magnetic field in the z-direction is designed so that it is sinusoidal along the y-direction. The electron motion is then also sinusoidal in the x-y plane.

Magnetic Parameter	Value
Magnetic Period	1.1 cm
Number of Magnetic Periods	31
Peak on-axis field ( gap =3.3 mm )	0.678 T
Deflection Parameter , K ( gap =3.3 mm )	0.7
Magnetic Gap	3.7 mm – 10 mm

Table 3-2: IVUN Magnetic Parameters.

<sup>†</sup> Hard x-ray wiggler devices can behave like undulators at photon energies  $\ll 1$  keV .<sup>101</sup>

All periodic magnetic arrays can be classed as either undulators or wigglers through the deflection parameter,

$$K \sim 0.934 \lambda_u [\text{cm}] B_o [\text{T}] \quad \{3.11\}$$

where  $B_o$  is the peak on-axis field (depends on gap) and  $\lambda_u$  is the magnetic period.

For IVUN,  $B_o = 0.678 \text{ T}$  at a magnetic gap of  $3.3 \text{ mm}$ , giving a deflection parameter,  $K \sim 0.7$ . As this value is less than 1, the device is categorised as an undulator: The deflection angle of the electron trajectory through the magnetic structure is less than the natural emission angle of the synchrotron radiation and this phenomenon gives rise to coherence effects. Coherency provides a large increase in intensity given by,

$$I_{\text{undulator}} \propto N_p^2 E^{*2} [\text{GeV}] \quad \{3.12\}$$

where  $N_p$  is the number of poles (and the dominant factor),  $E^*$  is the electron energy, and the intensity is much larger than that of a wiggler (Equation {3.15}).

Collecting the photons within a small on-axis cone, the peak wavelengths of the emitted radiation are given by,

$$\lambda_n \sim \frac{\lambda_u}{2n \gamma^2} \left( 1 + \frac{K^2}{2} + \gamma^2 (\theta^2 + \psi^2) \right) \quad \{3.13\}$$

where  $\theta, \psi$  are the angles of observation in the horizontal and vertical planes,  $n$  is the harmonic number, and  $\gamma$  is the synchrotron opening angle. In theory,  $n = 1, 3, 5, \dots$  and even harmonics are excluded.

The flux of the IVUN first harmonic (at  $\sim 5.5 \text{ keV}$ ) is almost an order of magnitude greater than that of the corresponding NSLS bending magnet (Figure 3-3), and the small opening angle of the undulator radiation produces a brightness of over two orders of magnitude more between the two sources (Figure 3-2). Further gains can



be found at the second<sup>†</sup> and third harmonics where the intensity of the corresponding dipole bending magnet spectra falls drastically. Due to the coherency of the undulator source there are also angular harmonics given by,

$$\phi_{n,l} \sim \frac{1}{\gamma} \sqrt{\frac{1}{n} \left[ 1 + \frac{K^2}{2} \right]} \quad \{3.14\}$$

where  $n$  is the energy harmonic number as in Equation {3.13} and the angular harmonics are indexed by  $l = 0, 1, 2, \dots$

For example, for 2.8 GeV operations (relativistic factor  $\sim 5480$ ) and a  $K$  value of  $\sim 0.7$  (IVUN magnetic gap = 3.3 mm), the first harmonic of IVUN is found at a wavelength of 2.28 Å (5.4 keV), the third harmonic at 16.2 keV and emittance effects produce the second harmonic at 10.8 keV. Selecting the first harmonic by the double-crystal monochromator at the X13B beamline and moving off-axis, one would expect to see enhancements in flux at:  $\theta_{1,0} = 0$  mrad,  $\phi_{1,1} = 0.2$  mrad and  $\phi_{1,2} = 0.28$  mrad. However, with the inclusion of emittance effects, the angular harmonics become ‘smeared out’ and the undulator structure disappears. As can be understood from the above discussion, emittance plays a major role in determining the overall undulator emission structure. Using the source and magnetic characteristics for IVUN as defined in Table 3-1 and Table 3-2, the photon characteristics can be computed and compared to a ‘perfect’ source with zero emittance. This is visualised in Figure 3-5, where the undulator spectra were calculated by the insertion-device module within the SHADOW ray-tracing package (Section 4.5).<sup>102</sup> In Figure 3-5, notice how the angular rings are clearly visible for a source with zero emittance and how these disappear using the IVUN source characteristics. However, even with the inclusion of emittance, the vertical photon beam opening angle is significantly smaller than that from a dipole bending magnet source and the undulator is well suited for small-aperture x-ray micro-probe optics.

---

<sup>†</sup> The second harmonic ( $n = 2$ ) is found strongly on axis primarily due to emittance effects within the X13 straight section.

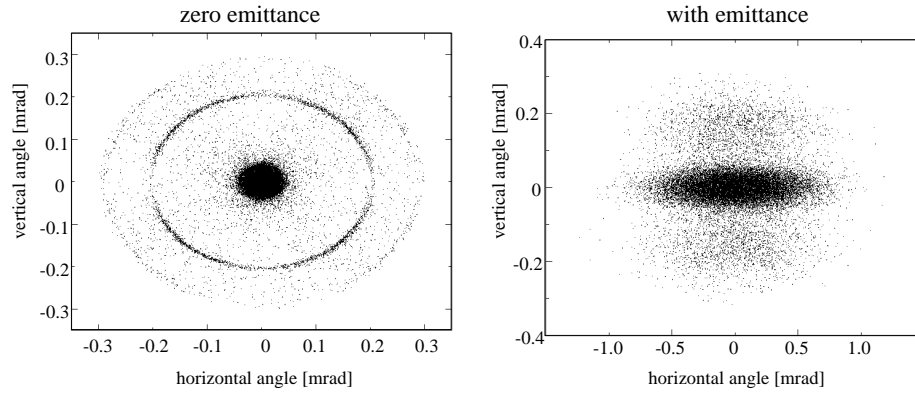


Figure 3-5: Emittance effects on undulator angular photon distribution at the IVUN first harmonic.

A plot of the calculated flux for the first three harmonics of IVUN (magnetic gap = 3.7 mm) is shown in Figure 3-6. This plot was generated using the computer code ‘XURGENT’.<sup>103</sup>

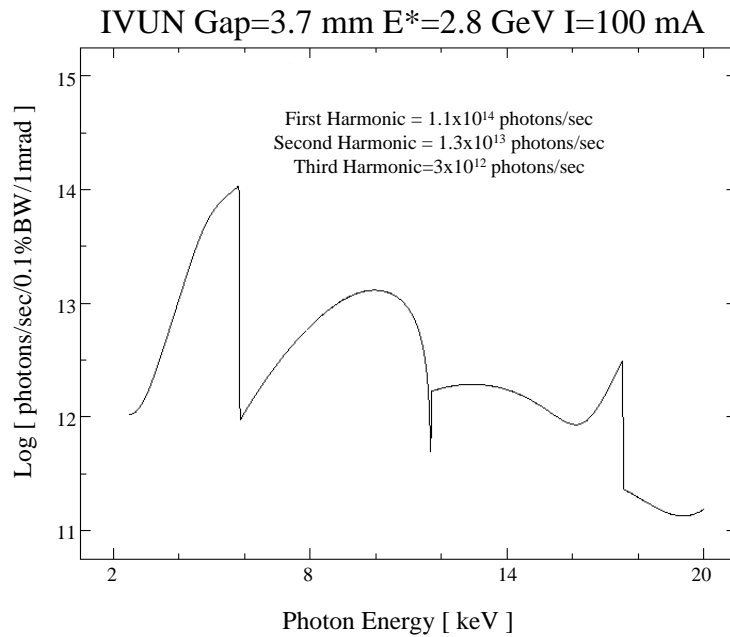


Figure 3-6: Calculated IVUN on-axis spectra integrated over all vertical emission angles.

### 3.3.2 EPW

Wiggler devices are distinguished from undulator arrays by a larger K-parameter. As the value of K increases, interference effects become less important. The critical energy of a single magnetic dipole can be simply expressed by Equation {3.5}, and by increasing the magnetic field, a ‘harder’ synchrotron spectrum is obtained that allows

for medium energy storage rings to greatly increase their critical energy (superconducting magnets can reach fields in excess of 10 Telsa<sup>104</sup>). By combining many of these magnetic periods together, the radiation from the different bends of the electron trajectory add together to give a total intensity of

$$I_{\text{wiggler}} \propto N_p E^{*4} [\text{GeV}] \quad \{3.15\}$$

where  $N_p$  is the number of magnetic poles and  $E^*$  is the electron energy.

The X13 EPW<sup>97-99</sup> is situated in the X13 straight section and is 24.731 m from the centre of the X13B experimental hutch (Figure 3-7). This EPW differs somewhat from a standard wiggler in that as well as having the usual magnetic array in the vertical plane, there is also an interlaced periodic array in the horizontal plane. However, unlike the permanent magnetic field, the horizontal field is electromagnetic, having the ability to switch the direction of magnetisation by up to 100 Hz . By applying this time-varying horizontal field, the electrons are made to travel in a helical trajectory about their ideal orbit and the emitted radiation is circularly polarised. Circular polarised photons are used extensively in x-ray magnetic circular dichroism (XMCD) experiments. For the experiments in this thesis that utilised the EPW device, the electromagnetic field was switched off. The parameters of the EPW are displayed in Table 3-3.

Magnetic Parameter	Permanent Magnet Value	Electromagnet Value
Magnetic Period	16 cm	16 cm
Full strength Poles	5	6
Peak Field [T]	0.8	0 – 0.2
Deflection Parameters	Kz = 12	Kx = 0 – 3
Magnetic Gap	2.7 cm	5.3 cm

Table 3-3: NSLS X13 EPW magnetic parameters.

### 3.3.3 The X13B beamline

A schematic of the X13B beamline is shown in Figure 3-7. The X13 straight section has two beamlines through which the synchrotron radiation can be directed, X13B and X13A.<sup>105</sup> X13A (not shown) is a soft x-ray beamline that can be fed from the photons

that are deflected from their original direction by a copper-coated silicon mirror located immediately after the shield wall. As the fan of synchrotron radiation is finite, this mirror can be inserted halfway into the beam to allow simultaneous operation of X13A and X13B. There are a set of copper-coated water-cooled slits that are situated behind the shield wall and 10 m from the centre of the X13 straight section. These slits can be opened and closed in the horizontal and vertical directions. Closing them in the vertical direction limits the angular divergence of the photon beam on the X13B monochromator and improves energy resolution. In addition, there are also four sets of copper water-cooled slits that form the slit ladder that is situated upstream of the X13B monochromator.<sup>†</sup> This ladder has settings of 4 mm and 2 mm and also improves energy resolution. Two slits of openings 4 mm and 2 mm are uncovered, and the other two have a 127  $\mu\text{m}$  amorphous graphite attenuator placed over them. This filter limits the incident power on the monochromator and is important for stable use when the IVUN insertion device is used.

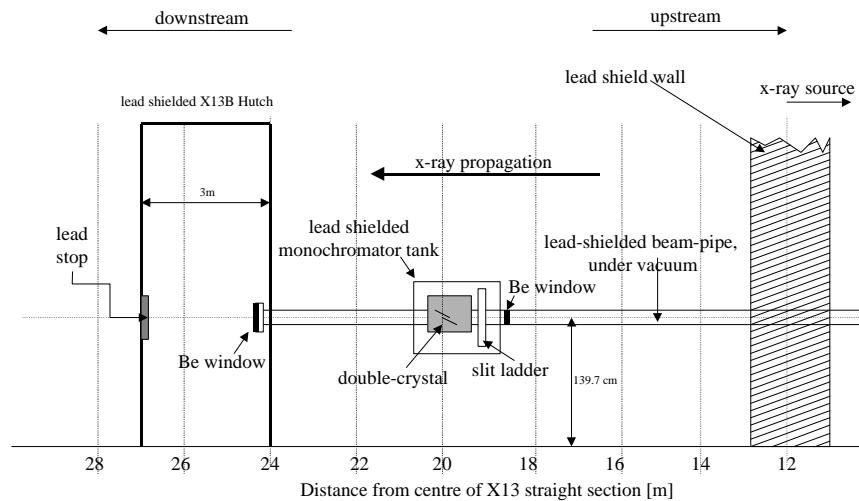


Figure 3-7: X13B Beamline Schematic. The insertion devices, IVUN and the EPW are 25.631 metres and 24.731 metres from the centre of the hutch respectively. The monochromator is a Si (111) water-cooled channel-cut device in the parallel geometry.

Various sections of the X13B beamline are segmented by 127  $\mu\text{m}$  thick plates of beryllium to isolate it from the storage ring vacuum. There are three Be windows on the

<sup>†</sup> There is also a variable horizontal aperture here too.

X13B beamline, two are shown in Figure 3-7 and the other one is nearer to the storage ring. A plot of the transmission of these with respect to x-ray energy is shown in Figure 3-8.

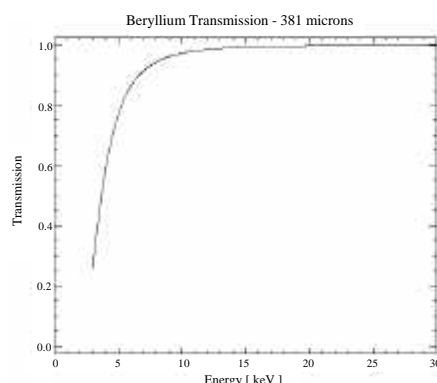


Figure 3-8: Plot of the x-ray transmission through the combined beryllium window thickness at the NSLS X13B beamline.

The reliability and performance of the X13B monochromator has to be well-defined for a successful experiment and will be described in some detail: Many experiments use monochromatic radiation. The most popular way of singling out a narrow band of wavelengths from a broad-band source is through crystal optics. Crystals such as silicon and germanium are excellent materials for manufacturing a monochromator as they can be grown to high purity specifications, large dimensions and can be easily machined. The inter-atomic plane spacing in crystals are well matched to x-ray wavelengths, and from Bragg's law,<sup>3</sup>  $n\lambda = 2d \sin \theta_i$ , a photon of wavelength  $\lambda$  incident on a crystal at an angle  $\theta_i$  to the lattice planes of spacing  $d$  will be reflected if this equation is satisfied. From a synchrotron source, the radiation is divergent and the incident photon beam makes a range of angles to the crystal planes. As the incident radiation consists of a very broad band of frequencies, there will be a range of energies that satisfy the Bragg condition due to the divergent property of the radiation. X13B uses a double-crystal monochromator in the non-dispersive (+,-) geometry. The crystal is machined from a block of high-purity silicon, which has minimal defects, and cut by a diamond saw so that the (111) planes are parallel to the crystal surface. By cutting a channel within the silicon, the beam is made to undergo two Bragg reflections in this case (Figure 3-9), and the direction of propagation is preserved. The lower crystal is mounted onto the top of a

water-cooled copper heat sink, that is in contact with an indium-gallium heat transfer medium, and this dissipates the incident heat load very efficiently.

Crystal heating is a serious problem in monochromators as the power dissipated in the first crystal produces a temperature rise with a corresponding increase in the lattice spacing. The temperature increase is non-uniform, with a heat-bump situated at the place of photon impingement.<sup>106</sup> The overall effect is to decrease the energy resolution and reduce the reflected intensity. Due to the gradual decay of the stored electron beam current, the dissipated power falls, and the lower crystal cools down. Due to this, the peak energy of Bragg reflection can drift during an experiment which can be the order of 1 eV if adequate cooling is not provided. At third-generation sources where the incident power can be several orders of magnitude greater than that at a second-generation storage facility, liquid-nitrogen cooling is often used.<sup>107</sup> In experiments where energy drifts cannot be tolerated, precise characterisation of the monochromator is required to determine its performance. If energy drifts do occur, it may be possible to compensate for them. One method is to perform periodic absorption scans through a known metal foil to determine absorption-edge location.

By thorough analysis of the X13B monochromator, it was discovered that within the first hour of operation when the lower crystal was heating up, the energy was unstable and reached equilibrium after this period with no noticeable drift. The electron beam is refilled every twelve hours at the NSLS, and the crystals are allowed to stabilise before any measurements are undertaken. The physical dimensions and orientation of the crystals determine the energy range that can be used. Simple geometry reveals that the vertical displacement between the incident and diffracted beams is twice the crystal gap multiplied by the cosine of the incidence angle. The geometry of the X13B monochromator crystals is shown in Figure 3-9.

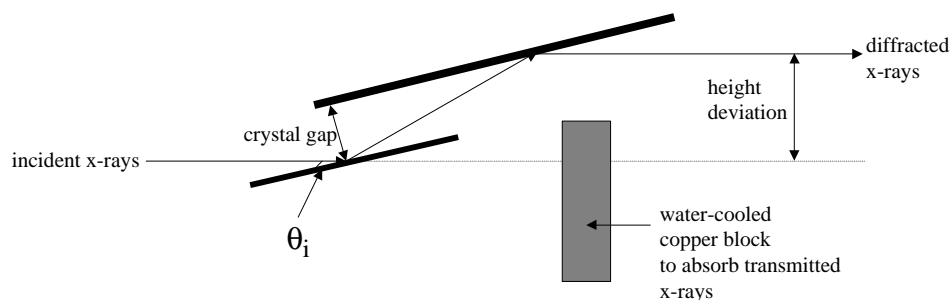


Figure 3-9: X13B monochromator schematic.

The crystal gap of the X13B monochromator is 6.858 mm and the effect of varying the incidence energy from 4 keV → 12 keV is shown in the graph below.

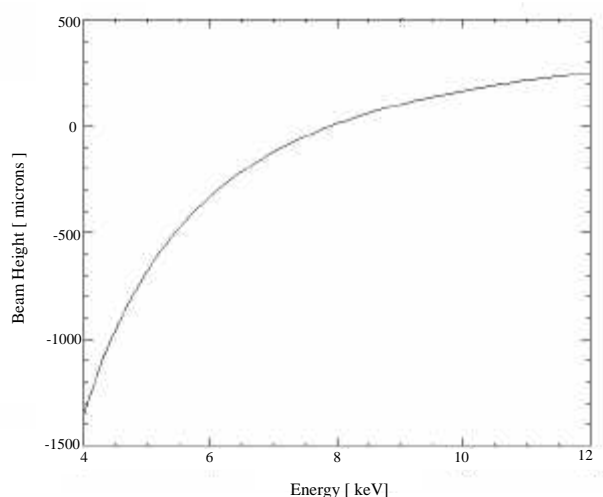


Figure 3-10: Vertical beam height change from the X13B double-crystal monochromator.

The angular photon distribution can be approximated by calculating the opening angle of the synchrotron radiation<sup>91</sup> (Equation {3.1}), which is of the order of 0.2 mrad at the NSLS for the wiggler source. Thus the X13B monochromator is subjected to a large range of incidence angles and the energy resolution is broadened because of this. By closing the front-end slits or utilising the slit-ladder upstream of the monochromator, the angular spread is reduced and energy resolution is improved. For micro-focusing optics situated within the X13B experimental hutch that have acceptance apertures of a few hundred microns, the incident photon beam will overflow these. However, when energy is tuned, the beam will move across them as displayed in Figure 3-10. This is not so crucial during an experiment where energy ranges of < 2 keV are often used, and the

effect is further minimised at higher photon energies. However, experiments conducted at markedly different energies may require for the micro-focusing optics to be raised or lowered to intercept the radiation emerging from the monochromator before measurements are undertaken.

The 2d spacing for the X13B monochromator Si (111) reflection is  $6.271 \text{ \AA}$ , and x-ray energies from 3 keV to 30 keV correspond to incidence angles of  $41^\circ$  and  $3.8^\circ$ . For shorter wavelengths, the incidence angle becomes very shallow and a longer upper crystal is needed to intercept the reflected radiation from the lower crystal. The lower and upper crystals of the X13B monochromator are 3.81 cm and 8.509 cm in length respectively and are separated by a gap of 6.858 mm. This monochromator was designed to operate in the energy range of  $\sim 4 \text{ keV} \rightarrow 26 \text{ keV}$ . The double-crystal is cut from the same block of silicon thus allowing the upper and lower portions to remain linked. It is mounted to a pivot, which is connected to a 30 cm tangent arm that is rotated by the combination of a five-phase Berger-Lahr rotational motor (with a 10:1 gear reducer) and a high-precision micrometer screw. With a half step-size of  $0.5 \mu\text{m}$ , this provides an angular resolution of  $0.17 \mu\text{rad}$ . This turns the lower crystal so that the centre of rotation lies halfway along the surface. Also, a piezo-driven screw is incorporated into the monochromator design, which can be used to slightly alter the angle of the upper crystal and is extremely important for eliminating higher order harmonics emerging from the lower crystal.

### **3.3.4 X13B monochromator characterisation**

The following graphs show a selection of measurements that were performed at X13B to enable characterisation and calibration of the double-crystal Si (111) monochromator. All measurements were recorded using a 30 cm ionisation chamber with an applied 1 kV voltage within the X13B experimental hutch, with the exception of data displayed in Figure 3-12 that used a silicon-pn-photodiode to capture the diffracted x-rays emerging from the analyser crystal.



Figure 3-11 shows the broad nature of the IVUN second harmonic. The measurement was performed at the electron energy,  $E^* = 2.8 \text{ GeV}$  and magnetic gap of 3.7 mm. The energy was scanned by varying the incidence angle of the X13B monochromator, and the photon flux was detected by measuring the current produced from a 30 cm ionisation chamber (inside the experimental hutch) as the x-rays passed through it. The peak is located at  $\sim 10.7 \text{ keV}$ , and there are sharp drops in intensity in parts of the spectrum that are due to various reflections being brought into the Bragg condition as the crystals are rotated. These are referred to as glitches.

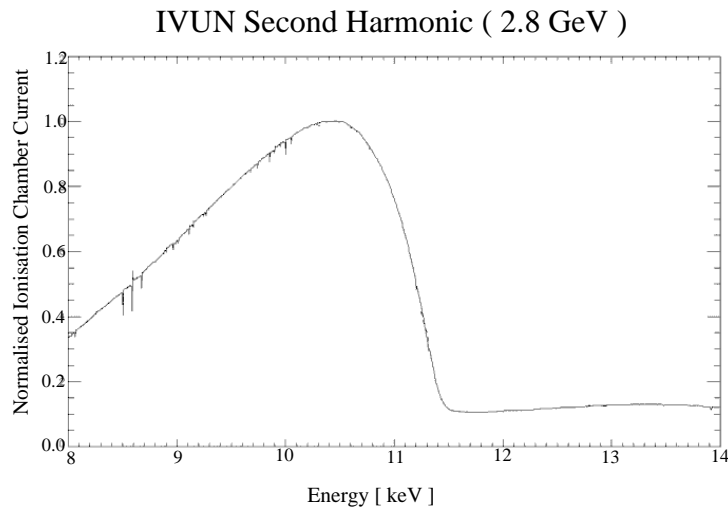


Figure 3-11: IVUN second harmonic. Magnetic parameters are shown in Table 3-2.

Figure 3-12 shows two measurements, which were used to examine the energy resolution of the Si (111) monochromator. For this measurement, the front-end slits were closed to limit the source acceptance to  $\sim 0.005 \text{ mrad}$ . A single Si (220) analyser crystal was fixed to a rotatable goniometer head inside the X13B experimental hutch and the EPW was the source of x-rays for this measurement. The analyser crystal was aligned with the incident x-ray beam, and a silicon-pn-photodiode was used to detect the Bragg reflected rays emerging from it. The incident x-ray energy was selected by setting the X13B monochromator angle, and the analyser crystal was rotated to reflect the incident x-rays. This measurement provides a distribution called a ‘rocking curve’<sup>3</sup> which gives a measure of the energies emerging from the X13B monochromator crystal i.e. the energy resolution.

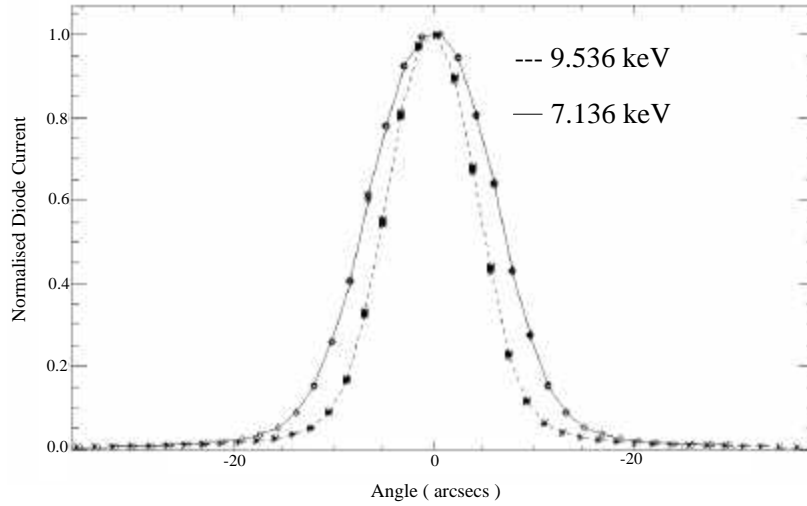


Figure 3-12: Si (220) rocking curves at two incident x-ray energies as selected by the X13B monochromator.

Two measurements are shown in the above graph at energies of 9.536 keV and 7.136 keV with FWHMs of 10.7(8.76) arcsecs and 14.7(12.79) arcsecs, where the numbers in parentheses are the calculated values.<sup>†</sup> These widths are increased slightly from the calculated values due to the angular divergence of the photons incident on the monochromator and analyser crystals. The energy resolution of the X13B monochromator at these energies and front-end slit settings can then be estimated by multiplying the intrinsic resolution<sup>3</sup> of the Si(111) reflection by the broadened values of  $\frac{10.7}{8.76}$  and  $\frac{14.7}{12.79}$ . For example, at 9.536 keV the intrinsic resolution of the Si(111) reflection is  $\sim 1.3$  eV and the energy resolution due to photon divergence in this experiment is  $\sim 1.59$  eV.

The 127  $\mu\text{m}$  thick graphite filters that overlay two of the openings on the slit-ladder are important for stable operation of the X13B monochromator, especially when the higher power IVUN source is selected. IVUN was the source of x-rays for the following measurements: The front-end slits were fully opened and the slit ladder (upstream of the monochromator) was set at an opening of 2 mm. Figure 3-13 shows an energy scan of the undulator first harmonic with and without the graphite filter in place. The photon flux was detected by measuring the current produced from a 30 cm ionisation chamber (inside the experimental hutch) as the x-rays passed through it. With

<sup>†</sup> Considering darwin-widths of monochromator and analyser crystals.

the filter in place, most of the low-energy photons below  $\sim 5$  keV are absorbed. This reduces the incident power on the silicon crystals, with negligible effect on the harder x-ray photons. This is desirable in x-ray absorption spectroscopy where energy drifts are intolerable, which is exasperated at greater incident powers and inadequate cooling.

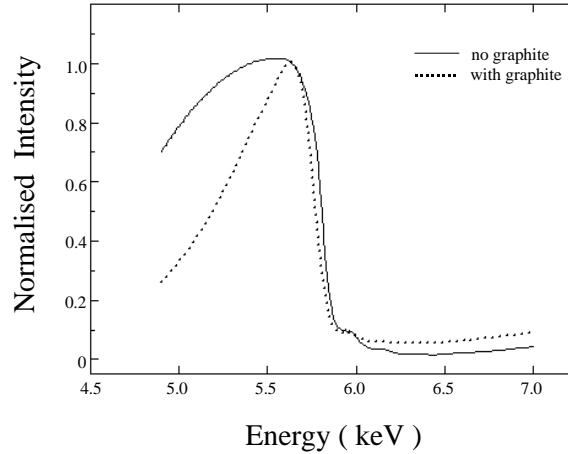


Figure 3-13: Effect of graphite filter in front of X13B monochromator.

Figure 3-14 shows the measurement of the rocking curve (i.e. the width of Bragg reflection) around the first harmonic of IVUN. This measurement was performed by tilting the upper crystal of the X13B monochromator by the piezo-driven screw, both with and without the graphite filter in place. By rotating the upper crystal, the intensity of reflected rays changes as they make varying angles of incidence to the crystal planes. There is a reduction in the rocking-curve width, which signifies increased energy resolution with the graphite filter in place, and can be attributed to the enhanced cooling efficiency due to the lower incidence power. Due to this reduced power, the heat-bump that is created with impinging x-ray beam is significantly diminished, and there is negligible variation of the lattice constant in this region. The ragged profile in Figure 3-14 is due to the non-linear motion of the piezo screw driving the upper crystal.

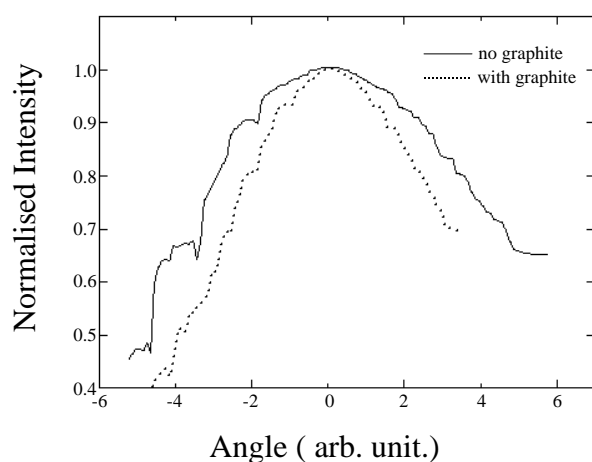


Figure 3-14: First harmonic rocking curve.

Figure 3-15 shows the energy scan for the third harmonic with and without the graphite filter in place. The energy axis corresponds to that calculated for the Si(111) reflection and the peak corresponds to the third harmonic that is chosen by the Si(333) Bragg planes. The third harmonic is found at approximately 16.3 keV and aluminium filters were placed in front of the ionisation detector to absorb the first order reflection, so that the harder x-rays could to be detected. This is an important point to emphasise as higher-order harmonics can be transmitted by the double-crystal monochromator.

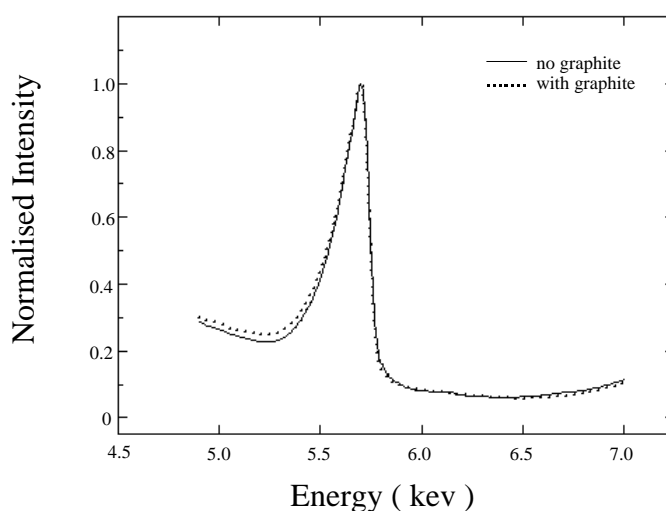


Figure 3-15: Third harmonic energy scan using the Si (333) reflection.

These higher-order harmonics are detrimental for x-ray absorption spectroscopy measurements that require a clean monochromatic beam. Hence, the piezo-driven screw connected to the upper crystal is applied to tilt the upper crystal and thus move the

higher harmonics to a point on the rocking curve where they cannot be reflected. This is called ‘de-tuning’ and works because the darwin-widths<sup>3</sup> (i.e. the width of the Bragg reflections) of the higher order harmonics are much narrower than the fundamental, and are positioned at slightly different angles. Figure 3-16 shows the rocking curve for the Si (333) reflection obtained through rotation of the upper monochromator crystal. As the Darwin-width is significantly narrower than the Si(111) reflection, the improved energy resolution with the graphite filter in place is more difficult to observe than using the Si (111) reflection (Figure 3-14) (also complicated profile with the addition of uneven piezo-screw motion).

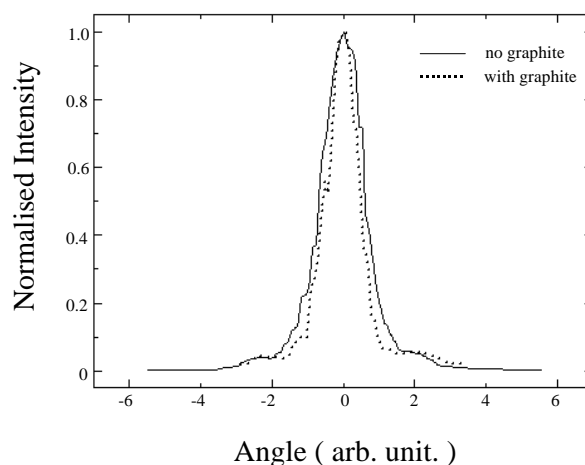


Figure 3-16: Third harmonic rocking curve.

### 3.4 Summary

This chapter has described the unique and powerful characteristics that synchrotron radiation can offer to the experimentalist. The X13 straight section that houses the IVUN and EPW magnetic insertion devices have been described in detail. Characterisation of the X13B double-crystal monochromator has been described fully and performs to the high standards that are required for synchrotron radiation research. The small emittance and vertical electron beam dimension of IVUN makes it an ideal source for x-ray micro-focusing optics.

## Chapter 4 Design and simulations of X13B reflective x-ray optics

The design of the X13B elliptical x-ray micro-focusing mirrors was facilitated using a ray-tracing computer program called SHADOW<sup>102†</sup> which allowed the mirror parameters to be calculated and effects of misalignments to be studied. SHADOW uses a Monte-Carlo algorithm to simulate a photon beam propagating through an optical system. This computer software was developed at the University of Wisconsin and is widely used throughout the x-ray synchrotron-radiation community for designing beamlines. A detailed description of the input parameters for the program can be found in Appendix C.

### 4.1 Fundamental x-ray interactions

The description of the passage of x-rays through a medium is important to the understanding of the properties for the X13B micro-probe Kirkpatrick-Baez mirror arrangement, and in later experimental procedures. Many of the formula and derivations described below can be found in the Lawrence Berkeley x-ray data booklet.<sup>85</sup>

A travelling electromagnetic wave can be represented by the time-varying sinusoidal wave function,

$$A(x, t) = A_0 e^{i(\tilde{n} k x - \omega t)} \quad \{4.1\}$$

where  $\tilde{n}$  is the energy-dependent complex refractive index,  $k$  is the wave-number of the radiation,  $x$  is the spatial position along the wave direction, the frequency of oscillation is  $\omega$ ,  $A_0$  is the amplitude and  $t$  represents the time.

The complex refractive index is related to the phase-change and absorption of the electromagnetic wave through the medium and is given by,

$$\tilde{n} = 1 - \delta - i\beta \quad \{4.2\}$$

---

<sup>†</sup> The source code can be downloaded from the 'center for x-ray lithography', University of Wisconsin, USA at <http://www.xraylith.wisc.edu/shadow/shadow.html>

where the energy-dependent optical constants,  $\delta$  and  $\beta$  are the refractive index decrement and absorption index of the material respectively.

For a monochromatic pencil beam of x-rays passing through a homogenous medium of thickness  $x$ , the transmitted and incident intensities are related by the Lambert-Beer Law,

$$I = I_0 e^{-\mu_x x} \quad \{4.3\}$$

where,  $I$  is the exponential decrease in intensity when transversing a distance  $x$  through the medium from a starting value of  $I_0$ , and  $\mu_x$  is the energy-dependent total linear absorption coefficient.

The x-ray intensity is proportional to the square of the modulus of the electric field vector. Hence, the linear absorption coefficient is related to the absorption index by,

$$\mu_x = 2\beta k = \frac{4\pi\beta}{\lambda} \quad \{4.4\}$$

where  $\lambda$  is the wavelength of the radiation.

The associated phase change of the radiation in passing a distance  $x$  through the media is given by,

$$\Delta\phi = \frac{2\pi\delta x}{\lambda} \quad \{4.5\}$$

The x-ray/material interactions can be represented through the atomic scattering factors<sup>†</sup>,  $f_1$  and  $f_2$ . When an atom is illuminated by x-rays there are three basic mechanisms by which the x-rays can interact with the electrons surrounding the

---

<sup>†</sup> Values for these and other x-ray constants can be found in the Henke tables,<sup>1</sup> which are obtained from theoretical calculations and through experimental data, and are very precise away from the absorption edges. They can also be found at [http://www-cxro.lbl.gov/optical\\_constants/](http://www-cxro.lbl.gov/optical_constants/) and in the XOP computer package.<sup>84</sup>

nucleus: In coherent scattering, the x-rays elastically interact with the free (Thompson scattering) or more strongly bound electrons (Rayleigh scattering). Compton scattering is an inelastic process involving an energy exchange from the incident photon to the electron. Finally, x-rays have the ability to excite electrons to unoccupied energy levels known as photoelectric absorption. Neglecting Compton scattering, which is only important for very high x-ray energies and light atoms (Figure 4-1), and the angular dependence of scattering due to charge distribution, these x-ray interactions are subsequently included into the complex amplitude,

$$A(E) = A_T [f_1(E) + if_2(E)] \quad \{4.6\}$$

where,  $A_T$  is the Thompson scattering amplitude from a free electron.  $f_1$  describes the overall scattering from the atom and  $f_2$  describes the absorption of x-rays due to raising of electrons to bound or continuum states. These atomic scattering factors are related to the optical constants by,

$$\delta = K f_1 \quad \{4.7\}$$

$$\beta = K f_2 \quad \{4.8\}$$

and  $K$  is a wavelength dependent variable,

$$K = \frac{r_e \lambda^2}{2\pi} \frac{N_A}{A} \rho \quad \{4.9\}$$

where  $r_e$  is the classical electron radius,  $N_A$  is Avagadro's number, with  $A$  and  $\rho$  being the atomic weight and density of the material respectively.

Using relativistic quantum dispersion theory, the atomic scattering factors can be calculated by,



$$f_1(E_{\text{inc}}) \sim Z + \frac{4\epsilon_0 m_e c}{h e^2} \int_0^\infty \frac{E^2 \mu_{\text{ab}}(E)}{E_{\text{inc}}^2 - E^2} dE - \Delta_{\text{rel}} \quad \{4.10\}$$

$$f_2(E_{\text{inc}}) \sim \frac{2\epsilon_0 m_e c}{h} E_{\text{inc}} \mu_{\text{ab}}(E_{\text{inc}}) \quad \{4.11\}$$

where  $Z$  is the atomic number,  $\mu_{\text{ab}}(E)$  is the atomic photo-absorption cross section, and  $E_{\text{inc}}$  is the incident x-ray energy. A correction factor to accommodate the complicated mechanisms that exist in the immediate vicinity of absorption edges is represented by  $\Delta_{\text{rel}}$ .

The atomic photo-absorption cross section,  $\mu_{\text{ab}}$  is related to the linear ( $\mu_x$ ) and mass ( $\mu_{\text{mass}}$ ) absorption coefficients by,

$$\mu_{\text{ab}} = \frac{A}{N_A}, \quad \mu_{\text{mass}} = \frac{A}{N_A \rho} \mu_x \quad \{4.12\}$$

Away from threshold, the photo-absorption cross section varies roughly as

$$\mu_{\text{ab}}(E) \propto \frac{Z^3}{E^3} \quad \{4.13\}$$

An accurate determination of the optical constants is essential in the design of x-ray optics. As the refractive index decrement is slightly less than unity and small ( $\delta \sim 10^{-4} \rightarrow 10^{-7}$ , in the x-ray region), direct experimental measurements are difficult. Determination of critical angles by specular reflection or deviations of the light in prisms do not have the required sensitivity in the x-ray region. In the hard x-ray region, there are several methods in determining the atomic scattering factors such as employing interferometry or x-ray diffraction techniques.<sup>108</sup>

However, considering Equations {4.10} and {4.11}, it is possible to determine the optical constants by an accurate determination of the photo-absorption cross section. This is because  $\delta$  can be derived from the absorption index,  $\beta$ : The x-ray transmission through a thin film of known thickness is measured which leads directly to

$f_2$  ( $\beta = K f_2$ ). Extrapolations between spectral regions have to be employed to cover a sufficient energy range to evaluate  $f_1$ , and thus determine  $\delta$ .

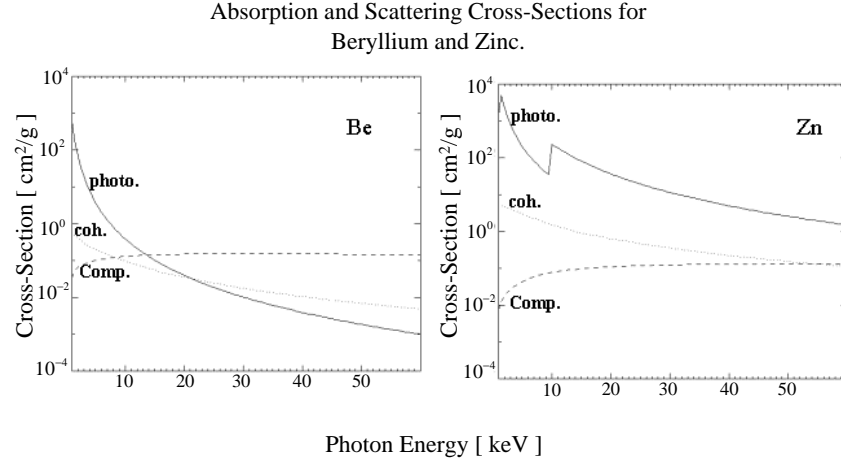


Figure 4-1: Energy dependence of x-ray cross-sections.

Figure 4-1 shows the photoelectric, coherent and Compton x-ray scattering cross-sections for beryllium and zinc. As the x-ray energy decreases, coherent elastic-scattering begins to dominate and the Compton cross-section begins to fall. Also, the photoelectric cross section decreases with energy, except near the absorption edges. A sharp resonance is found for zinc at 9.659 keV which corresponds to the ejection of an electron from the  $n = 1$  energy level of that atom.

## 4.2 Grazing incidence x-ray reflectivity

To describe the small-angle nature of x-ray micro-probe optics, it is first necessary to consider the interactions of an electromagnetic wave incident on a vacuum/material boundary, as depicted in Figure 4-2: An electromagnetic plane wave propagating through a vacuum impinges on a planar surface, with incident, reflected and transmitted wave-vectors,  $\tilde{S}_i$ ,  $\tilde{S}_r$ ,  $\tilde{S}_t$ , at angles  $\theta_i$ ,  $\theta_r$  and  $\theta_t$  to the interface respectively.  $A$ ,  $T$  and  $R$  are the amplitudes of the incident, transmitted and reflected electric-field vectors, and the subscripts,  $\parallel$  and  $\perp$ , are the orthogonal components of polarisation. Propagation between two media can be described using the Fresnel equations that relate the reflected and transmitted modulus of the electric field vectors to those of the incident wave.

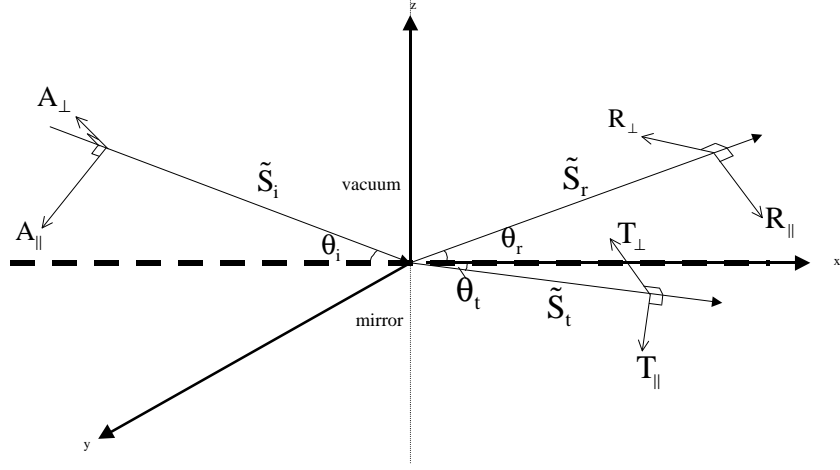


Figure 4-2: Reflection of an electromagnetic wave at a planar boundary.

In conjunction with Snell's law and considering a vacuum/material interface, with the complex refractive index of the material  $= \tilde{n}$ , the Fresnel equations reduce to:

$$r_{\parallel} = \frac{\tilde{n}^2 \sin \theta_i - \sqrt{\tilde{n}^2 - \cos^2 \theta_i}}{\tilde{n}^2 \sin \theta_i + \sqrt{\tilde{n}^2 - \cos^2 \theta_i}} \quad \{4.14\}$$

$$r_{\perp} = \frac{\sin \theta_i - \sqrt{\tilde{n}^2 - \cos^2 \theta_i}}{\sin \theta_i + \sqrt{\tilde{n}^2 - \cos^2 \theta_i}} \quad \{4.15\}$$

$$t_{\parallel} = \frac{2\tilde{n} \sin \theta_i}{\tilde{n}^2 \sin \theta_i + \sqrt{\tilde{n}^2 - \cos^2 \theta_i}} \quad \{4.16\}$$

$$t_{\perp} = \frac{2 \sin \theta_i}{\sin \theta_i + \sqrt{\tilde{n}^2 - \cos^2 \theta_i}} \quad \{4.17\}$$

where  $r$  and  $t$  are reflected and transmitted electric-field amplitudes relative to the incident field.<sup>†</sup>

The above formulae are also applicable to curved geometries, where the wavelength of x-rays is much smaller than the radius of curvature.

<sup>†</sup> Taking atomic contributions into account slightly alters the reflectivity by contributing second order terms in  $\delta$  and  $\beta$ , which are small and can be safely ignored.

The critical angle at which reflection begins to occur (proceeding from a steeper angle) at a vacuum/material interface is given by

$$\cos \theta_c = 1 - \delta = 1 - \frac{r_e \lambda^2}{2\pi} \frac{N_A}{A} \rho f_1 \quad \{4.18\}$$

For an intuitive understanding of x-ray reflectivity from a smooth surface, it is beneficial to devise a simple method for estimating the refractive index decrement and critical angles: In the hard x-ray region and away from absorption edges,  $f_1 \sim Z$ , and the atomic weight can be approximated by  $A \approx C Z$ , where the factor  $C$  is used to account for the greater number of neutrons in the nucleus for the heavier elements that are used for mirror coatings. It follows that (using  $C \sim 2.4$  for  $Z \sim 40-80$ ), that the refractive index decrement and critical angles can be estimated very well by the following equations,

$$\delta \approx 1.12 \times 10^{-4} \lambda [\text{nm}]^2 \rho [g/cm^3] \approx \frac{1.72 \times 10^{-4} \rho [g/cm^3]}{E [\text{keV}]^2} \quad \{4.19\}$$

$$\theta_c \approx 0.015 \lambda [\text{nm}] \sqrt{\rho [g/cm^3]} \approx 0.019 \frac{\sqrt{\rho [g/cm^3]}}{E [\text{keV}]} \approx \sqrt{2 \delta} \quad \{4.20\}$$

Hence, the critical angle<sup>†</sup> is inversely proportional to the x-ray energy, and as the photon energy is increased, the grazing angle has to be reduced to maintain adequate reflectivity and longer mirrors are needed to intercept the radiation. Table 4-1 shows the comparison between the established Henke data and the estimations as described above, for two popular x-ray mirror coatings.<sup>‡</sup> Evidently, heavier coatings are more desirable for x-ray optics due to the larger critical angles which lead to greater acceptance apertures.

---

<sup>†</sup>  $\theta_c$  has been calculated using the small angle approximation,  $\cos \theta_c \approx 1 - \frac{\theta_c^2}{2}$  in Equation {4.20}.

<sup>‡</sup> These are calculated away from any absorption edges where the refractive index behaves well.

Element	density	E ( keV )	$\delta$ ( Henke )	$\theta_c$ ( Henke )	$\delta$ (approx)	$\theta_c$ (approx)
Rhodium	12.4 g / cm <sup>3</sup>	5	$8.89 \times 10^{-5}$	$0.76^0$	$8.53 \times 10^{-5}$	$0.75^0$
		10	$2.25 \times 10^{-5}$	$0.38^0$	$2.13 \times 10^{-5}$	$0.37^0$
		15	$9.88 \times 10^{-6}$	$0.25^0$	$9.45 \times 10^{-6}$	$0.25^0$
		20	$5.43 \times 10^{-6}$	$0.19^0$	$5.33 \times 10^{-6}$	$0.19^0$
Gold	19.32 g / cm <sup>3</sup>	5	$1.21 \times 10^{-4}$	$0.89^0$	$1.33 \times 10^{-4}$	$0.93^0$
		10	$2.99 \times 10^{-5}$	$0.44^0$	$3.32 \times 10^{-5}$	$0.47^0$
		15	$1.35 \times 10^{-5}$	$0.30^0$	$1.48 \times 10^{-5}$	$0.31^0$
		20	$7.94 \times 10^{-6}$	$0.23^0$	$8.31 \times 10^{-6}$	$0.23^0$

Table 4-1: Values of the critical angle and refractive index decrement using Henke tables and estimations.

### 4.3 Optical Surface errors

The description of a surface is complex, but it can be basically broken into four components, as visualised in Figure 4-3:<sup>109</sup> The profile is that which is actually produced by the manufacturing process. Irregular high-frequency errors are known as surface roughness, and generally depend on how well the optical surface can be polished. Waviness (often referred to as slope error) is the ripple-like texture of the surface induced by the polishing or deposition process. The geometry error is the large-scale deviations of the overall shape from the ideal, and can also be induced by the polishing process.

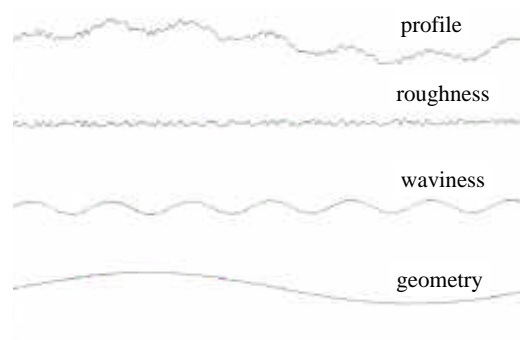


Figure 4-3: An optical profile can be represented by roughness, waviness and geometry terms.<sup>109</sup>

### 4.3.1 Surface roughness considerations

Deviations from the ideal optical surface over short-length scales are referred to as “surface roughness.” It has period and height deviations on the length-scale of angstroms.<sup>109</sup> It is these short-length variations in the surface quality that has the potential of reducing flux at the focal position. The improvement in x-ray optical manufacturing techniques ensures that mirror surfaces can be polished to extremely low roughness values.<sup>†</sup> Nevertheless, it is beneficial to discuss how roughness can have a detrimental effect on mirror performance. There are several models that can be used to incorporate surface roughness. The most common one in operation is that proposed by Debye,<sup>3</sup> and the decrease in reflectivity from a rough surface is given by,

$$\langle I \rangle = \langle I_{\text{smooth}} \rangle \exp \left[ - \left( \frac{4\pi \sigma_{\text{rough}} \sin \theta_i}{\lambda} \right)^2 \right] \quad \{4.21\}$$

where  $\langle I_{\text{smooth}} \rangle$  is the mean reflected intensity from the smooth surface,  $\sigma_{\text{rough}}$  is the RMS roughness, and the incident angle with respect to the surface is denoted by  $\theta_i$ , with  $\lambda$  being the x-ray wavelength.

For example, a 90 % reflectivity using 10 keV x-rays and a grazing incidence angle of 4 mrad requires that the RMS roughness,  $\sigma_{\text{rough}}$  be less than 8 Å.

Equation {4.21} was used to calculate roughness-dependent x-ray reflectivities from various metallic surfaces. It is useful to show how reflectivity profiles depend on incidence angles, composition and roughness. Figure 4-3A shows how the reflectivity varies with roughness for several energies at a grazing incidence angle of  $0.22^\circ$ .<sup>‡</sup> As the roughness is increased, the reflectivity falls and rapidly decreases with increasing photon energy. Figure 4-3B illustrates how the reflectivity varies with energy for a

---

<sup>†</sup> A roughness of  $< 5 \text{ Å}$  is routine in polishing optical surfaces for use in the x-ray region. The continuous polishing technique currently produces the best results.

<sup>‡</sup> A rhodium coating and an incidence angle of  $\sim 0.22^\circ$  was chosen for the subsequent design of the X13B KB optics. This angle was a compromise between a high acceptance aperture and operating up to energies of  $\sim 12 \text{ keV}$ . Although the critical energy is nearer  $15 \text{ keV}$ , the variation in incidence angle along the mirror length reduces this value.

rhodium coated mirror at a fixed grazing angle of  $0.22^\circ$  and for a roughness of  $3 \text{ \AA}$ . For higher energies, the critical angle falls, and the acceptance aperture of the KB mirrors decreases. To enable the use of higher photon energies, a heavier reflective coating should be used. The platinum and gold reflectivity characteristics exhibit sharp decreases at various energies as shown in Figure 4-3C. These correspond to the  $L_3$ ,  $L_2$  and  $L_1$  edges for these materials and could prove troublesome for x-ray absorption studies in this energy range. The final graph, figure 4-3D, depicts the impact that the variation of grazing incidence angle has upon reflectivity. As there is always some absorption within the mirror material, the reflectivity can never be 100 % and begins to fall rapidly as the roughness is increased above  $\sim 10 \text{ \AA}$ , in the vicinity of the critical angle.

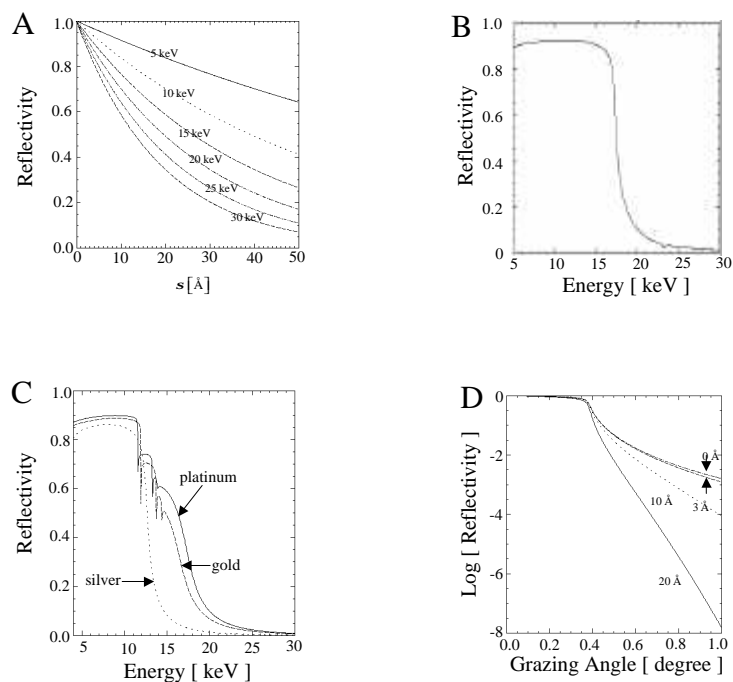


Figure 4-4: Energy and roughness effects on mirror reflectivity. A) Roughness effect on reflectivity at different energies for a grazing incidence angle of  $0.22^\circ$  for a rhodium coating. B) Rhodium reflectivity dependence on energy at a grazing incidence angle of  $0.22^\circ$ . C) Reflectivity dependence on energy for various optical coatings at a grazing incidence angle of  $0.22^\circ$ . D) Reflectivity dependence on grazing incidence angle, at various degrees of roughness, at an incident x-ray energy of 10 keV for a rhodium coating.

### 4.3.2 Slope error considerations

Medium-scale deviations from the optical profile, inherent in any manufacturing process, can produce severe image degradation. It is the minimisation of such slope errors that are capable of delivering x-ray micro-focused beams. These errors have periods of less than a few mm, and progressively superior focal properties will require further improvements in the fabrication techniques. An explanation of image degradation due to slope error can be understood with the aid of Figure 4-5, where grazing incidence is assumed and the approximation  $\sin \theta \approx \theta$  is justified.

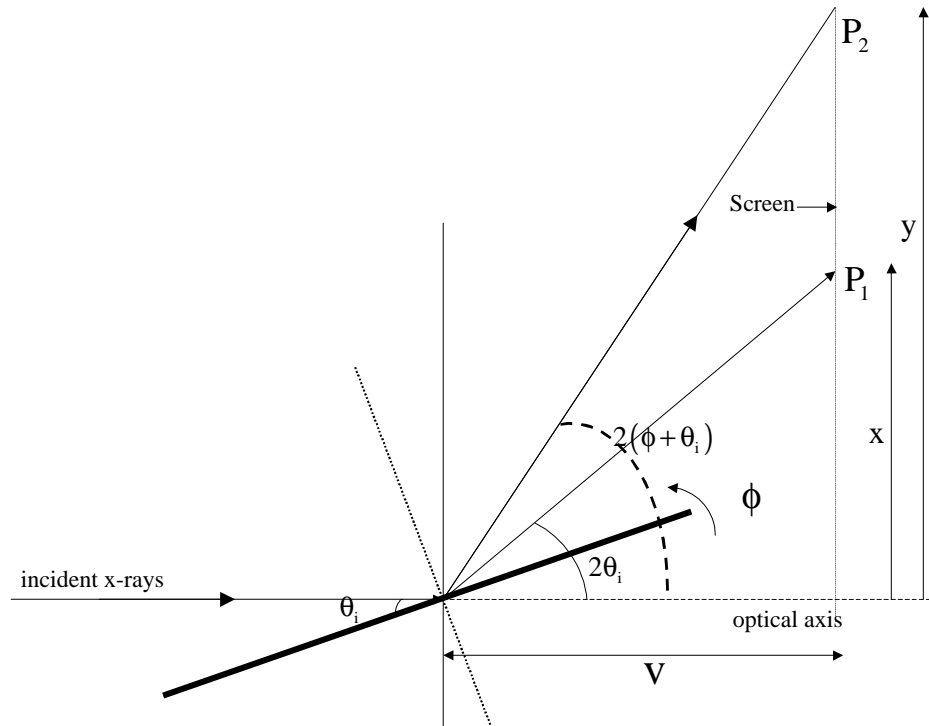


Figure 4-5: Slope error effect on image quality.

Consider an x-ray beam incident at a planar surface, at an angle  $\theta_i$  with respect to the mirror surface. This ray is reflected and strikes a screen a distance  $v$  along the optical axis, and with a vertical displacement of  $x \sim 2\theta_i v$  with respect to the incident direction. Then, suppose that the surface is rotated about the point of impingement by an angle  $\phi$ , which reflects the beam to a position  $y \sim 2(\phi + \theta_i)v$  on the screen. The vertical displacement due to this angular rotation is simply,



$$y - x = \sigma_{\text{blur}} \sim 2 \phi v \quad \{4.22\}$$

This essentially defines the 'blur' in the image due to the slope error. Slope errors are usually quoted as 'root mean square (RMS)' values and optical manufacturers are able to polish and differentially coat mirror surfaces to an RMS value of less than  $2 \mu\text{rad}$ .

The angle,  $\phi$  can be equated with the slope error,  $\sigma_{\text{slope}}$  and the demagnification term is,  $M \sim \frac{v}{u} \sim \frac{\sigma'}{\sigma}$  where  $u$  and  $v$  are the source-to-mirror and mirror-to-focus distances respectively.  $\sigma$  and  $\sigma'$  are the source size and perfectly demagnified image size respectively and it follows from Equations {2.2} and {2.3} that,

$$\sigma_{\text{blur}} \sim 2 \sigma_{\text{slope}} u \frac{\sigma'}{\sigma} \quad \{4.23\}$$

where  $\sigma_{\text{blur}}$  is the standard-deviation blur of the image.

Padmore *et al.*<sup>32</sup> used the criteria that the blur in the image should be less than half the demagnified source size i.e.  $\sigma_{\text{blur}} < \frac{1}{2} \sigma'$  giving,

$$\sigma_{\text{slope}} < \frac{\sigma}{4u} \quad \{4.24\}$$

where  $\frac{\sigma}{u}$  is the angular acceptance of the source from the mirror pole.

At the X13B beamline, the location of the experimental hutch sets  $u \sim 25 \text{ m}$  and the vertical source size is  $\sigma_z \sim 6 \mu\text{m}$ , which specifies a figure error requirement of  $\sigma_{\text{slope}} < 0.06 \mu\text{rad}$ . The current manufacturing capability can reduce slope errors to values that are two orders of magnitude greater, and slope deviations are the dominant contribution to image degradation. However, by increasing the demagnification of the system by specifying a shorter focal length, the image blur can be minimised, and this has been the method for producing sub-micron focused beams in the x-ray region to-date.<sup>32,42</sup>

#### **4.4 Geometrical description of reflective optics**

Grazing incidence x-ray optics dictate a stringent requirement on the overall mirror surface quality as deviations from the ideal are compounded at smaller angles, unlike visible optics which operate at much steeper angles. For moderate numerical apertures, long mirrors are required at synchrotron radiation sources to collect the diverging x-ray beam, which pushes mirror manufacturing capabilities to their limits. The processing techniques that are needed to achieve good roughness and slope errors over the entire optical surface are in continual advancement. Conventional grinding and polishing cannot achieve the necessary figure quality that micro-probe optics require. Continuous polishing can achieve excellent surface quality, but only on a surface of revolution. However, it is possible to pre-stress the optic before polishing to satisfy this requirement for other geometries such as ellipses, toroids and cylinders. The slope error using this manufacturing process is thus determined by the accuracy to which the bending can satisfy the equation of the surface, which returns to the disadvantages of this technique as described in Section 2.1.

Focusing is a relatively simple concept where the radiation emitted from a source is brought to a point, some distance away, by means of an optical device that re-images it. Focusing can be accomplished in either the meridional (tangential) plane, where the mirror surface is curved along the direction of the incident photons, or sagittally in the plane perpendicular to the direction of incidence. Although elliptical mirrors are ideally suited to synchrotron radiation sources, it is advantageous to discuss why cylindrical mirrors can only achieve micro-focusing for small acceptance angles, and a straightforward description of focusing is introduced. The idea of achieving x-ray focusing using cylindrical mirrors was first proposed by Kirkpatrick and Baez<sup>37</sup> and the geometry of a single optic is shown in Figure 4-6.

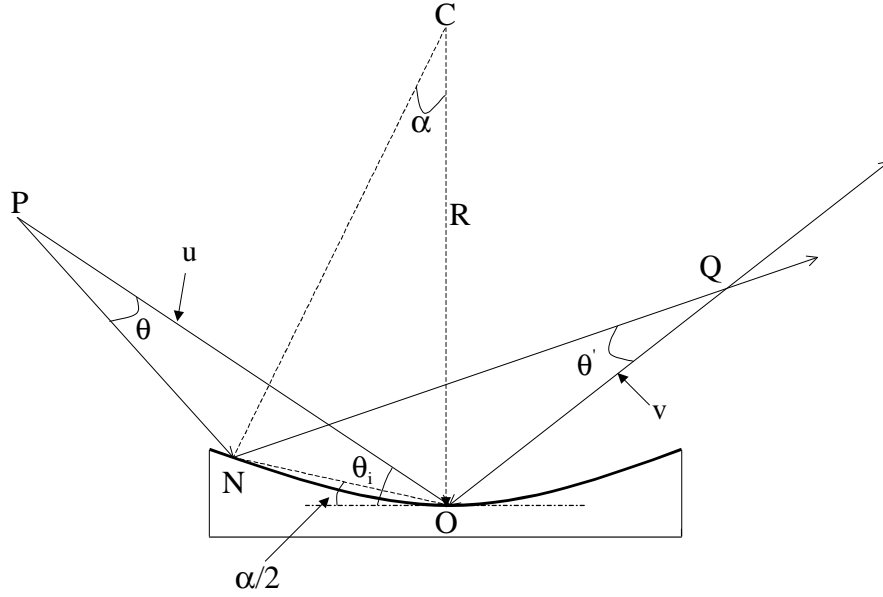


Figure 4-6: Formation of an image by a concave mirror at grazing incidence.

X-ray optics necessitate grazing incidence angles and using the assumption that the length of the chord,  $NO \ll R$  where  $R$  is the radius of curvature, then it follows that  $\alpha$ ,  $\theta$  and  $\theta'$  are small. Through simple geometry,<sup>†</sup> the angles  $\theta$  and  $\theta'$  are given by,

$$\theta \approx \frac{\alpha R \left( \theta_i - \frac{\alpha}{2} \right)}{u - \alpha R} \quad \{4.25\}$$

$$\theta' \approx \frac{\alpha R \left( \theta_i + \frac{\alpha}{2} \right)}{v + \alpha R} \quad \{4.26\}$$

and from the law of reflection,

$$\theta + \theta' = 2\alpha \quad \{4.27\}$$

and as  $\alpha \rightarrow 0$ ,

$$\frac{2}{R \theta_i} \approx \frac{1}{u} + \frac{1}{v} \quad \{4.28\}$$

<sup>†</sup> Using the small angle approximation,  $\sin \theta \approx \theta$

Using the equation of a thin lens as derived in visible optics the meridional focal length can be defined as,

$$f_m \approx \frac{R \theta_i}{2} \quad \{4.29\}$$

However, as the angle  $\alpha$  is opened up for larger numerical apertures, the rays are gradually deviated by increasing amounts and spherical aberration intensifies. For large demagnification and  $\frac{\alpha}{\theta_i} \ll 1$ , the amount of spherical aberration can be approximated by,<sup>37</sup>

$$S \approx 1.5 \frac{k^2}{2R} \quad \{4.30\}$$

where  $k$  is approximately the length of the mirror.

As an example for the requirements of x-ray micro-focusing, the demagnifications demanded at a synchrotron radiation facility are of the order of  $\frac{1}{100}$  and mirror lengths are typically  $\sim 10$  cm. The focal length is  $\sim v$  and grazing angles are a few milli-radians specifying radii of curvatures of  $R \sim 5 \text{ m} \rightarrow 200 \text{ m}$ . Thus for the optics subsequently designed in this thesis ( $R \sim 200 \text{ m}$ , for the vertical focusing mirror), a spherical aberration of  $1 \mu\text{m}$  would dictate a mirror length of only  $\sim 1.6 \text{ cm}$ , with a corresponding low photon collection. For smaller spot sizes and larger demagnifications, smaller radii of curvature compound this hindrance.

In the sagittal direction for this single optic (Figure 4-6), the focal length is given by (e.g see Equation (8.100) by Michette *et al.*<sup>43</sup>),

$$f_s = \frac{R}{2 \theta_i} \quad \{4.31\}$$

Thus the sagittal focal length is much longer than the meridional focal length for grazing angles of incidence, and the image suffers from astigmatism. However, if the

radii of the curvature in the sagittal and meridional directions are different, such that  $f_m = f_s$  then,

$$R_s = R_m \theta_i^2 \quad \{4.32\}$$

where  $R_m$  and  $R_s$  are the meridional and sagittal radii of curvature respectively.

Astigmatism is removed in this configuration for a single incidence angle, and the surface is toroidal. Toroids are often used at synchrotron radiation facilities to provide 1:1 focusing, and are accordingly well suited in this geometry. An example of the toroidal configuration is shown in Figure 4-7.

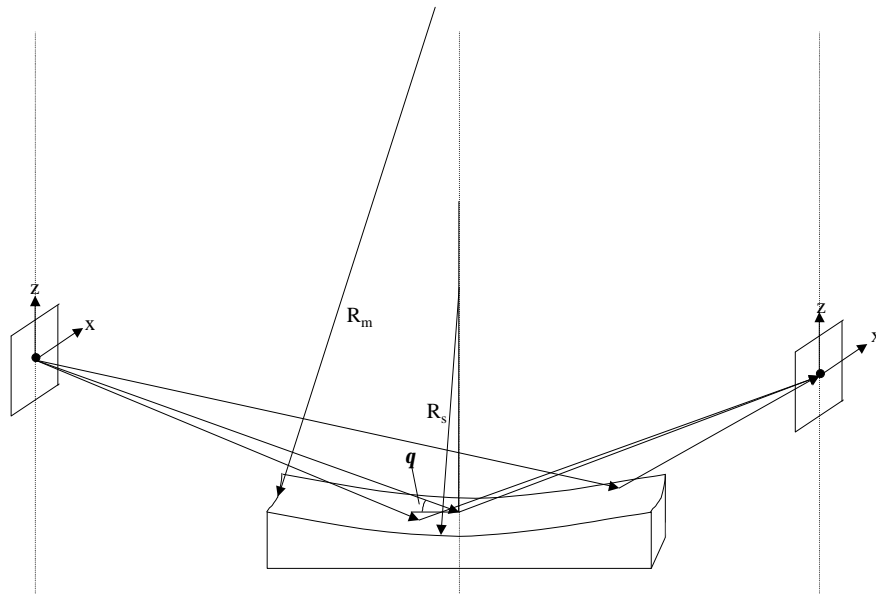


Figure 4-7: Toroidal Focusing.

For high demagnification, elliptical mirrors in the KB arrangement are required for point-to-point focusing at a synchrotron radiation source, and aberrations are minimised in this geometry.<sup>43</sup> The geometry of an ellipse is depicted in Figure 4-8.

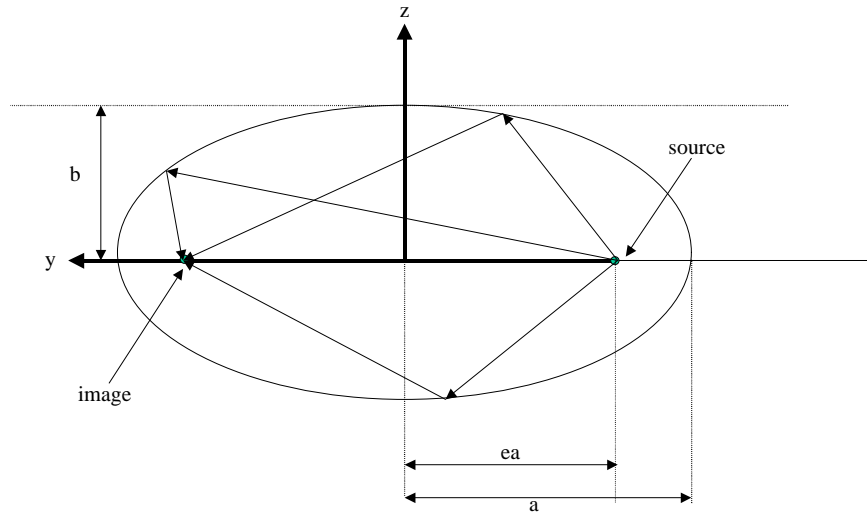


Figure 4-8: Focusing properties of an ellipse.

In this arrangement, the point source and image are located at the opposing foci. The equation and eccentricity of the ellipse are given by the following equations,

$$\frac{y^2}{a^2} + \frac{z^2}{b^2} = 1 \quad \{4.33\}$$

$$e = \frac{\sqrt{a^2 - b^2}}{a} \quad \{4.34\}$$

where  $a$  and  $b$  are the semi-major and semi-minor axes respectively,  $e$  is the eccentricity, and the distance from the centre of the ellipse to either foci is equal to  $ea$ . At a synchrotron radiation source, the geometrical profile of the ellipse is extremely elongated due to the grazing incidence nature of the x-ray optics and the distances involved. A schematic of a single elliptical mirror at an x-ray synchrotron facility is shown in Figure 4-9.

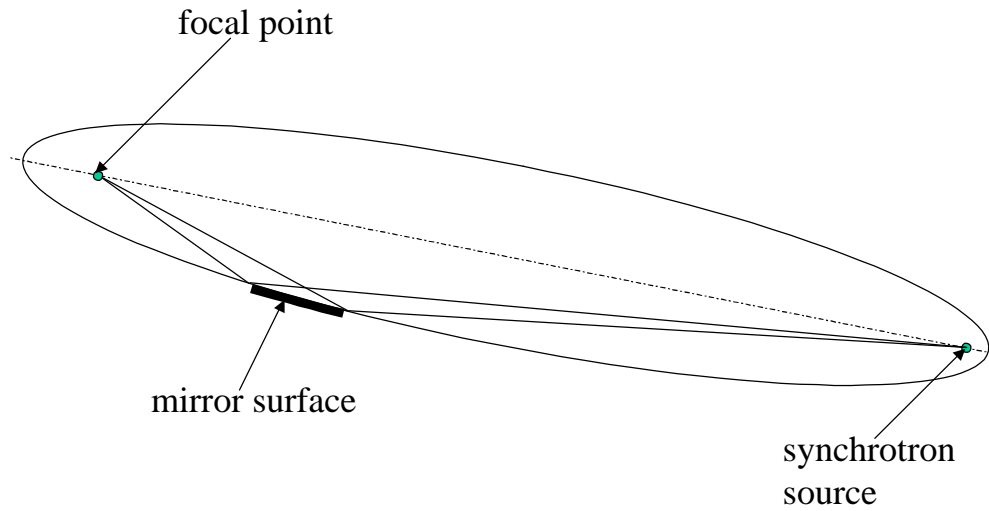


Figure 4-9: Orientation of an elliptical mirror at a synchrotron radiation source.

#### 4.5 Ray-tracing using SHADOW

SHADOW consists of three major components in which to construct and test the proposed optical design for the X13B micro-probe. In order of completion, these are the source definition, the geometrical layout, and the analysis of the photon beam through the system after it has been traced. By specifying the focal parameters of the system, SHADOW computes the required figures that are needed to focus the x-ray beam. By introducing placement and rotational errors for the optics, effects of misalignments can be studied. With the introduction of figure errors and roughness values, an estimate of the image quality and expected intensity can be predicted.

The manufacturing specifications for the X13B micro-probe were that a slope error (Section 4.3.2) of less than  $2\text{ }\mu\text{rad}$  was achievable, together with a surface roughness (Section 4.3.1) of less than  $3\text{ }\text{\AA}$ . It is the deviation from the ideal surface (slope error) which is the dominant factor in image degradation. The following sections discuss the source characteristics, optical design and image properties as calculated through the SHADOW ray-tracing program. Some equations that are useful in determining the optimal performance of these optics are described in Section 2.1.

#### 4.5.1 X13 source definition

The wiggler (EPW) and small-gap undulator (IVUN) insertion devices in the X13 straight section provide two sources that can be used for the X13 x-ray micro-probe. Due to the different locations of these devices in the X13 straight section (Section 3.3), the optical layout should be translated along the x-ray beam direction to satisfy the fixed source-to-optics distances for the X13B differentially coated optics. The source parameters that were entered into the SHADOW program can be found in Table 3-1 (page 40), Table 3-2 (page 43) and Table 3-3 (page 47), and the properties of these magnetic devices can be found in Section 3.3.1 and Section 3.3.2.

#### 4.5.2 Optical configuration

Elliptical mirrors are able to provide point-to-point achromatic focusing. As described previously, one way of creating this shape is by bending a flat trapezoidal mirror by the application of unequal moments (Section 2.1). The potential advantage of such a technique is that the mirrors can be in-situ bent, thereby allowing the focal properties to be dynamically changed. The major drawback of this system is that the substrate (usually float glass, metal or silicon) is very difficult to bend to the exact elliptical shape. NSLS in-situ bendable x-ray focusing optics routinely achieve vertical spot sizes of around  $10\text{ }\mu\text{m} \rightarrow 20\text{ }\mu\text{m}$ ,<sup>14</sup> but never significantly below these values.<sup>†</sup> Some papers have reported that spot sizes approaching  $1\text{ }\mu\text{m}$  in the vertical have been achieved with such systems, but they tend to ignore the large scattering lobes in the vicinity of the focal spot.<sup>38</sup> In addition to these defects, to obtain sub-micron focusing, a small percentage of the mirror is often selected. This is achieved by scanning a slit in front of the mirrors, and has been necessary in the past as only certain sections match the required figure specifications. Obviously, this has a significant impact on the available flux for experiments. It is the goal of this thesis to overcome these issues using a differential coating technique.

---

<sup>†</sup> A NSLS experiment has claimed a significant smaller size of  $\sim 2.5\text{ }\mu\text{m}$  at a single focal position.<sup>40</sup>



A schematic of the X13B optical layout is shown in the diagram below, with the first mirror providing focusing in the vertical direction and the proceeding mirror focusing in the horizontal direction.

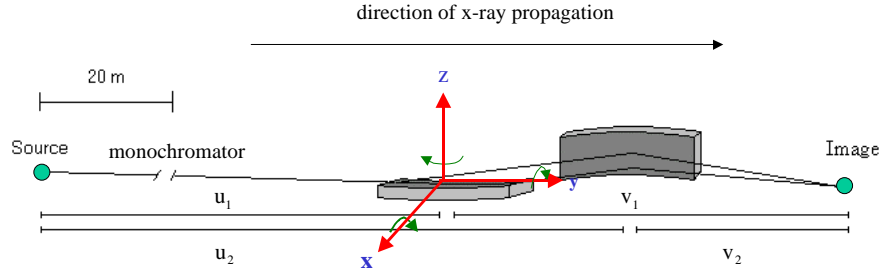


Figure 4-10: X13B micro-probe optical layout.

The distances  $u_1$ ,  $u_2$  and  $v_1$ ,  $v_2$  are measured from the source position to the poles of the mirrors, and from the mirror poles to the focal point respectively, and are determined by the location of the X13B experimental hutch in relation to the source.  $u_1$  was set at 25.5 m and the second mirror was positioned 2 cm in front of this. The mirror lengths were fixed at 10 cm, and this set the value of  $u_2$  at 25.62 m. The grazing incidence angle was chosen to be  $0.22^\circ$  to achieve a reasonable numerical aperture for energies less than  $\sim 12$  keV. These mirrors were designed to improve upon the current NSLS micro-probe capabilities and to allow high-pressure investigations using the diamond-anvil cell (Chapter 6). High-pressure experiments require relatively long working distances due primarily to sample-cell size. With this in mind, the focus was set at 40 cm from the vertical mirror pole. With these optical parameters, this gave a demagnification of  $M_z \sim \frac{1}{64}$  and  $M_x \sim \frac{1}{92}$  in the vertical and horizontal directions respectively (Equation {2.3}). Using the IVUN source size parameters, this should produce a demagnified image size of  $\sim 0.2 \mu\text{m}$  in the vertical by  $\sim 10 \mu\text{m}$  in the horizontal, where all beam dimensions are quoted as FWHM. The optical manufacturer quoted an upper level of the RMS slope error to be  $2 \mu\text{rad}$ , and adding this in quadrature to the demagnified image size of  $0.2 \mu\text{m}$  in the vertical direction, would produce a final vertical image size of  $3.8 \mu\text{m}$  (FWHM), and it was hoped that a better slope error may be accomplished.

### 4.5.3 Mirror parameters

With the mirror geometry and source parameters defined, the photon beam can be traced through the system using the SHADOW program. The differential deposition needed to form the elliptical figures can then be computed. Shown in Figure 4-11 is the simulated x-ray photon profile incident on the surface of the vertical and horizontal focusing mirrors. The shape has been defined as elliptical in the tangential, and planar in the sagittal directions. This is strictly not the same as in the real case, as the mirrors will be cut from a spherical single-crystal silicon substrate, but this has negligible effect on image quality in the KB arrangement. A clearer picture of the mirrors elliptical form is shown in Figure 4-12, where the beam height profile is viewed across the length of the mirror, and thus defines the optical surface. As the substrate will be spherical, the radii of curvature for the mirror substrates can be determined from a circular fit to the elliptical profile.

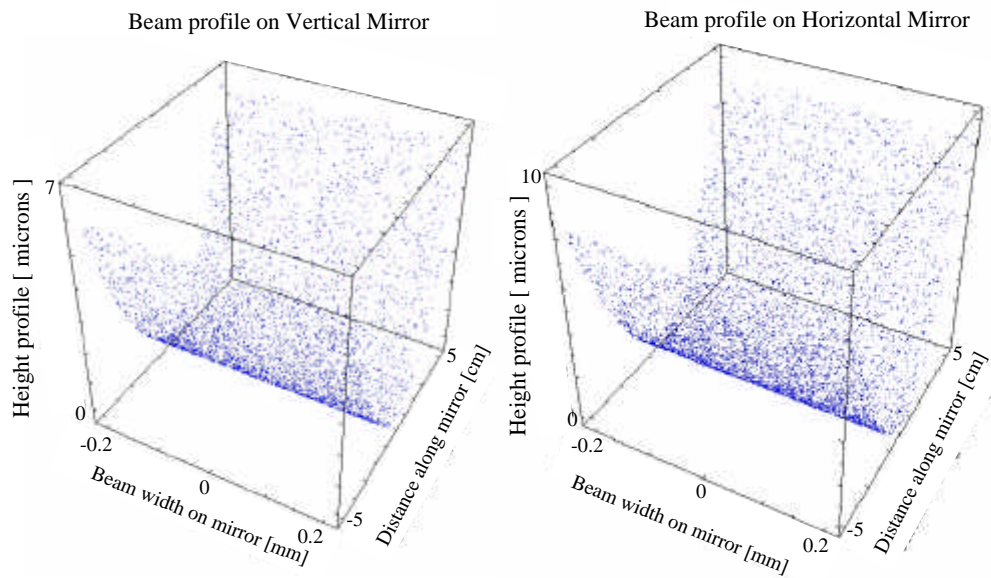


Figure 4-11: Simulated x-ray beam profile incident upon X13B elliptical mirrors.

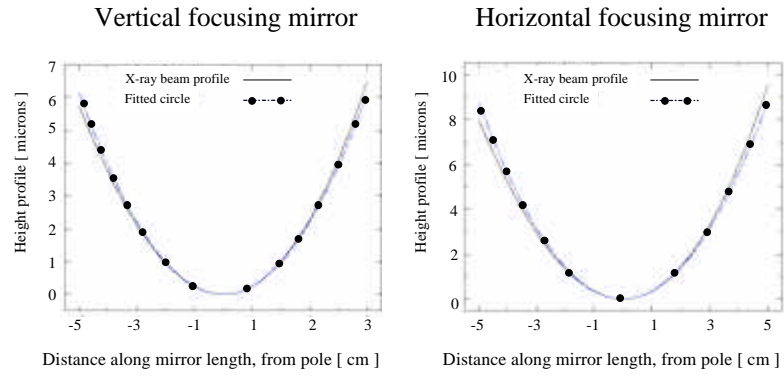


Figure 4-12: Height profile of photon beam along the mirror lengths for X13B micro-probe.

The fitted circles almost overlap the elliptical profiles, with radii of  $\sim 204$  m (vertical) and  $\sim 143$  m (horizontal). The required deposition profile of the coating can be deduced from the difference between the spherical and the required elliptical figures,

$$\text{Spherical}(y) + \text{Differential}(y) = \text{Elliptical}(y) \quad \{4.35\}$$

The residual profiles for the differential coatings are shown in Figure 4-13. As the height profile has both negative and positive values, the reference point for the deposition process is taken to be the start of the mirror (distance from mirror pole =  $-5$  cm).<sup>†</sup> An undercoat of chromium (typically a few hundred angstroms) is first applied to the substrate onto which the differential coating is deposited. This ensures a strong binding between the substrate and differential coating.

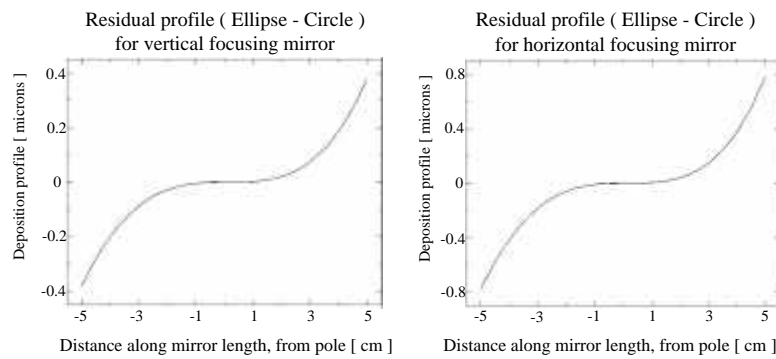


Figure 4-13: X13B micro-probe calculated residual specifications.

<sup>†</sup> Shifting the profile upwards is equivalent to adding a constant to Equation {4.35} and does not change the elliptical shape.

#### 4.5.4 Simulations

With both the source and optical configuration defined within the SHADOW ray tracing code, the photon beam was traced through the system to analyse the focal and misalignment properties of the system and to compare previous estimates of x-ray beam size. Figure 4-14 reveals how the vertical x-ray beam size varies from the focal position. The computed beam dimensions (twice the standard deviation) at the focal position were  $\sim 0.2 \mu\text{m}$  ( $\sim 0.24 \mu\text{m}$  FWHM) and  $\sim 7.8 \mu\text{m}$  ( $9.2 \mu\text{m}$  FWHM) for the vertical and horizontal dimensions respectively for a perfectly formed surface with no slope error. These values compare well using the source dimensions of the X13 straight section  $\sigma_z = 6.1 \mu\text{m}$  and  $\sigma_x = 404 \mu\text{m}$ , producing theoretical demagnified image sizes of  $\sigma'_z \sim 0.1 \mu\text{m}$  and  $\sigma'_x \sim 4.3 \mu\text{m}$ . It is clear that the slope error dominates the vertical image dimension. For a slope error of  $2 \mu\text{rad}$ , the computed beam size agrees well with results obtained by adding the image blur and demagnified image size in quadrature. The effect, although not plotted, is much less in the horizontal dimension as the greater source size is the dominant factor here.

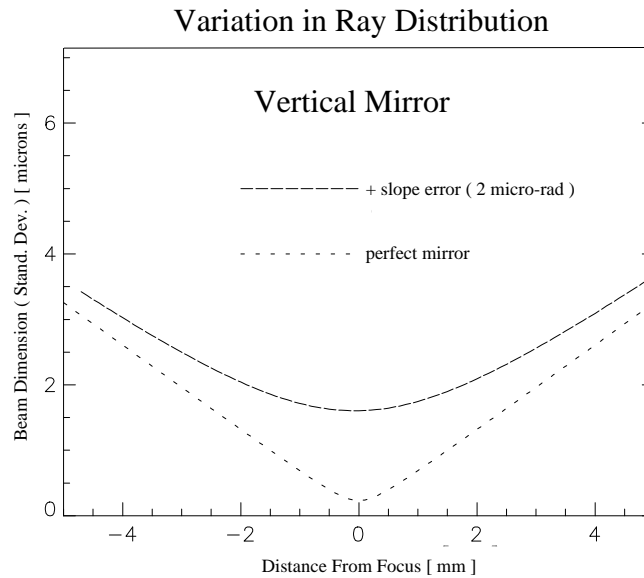


Figure 4-14: Simulated image size variations from focal position.

Also, it can be seen that within  $\pm 1 \text{ mm}$  of the focal position, the beam dimensions do not increase significantly, and the sensitivity required for sample positioning can be designed with this in mind. The photon beam dimensions are graphically displayed in

Figure 4-15 at the focal position, with both perfect and  $2\text{ }\mu\text{rad}$  slope errors included.<sup>†</sup> Misalignments of the system were also extensively studied using the SHADOW ray-tracing code, and were used to select the resolution of the motorised components needed to position the optics into the x-ray beam. These are specified in section 5.2.

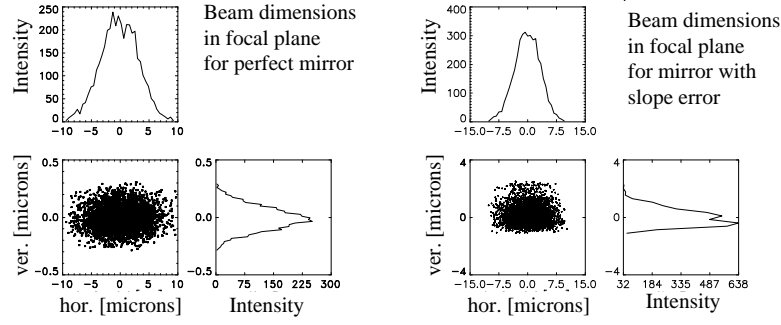


Figure 4-15: Simulated image size at focal position.

Referring back to Figure 4-10, the effects on mirror rotational errors are labelled as follows: The rotational errors around the x, y and z axes are conventionally referred to as pitch, yaw and roll respectively. The effect of a roll-error on the vertical focusing mirror is displayed in Figure 4-16 (with the horizontal mirror out of the x-ray beam). As can be seen, the effect of roll does not increase the vertical beam size but does focus it into the plane that would subsequently contain the horizontal mirror surface. This beam deflection couples strongly with the horizontal mirror as now the incidence angle is changed.

The mirror pitch angles were to be controlled precisely through computer-controlled pico-motor actuators. As the mirror surface has to lie on the exact ellipse, deviations from this figure are highly sensitive and an angular resolution of  $<10\text{ }\mu\text{rad}$  is required.<sup>42‡</sup> As the effect of roll is not as sensitive (verified using SHADOW), it can be controlled by manual adjustment and pre-alignment with a laser. Ray tracing also confirmed that yaw errors have a relatively large angular tolerance and can also be pre-

<sup>†</sup> The double-peaked structure in the right-hand side graph of Figure 4-15 is due to the finite number and binning of the photons.

<sup>‡</sup> As verified in subsequent SHADOW ray-tracing simulations.

aligned with a laser. The actual procedure for the positioning of the optics is explained in section 5.3.

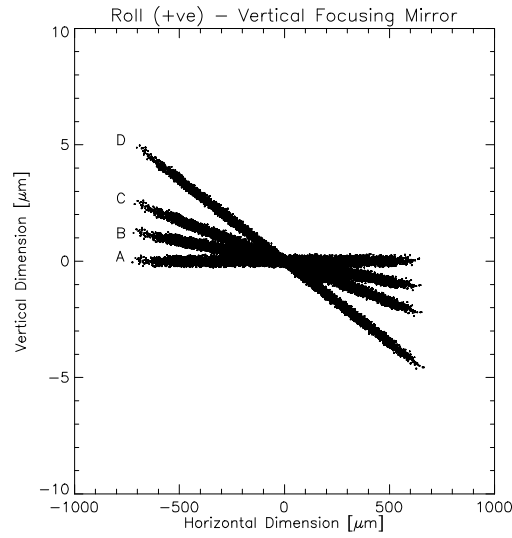


Figure 4-16: Roll effect on vertical focusing mirror. A) - Mirror parallel. B) -  $0.1^\circ$  error. C) -  $0.2^\circ$  error. D) -  $0.3^\circ$  error.

## 4.6 Summary

This chapter had introduced the geometrical and physical nature of x-ray reflectivity using grazing angles of incidence. A complete description of these is needed in the design of the X13B micro-probe. A concise description of aberrations introduced by spherical surfaces has been described, and the need for elliptical surfaces is evident. Differential coating of a mirror substrate with rhodium has been chosen as the method for manufacturing the X13B micro-probe. Effects of roughness and slope error have been considered and estimations of the focal properties have been investigated using the SHADOW ray-tracing code. Ray-tracing simulations have also been performed to assess the resolution needed for the X13B micro-probe rotational/translational stages. Focused beam dimensions of  $\sim 3.8\mu\text{m}$  in the vertical direction and  $\sim 10\mu\text{m}$  in the horizontal directions are expected for an RMS slope error of  $2\mu\text{rad}$ .

## Chapter 5 Manufacture and characterisation of the NSLS X13B KB optics

This chapter describes the mirror manufacturing process and the eventual incorporation of the micro-focusing mirror assembly into the X13B experimental end-station. The description is in chronological order, and the various problems encountered and subsequent remedies are outlined. The characterisation of the optics is detailed, and their performance is evaluated.

### 5.1 Optical manufacture and surface profile measurement

'Beamline Technologies Corporation'<sup>†</sup> was the manufacturer for the differentially deposited X13B x-ray micro-focusing mirrors. There is no known technique for polishing elliptical figures to the accuracy required for micro-focusing, and differential deposition is the only viable alternative to asymmetric bending. There are several high-density coatings that can be applied to the substrate, and rhodium was chosen due to the high reflectivity characteristics in the desired energy range up to  $\sim 12$  keV, and with no absorption-edges in this x-ray region (Figure 4-4).

Single crystal silicon is an ideal optical substrate as it can be polished to an extremely low roughness of  $< 3 \text{ \AA}$  which is necessary to maximise reflectivity (Section 4.3.1).<sup>‡</sup> A large silicon substrate (of length  $< 1 \text{ m}$ ) is ultra-smoothly polished to the required radius. A diamond saw is then used to segment it into smaller pieces, corresponding to the requested mirror dimensions. This ensures that round-off errors at the edges of each centrally located individual optical element are minimised, compared to if they were each separately polished.<sup>§</sup> From the SHADOW simulations for the X13B beamline configuration, the closest spherical radii of  $\sim 204 \text{ m}$  and  $\sim 143 \text{ m}$ , for the vertically and horizontally focusing mirrors were provided to the vendor. After the polishing process had been completed, the individual mirrors were separated and

---

<sup>†</sup> Mirror manufacturer and list of companies used to build the X13B micro-probe can be found in Appendix D.

<sup>‡</sup> This can be measured using a WYKO-TOPO<sup>®</sup> surface profiler which has a vertical resolution of  $\sim 1 \text{ \AA}$ .

<sup>§</sup> The outer-sections are not used.

accurate determinations of the radii were obtained using a long trace profiler (LTP).<sup>110</sup> A photograph of the two mirror blanks is shown in Figure 5-1.



Figure 5-1: X13B spherical silicon substrates to be used for x-ray micro-focusing.

Accurate radii measurements are required to calculate the differential coating profiles. These measurements were carried out at the Advanced Photon Source (APS)<sup>111</sup> using an LTP II<sup>®</sup> profiler,<sup>112</sup> within a state-of-the-art metrology clean room, where such evaluations are routinely performed. The LTP, which was originally developed at Brookhaven National Laboratory, calculates the slope function of the optical surface by measuring the phase difference between two collinear laser beams, separated by a small distance ( $<1\text{ mm}$ ) that are reflected from the surface. By integration of the slope function, the height profile of the surface can be calculated and the radius determined. The radii of curvature of the vertical and horizontal focusing mirrors, as measured using the LTP II<sup>®</sup> were  $(199.5 \pm 1.0)\text{ m}$  and  $(146.3 \pm 0.7)\text{ m}$  respectively.<sup>†</sup> The quoted error corresponds to the standard deviation averaged over ten scans. Figure 5-2 shows the slope error of one of the spherical silicon substrates. This was obtained by subtracting the perfect circular fit to the substrate from the measured surface profile, and the RMS value is  $\sim 0.8\text{ }\mu\text{rad}$ .

Differential deposition was the next stage in the manufacturing process, and the substrates were returned to the vendor so this could be performed. After coating the vertical focusing substrate, these were transferred back to the APS to check that the deposition process had been successful. This was achieved by measuring the height profiles of the optical surface using the LTP. The mirrors are rectangular, with surface

---

<sup>†</sup> Initially, similar measurements were performed using the NSLS LTP equipment, but temperature gradients in the dated metrology laboratory gave erroneous results that were only noticed after differential deposition had been completed. Subsequently, the metallic coatings had to be chemically stripped from the substrates so that deposition could be reapplied based on the true radii. This emphasises that care needs to be taken in this stage of production so that accurate deposition profiles are calculated.



dimensions of  $1\text{ cm} \times 10\text{ cm}$  (width x length), and the coating is in the form of a thin ( $\sim 0.5\text{ cm}$ ) strip along the central portion of each optic.

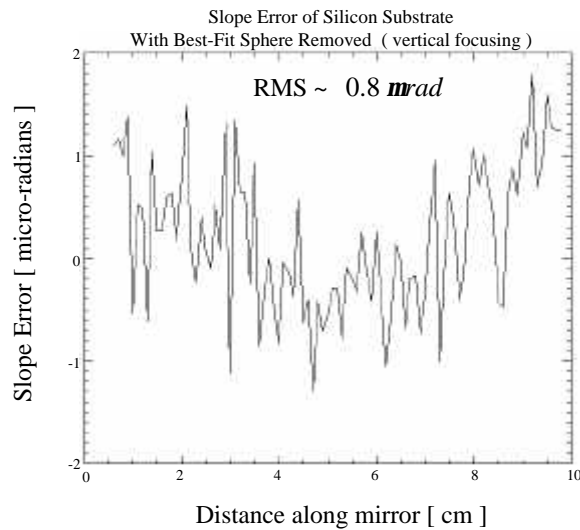


Figure 5-2: Slope error of a silicon substrate with best-fit sphere removed, to be used in the X13B micro-probe end-station.

By subtracting the height profile of the rhodium stripe from that of the spherical substrate, the differential coating profile is obtained and is shown in Figure 5-3. Based on these results, the ramp rates of the deposition machine were deemed good and the horizontal focusing mirror was subsequently coated. An important point to emphasise is the potential of the differential-deposition process for correcting low frequency errors that can occur during polishing.<sup>42†</sup>

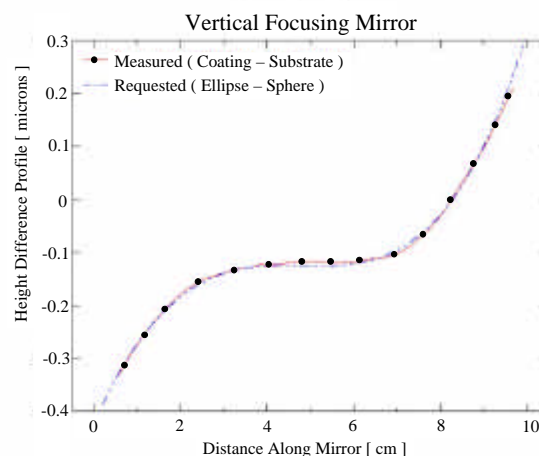


Figure 5-3: Comparison between measured and specified deposition profiles of the vertical focusing mirror.

<sup>†</sup> This procedure was not performed but is envisaged in the future design of sub-micron focusing optics.

## 5.2 Experimental set up and control

The motorised mirror stages, sample translation stages and various motor drivers are detailed in Appendix D, together with other equipment used to construct and utilise the X13B micro-probe. To provide stability, the apparatus was fixed to a vibration-damping granite slab of the same type used for nanometre focusing at the NSLS X1A beamline. The slab was placed on air cushions and fixed to a steel table that enabled height adjustment. A schematic of the set-up is shown below and the equipment is described in-turn.

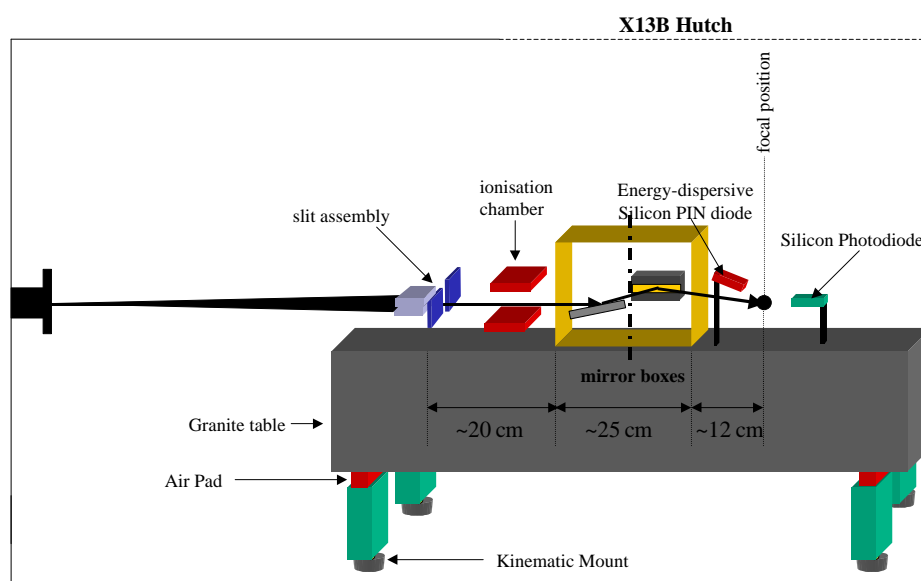


Figure 5-4: Schematic of X13B micro-probe assembly. The optical camera system has been omitted for clarity.

### 5.2.1 Mirror assembly

The optical mounts were carefully designed and selected so that the positioning of the mirrors into the x-ray beam could satisfy the stringent focal requirements as outlined in Section 4.5.4. The mirrors were each separately mounted in an in-house machined aluminium holder that was subsequently fixed to the inside of an aluminium die-cast gas-tight box. Furthermore, two pipe-fittings were threaded into each container to provide the option of helium gas-flow through the system. Each box had two square windows milled out to provide entrance and exit apertures for the x-ray beam, which were sealed using thin polyimide Kapton<sup>®</sup> tape. A schematic of the holder is shown

below, and the mirror is inserted between the grooves and held in position by clamping between the two ball bearings and set-screws.

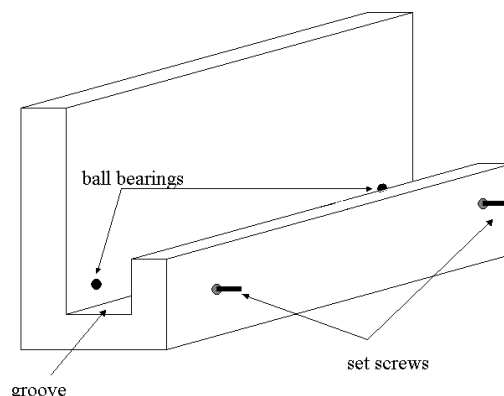


Figure 5-5: An X13B micro-focusing mirror mount.

The mirror stages provided the necessary degrees of freedom (pitch, roll, yaw and translation – Section 4.5.4), and were arranged so that the rotational degrees of freedom revolved about the centre of the reflecting surfaces. The mirror angle adjustment is the most sensitive part of the alignment process and high resolution is mandatory. The rotation stage motion was provided by a computer-controlled (CC) picomotor-driven screw, which resulted in an angular resolution of  $\sim 0.3 \mu\text{rad}$  ( $0.06 \text{ arcsec}$ ). The roll and yaw degrees of freedom were provided by manually adjustable multi-axis tilt stages, each with a resolution of  $10 \mu\text{rad}$ . To accurately locate the mirrors in the x-ray beam, the vertical focusing mirror was mounted onto a CC translation stage that provided motion in the vertical direction. Similarly, the horizontal focusing mirror was fixed to an identical stage to provide horizontal translation. These stages had a stepper-motor resolution of  $1 \mu\text{m}$  with  $25.4 \text{ mm}$  of linear travel, and orthogonal linear motion for each mirror was unnecessary due to the finite width of the rhodium coating. A photograph of the mirror assembly is shown in Figure 5-6. The mirror covers have been removed to enable viewing of the optical surfaces, and the two connectors on each box permits helium flow, once the assembly has been sealed.

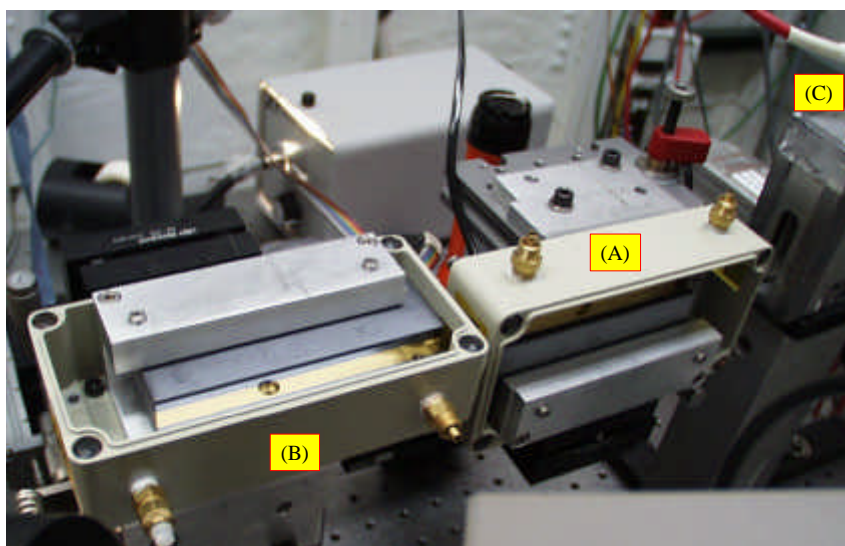


Figure 5-6: X13B micro-probe mirror assembly. (A) - Vertical focusing mirror, (B) -Horizontal focusing mirror and (C) - Ionisation chamber. The x-ray beam direction is from right to left in the photograph.

### 5.2.2 Mirror acceptance-slit assembly

Due to photon beam divergence from the synchrotron source, and the finite length of the mirrors, only a portion of the incident x-ray beam can be collected. It was therefore necessary to limit the spatial extent of the incident x-ray beam with a crossed-slit assembly. The slits were made from rectangular tantalum blocks which were first cut using a diamond saw, coarsely polished with emery paper and then finely polished by immersing in an alumina-oxide bath with a rotational bar that moved them across the crystal/slurry surface. The blocks were clamped together with aluminium spacers of thickness  $\sim 300\mu\text{m}$  to set the slit width. The whole assembly was fixed to a CC positioning stage that provided micro-metre translation and micro-radian angular resolution to enable accurate alignment with the x-ray beam.

### 5.2.3 Sample stage assembly

The sample stage was designed to provide motion along the x-y-z axes. For accurate determination of the beam size, two CC sub-micron linear positioning stages, each with  $0.074\mu\text{m}$  resolution were obtained. These were connected in a crossed-fashion to provide vertical and horizontal motion for the nickel dot (Section 5.4) and calcium (Chapter 9) imaging experiments. For high pressure studies (Chapter 7, Chapter 8), the sample size is much larger than the predicted vertical beam dimensions and the sample-

cell is relatively heavy. Thus, a heavy-duty CC motorised jack with a half-step mode resolution of  $2.5\text{ }\mu\text{m}$  was provided for this case. To fix the sample at the focal point, a micro-metre translation stage was incorporated to provide motion along the direction of x-ray propagation.

#### **5.2.4 Optical and x-ray detectors**

A variety of detectors were used in the X13B micro-beam set up to allow mirror alignment and experimental data acquisition. An optical system was incorporated to monitor sample position and enable optical alignment of the micro-probe mirrors. A thin-plate yttrium-aluminium garnet YAG:Ce crystal ( $\text{Y}_3\text{Al}_5\text{O}_{12}$ ) was used for mirror alignment (Section 5.3). The visible yellow light, which is emitted by the impinging x-ray beam on the scintillator, was imaged by a high-resolution microscope and ccd optical system. The microscope and camera were mounted on an x-y-z CC micro-metre resolution translation stage to enable tracking of the x-ray beam with rotational and height adjustments to the mirror pair. To monitor fluorescence photons, an energy-dispersive peltier-cooled silicon-pin-diode was positioned in the back-scattering geometry, and a silicon-pn-photodiode was placed downstream of the sample position to monitor transmitted/incident flux. A photograph of both the detector and sample set up is shown in Figure 5-7. As the electron beam in the storage ring decreases exponentially with time, it is necessary to incorporate an ionisation chamber into the apparatus for normalisation purposes. Although the working-distance is relatively large in the X13B micro-probe set up, there is still insufficient space to place such a detector immediately upstream of the sample position. However, by locating the ionisation chamber (6 cm active length) directly downstream the slit assembly, it is possible to correct for beam-decay and also beam motion. X-ray beam motion changes the beam height on the mirror acceptance slits and is due to the double-crystal monochromator geometry (Figure 3-10). The normalisation procedure is described in Section 5.6.

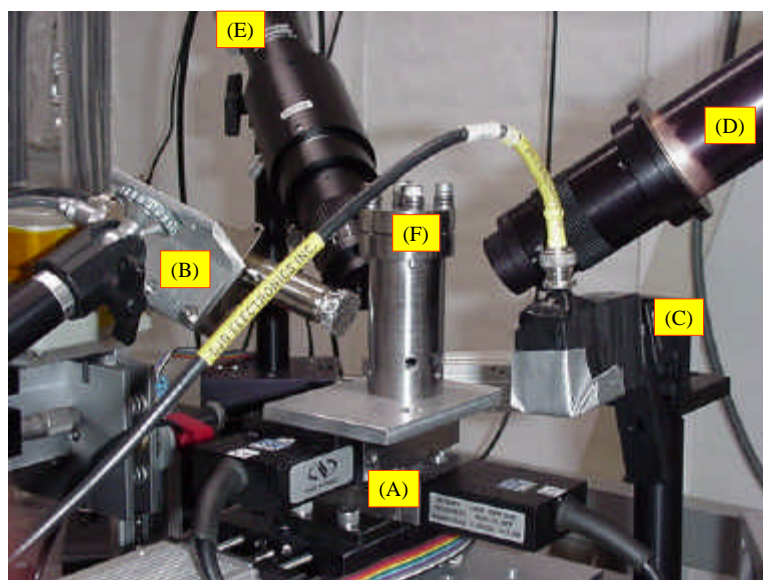


Figure 5-7: Sample positioning stage and detector system for the X13B micro-probe during the high-pressure praseodymium experiment (Chapter 8). The direction of x-ray propagation is from left to right, passing through the sample-cell and into the diode. The labels are as follows:- (A) - Sample positioning stage. (B) – Energy dispersive silicon-pin-photodiode. (C) – Silicon-pn-photodiode. (D) , (E) ccd optical microscopes. (F) - High-pressure sample cell.

### 5.3 Alignment of the X13B micro-probe

To install the mirrors in their approximate locations, a laser was used to perform pre-alignment. This was then followed by a microscopic optical alignment using the visible light emitted from the YAG:Ce scintillator crystal due to the impinging x-ray beam. The initial procedure for the successful implementation of the optics will be described in detail due to the importance of each step:

The bare granite table assembly was placed in the approximate position within the X13B experimental hutch so that the micro-focusing optics could be situated at the correct location in relation to the synchrotron source. By adjustment of the kinematic mounts, the table was then aligned along the propagation of the x-ray beam (which had been pre-determined). Next, the slit assembly was secured and aligned with the x-ray beam by monitoring the transmitted photons incident upon a silicon-pn-photodiode. A laser was then directed through the slits, and along the x-ray beam direction, and the mirrors inserted optically into their respective positions. Consequently, the roll and yaw of the mirrors were aligned in this manner. Once the mirrors had been positioned,

further alignment was achieved using the x-ray beam, by observing the emitted light from the YAG:Ce crystal placed at the pre-determined focal position, via the optical microscope assembly. The strategy was to first place the vertical focusing mirror into the x-ray beam and adjust the mirror to its correct angle. This was performed by first ensuring that the mirror was aligned approximately parallel to the incident photon beam. The mirror was then positioned mid-way into the x-ray beam, and rotated until the reflected rays were deflected by an amount corresponding to the calculated angle. Further accurate alignment was achieved by slightly varying the rotation angle until the best line-focus was observed. The vertical mirror was then withdrawn from the x-ray beam, by means of the motorised translation stage, and the above procedures were performed for the horizontal-focusing mirror. Once this step had been completed, the vertical mirror was returned to its previous position, and the x-ray beam was focused in both directions. A photograph of the X13B micro-probe set up is shown below, and x-ray propagation is from right to left.

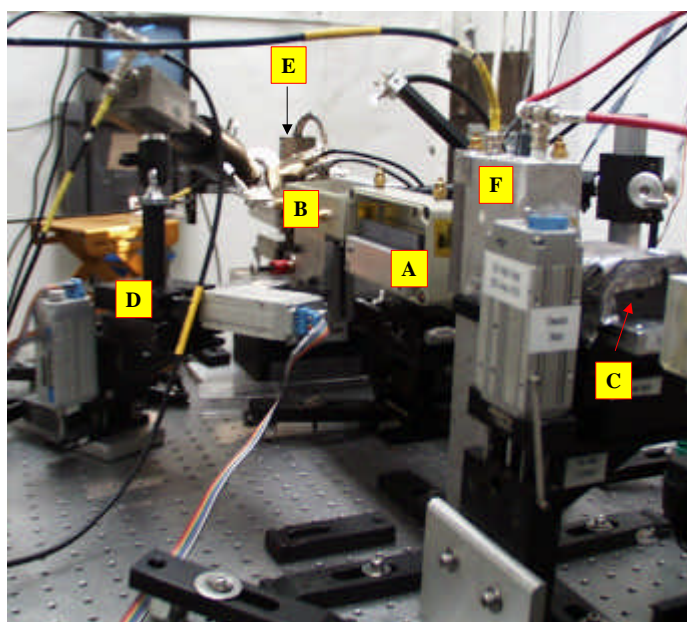


Figure 5-8: Wide-angle photograph of the X13B micro-probe set up. The labelling is as follows:- (A) - Vertical focusing mirror. (B) - Horizontal focusing mirror. (C) - Slit assembly, surrounded by lead shielding. (D) - High-power optical microscope. (E) - Sample stage. (F) - Ionisation chamber.

## 5.4 Nickel dot fluorescence x-ray beam profile measurements

Measurements of the nickel fluorescence intensity from an array of nickel dots were performed to determine the profile of the focused x-ray beam. These dots had been evaporated onto a silicon (111) substrate and had a diameter of  $1\text{ }\mu\text{m}$ , a thickness of  $2000\text{ }\text{\AA}$  and a separation of  $50\text{ }\mu\text{m}$ . These were identical to those used by Noyan *et al.*<sup>67</sup> As these small structures are extremely thin, this procedure is very slow. Count rates approaching 10 cps were anticipated and long exposure times were needed to obtain good statistics.

The sample was placed in an upright position on the x-y-z micro-positioning stage (where  $x$  and  $z$  measure the width and height of the x-ray beam respectively, and  $y$  provides translation along the optical axis). An incident x-ray energy of 8.8 keV (from the wiggler insertion device) was selected by the X13B monochromator to remove electrons from the nickel K-shell. An amptek XR-100CR energy-dispersive silicon-pin-photodiode detector ( $7\text{ mm}^2$  area) was used to collect the fluorescence photons, and the Ni  $K_{\alpha}$  fluorescence line was selected using a Nucleus PCA-II<sup>®</sup> multi-channel analyser. The incident energy was significantly high enough to reduce Compton scattering into the fluorescence line, and provides a higher signal-to-background than would have been otherwise achievable for energies nearer the absorption-edge. Figure 5-9 shows a contour plot of three nickel dots which were selected from the array, and were acquired around the best focal position as determined by the YAG:Ce output. The two vertically aligned images on the right-hand side of Figure 5-9 show the expected elliptical profiles, as opposed to the image on the left hand-side which is asymmetric and much broader. This discrepancy is attributed to sample preparation error. A number of similar measurements were performed at different locations on the array, and no other asymmetric profiles were detected. A three-dimensional representation of a single nickel dot is shown in Figure 5-10, and the background surrounding the peak is mainly due to scatter from the silicon substrate.



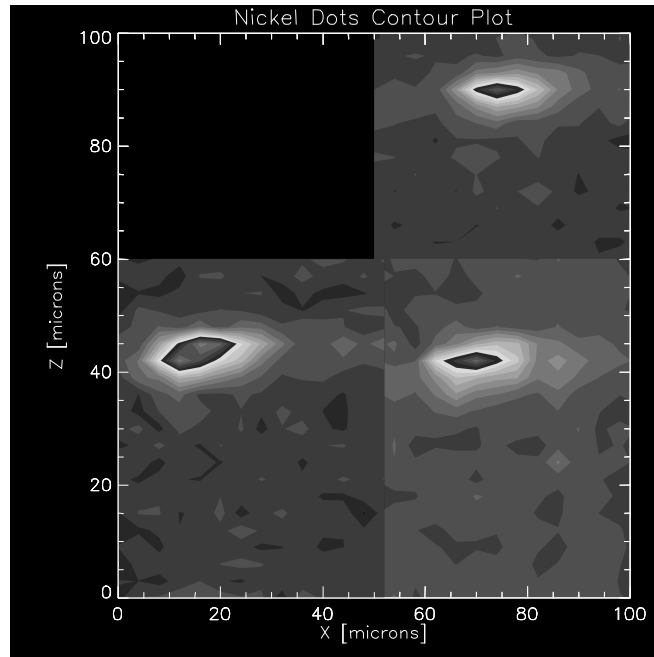


Figure 5-9: Contour plot of nickel dot fluorescence intensity.

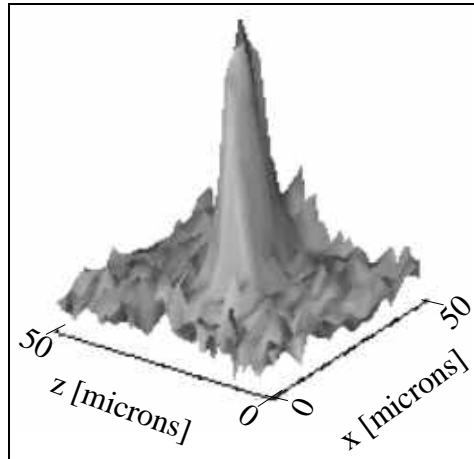


Figure 5-10: 3D plot of Ni  $K_{\alpha}$  fluorescence intensity from a single nickel dot.

By performing measurements along the centre of a dot, it was possible to determine the x-ray beam dimensions. Figure 5-11 and Figure 5-12 display the width of the focused beam in the vertical and horizontal directions, with FWHMs of  $\sim 6\mu\text{m}$  and  $\sim 15\mu\text{m}$  respectively. However, it was not clear whether the sample was at the correct focal position, and the large side-lobe in Figure 5-12 suggested optical misalignment. Unfortunately, acquiring the beam dimensions using this method is very slow and

precise alignment is difficult. It was therefore decided to employ a more rapid technique for acquiring the x-ray beam profiles, thus allowing the dimensions to be quickly measured along the optical axis, and subsequent realignments to be performed.

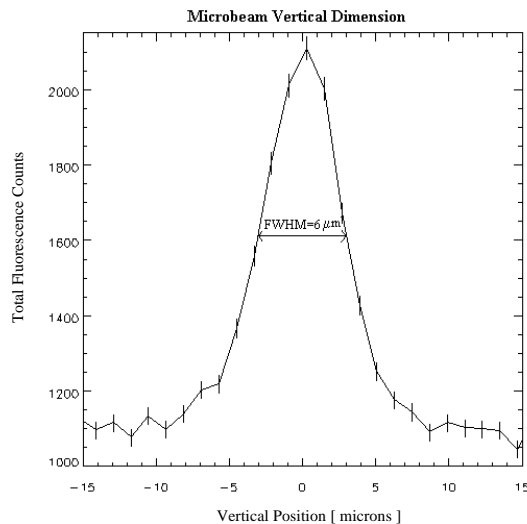


Figure 5-11: Vertical beam size measurement through nickel dot fluorescence detection.

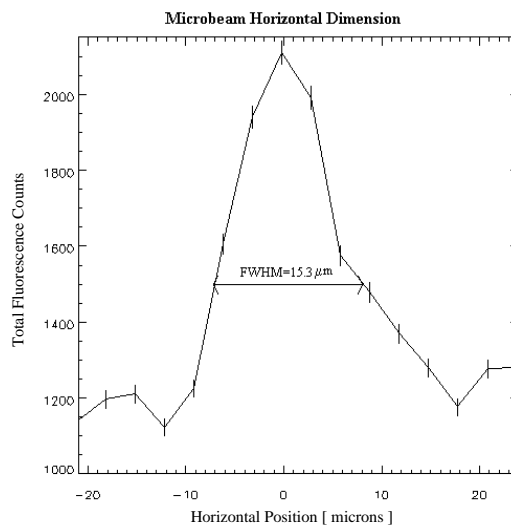


Figure 5-12: Horizontal beam size measurement through nickel dot fluorescence detection.

## 5.5 Blade-scan x-ray beam profile measurements and focal considerations

A rapid determination of focal properties can be obtained by translating a high-Z material through the focused x-ray beam and monitoring the photon flux downstream. It was subsequently decided to scan the focal beam dimensions with a straight-edged tantalum block of the same grade as that used for the slit assembly (Section 5.2.2). In

this experiment, the mirror locations were translated along the optical axis to employ the undulator source, and the electron beam energy was 2.8 GeV. The block was placed on the sample stage and the downstream silicon-pn-photodiode was used to monitor transmitted flux. The sample stage was scanned in the vertical and horizontal directions and the beam profile was determined by the derivative of the flux throughput. This procedure was repeated at various points along the optical axis and the results are presented in Figure 5-13. The vertical and horizontal beam sizes (solid lines) rise noticeably within  $\sim \pm 5$  mm of the focal point and have a shape similar to that determined by prior ray-tracing results (Figure 4-14). Subsequently, it was concluded from the dimensions, as determined in the nickel dot fluorescence experiment (Section 5.4), that there was an error in determining the best focal position during that measurement.

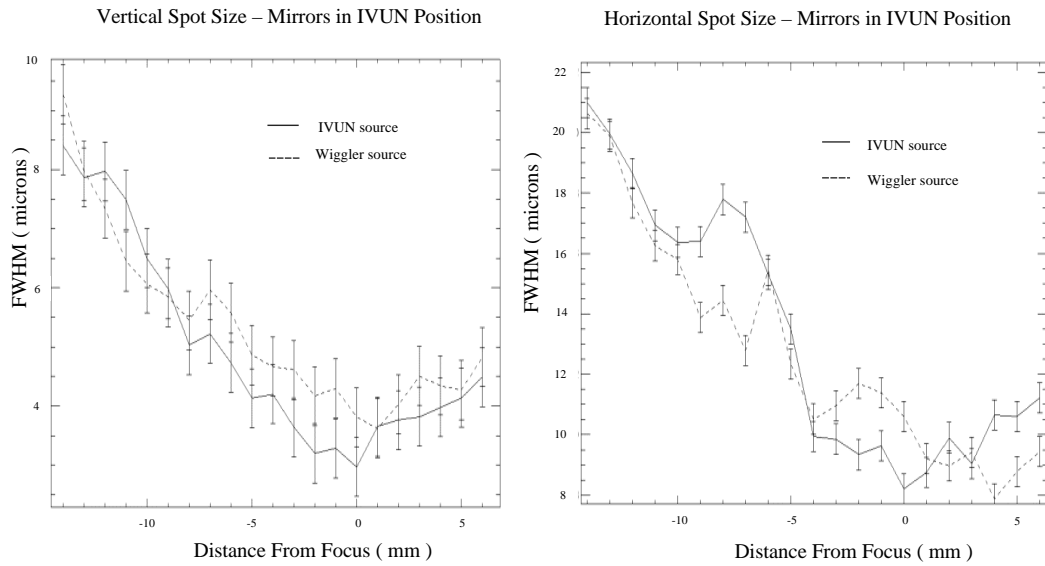


Figure 5-13: X13B micro-probe focal properties as measured from blade scan derivatives, using the two different sources in the X13 straight-section.

To analyse the variation in image size when the source-to-optics distance is changed, the wiggler source was implemented (by opening the IVUN magnetic gap fully and closing the wiggler magnetic gap), with the mirrors remaining in the location to utilise IVUN. The results are represented by the dotted lines in Figure 5-13 and the best FWHM in the vertical direction was  $\sim 4 \mu\text{m}$ . This situation is useful for the X13B

micro-probe end-station, as it allows the sources to be interchanged, with only small changes to the focal spot size. These increases are certainly tolerable in high-pressure experiments, with the benefit that the need for translating the optics is eliminated.

Figure 5-14 displays the derivatives of the transmitted flux at the best focal position, as determined from Figure 5-13 ( and using the IVUN source). The measured FWHM of the vertical and horizontal dimensions are  $(3 \pm 0.5) \mu\text{m}$  and  $(9 \pm 2) \mu\text{m}$  (errors are due to fitting). An estimation of the vertical focusing mirror slope error can be deduced from these measurements, assuming a perfectly aligned system. As the vertical source size is small, the contribution to the image by geometrical demagnification is negligible and the blur due to slope error is the dominant factor. The slope error was calculated to be  $\sim 1.6 \mu\text{rad}$  , by employing Equation {4.22}.

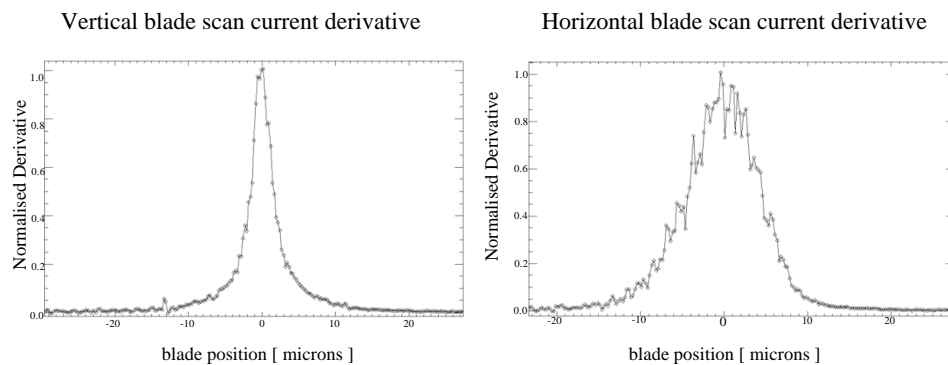


Figure 5-14: Blade scan derivative for focused beam measurement.

Using this value and taking into account the demagnified source contribution, the predicted image dimension in the horizontal direction should be  $\sim 10.9 \mu\text{m}$  , and agrees well with the above measurement and exceeds design expectations.

## 5.6 Estimation and measurement of photon flux

It is necessary, in any experiment, to have an estimate of the flux that will be delivered to the sample. This can then be used to determine the expected signal and experimental feasibility. By employing the brightness curves as shown in Figure 3-2 for the wiggler or undulator devices, the flux that will be delivered to the sample can be

determined. An example of the flux measured during the nickel-dot experiment in Section 5.4 is given, and all data were recorded at an electron beam current of  $\sim 200$  mA :

Prior to the installation of the x-ray micro-probe optics, a knife-edge scan (using a straight-edged piece of tantalum) was used to accurately determine the aperture of the slit assembly and was found to be  $\sim 270 \mu\text{m} \times 270 \mu\text{m}$ . For 2.584 GeV operations, and an incident x-ray energy of 8.8 keV, a corresponding brightness of  $\sim 4 \times 10^{13}$  photons/sec/0.1 % BW / mA / mm<sup>2</sup> / mrad<sup>2</sup> is emitted by the wiggler source. The band-pass of the X13B monochromator is approximately  $\frac{\Delta E}{E} \sim 10^{-4}$  for the Si (111) reflection and the FWHM source size is approximately  $\sim 1.1 \text{ mm} \times 37.5 \mu\text{m}^\dagger$  in the horizontal and vertical directions respectively. The entrance slits to the mirrors accept  $\sim 10.5 \mu\text{rad}$  in both the horizontal and vertical directions, and in-vacuum, an incident flux of  $\sim 3.6 \times 10^9$  photons/sec is expected. This value can now be compared to that which is actually measured:

The 60 mm ionisation chamber, directly downstream of the slit assembly, absorbs approximately 4.6 % of the incident radiation at this x-ray energy. Thus, by measuring the current from the ionisation chamber, the incident flux can be calculated (before the micro-focusing mirrors) through the relationship:

$$F \times N \times \frac{E}{\Omega} \times e = I \quad \{5.1\}$$

where F is the fraction of photons absorbed along the ionisation chamber path, N is the number of photons travelling through the ionisation chamber, E is the incident photon energy,  $\Omega$  is the ionisation potential of air (  $\sim 34$  eV ), e is the electronic charge and I is the current.

A current of  $\sim 0.7$  nA was measured by the ionisation chamber and using the values for F and  $\Omega$  as given above, this corresponds to a value of  $N \sim 3.7 \times 10^8$  photons/sec before

---

<sup>†</sup> The larger vertical source size than that of IVUN, is due to the effect of source divergence and the location of the EPW device within the X13 straight-section.

the mirrors. There are three beryllium windows in the X13B beamline which absorb  $\sim 8\%$  of the photons from the source (Figure 3-8). There is also a  $\sim 1.5$  m long air-path between the end of the X13B beamline and the slit-assembly, which absorbs  $\sim 69\%$  of the remaining photons. Replacing the air path with a vacuum or helium path, and neglecting beryllium absorption, would increase the flux to  $\sim 1.3 \times 10^9$  photons/sec, which is almost a factor of three less than the expected value of  $\sim 3.6 \times 10^9$  photons/sec. This can be attributed to the intensity loss in the monochromator due to the heat-load induced by the photon beam and de-tuning of the upper-crystal.

However, downstream of the slit-assembly, the x-ray beam has to pass through the mirror chambers and along an air-path before reaching the sample. Hence, the helium flow that can be provided through the optical chambers is beneficial. Further upgrades to the system are planned so that the complete micro-probe station is housed within a helium/vacuum environment. A silicon-pn-photodiode detector was placed approximately 5 cm downstream of the intended focal position, to be used in transmission experiments, and was also a necessary aid for aligning the slits and mirrors. The diode can be used to verify the previous result and confirm that no unexpected intensity loss is encountered through the optical configuration. The detector is linear up to around 10 keV and a plot of the manufacturer's data is shown below:

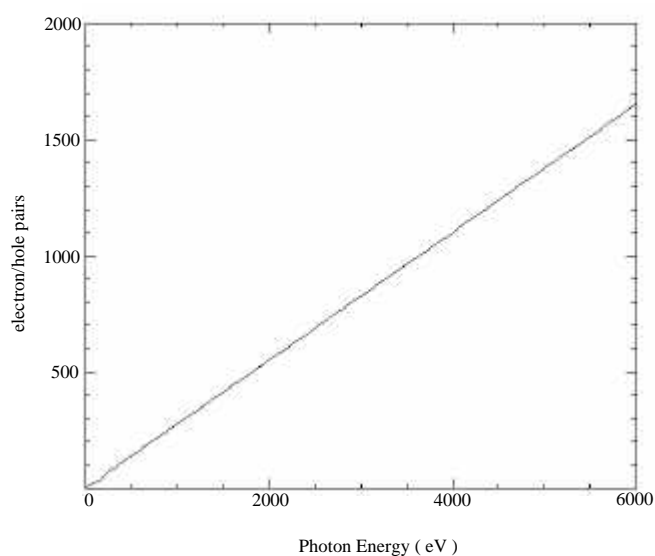


Figure 5-15: Silicon-pn-photodiode data.

A sheet of aluminium (25  $\mu\text{m}$ ) was used to prevent any visible light from reaching the diode. A measurement of the flux in the Si-pn-photodiode, corrected for the aluminium window absorption, is given by the following relationship:

$$(1 - F) \times N \times \frac{E}{\chi} \times e = I \quad \{5.2\}$$

where  $F$  is the fraction of photons absorbed in the aluminium window,  $N$  is the number of incident photons at the window,  $\chi$  is the ionisation potential for producing electron-hole pairs (3.63 eV) and  $I$  is the Si-pn-photodiode current.

At 8.8 keV the aluminium window absorbs  $\sim 22\%$  of the incoming flux. With the mirrors in place the diode current was  $\sim 45$  nA, and the number of photons incident at the detector window was calculated to be  $\sim 1.48 \times 10^8$  photons/sec. Between the ionisation chamber and diode there is  $\sim 67$  cm of air (including mirror chambers, which were not filled with helium for this measurement) that absorbs  $\sim 41\%$  of the incident photons. If this air-path were replaced by vacuum, the number of photons would increase to  $2.5 \times 10^8$  photons/sec. Additionally, the removal of the air-path before the slits would boost the number of photons to  $1.04 \times 10^9$  photons/sec. This agrees well with the measured flux after the slits for a vacuum-path ( $1.3 \times 10^9$  photons/sec), with the only factor contributing to flux loss being the mirror reflectivity. A table representing the measured and estimated flux (in-vacuum) is presented in Table 5-1.

	Ionisation Chamber	Silicon-pn-Photodiode
	( Photons through slit assembly )	(Photons in focal spot).
Measured Current	0.7 nA	45 nA
Measured Flux ( Air )	$3.7 \times 10^8$ photons/sec	$1.48 \times 10^8$ photons/sec
Estimated Flux ( Vacuum )	$3.6 \times 10^9$ photons/sec	$3.6 \times 10^9$ photons/sec

Table 5-1: Measured flux for the X13B micro-probe end-station at an incident x-ray energy of 8.8 keV.

The overall gain of the system is given by,

$$g = \frac{\text{Number of photons in focal spot}}{\text{Number of photons through slit assembly}} \times \frac{\text{Slit area}}{\text{Focal spot area}} \quad \{5.3\}$$

and the estimated gain in air at 8.8 keV is  $g_{air} \sim 1.35 \times 10^3$ . In a perfect system with 100 % reflectivity for the optics and in-vacuum, the gain is simply given by the ratio of the slit area to that of the focal spot (ignoring photon beam divergence).

## 5.7 Summary

In concluding this chapter, the successful completion of the elliptical shape to provide point-point focusing using the NSLS synchrotron source in the X13 straight-section has been achieved. The new technique of differential coating has provided optics with low slope errors and has enabled long working distances to be employed in the X13B micro-probe end-station. Testing of the optics has produced excellent results, with a focused x-ray beam of  $\sim 3 \mu\text{m}$  in the vertical and  $\sim 9 \mu\text{m}$  in the horizontal directions. Further improvements in the manufacturing process are anticipated. Flux throughput of the system closely matches that predicted, and there is little intensity loss due to the low roughness of the optical surfaces. Finally, stability of the set up is excellent (provided by the granite table assembly), which is necessary for operation of these optics. These optics and their potential applications were presented at the '2000 Synchrotron Radiation Instrumentation Conference.'<sup>113</sup>



## Chapter 6 High-pressure x-ray absorption spectroscopy

Most materials undergo dramatic phase transitions when subjected to high enough pressures. It is the nature of these phase changes, which are of interest, and which may be revealed by x-ray absorption studies.<sup>114,115</sup> X-ray analysis in the high-pressure region is extremely important in that it has the potential of directly revealing both the structural and electronic information of materials.

The nature of high-pressure experiments dictates a small sample size, through the use of a pressure-generating device known as a diamond-anvil cell (Section 6.1), and the implementation of x-ray micro-beam focusing optics is required to deliver a sufficient number of photons to the inherently small sample. Chapter 7 and Chapter 8 describe two high-pressure experiments which were conducted at the NSLS X13B beamline using the differentially deposited x-ray micro-focusing optics designed in this thesis.<sup>116</sup> This chapter will describe the diamond-anvil cell and the x-ray spectroscopic methods used for investigating materials under high-pressure.

### 6.1 The diamond-anvil cell and high-pressure generation

Very high pressures can be generated by a device known as a diamond-anvil cell (DAC). There are a few flavours of this device but the general mechanisms of pressure generation are similar, and a schematic of a cell is shown in Figure 6-1. In this thesis, DACs of the Mao-Bell type were used.<sup>117-119</sup> Pressure is usually quoted in units of gigapascals (GPa), kilo-bars (kbar), atmospheres or mega-torr (M torr).  $1 \text{ GPa} = 10 \text{ kbar} \sim 9.87 \times 10^3 \text{ atmospheres} \sim 7.5 \text{ M torr}$ , and the pressure at the Earth's centre is estimated to be approximately 370 GPa at a temperature of 3500 K.<sup>120</sup>

Diamond is pure crystallised carbon and the hardest natural material found on Earth, and depending on the DAC geometry, pressures up to 4.6 Mbar have been demonstrated.<sup>121</sup> High temperature can also be incorporated into such a device by resistive heating wires<sup>120</sup> or by laser heating of the sample,<sup>122-126</sup> and temperatures exceeding 4000 K can be achieved.<sup>123</sup>

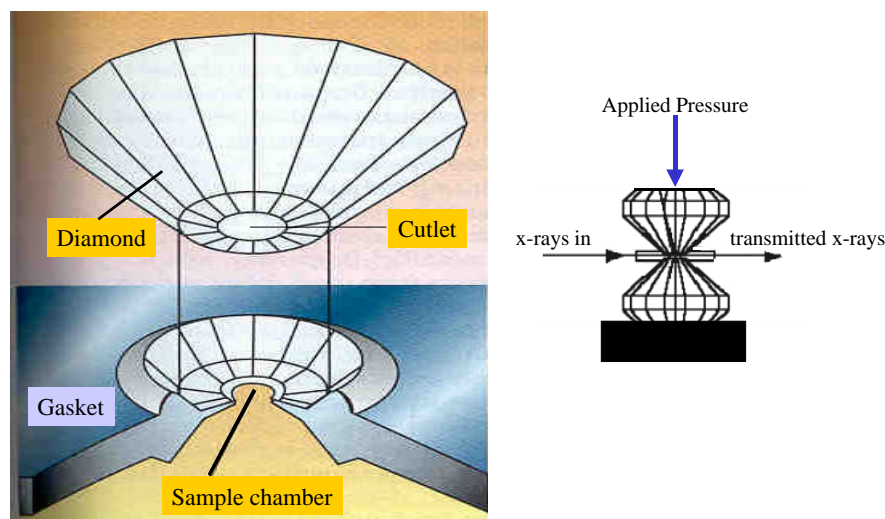


Figure 6-1: The diamond-anvil pressure cell.

The pressure is applied to the sample cell by means of the small-area part of the diamond known as the cutlet, which is highly polished to produce an extremely parallel and smooth surface. To create ultra-high pressures, this area is very small and typically in the range  $100\text{ }\mu\text{m} \rightarrow 400\text{ }\mu\text{m}$  in diameter, with smaller cutlets having the ability to produce larger pressures. Typical weights of the diamonds are measured in carats, and are of the order of  $\sim 0.1 \rightarrow 0.5$  carats, where  $1\text{ carat} = 0.2\text{ g}$ .

Pressure gradients in the sample can be reduced if a hydrostatic environment is incorporated into the system.<sup>122,127,128</sup> This can be achieved by filling the sample-chamber with a fluid such as mineral-oil, or loading the sample under an inert gas such as argon: When the diamonds are brought close together with moderate pressure ( $< 0.6\text{ GPa}$ ) they trap the fluid or gas inside the gasket material and a tight seal is formed.

The pressure in the cell can be measured by inserting ruby chips, along with the sample, into the DAC. By using an argon ion laser to excite the ruby fluorescence lines, R1(694.2 nm) and R2(692.8 nm), pressures up to  $\sim 150\text{ GPa}$  can be determined by measuring the pressure-induced shifts of these spectral lines.<sup>120</sup> For example, the shift in the R1 line is  $\sim 0.03\text{ nm/kbar}$  at room temperature, with an estimated error of

$\sim \pm 10\%$ .<sup>128-130</sup> These shifts can be measured using a fluorescence grating spectrometer, similar to the type described elsewhere.<sup>130†</sup>

For the high-pressure experiments performed in this thesis, the DAC had the following specifications:

- Pressure was generated by turning screws along the top of the DAC structure to close the diamond-anvils. A series of four holes consisting of two sets of directly opposed apertures, rotated by  $90^\circ$  with respect to each other, were drilled into the solid-steel DAC structure. This arrangement enabled x-ray experiments to be performed in transmission (Section 7.1), and  $90^\circ$  (Section 7.2) or  $180^\circ$  / back-scattering (Section 8.1) fluorescence geometries. A photograph of the DAC used in high-pressure experiments at the NSLS X13B beamline is shown in Figure 5-7.
- The gasket material was manufactured from beryllium which was 3 mm in diameter and 1 mm thick, and indented in the centre to form the sample chamber (Figure 6-1). This is a major improvement on previous DAC designs which typically used stainless steel to form the gasket, and experiments were constrained to higher energies ( $> \sim 10$  keV) as the x-rays had to pass through the diamond anvils before reaching the sample. The new design of employing beryllium gaskets allows for softer x-ray studies to be performed.

## 6.2 Extended X-ray Absorption Fine Structure ( EXAFS )

X-rays are an ideal probe of the structure of materials as their wavelengths are ideally matched to the electronic energy levels and inter-atomic distances. X-ray absorption spectroscopy measures the absorption of x-rays as a function of the incident photon

---

<sup>†</sup> High pressure experiments conducted in this thesis utilised the high-pressure loading and measurement facilities which were kindly provided by the X17c beamline at the NSLS.  
<http://angi7.nsls.bnl.gov/~x17c/x17chome.bnl>

energy. By measuring the transmission of x-rays of energy  $E$  through a material of known thickness the linear absorption coefficient,  $\mu_x(E)$  can be obtained (Section 4.1).

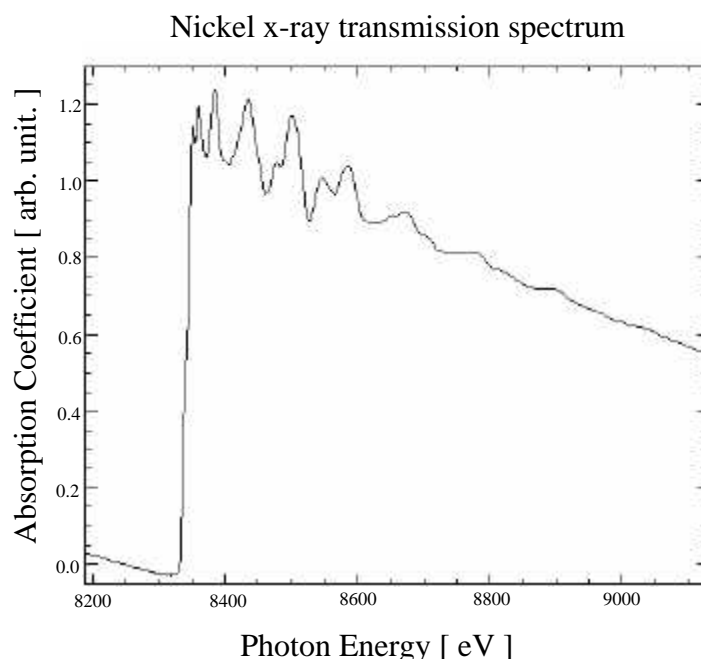


Figure 6-2: X-ray transmission through a thin nickel foil.

Figure 6-2 shows the linear x-ray absorption coefficient (arbitrary units) obtained by measuring the transmission of x-rays through a thin nickel foil.<sup>†</sup> Some of the important areas of the spectra are described below:

- There is a sharp increase in the absorption cross-section just below 8.35 keV which corresponds to excitation of a core 1s electron to a higher unoccupied state. This is the nickel K-edge that is located at 8.333 keV. Positions of absorption edges can be extremely sensitive to the chemical environment of the absorbing atom.<sup>131-133</sup>

<sup>†</sup> The data were collected at the NSLS X23A2 beamline using a double-crystal Si (311) monochromator. Nitrogen filled ionisation chambers were placed before and after the sample to record the data. The nickel foil was approximately 12.5  $\mu\text{m}$  thick and the data was collected courtesy of Dr. J. Woicik.

- Below the absorption-edge, the x-ray absorption decreases monotonically with increasing incident energy which is due to the absorption by electrons occupying the higher-energy shells within the material. This is known as the pre-edge region.
- Above the absorption edge, the x-ray absorption coefficient shows complicated behaviour. This region reflects the raising of the inner electrons to bound empty states, and the scattering of the ejected photoelectrons from neighbouring atoms. Generally, these are referred to as the XANES (X-ray Near-Edge Structure) and EXAFS (Extended X-ray Absorption Fine Structure) parts of the x-ray absorption spectra respectively.
- The XANES region of the spectrum is that in the immediate vicinity of the edge, and typically extends out to a further  $30\text{ eV} \rightarrow 50\text{ eV}$ . In this region, the excited electron probes the band-structure of the material and is often complicated to interpret. It is highly sensitive to the chemistry and the long-range order of the system.<sup>134,135</sup>
- As the incident energy of the x-rays is increased above the XANES region, the ejected photoelectrons have high kinetic energies and are generally insensitive to inter-atomic charge distributions and bound-states. Instead, they scatter off the core-electron clouds surrounding the neighbouring atoms and this gives rise to periodic modulations in the absorption spectra. This is the EXAFS region of the spectrum. These modulations are typically a few per cent of the absorption cross-section, and are superimposed onto a monotonically decaying background with increasing photon energy.

It is important to recognise the quantum mechanical nature of EXAFS: For incident x-rays of polarisation  $\underline{\varepsilon}$  and energy  $h\nu$ , inner electrons can be excited to unoccupied states in the absorption process. Electrons in an initial bound state described by the wavefunction  $\psi_i$  and energy  $E_i$ , can be promoted to a final state of wavefunction  $\psi_f$  and energy  $E_f$ . The absorption coefficient is then proportional to the absorption transition rate and can be derived from Fermi's Golden Rule:<sup>135,136</sup>

$$\mu \propto \sum_f \left| \langle \psi_f | \sum_j \underline{\varepsilon} \cdot \underline{p}_j | \psi_i \rangle \right|^2 \rho(E_f) \quad \{6.1\}$$

where  $\underline{\varepsilon}$  is the polarisation of the incoming photon,  $\underline{p}_j$  is the momentum operator acting on the  $j^{\text{th}}$  electron of wavefunction  $\psi_i$ , and  $\rho(E_f)$  is the density of final states.

In the EXAFS region, the final state energy lies well above the Fermi level and the excited state is that of a free electron. The core-electron wave function  $\psi_i$  is fixed and the only factor that can give rise to oscillatory behaviour in the absorption coefficient is  $\psi_f$ . This final state wavefunction is sensitive to the environment of the neighbouring atoms (see below). This oscillatory structure is a unique signature of a material and important structural information can be obtained from such a measurement. EXAFS probes the short-range order of systems which is important as non-crystalline materials can be studied such as liquids and glassy materials. Stern *et al.* first presented the actual interpretation and theory of EXAFS in three fundamental papers<sup>136-138</sup> and an excellent review of the theoretical development of EXAFS is present in a paper by Rehr *et al.*<sup>135</sup>

A simple insight into how this oscillatory behaviour occurs is depicted in Figure 6-3. Due to absorption of an incident x-ray, a photoelectron is ejected from the atom, which can be represented by an outgoing spherical wave. This wave can reflect off the surrounding atoms which gives rise to interference between the outgoing and scattered waves. As the incident x-ray energy is increased above the absorption edge, the

wavelength of the photoelectron varies, and constructive or destructive interference occurs depending upon the photoelectron wavelength and distance to the scattering atom. This interference modulates the final-state wavefunction in Equation {6.1}, which in turn, modulates the absorption coefficient. The beauty of EXAFS is that in general, only a few multiple scattering paths are important in generating the fine structure, which reflects the dying out of the spherical waves as they are scattered from one atom to another.<sup>135</sup>

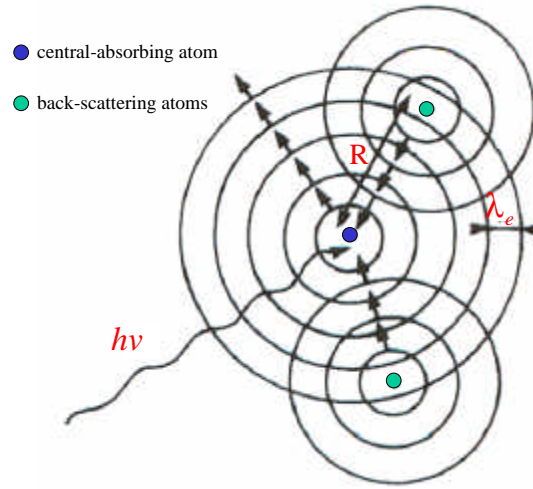


Figure 6-3: Example of back-scattering of the photoelectron wave from neighbouring atoms surrounding the central-absorbing atom.

By conservation of energy, the photoelectron's energy is given by,

$$\frac{\hbar^2 k_e^2}{2m_e} = h\nu - E_i \quad \{6.2\}$$

where  $k_e$  is the wave-number of the photoelectron,  $h\nu$  is the incident x-ray energy, and  $E_i$  is the binding energy of the ejected electron originally occupying the  $i^{\text{th}}$  atomic energy level.

Then, the phase-shift of the photoelectron wave on its return to the central-absorbing atom is given by,

$$\phi = \frac{2\pi}{\lambda_e} \times 2R \quad \{6.3\}$$

where  $R$  is the distance from the central-absorbing atom to the back-scattering atom,<sup>†</sup> and  $\lambda_e$  is the wavelength of the photoelectron.

Thus constructive interference will occur when

$$\phi = 2\pi n \quad \{6.4\}$$

where  $n$  is an integer, and is given by,

$$n = \frac{2R}{\lambda_e} = \frac{R k_e}{\pi} \quad \{6.5\}$$

Therefore, as the incident x-ray energy is scanned above the absorption edge, the EXAFS modulations are periodic when plotted against the photoelectron wave-number.

The EXAFS function  $\chi$  is defined as the normalised oscillatory part of the absorption coefficient,

$$\chi = \frac{\mu - \mu_o}{\mu_o} \quad \{6.6\}$$

where  $\mu$  is the absorption coefficient of the atom in condensed matter, and  $\mu_o$  is the absorption coefficient of the atom in the absence of neighbouring scatterers. A very important development in the theory of EXAFS was that this function can be related to the short-range structural order surrounding the absorbing atom and can be written with respect to the photoelectron wave-number as,<sup>135</sup>

$$\chi(k_e) = \sum_j S_o^2 N_j \frac{|f(k_e)|}{k_e R_j^2} \sin(2k_e R_j + 2\delta_c + \phi) \exp\left[-\frac{2R_j}{\lambda_e(k_e)}\right] \exp\left[-2\sigma^2 k_e^2\right] \quad \{6.7\}$$

where the summation is taken over all near-neighbour distances and,

---

<sup>†</sup> Only back-scattering is considered as this is generally the most dominant process contributing to EXAFS oscillations.



- $R_j$  are the inter-atomic distances at which  $N_j$  atoms can be found (the coordination number).
- $\sigma^2$  is an RMS disorder parameter that reflects the temperature dependence of the EXAFS signal and structural variations within the coordination shell. A coordination shell is a group of atoms that are at similar radial distances from the central absorbing atom but cannot be separately resolved.
- $f(k_e)\exp(i\phi)$  is the back-scattering function. The modulus  $|f(k_e)|$  is the back-scattering amplitude, which depends upon the scattering atom and contributes to the magnitude of the EXAFS signal, and  $\phi$  is the phase-shift induced by the scattering process.
- $\delta_c$  is the central-atom partial wave shift of the final state.
- $\lambda_e(k_e)$  is the energy dependent mean free path of the photoelectron. EXAFS can only measure the local atomic structure over a very short range as determined by this function, and is typically a few tens of angstroms.<sup>91</sup>
- $S_0$  is the amplitude-reduction factor. X-ray absorption is a many-body process and all possible final states have to be taken into account when the core-hole is created. This reduces the EXAFS amplitude by a factor of between  $\sim 0.7 \rightarrow 1$ .<sup>135</sup>

The oscillatory nature of EXAFS is clearly reflected in the  $\sin(2k_e R + 2\delta_c + \phi)$  term, with longer periods of oscillation reflecting shorter bond distances. The  $2\delta_c + \phi$  term is the total EXAFS phase-shift due to the scattering process itself. This results in a small error in the measured inter-atomic distances which can be corrected for using theoretical or experimental reference standards. The short-range order of EXAFS is manifested in the  $\exp[-2R_j/\lambda_e(k_e)]$  and  $(k_e R_j^2)^{-1}$  terms which describe the decay of the photoelectron

wave as it propagates through the material. The strength of the EXAFS oscillations depends on the type and number of scattering neighbours and is expressed through the modulus of the back-scattering amplitude  $|f(k_e)|$  and the coordination number  $N_j$ . The Debye-Waller factor,  $\exp(-2\sigma^2 k_e^2)$  accounts for thermal vibrations and structural disorder, and the overall effect is to damp the EXAFS amplitude. As this damping increases with incident photon energy, the EXAFS signal dies out at around  $\sim 10 \text{ \AA}$  at room temperature.<sup>135</sup>

By careful Fourier analysis of the EXAFS spectrum, it is possible to reveal important structural parameters of the material. By taking the Fourier transform of  $\chi$  with respect to the wave-number of the photoelectron, a radial distribution function is obtained.<sup>138,139</sup> This function will show peaks at distances corresponding to the nearest-neighbour atoms and whose height and width are related to the number of atoms in particular coordination shells and the thermal/structural disorder of the system.

The main difficulty in interpreting EXAFS data is the extraction of the structural parameters from the standard EXAFS formula (Equation {6.7}), and therefore it is highly desirable to have accurate theoretical models to calibrate the measurements.<sup>140</sup> Due to the fact that the core absorption-edges of the elements are well separated in energy, the incident x-ray energy can be tuned with a crystal monochromator to probe each type of central-absorbing atom within the sample. Experimentally, EXAFS only requires modest energy resolution ( $\sim 1 \text{ eV} \rightarrow 2 \text{ eV}$ ). However, good statistics are necessary since the signal-to-background is intrinsically poor.

An example of the EXAFS technique employed in a high-pressure study on rhenium oxide has been given by Houser *et al.*:<sup>141</sup> The oxygen cage that surrounds the rhenium atom undergoes a distortion at  $\sim 0.5 \text{ GPa}$ , whereby the oxygen atoms undergo a shift from their equilibrium positions. By measuring the transmission of x-rays through the sample at the Re  $L_3$  absorption-edge, the bond-angle change between the rhenium and nearest-neighbour oxygen atoms at the phase-transition could be determined.

### 6.3 Extracting absorption coefficients from thick concentrated samples

In high-pressure experiments it is not always possible to perform x-ray measurements in the transmission geometry. For the heavier elements, and absorption through the diamond anvils and/or beryllium gasket in the DAC, absorption is sometimes too high to obtain a measurable signal. One then has to revert to alternative methods of measuring the absorption coefficient.

By directing x-rays onto the sample, electrons and fluorescence photons are created which can provide a measure of the electronic and structural properties of the material. However, measurement of the electron-yield can only provide surface sensitive information due to the short escape-depth of electrons ( $\sim 10\text{\AA}$ ).<sup>91</sup> Alternatively, collecting the fluorescence photons that result from the decay of excited states as a function of incident x-ray energy can provide bulk-sensitive information.

For dilute samples, the absorption of the central-absorbing atom is much less than that of the other atoms forming the material, and the fluorescence intensity is directly proportional to the absorption coefficient.<sup>142</sup> Conversely, for thick concentrated samples, the attenuation experienced by the incident and fluorescence photons as they transverse the sample results in a reduction in the fluorescence intensity compared to the true absorption coefficient. In this situation, XANES resonances and EXAFS oscillations appear damped. However, through knowledge of the well-known atomic absorption coefficients away from resonance and the detector geometry, the true absorption coefficient can be retrieved from fluorescence intensity measurements.<sup>143-147</sup>

Figure 6-4 shows the general set-up of a fluorescence experiment on a thick concentrated sample, where  $\theta_i$  is the angle of incidence and  $\Omega$  is the angle that the detector makes with the sample surface.

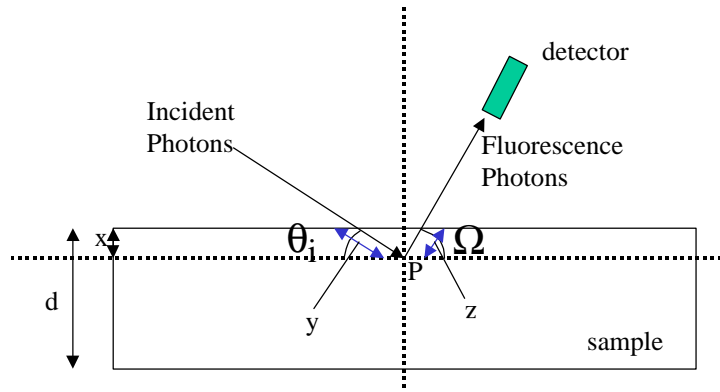


Figure 6-4: Geometry of a fluorescence measurement.

- First, consider when the incidence angle is small ( $\theta \rightarrow 0^\circ$ ) and the detector is normal to the sample surface. Then, if the incident energy is higher than an absorption edge, fluorescence photons are created close to the surface and have only a small distance to travel through the sample before reaching the detector. In this arrangement, the fluorescence intensity is almost independent of the exciting energy and saturated. It is the lack of adequate absorption of the outgoing photons that produces severe distortion of the fluorescence spectra.
- Secondly, consider when the incidence angle is increased ( $\theta_i \rightarrow 90^\circ$ ), and the detector is normal to the sample surface. At an absorption-edge, the absorption coefficient is large and fluorescence photons are created nearer to the sample surface. In this situation, the fluorescence signal is high. Then, as the absorption coefficient decreases with increasing incidence energy, fluorescence photons are produced further into the bulk and the fluorescence signal is reduced. For this geometry, the fluorescence intensity begins to mimic the absorption coefficient of the sample.

A simple description of the steps required to transform the fluorescence intensity into a measure of the absorption coefficient, and the effect that the geometrical arrangement has on the fluorescence signal is now explained.<sup>146,147</sup> Considering Figure 6-4, after the incident photon beam has propagated a distance  $y$  through the sample on reaching a point  $P$ , the transmitted intensity is given by,

$$I_t(E) = I_o(E) e^{-\mu_{\text{tot}}(E) y} \quad \{6.8\}$$

where  $\mu_{\text{tot}}(E)$  is the total linear absorption coefficient,  $E$  is the incoming x-ray energy and  $I_o$  is the incident intensity.

These transmitted photons may have sufficient energy to promote electrons from inner atomic levels to higher bound or continuum states. The decay of these excited states can then be measured by collecting the characteristic fluorescence x-rays. The fluorescence events produced by these photons at the point  $P$  through an infinitesimal distance  $dy$  along the photon beam direction is then,

$$I_f = I_t(E) \mu_{\text{sub}}(E) \epsilon_{\text{sub}} dy \quad \{6.9\}$$

where  $\mu_{\text{sub}}(E)$  is the sub-shell linear absorption coefficient for that atomic level being probed, and  $\epsilon_{\text{sub}}$  is the fluorescence yield of that sub-shell.<sup>148</sup>

The total absorption coefficient in Equation {6.8} is related to the sub-shell coefficient and the absorption coefficient due to the valence electrons, shallower core-electrons and other elements within the sample by,

$$\mu_{\text{tot}}(E) = \mu_{\text{sub}}(E) + \mu_{\text{other}}(E) \quad \{6.10\}$$

Assume that the detector of area  $A$  and efficiency  $\eta(E)$ , subtends a small solid angle with the sample surface such that the distance from the sample to the detector,  $r \gg \sqrt{A}$ .

Then, the angular deviation from  $\Omega$  for all of the detected photons is negligible and subsequent equations are applicable.<sup>†</sup>

The fluorescence photons that are created at the point P are attenuated on their way-out of the sample to the detector and the intensity is given by,

$$I_t \mu_{\text{sub}}(E) \epsilon_{\text{sub}} \times e^{-\mu_{\text{tot}}(E_f)z} dy = \eta(E) \frac{A}{r^2} I_o \mu_{\text{sub}}(E) \epsilon_{\text{sub}} \frac{1}{\sin \theta_i} \exp \left\{ - \left[ \frac{\mu_{\text{tot}}(E)}{\sin \theta_i} + \frac{\mu_{\text{tot}}(E_f)}{\sin \Omega} \right] x \right\} dx \quad \{6.11\}$$

Integrating over the entire sample thickness, the total detected fluorescent intensity exiting a sample of thickness d is given by,

$$I_f(E) = \eta(E) \frac{A}{r^2} I_o(E) \mu_{\text{sub}}(E) \epsilon_{\text{sub}} \times \frac{1}{\mu_{\text{tot}}(E) + \mu_{\text{tot}}(E_f) \frac{\sin \theta_i}{\sin \Omega}} \times \left[ 1 - \exp \left\{ - \left[ \frac{\mu_{\text{tot}}(E)}{\sin \theta_i} + \frac{\mu_{\text{tot}}(E_f)}{\sin \Omega} \right] d \right\} \right] \quad \{6.12\}$$

→

$$\frac{I_f(E)}{I_o(E)} \propto \frac{\mu_{\text{sub}}(E)}{\mu_{\text{tot}}(E) + \mu_{\text{tot}}(E_f) \frac{\sin \theta_i}{\sin \Omega}} \times \left[ 1 - \exp \left\{ - \left[ \frac{\mu_{\text{tot}}(E)}{\sin \theta_i} + \frac{\mu_{\text{tot}}(E_f)}{\sin \Omega} \right] d \right\} \right]$$

For a sample with a thickness much greater than the photon attenuation length, which is applicable for many situations in high-pressure x-ray spectroscopy, the exponential term in Equation {6.12} can be neglected giving,

---

<sup>†</sup> In this thesis, small area energy dispersive detectors were used and this assumption is valid. For larger area detectors, it is possible to modify the formula by integrating over all possible angles.<sup>147</sup>

$$\begin{aligned}
\frac{I_f(E)}{I_o(E)} &\propto \frac{\mu_{\text{sub}}(E)}{\mu_{\text{tot}}(E) + \mu_{\text{tot}}(E_f) \frac{\sin \theta_i}{\sin \Omega}} + \frac{I_{\text{bac}}(E)}{I_o(E)} \\
&\propto \frac{\mu_{\text{sub}}(E)}{\mu_{\text{sub}}(E) + \mu_{\text{other}}(E) + \mu_{\text{tot}}(E_f) \frac{\sin \theta_i}{\sin \Omega}} + \frac{I_{\text{bac}}(E)}{I_o(E)}
\end{aligned}
\tag{6.13}$$

where  $\frac{I_{\text{bac}}(E)}{I_o(E)}$  represents the normalised background due to scattered radiation entering the detector.<sup>147</sup>

To obtain the sub-shell absorption coefficient  $\mu_{\text{sub}}(E)$  of a thick concentrated sample, the detector geometry must be well defined so that an accurate value of  $\frac{\sin \theta_i}{\sin \Omega}$  can be obtained. The absorption coefficients,  $\mu_{\text{tot}}(E_f)$  and  $\mu_{\text{other}}(E)$ , can be calculated from the data in the Henke tables<sup>1</sup> or the XOP x-ray computer data package,<sup>84</sup> and together with knowledge of the experimental geometry, Equation {6.13} can be solved. Considering a single elemental material,  $\mu_{\text{other}}(E)$  can be extracted by extrapolating the pre-edge region of  $\mu_{\text{tot}}(E)$  (which is equal to  $\mu_{\text{other}}(E)$  here as  $\mu_{\text{sub}}(E) = 0$ ) through the post-edge region.<sup>†</sup> An example of how to perform this for nickel is depicted in Figure 6-3, where a Victoreen function<sup>149</sup> was fit to the pre-edge region.

Fluorescence detection is a standard tool for measuring absorption coefficients of dilute samples at synchrotron radiation facilities.<sup>142</sup> The reason why such measurements provide fluorescence intensities that are directly proportional to the sub-shell absorption coefficients is that  $\mu_{\text{sub}}(E)$  makes a small contribution to the denominator in Equation {6.13}, which is then approximately constant. However, this assumption is not valid for thick concentrated samples, and the fluorescence intensity is damped due to the contribution of  $\mu_{\text{sub}}$  to the total absorption coefficient. The damping of the fluorescence intensity due to this effect and the geometrical term  $\frac{\sin \theta_i}{\sin \Omega}$ , is called self-absorption. By reverting to a near-normal incidence grazing take-off geometry,  $\frac{\sin \theta_i}{\sin \Omega}$  is large and the denominator in Equation {6.13} is approximately constant. For this

---

<sup>†</sup> For a sample consisting of more than one element, the relative concentrations have to be considered to calculate the total absorption coefficients.<sup>146</sup>

situation, the fluorescence intensity is also directly proportional to the absorption coefficient.<sup>144</sup>

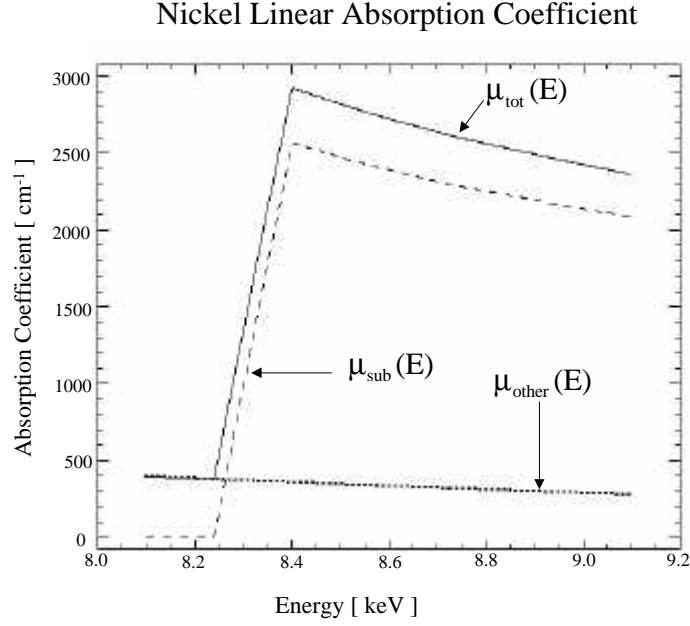


Figure 6-5: Calculated contributions to the total linear absorption coefficient of nickel.

For completeness, it is useful to estimate the amount of the sample that contributes to the fluorescence measurement. This can be obtained through the probability of detecting a fluorescence event, which is represented by the exponential term in Equation {6.11},

$$P(x) = \exp \left[ - \left( \frac{\mu_{\text{tot}}(E)}{\sin \theta_i} + \frac{\mu_{\text{tot}}(E_f)}{\sin \Omega} \right) x \right] \quad \{6.14\}$$

Then, an information depth,  $\lambda_f$  can be defined as,

$$\lambda_f = \frac{\int_0^\infty x P(x) dx}{\int_0^\infty P(x) dx} = \frac{\sin \theta_i}{\mu_{\text{tot}}(E) + \mu_{\text{tot}}(E_f) \frac{\sin \theta_i}{\sin \Omega}} \quad \{6.15\}$$

For example, consider a photon energy of 9 keV incident upon pure nickel with absorption coefficients,  $\mu_{\text{tot}}(9 \text{ keV}) \sim 2430 \text{ cm}^{-1}$  and  $\mu_{\text{tot}}(E_f) = \mu_{\text{tot}}(7.47 \text{ keV}) \sim 500 \text{ cm}^{-1}$ . In the back-scattering geometry ( $\theta = \Omega = 90^\circ$ ), the information depth is maximised and is



given by  $\lambda_f = 3.4 \mu\text{m}$ . It can be easily seen from Equation {6.15} that this information-depth approaches zero for grazing incidence and/or small take-off angles.

In Section 6.3.1, an experiment was performed to demonstrate the validity of the fluorescence technique for determining absorption coefficients from thick concentrated samples. It was decided to perform this measurement in the back-scattering geometry ( $\theta = \Omega = 90^\circ$ ) so that the geometrical term  $\frac{\sin \theta_i}{\sin \Omega}$  was well known ( $\sim 1$ ) and the information-depth was maximised. It should also be noted that in this arrangement, small errors in the estimation of the geometry can be tolerated due to the small change in the sine function near  $90^\circ$ . In Chapter 8, this technique was also used to measure the intensity of the white-line feature in the XANES part of the spectra of praseodymium metal.

### **6.3.1 Self-absorption correction of thick nickel sample fluorescence data**

This section will describe how self-absorption corrections can be used to extract the absorption coefficient from an intensity measurement recorded on a thick nickel sample in the back-scattering geometry. This data will then be compared to that taken on a thin nickel foil in transmission mode at the NSLS X23A beamline (Figure 6-2).

For this experiment, the X13B KB micro-probe was employed to focus the incident x-rays onto an infinitely thick ( $\sim 200 \mu\text{m}$ ) sample of nickel. This is an important experiment as it will demonstrate the validity of self-absorption corrections and its application to high-pressure studies, where transmission measurements may not be feasible. The EPW (Section 3.3.2) was the source of x-rays, and the NSLS electron energy and maximum current were 2.8 GeV and 200 mA respectively. The experimental arrangement is shown in Figure 6-6. The X13B double-crystal monochromator was initially calibrated to the nickel K-absorption edge (8.333 keV) by measuring the absorption through a thin nickel foil, and the upper crystal was detuned to  $\sim 50\%$  of the peak Bragg-reflected intensity to suppress higher-order harmonics emerging from the lower crystal (Section 3.3.4).

With the sample in place, the incident x-ray energy was scanned across the nickel K-absorption edge: The pre-edge region was scanned between 8.1 keV  $\rightarrow$  8.279 keV in steps of  $\sim 5$  eV . A large part of the XANES and EXAFS region was scanned in fine-steps of 0.5 eV in the range 8.280 keV  $\rightarrow$  8.529 keV , and further data were recorded out to 9.1 keV with a 5 eV step-size. An amptek XR-100CR energy-dispersive silicon-pin-photodiode of area 7 mm<sup>2</sup> was used to collect the fluorescence photons, and a Nucleus PCA-II<sup>®</sup> multi-channel analyser was the used to select the Ni K $\alpha$  fluorescence line. The detector was placed  $\sim 2$  cm from the sample surface, and an ionisation chamber (Figure 6-6) was used to normalise the data. This normalisation accounts for the decay of the electron beam in the NSLS storage ring and the energy dependence of air absorption (see later). The counting time per point was 5 seconds and a total number of 20 scans were recorded.

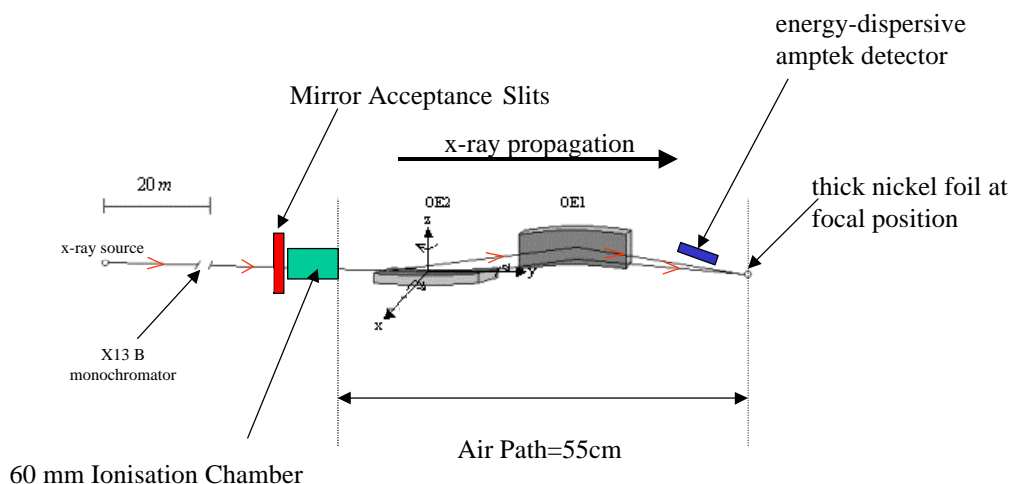


Figure 6-6: Experimental configuration for collecting fluorescence photons in the back-scattering geometry at the NSLS X13B beamline using the KB x-ray micro-focusing optics.

Figure 6-7 shows the raw nickel K-fluorescence data. Notice how the data is severely distorted from that obtained in transmission (Figure 6-2). Also, the data appears noisier after  $\sim 8.5$  keV , which is due to the larger energy step-size after this point and the dying out of the EXAFS oscillations as the energy is increased (Section 6.2).

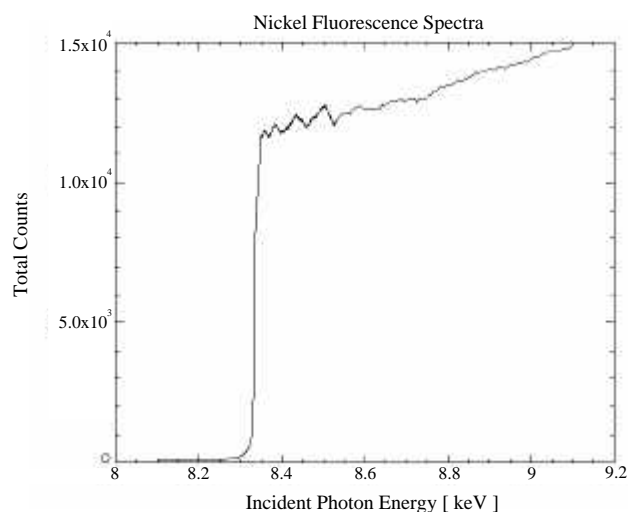


Figure 6-7: Total collected fluorescence counts obtained on a thick concentrated nickel foil.

The rise in fluorescence intensity with increasing photon energy appears not to be consistent with a decreasing absorption coefficient. This is because normalisation has not been applied to this data: In this experiment, no helium flow was used in the mirror chambers and with increasing x-ray energy, more photons can reach the sample due to decreased air-absorption.<sup>†</sup> However, by measuring the current through the 60 mm ionisation chamber, the number of photons incident upon the sample surface can be calculated. This can be achieved by applying Equation {5.1} together with an energy-dependent function to compensate for absorption through the 55 cm air-path that is located between the ionisation chamber and the sample surface. Air-absorption provides a significant contribution to the decrease of fluorescence intensity in this experimental layout. The effect of air absorption versus energy is shown in Figure 6-8.

---

<sup>†</sup> As there are always some air paths in any experiment (unless the apparatus is completely sealed under a helium environment), it is a useful exercise to demonstrate that successful corrections can be achieved for a large air-path.

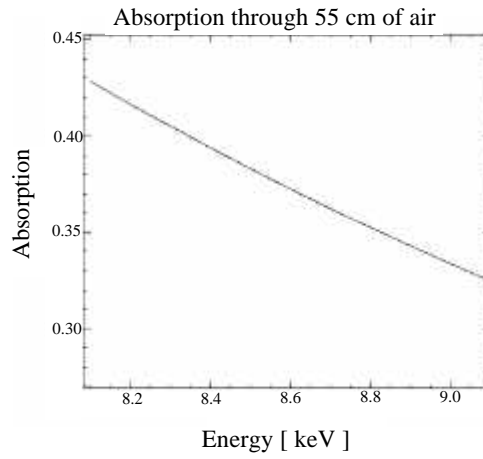


Figure 6-8: Energy dependence on absorption through 55 cm of air.

Once normalisation has been performed, corrections can then be applied to the data to retrieve the absorption coefficient. The important assumption is that the background function,  $\frac{I_{\text{bac}}(E)}{I_o(E)}$  is a slowly varying function of incident x-ray energy. This certainly is the case in the pre-edge region of Figure 6-7, where the background is approximately constant, and is mainly due to Compton and elastic scattering into the energy window defined on the multi-channel analyser. This background can be subtracted from the whole spectra by forcing  $\mu_{\text{sub}}(E) = 0$  in the pre-edge region, and Equation {6.13} becomes

$$\frac{I_f(E)}{I_o(E)} \propto \frac{\mu_{\text{sub}}(E)}{\mu_{\text{sub}}(E) + \mu_{\text{other}}(E) + \mu_{\text{tot}}(E_f)} \quad \{6.16\}$$

Using the Henke tables<sup>1</sup> or XOP x-ray data package,<sup>84</sup>  $\mu_{\text{tot}}(E_f)$  and  $\mu_{\text{other}}(E)$  can be obtained (see Figure 6-5 for method of obtaining  $\mu_{\text{other}}(E)$ ), and Equation {6.16} can be rearranged to provide fluorescence data which is directly proportional to the value of  $\mu_{\text{sub}}(E)$ . This was applied to the fluorescence measurements taken on the thick nickel sample, and a direct comparison with the thin nickel foil transmission data is shown in Figure 6-9.<sup>†</sup> Both data have been scaled so that they can be displayed on the same graph. The excellent transformation of the damped fluorescence data (Figure 6-7) to a

<sup>†</sup> The transmission data used is that shown in Figure 6-2, with the pre-edge removed so that only the contribution to the absorption from the 1s core electrons are considered. This was achieved by fitting a Victoreen function<sup>149</sup> to the pre-edge region, extrapolating to higher-energies, and subtracting from the data.

measure of the absorption coefficient by applying self-absorption corrections is clearly evident, and there is good agreement between the two sets of data. There seems to be a slightly larger fall of the monotonically decaying background in the post-edge region of the transmission data than compared with the fluorescence measurement, and this may be due to various energy-dependent factors which were not considered during the transmission measurement. The important point to emphasise is that self-absorption corrected fluorescence data taken on samples subjected to high-pressures in the diamond-anvil cell can provide an accurate measurement of real absorption coefficients. Finally, the quality of the data is limited to counting statistics, and the sensitivity can be improved by increasing the counting time per point.

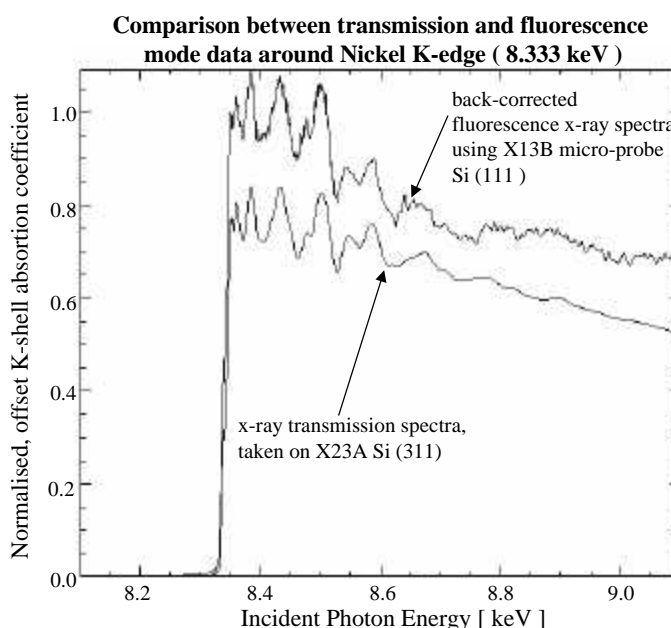


Figure 6-9: Comparison between absorption coefficient obtained by measuring the x-ray transmission through a thin nickel foil, and the corrected fluorescence intensity taken from a thick concentrated nickel sample.

## 6.4 Summary

This chapter has outlined the x-ray spectroscopic methods that can be applied in extracting important information from measurements performed in transmission and fluorescence geometries. Analysis of EXAFS spectra is a powerful tool for extracting

the local structure surrounding the central absorbing atom, and is important in high-pressure studies where abrupt structural phase-transitions can occur. XANES measurements can provide a direct measure of the electronic structure of the material under investigation, pressure-induced changes in the valence-state, and structural changes can also be inferred from such measurements. Chapter 7 describes an x-ray transmission experiment on thallium-rhenium oxide which exhibits a large phase-transition at  $\sim 10$  GPa. In this measurement, the pressure-effects on the XANES region of the absorption spectra were studied. Also, a fluorescence EXAFS experiment was performed on this compound to investigate the structural nature of this transition.

It is preferable to conduct XANES and EXAFS measurements in a transmission geometry, due to the direct relationship between the transmission data and absorption coefficient. However, sometimes this arrangement is not feasible. A model has been developed in Section 6.3 that enables absorptions coefficients to be extracted using the fluorescence data from thick concentrated samples. Section 6.3.1 confirmed the validity of this model. This new method of retrieving absorption coefficients from thick samples under high-pressure was applied in Chapter 8 to study the effect of pressure on the white-line feature in praseodymium metal.

## Chapter 7 Electronic and structural changes in thallium-rhenium oxide under high-pressure

There are many interesting compounds which have the ternary oxide formula  $ABO_4$  ( $A=B$ = metals, and O represents oxygen), and most undergo high-pressure phase transitions.<sup>150</sup> Some of these compounds are of great interest because of their importance as scintillator crystals ( $CdWO_4$ <sup>151</sup> and  $PbWO_4$ <sup>152-156</sup>). Previous theoretical considerations have used the ionic size and valency of the A and B cations from which to postulate the  $ABO_4$  crystal-structures.<sup>150</sup> These generally consist of linked-polyhedra in orthorhombic (lattice parameters:  $a \neq b \neq c$ ,  $\alpha = \beta = \gamma = 90^\circ$ ) or tetragonal (lattice parameters:  $a = b \neq c$ ,  $\alpha = \beta = \gamma = 90^\circ$ ) arrangements.<sup>157</sup> Thus, by varying the atomic species and application of pressure, these related families of materials provide an opportunity to study the stability of these structures and pressure-induced phase transitions in general.

A number of  $ABO_4$  compounds crystallise in the scheelite (body-centred tetragonal, space group  $I4_1/a$ ) or pseudoscheelite (orthorhombic, space group  $P_{nma}$ ) structures under ambient conditions. For example,  $CdMoO_4$  has the scheelite structure.<sup>151</sup> The molybdenum atom in this material is surrounded by four oxygen atoms with bond lengths of 1.75 Å. The cadmium atom is eight-fold oxygen coordinated with larger bond lengths of 2.40 Å and 2.44 Å. Other examples of  $ABO_4$  scheelite compounds forming under ambient conditions are  $RbIO_4$ ,<sup>158</sup>  $KReO_4$ ,<sup>159</sup>  $PbWO_4$ ,<sup>152-156</sup>  $AgReO_4$ ,<sup>160</sup>  $BaWO_4$ <sup>161,162</sup> and  $RbReO_4$ .<sup>159</sup> Examples of those that crystallise in the pseudoscheelite structure are  $CsIO_4$ ,<sup>163</sup>  $TlReO_4$ <sup>164-166</sup> and  $CsReO_4$ .<sup>159</sup>

An example of the pseudoscheelite structure of  $TlReO_4$ ,<sup>152,167</sup> as formed under ambient conditions, is shown in Figure 7-1. When the body-centred orthorhombic primitive cell is transferred onto the body-centred tetragonal lattice sites, the pseudoscheelite structure is formed from isolated  $(ReO_4)^-$  anion tetrahedra running along the c-axis as depicted in Figure 7-2.

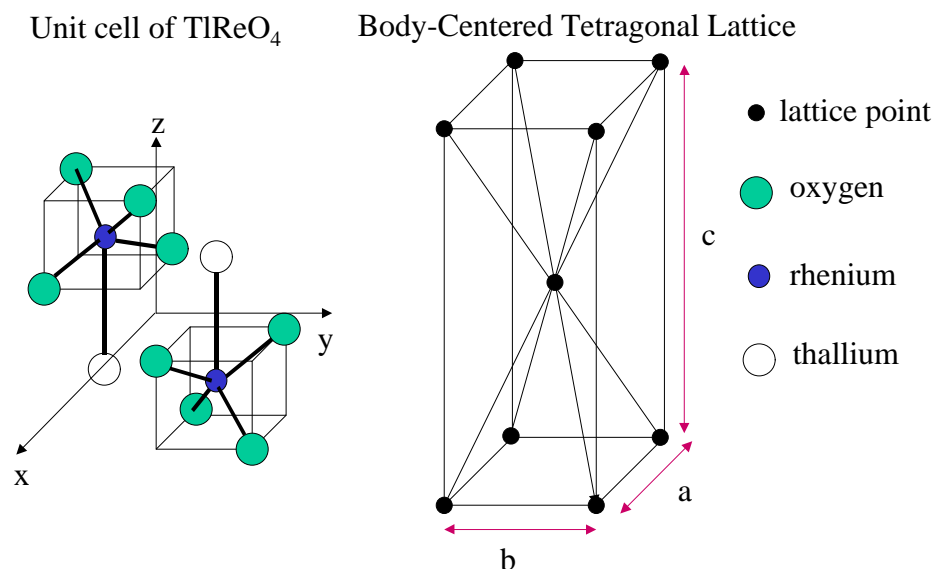


Figure 7-1: Example of pseudoscheelite structure of  $\text{TlReO}_4$  as formed under ambient conditions. There are two formula units in the primitive cell, and the lattice is body-centred tetragonal.

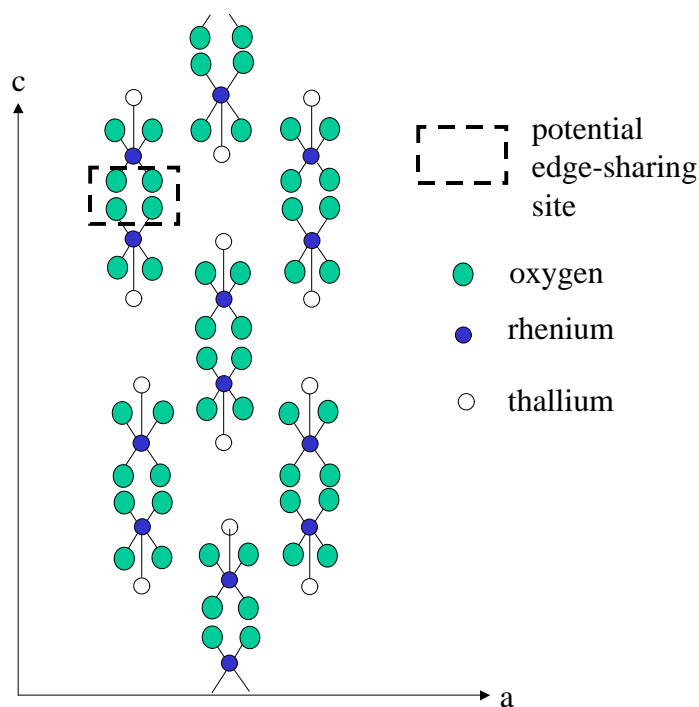


Figure 7-2: Pseudoscheelite structure as projected along the  $b$ -axis, as derived from Figure 7-1. A potential site where the oxygen atoms can edge-share is also shown. When edge-sharing occurs, the structure is wolframite and the structure is shown in Figure 7-3.

Wolframite structures (space group  $P 2_1/c$ ) are less likely to be found under ambient conditions. However, some scheelite-type crystals are assumed to transform to this structure when pressure is exerted on them.<sup>150,158,164,166,168</sup> An example of an



ambient wolframite structure is  $\text{CdWO}_4$ .<sup>151</sup> The tungsten atom in this material is surrounded by a cage of oxygen atoms in approximately octahedral symmetry (as in Figure 7-3), by edge-sharing. Although the tungsten atom is said to be six-fold coordinated, there are a range of O-W bond lengths in this cage at 1.78 Å, 1.91 Å and 2.15 Å. Other examples of ambient wolframite structures are  $\text{NiWO}_4$ ,  $\text{FeWO}_4$  and  $\text{FeTaO}_4$ .<sup>150</sup> The crystal volume change between the wolframite and scheelite structures is very small and of the order of  $< 2\%$ .<sup>151,161,164,165</sup>

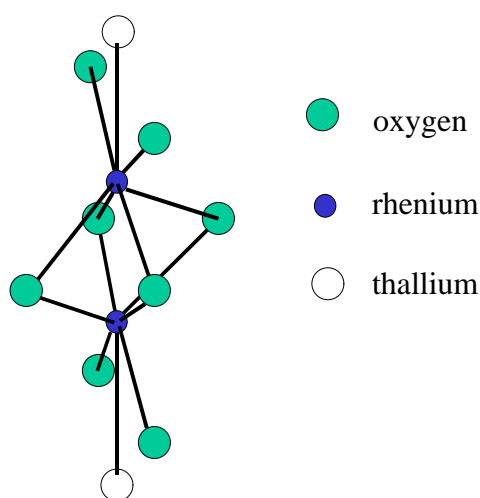


Figure 7-3: Octahedral symmetry surrounding the rhenium atom in the assumed high-pressure wolframite phase of  $\text{TlReO}_4$ .

Structural stability and pressure induced phase transitions of  $\text{ABO}_4$  compounds which crystallise in the tetragonal-scheelite or orthorhombic-pseudoscheelite structure at ambient pressure have been studied using high pressure Raman spectroscopy for more than two decades. Among these compounds, the  $\text{AReO}_4$  perrhenates have been studied in detail by high-pressure Raman spectroscopy.<sup>159,164-166</sup> It has been suggested that they transform from the scheelite-type to wolframite-type structures with compression, and finally to an unknown denser triclinic matrix.

In particular, thallium-rhenium oxide has been studied using high-pressure Raman spectroscopic and x-ray diffraction techniques.<sup>164,166</sup> From these Raman data, it

was discovered that there were three distinct pressure-induced structural phase transitions:<sup>†</sup>  $\text{TlReO}_4$  crystallises in the orthorhombic pseudoscheelite structure at ambient conditions (Phase I). As pressure is applied to this compound, three phase transitions were encountered at  $\sim 1$  GPa (Phase II),  $\sim 2$  GPa (Phase III) and  $\sim 10$  GPa (Phase IV), as shown in Figure 7-4 and Figure 7-5. All transitions are first-order, and found to be reversible with some hysteresis and are summarised in Table 7-1. In the Raman spectra, there are only subtle changes between phases I and II. From this, it was suggested that phase II had a slightly lower symmetry than phase I, with perhaps a rotation or tilting of the  $\text{ReO}_4$  tetrahedra. The interpretation of x-ray diffraction data suggested that the Phase II transition is rather sluggish, and takes place within a pressure range of 2 GPa  $\rightarrow$  5 GPa into the assumed wolframite structure. In this structure, the rhenium atom becomes 6-fold coordinated, as depicted in Figure 7-3. The higher-pressure phase, that occurs at around 10 GPa was interpreted to be that of the high-temperature phase (type-2) of  $\text{BaWO}_4$ <sup>161,162</sup> due to similarities between the derived lattice parameters.

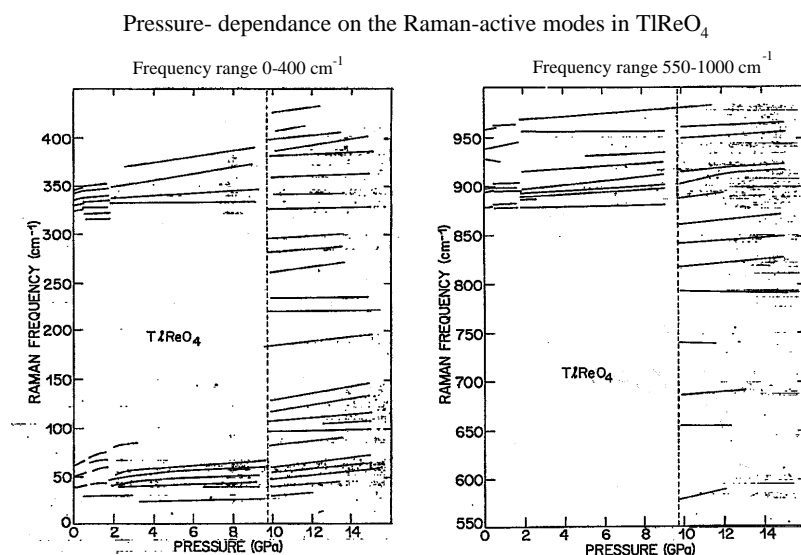


Figure 7-4: The change in the Raman-active modes of thallium-rhenium oxide with applied pressure.<sup>166</sup>

<sup>†</sup>  $\text{TlReO}_4$  is also found to undergo transformations to the tetragonal-scheelite structure at high (400 K) and low (70 K) temperatures.<sup>165</sup>

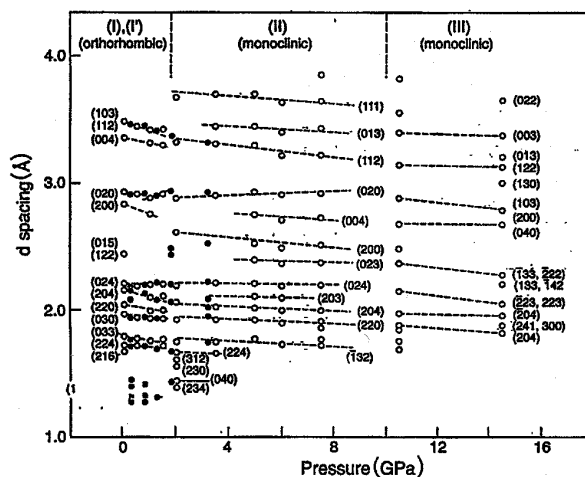


Figure 7-5: The change in the inter-planar lattice spacing in thallium-rhenium oxide with applied pressure, using x-ray diffraction techniques.<sup>164</sup>

	Phase I	Phase II	Phase III	Phase IV
Crystal structure	Pseudoscheelite	~ Phase I	Wolframite?	BaWO <sub>4</sub> (type-2)?
Applied pressure	Ambient	0.5 GPa → 1.0 GPa	~ 2 GPa	9.7 GPa → 10.5 GPa
Calculated volume change at phase transition	-	negligible	~ 2 %	~ 10 %

Table 7-1: Pressure-induced structural changes in the thallium-rhenium oxide compound as taken from Raman and x-ray diffraction data.<sup>164,166</sup>

Moreover, TlReO<sub>4</sub> transforms optically from a light-grey to black colour at the third phase transition (Phase IV),<sup>166</sup> with a volume-collapse of ~10 %.<sup>164</sup> It is this striking optical change of the compound that is of interest because it provides evidence of a large modification of the electronic structure. It was proposed that this dramatic colour change was due to a change in the valence state of the two cations:  $\text{Re}^{+7} \rightarrow \text{Re}^{+5}$ , accompanied by  $\text{Tl}^{+1} \rightarrow \text{Tl}^{+3}$ , to maintain charge neutrality.<sup>166†</sup> If this charge transfer does occur, an accompanying structural phase transition may take place due to the change in the size of the ionic radii.<sup>150</sup> Due to the change in optical absorption, this

<sup>†</sup> The atomic configuration of the rhenium atom is  $[\text{Xe}]4f^{14}5d^56s^2$  and that of the thallium atom is  $[\text{Xe}]4f^{14}5d^{10}6s^2p^1$ .

implies a change in the band-gap and hence an x-ray  $L_3$ -edge absorption study could provide some indication as to the nature of this transition.

X-ray absorption experiments conducted on various rhenium compounds have previously been performed at the NSLS to quantify the shift in the rhenium  $L_3$  absorption-edge (at  $\sim 10.535$  keV ) with respect to the valence state of the rhenium atom. This work is currently unpublished, and was performed by Dr. Mark Croft from Rutgers University, New Jersey, USA. The rhenium  $L_3$  near-edge structure is shown in Figure 7-6, which has been normalised to unit edge-jump in the post-edge region, and the absorption-edge shifts are plotted in Figure 7-7.<sup>†</sup>

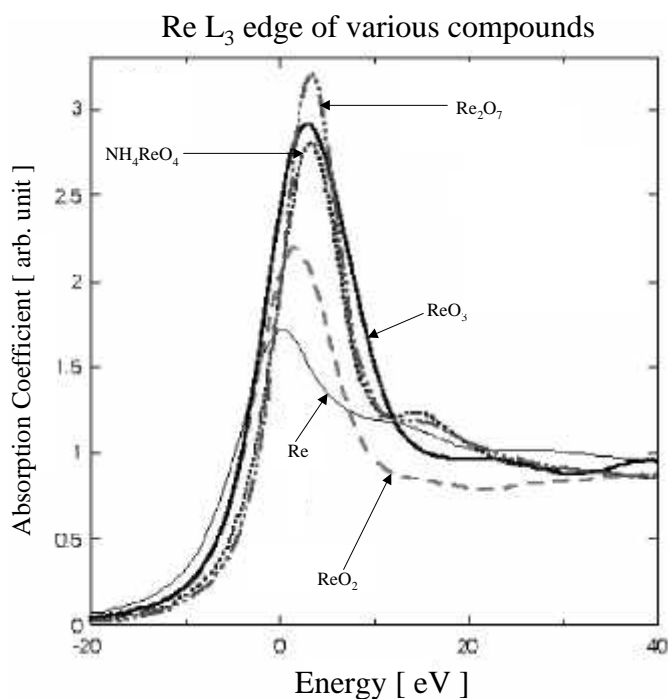


Figure 7-6:  $Re L_3$  absorption XANES spectral dependence on the valence state of rhenium. The peak in the absorption coefficient is called the “white-line” and corresponds to the transition of an excited core electron to an empty bound electronic state.

<sup>†</sup> The location of the absorption-edge was defined at the peak-position of the white-line derivative, as is standard practice.

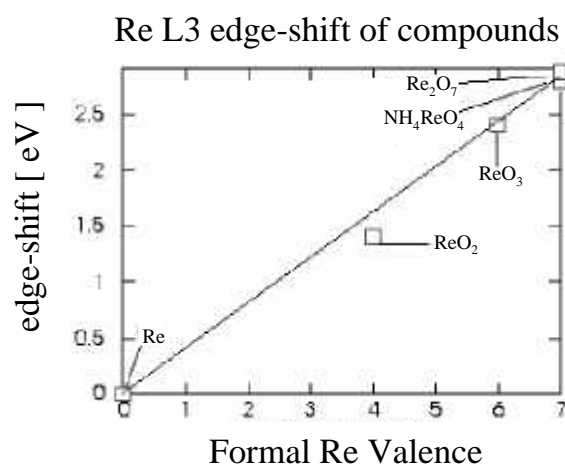


Figure 7-7: Quantification of the rhenium  $L_3$  edge-shift for the various rhenium valence states (as derived from Figure 7-6 data).

As the valence of the rhenium increases, the absorption-edge shifts towards higher energies. Thus, it may be possible to clarify the proposition that the transition  $\text{Re}^{+7} \rightarrow \text{Re}^{+5}$  occurs by measuring the rhenium  $L_3$  edge position as a function of pressure. From Figure 7-7, a valence decrease of two would signify a  $\sim 0.8 \text{ eV}$  shift towards lower incident x-ray energies. Also, it should be noted that the strength of the white-line feature reduces in intensity as the valence is decreased. This is because excitation of the  $L_3$  absorption edge probes the empty  $5d$  states which lie in the valence band, and due to the increased electron filling of the valence-band with decreasing valency, the probability of the x-ray transition is accordingly reduced.

Two high-pressure experiments were performed at room temperature on the perrenate compound  $\text{TlReO}_4$ , to examine the striking optical and structural phase transitions which occurs at a pressure of  $\sim 10 \text{ GPa}$ . Firstly, a XANES measurement was performed to assess the electronic changes that were expected to occur at the phase IV transition. This experiment used the high-flux IVUN insertion-device within the NSLS X13 straight section, and transmission experiments were feasible around the second harmonic, which encompasses the rhenium  $L_3$  edge. This data showed large changes in the XANES region, and it was subsequently decided that it would be beneficial to probe the local structure surrounding the rhenium atom using an EXAFS experiment. This was performed in fluorescence mode on a freshly prepared  $\text{TlReO}_4$  sample. For the EXAFS

measurement, it was necessary to collect data up to higher-energies than the IVUN second-harmonic would allow, thus the EPW source was utilised.<sup>†</sup> Good statistics are required to resolve the EXAFS data, which is essential in the EXAFS range where modulations are only a few per cent of the atomic-like background. Also, the geometry was arranged such that the x-rays were directed onto the sample through the beryllium gasket of the DAC, and the fluorescence photons were captured on their way out through it. Due to absorption considerations, this experiment would have been unfeasible if the x-rays were allowed to propagate through the diamond-anvils instead of the gasket material.

## 7.1 X-ray transmission experiment and results

For this experiment, the DAC was arranged so that the focused x-ray beam propagated through both the diamond-anvils and the sample, and the data were taken at room temperature and in air. Orientating the DAC in this way enabled the x-rays to travel through the thinnest part of the sample. The transmitted photons were detected by a silicon-pn-photodiode placed downstream of the sample position, as depicted in Figure 7-8. Normalisation was performed by dividing the diode current by the number of photons incident on the sample. Incident photon flux upon the sample was calculated by monitoring the current through an ionisation chamber of active length 60 mm placed before the micro-probe optics, and correcting for air absorption between the ionisation chamber and the sample. This technique compensated for the decay of the electron beam in the NSLS storage ring and the energy dependence of absorption through the air-path to the sample (see Section 6.3.1 for method). The electron energy and maximum current were 2.8 GeV and 200 mA respectively, and the X13 undulator insertion device was used for this experiment around the peak of the second harmonic (Figure 3-11), and at a magnetic gap of 3.7 mm.

---

<sup>†</sup> Transmission measurements were not feasible using the EPW source due to the relatively low flux at the rhodium L<sub>3</sub> edge.

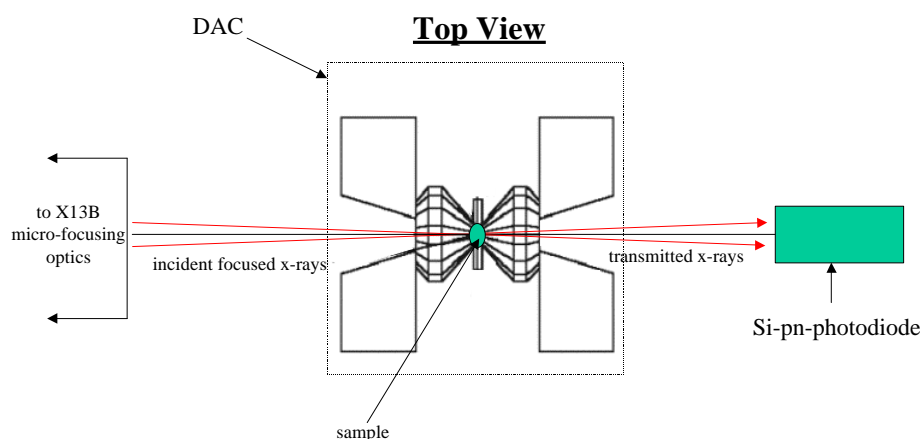


Figure 7-8: Top view (looking down onto the X13B micro-probe table) of the geometry for x-ray absorption spectroscopy using the diamond-anvil cell.

Although each diamond is 2.5 mm thick, the x-ray energy and flux is sufficiently high at the rhenium  $L_3$  absorption edge ( $\sim 10.535$  keV) that x-ray absorption spectroscopy can be performed (the transmission factor is  $\sim 10\%$  at this energy). The  $\text{TlReO}_4$  sample was in finely-ground powdered form and a few grains were loaded, together with ruby chips (to allow pressure calibration) into the DAC sample chamber.<sup>†</sup> The diamond-anvils were closed to create the seal with the gasket material, and the starting pressure was measured to be 0.6 GPa using the well-known shifts of the ruby fluorescence lines (Section 6.1). The DAC assembly was then transferred to the X13B micro-probe end-station and placed onto the micro-metre sample positioning stage. The sample was then positioned into the focused x-ray beam by monitoring the transmitted flux incident upon the Si-pn-photodiode. The photon flux on the sample was calculated to be  $6 \times 10^7$  photons/sec using the Si-pn-photodiode reading with no sample in place (see Section 5.6 for method).

X-ray absorption scans were then performed by varying the incident photon energy in steps of 0.2 eV across the rhenium  $L_3$  absorption edge.<sup>‡</sup> The pre-edge and post-edge regions were scanned in steps of 2 eV, which extended  $\sim 50$  eV below and

<sup>†</sup> An alcohol-methanol mixture was also transferred into the DAC to provide a hydrostatic environment for the sample.

<sup>‡</sup> No attempt to measure the thallium  $L_3$  absorption edge spectra was made due to insufficient x-ray flux at this energy and the added complication that the rhenium  $L_1$  absorption edge is very close.

100 eV above the absorption edge respectively. The calculated resolution of the double-crystal Si (111) monochromator was  $\sim 2$  eV in this energy range, and was detuned to approximately half of the maximum Bragg-intensity to prevent higher-order harmonics emerging from the lower crystal (Section 3.3.4). Precise energy calibration of the incident energy was ensured throughout the experiment by performing periodic absorption scans through a reference sample, and monitoring the absorption of the elastically scattered radiation through a  $\text{TiReO}_4$  foil placed in front of a sodium-iodide detector. Subsequent analysis later confirmed that energy stability at the X13B monochromator was excellent. Further absorption spectra were recorded at pressures of 2.18 GPa, 3.6 GPa and above the Phase IV transition at 10.8 GPa.<sup>†</sup> Optical inspection confirmed that the Phase IV transition had occurred at 10.8 GPa through the colour change of the  $\text{TiReO}_4$  sample.

Using the relationship,  $I = I_0 e^{-\mu x}$  (Equation {4.3}) , the product of the linear absorption coefficient and the sample thickness was obtained. The rhenium  $L_3$  absorption edge results are shown in Figure 7-9, which have been normalised to unit-edge jump to correct for differences in sample thickness between each pressure run, and the magnitude is proportional to the absorption coefficient. The diode current was  $\sim (4 \pm 0.01)$  nA below the absorption edge and  $\sim (2 \pm 0.01)$  nA after the white-line feature.

The near-edge spectra recorded at 0.6 GPa, 2.18 GPa and 3.6 GPa show little evidence of large electronic variations, but beyond the phase-transition where the sample turns black, there is a very large change in the white-line shape. This provides direct evidence of a large reconfiguration of the band structure (Section 7.3), and a probable significant structural phase-transition. Due to the large broadening of the white-line shape, determination of the absorption edge is hindered. Subsequently, quantification of the Re  $L_3$  edge position was not performed.

---

<sup>†</sup> Pressure increase was performed by removing the DAC assembly from the X13B micro-focusing end-station, tightening the gasket screws, and then measuring the pressure using the ruby fluoresce technique in the X17C Raman spectroscopy laboratory.



### Variation of Re $L_3$ edge with increasing applied pressure in $\text{TlReO}_4$

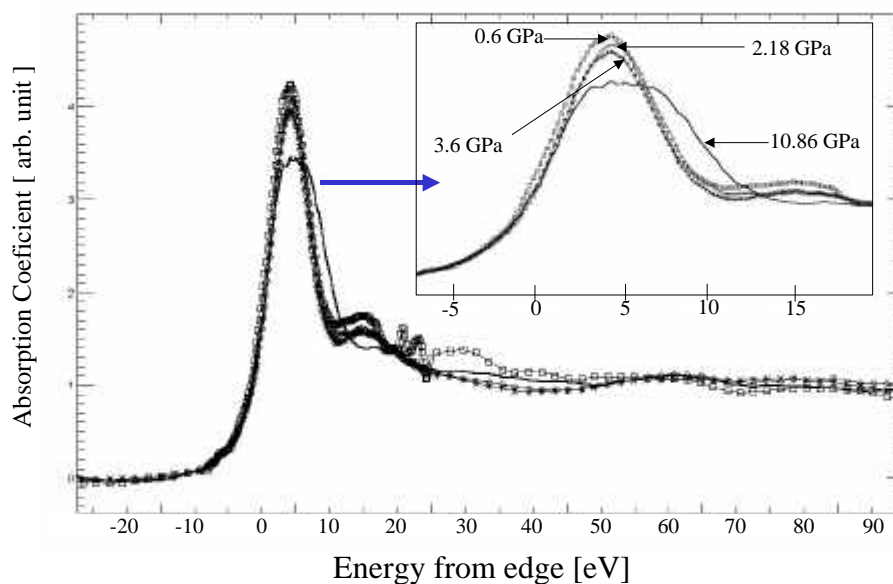


Figure 7-9: Near-edge structure at the rhenium  $L_3$  absorption-edge in thallium-rhenium oxide. The peak in the absorption coefficient is called the “white-line” and corresponds to the transition of an excited core electron to an empty bound electronic state.

## 7.2 X-ray fluorescence EXAFS experiment and results

To examine pressure-induced changes in the local structure surrounding the rhenium atom an x-ray fluorescence EXAFS experiment was conducted around the  $\text{Re } L_3$  absorption-edge on  $\text{TlReO}_4$ .

Figure 7-10 shows a schematic of the experimental arrangement for the fluorescence EXAFS measurement, and the DAC was arranged so that both the incident and fluorescence x-rays transversed the beryllium gasket material. The fluorescence photons were collected by a germanium ORTEC energy-dispersive liquid nitrogen cooled solid-state detector in the  $\sim 90^\circ$  take-off geometry.<sup>†</sup>

The electron beam energy and maximum electron current in the NSLS storage ring were 2.8 GeV and 200 mA respectively, and the EPW (Section 3.3.2) within the X13

<sup>†</sup> This geometry is beneficial in reducing the background as Compton scattering into the detector is minimised at ninety-degrees to the direction (and in the plane) of x-ray propagation.<sup>91,169,170</sup>

straight-section was the source of x-rays for this experiment. A fine powder of  $\text{TiReO}_4$  was loaded into the DAC sample chamber together with some ruby chips, and the diamond-anvils were closed to create the gasket seal. The starting pressure was measured to be 3.5 GPa using the well-known shifts of the ruby fluorescence lines (Section 6.1).

The DAC assembly was then transferred to the X13B micro-probe end-station and placed onto the micro-metre sample-positioning stage. The sample was then positioned into the focused x-ray beam by monitoring the incident flux on the Si-pn-photodiode placed downstream of the sample.

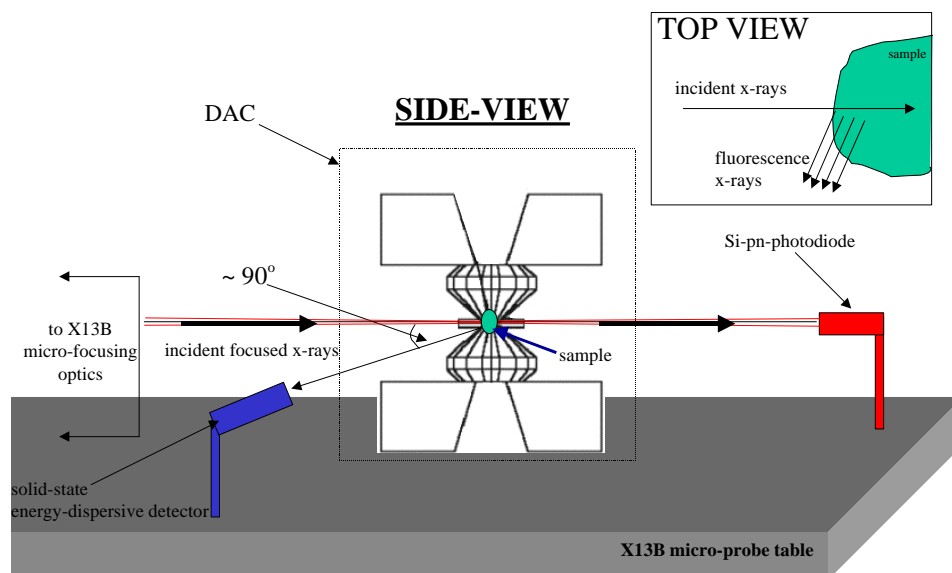


Figure 7-10: Side-view of geometry for ninety-degree x-ray fluorescence collection from thallium-rhenium oxide in the diamond-anvil cell. The micro-metre sample positioning stage has been omitted for clarity. The “TOP VIEW” inset shows a schematic of the geometry of the sample in relation to the incident x-ray beam and the fluorescence photons that are collected by the energy-dispersive detector.

X-ray fluorescence spectra were recorded by varying the incident photon energy from  $\sim 180$  eV below and up to  $\sim 700$  eV above the rhenium  $L_3$  absorption-edge, in steps of  $\sim 1$  eV, and the  $L_\alpha$  fluorescence line was selected using a Nucleus PCA-II<sup>®</sup> multi-channel analyser. All data were recorded at room temperature and in air. The resolution of the X13B double-crystal Si (111) monochromator was calculated to be  $\sim 2$  eV in this energy range, and was detuned to approximately half of the peak Bragg-reflected intensity to prevent higher-order harmonics emerging from the lower crystal. (Section

3.3.4). Further fluorescence EXAFS spectra were recorded at increasing pressures of 7.8 GPa and 12.4 GPa, and a thick thallium-rhenium foil was placed at the sample position to record ambient-simulated data (not within the DAC). At 12.4 GPa, optical inspection confirmed that the Phase IV transition had occurred. The total number of photons collected at each data-point was  $\sim 150\,000 \pm 387$  ( above the edge ), at a count rate of  $\sim 3000$  cps and the total integrated counting time was  $\sim 15$  hours for each pressure run. Detector dead-time effects were monitored during each pressure run and were found to be constant in the EXAFS region.

This experiment was aimed at probing the local oxygen structure around the central-absorbing rhenium atom. The EXAFS function  $\chi$  was extracted by normalising the fluorescence data to unit edge-jump, and subtracting the smooth atomic-like background. This subtraction was achieved by fitting a cubic spline to the post-edge region using the AUTOBK<sup>†</sup> EXAFS reduction program<sup>171</sup> and then subsequently converted to  $k_e$  space, where  $k_e$  is the photoelectron wave-number. The reduction in the EXAFS amplitude with increasing photoelectron energy (Section 6.2), was accounted for by weighting the EXAFS function by  $k_e^3$ . The weighted EXAFS function is shown in Figure 7-11, and the extent of the window reflects the omission of the XANES region from the analysis and the decrease in the statistical accuracy further out into the post-edge region. These two factors led to a  $k_e$  range from  $2.4 \text{ \AA}^{-1} \rightarrow 9.4 \text{ \AA}^{-1}$  (incident x-ray energy varying from  $70 \text{ eV} \rightarrow 330 \text{ eV}$  ) above the absorption-edge.

By Fourier transforming the EXAFS signal  $\chi(k_e) * k_e^3$  and plotting the modulus, the radial distribution function of the data is obtained and is shown in Figure 7-12. This shows directly the nature of the local-structure surrounding the rhenium atoms. The window taper and  $k_e$  range for the Fourier transform were the same for each pressure cycle so that windowing effects were identical.<sup>172</sup> It can be seen that the peak heights are located at approximately the same positions, and there is variation in the amplitude.

---

<sup>†</sup> The source code can be found at the web address, <http://cars9.uchicago.edu/~newville/autobk/>

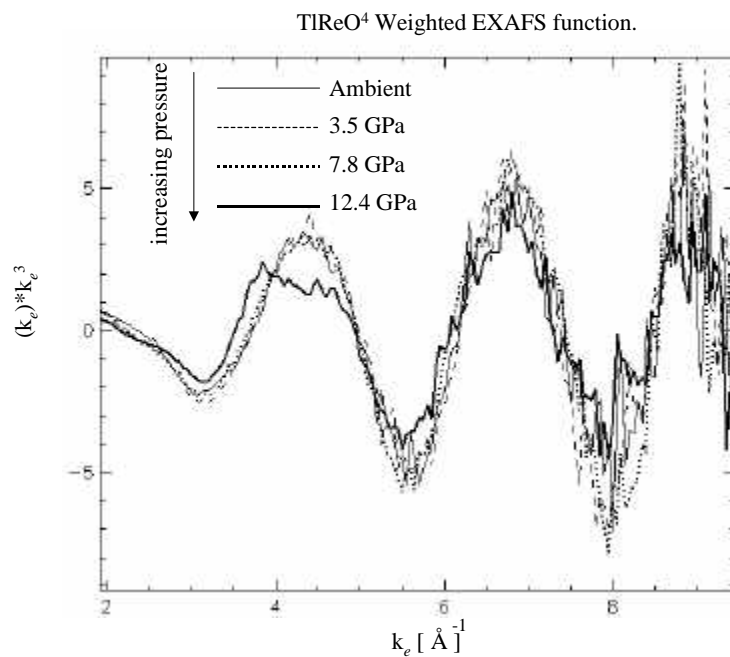


Figure 7-11: The weighted EXAFS signal extracted from the fluorescence spectra recorded at the rhenium  $L_3$  edge in thallium-rhenium oxide.

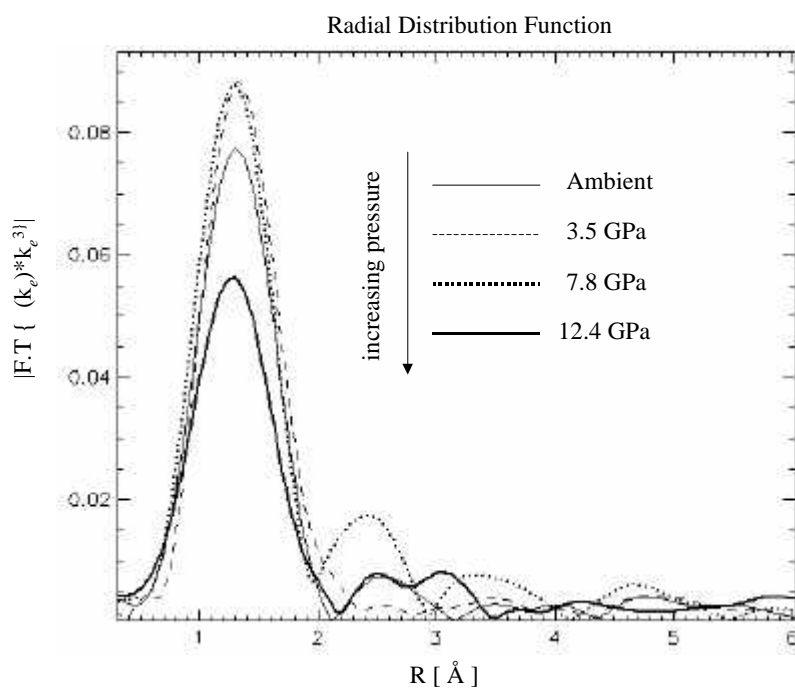


Figure 7-12: The radial distribution function of the weighted EXAFS signal ( Figure 7-11 ) from Fourier transformation in the window-range,  $k_e = 2.4 \text{ \AA}^{-1} \rightarrow 9.4 \text{ \AA}^{-1}$ .

### 7.3 Conclusion of XANES and EXAFS measurements

High-pressure x-ray spectroscopic investigations on thallium-rhenium oxide have been used to determine the nature of the optical and structural phase-transition that occurs at  $\sim 10$  GPa at the NSLS X13 micro-probe beamline. The XANES measurement showed a very large change in the white-line shape at this phase transition, which signifies that a large electronic structure change had taken place. In  $\text{PbWO}_4$ , band-structure calculations indicate that the valence band is dominated by  $\text{O } 2p - \text{W } 5d$  contributions and the lower part of the empty conduction band is mostly of  $\text{W } 5d$  character.<sup>156</sup>  $\text{TlReO}_4$  could be expected to have a similar make-up, with the electronic structure being dominated by effects within the  $\text{ReO}_4$  tetrahedra. It is therefore probable that any distortion of the oxygen around the rhenium atom could produce significant changes to the electronic structure and trigger structural instabilities, and the large broadening of the white-line feature at the optical/structural phase transition could be an important signature of this electronic structure change. A decrease of the band-gap could also be inferred from such a measurement because if this feature is due to empty  $5d$  states in the valence band, then the broadening of the white-line feature on the high-energy side of the spectra points to a movement of these states towards the conduction band. Optical investigation of the high-pressure phase transition indicate that  $\text{TlReO}_4$  still remains an insulator due to transmission in the deep red part of the spectrum,<sup>166</sup> and applied pressures exceeding 20 GPa have been proposed to turn the compound metallic.<sup>166</sup> This is obviously an area for further study.

The EXAFS measurement also displayed a large change in the local structure surrounding the rhenium atom. The large decrease in amplitude at 12.4 GPa may signify a distortion of the oxygen around the rhenium sites. However, the resolution of the experiment ( the extent of the photoelectron wave-number ) meant that separate bond-distances could not be resolved in this experiment, and determination of the oxygen sites could not be achieved.

## Chapter 8 High-pressure-induced volume-collapse in praseodymium metal

The lanthanides and actinides, which form the rare-earth series of the periodic table, can be distinguished by the gradual filling of the  $4f$  and  $5f$  shells respectively. The lanthanide series is mainly trivalent, except for cerium, europium and ytterbium.<sup>173</sup> In cerium, the  $4f$  electron can hybridise with the conduction band, leading to a valency of between 3 and 4, while europium and ytterbium are divalent due to the ground-state energy favouring the half-filled and completely-filled  $4f$  shells.<sup>174</sup> The remaining 11 lanthanides display trivalent character and are chemically similar, with three electrons in an  $sd$ -like conduction band. With increasing atomic number, electrons are deposited into localised  $4f$  states. These states are located within the interior of the atoms, and therefore do not affect the chemistry of these materials.

In general, most of the trivalent lanthanides follow a rich path of structural phase transitions with increasing pressure. Figure 8-1 shows the structural phase diagram of the lanthanides, where the shaded bars indicate structural anomalies.

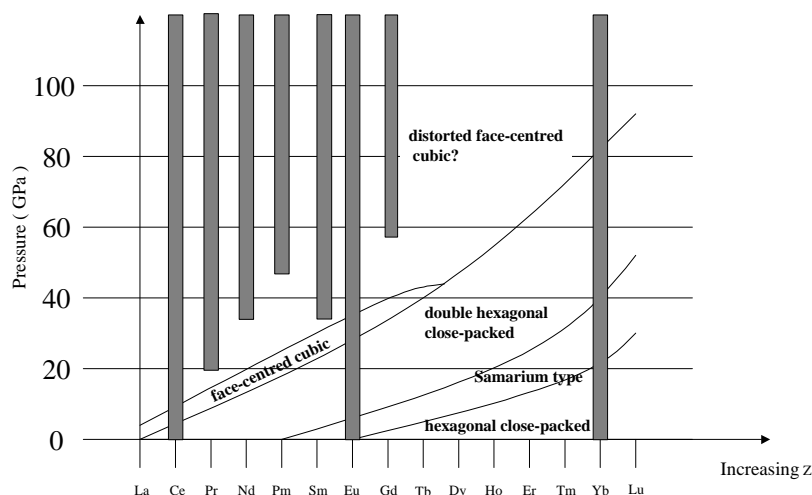


Figure 8-1: Structural phase diagram of the lanthanide series taken from a paper by Holzapfel *et al.*<sup>175</sup>

One way of viewing the systematic changes in the structures of the lanthanide series is by considering the valence electrons as being compressed either by external pressure or by the reduction in atomic number.<sup>174</sup> Generally, the low-pressure structures exhibit

high symmetry and the high-pressure structures have a low-symmetry or monoclinic nature. These well-documented low-pressure crystal structures that the lanthanides transform between are usually attributed to the  $s \rightarrow d$  transfer of the valence electrons.<sup>176,177</sup> The high-pressure low symmetry structures of the lanthanides are sometimes attributed to the delocalisation of the  $4f$  electrons because the early actinide series, which are known to have delocalised  $f$  electrons, also crystallise into similar structures.

In addition to these rich structural phases, there are anomalously large volume-collapses of between 10 %  $\rightarrow$  20 % encountered in cerium, praseodymium and gadolinium,<sup>178</sup> evidenced by the presence of a plateau region in the P-V relation of these three elements as shown in Figure 8-2.

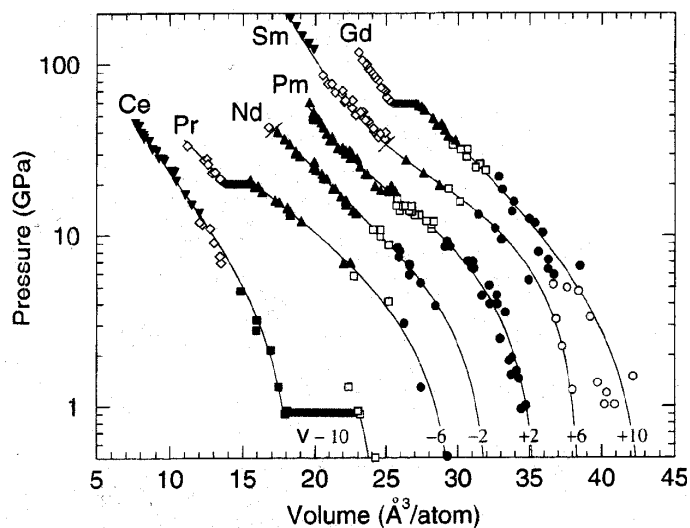


Figure 8-2: Pressure-induced phase diagrams of several members of the lanthanide family. For clarity, the curves have been displaced on the volume axis by an amount shown towards the bottom of each line. The volume-collapse in cerium, praseodymium and gadolinium are clearly visible and large. The symbols represent the different crystal structures that are encountered with increasing pressure, and the plot was taken from a paper by McMahan *et al.*<sup>178</sup>

This volume-collapse has attracted many theoretical studies over the years, and it is now well accepted that these large volume-collapses are associated with a significant change in the  $4f$  electron behaviour. At low-pressures, the  $4f$  electrons are localised, and possess a well-defined magnetic moment. With increasing pressure, the spatial extent of the valence electrons with respect to the atomic core decreases which can

strongly influence the behaviour of the  $4f$  electrons. Currently, there are two competing theories as to how the  $4f$  electrons drive the volume-collapse transition:

- The first class of theory asserts that the volume-collapse is due to a Mott transition.<sup>178,179</sup> In this model, the  $4f$  electrons are highly localised and form narrow energy bands. With applied pressure, these electrons can become delocalised and be made to participate in the crystal bonding, with an associated loss of magnetic moment.
- The second theory postulates that these abrupt phase-transitions are due to a Kondo volume-collapse.<sup>178,180,181</sup> In this model, increasing pressure can lead to a loss of the  $4f$  magnetic moments due to strong coupling of the  $4f$  electrons with the conduction electrons. This is different from the Mott transition model, in that the  $4f$  electrons are still localised and are not considered to form part of the crystal bonding.

The subject of this chapter is to investigate the volume-collapse transition that occurs in praseodymium metal at  $\sim 21\text{GPa}$ .<sup>†</sup> At ambient pressure, praseodymium is double hexagonal close-packed, at  $4\text{GPa}$  it transforms to face-centred cubic, and at  $6.2\text{GPa}$  it is distorted face-centred cubic, which are all high symmetry structures and no volume-collapse is observed. These crystal structures are attributed to  $s \rightarrow d$  electron transfer within the conduction band,<sup>176,177</sup> and the  $4f$  electrons are assumed to remain localised. In contrast, praseodymium at  $\sim 21\text{GPa}$  exhibits a structural phase transition and volume-collapse to the  $\alpha$ -Uranium structure and this is attributed to delocalisation of the  $4f$  electrons.<sup>‡</sup> These measurements are temperature dependent, and above  $573\text{K}$ ,

---

<sup>†</sup> The electronic-structure of praseodymium metal is  $(Xe)4f^2[5d6s]^3$ , where the  $sd$  electrons form the conduction band, and the  $4f$  electrons are localised.

<sup>‡</sup> This large volume-collapse has also been inferred from shock-wave<sup>182</sup> and resistivity measurements.<sup>183</sup>



the praseodymium collapse occurs directly from the face-centred cubic structure, defining a triple-point in the phase diagram as shown in Figure 8-3.<sup>184</sup>

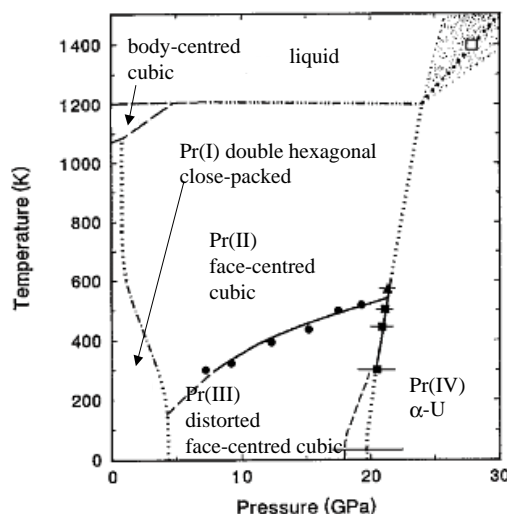


Figure 8-3: Phase diagram of praseodymium taken from a paper by Zhao *et al.*<sup>184</sup>

Lattice parameter determination by x-ray diffraction suggested the magnitude of the volume-collapse is between 9 % and 17 %.<sup>185-189</sup> More accurate ways of measuring itinerant behaviour is needed to refine the theoretical models. The nature of the experiment in the following section is to reveal the electronic structural changes associated with the high-pressure volume-collapse in praseodymium metal.

Most metals display strong resonances at photon absorption thresholds due to electron promotion into empty bound states, as can be seen at the rhenium  $L_3$  absorption edge spectra of various compounds in Chapter 7, Figure 7-6. These resonances are often referred to as “white-lines” and the area under such lines provides a measure of the density of empty bound states. In the Mott or Kondo models that try to explain the volume-collapse of the lanthanides, mixing of the  $4f$  with the  $sd$  conduction electrons is inferred. By measuring the  $2p \rightarrow 5d$  transitions around the praseodymium  $L_3$  absorption edge, any mixing of the  $4f$  states with the conduction electrons can be interpreted as a decrease in the “white-line” intensity due to the inferred increase in  $d$  band occupancy. Such measurements should provide significant input to theoretical models.

## 8.1 Fluorescence XANES measurement in back-scattering geometry

The X13B x-ray micro-focusing optics were used to investigate the volume-collapse transition in praseodymium metal that occurs at  $\sim 21$  GPa. The incident x-ray energy was to be scanned across the  $\text{Pr L}_3$  absorption edge, and the experiment was arranged to collect back-scattered fluorescence photons, as the sample is too thick and the x-ray energy too low to perform transmission measurements. In general, it must be emphasised that the majority of high-pressure x-ray investigations have used diffraction-based techniques, and transmission data have been limited to high-energy / medium-Z materials. This new method of extracting absorption coefficients from back-scattered fluorescence capture provides significant progress in experimental data collection. Self-absorption corrections were to be applied to the data (Section 6.3) to allow quantification of any pressure-induced intensity variations in the praseodymium “white-line” feature.

Figure 8-4 shows a schematic of the experimental arrangement for back-scattered collection of x-ray emission, and the diamond-anvil cell was arranged so that both the incident and fluorescence x-rays propagated through the beryllium gasket (Figure 6-1). The sample was placed at the focal point of the x-ray micro-beam, using pre-aligned optical ccd-cameras, and exact positioning was obtained by monitoring the photon flux incident upon the Si-pn-photodiode located downstream of the sample position. An amptek XR-100CR energy-dispersive Si-pin-photodiode was used to collect the back-scattered fluorescence x-rays, and all data were collected at room temperature and in air.

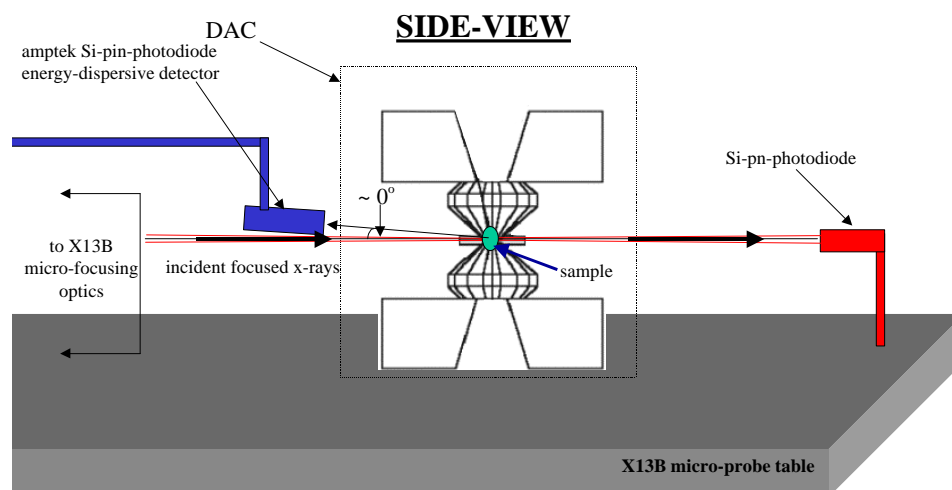


Figure 8-4: Side-view of geometry for back-scattering fluorescence collection from praseodymium in the diamond-anvil cell. The micro-metre sample positioning stage and optical ccd cameras have been omitted for clarity.

The electron beam energy and maximum electron current in the NSLS storage-ring were 2.8 GeV and 200 mA respectively, and the EPW (Section 3.3.2) was the source of x-rays for this experiment. To maximise flux on the sample, a helium atmosphere was provided to a large proportion of the x-ray path inside the X13B experimental hutch, including the micro-probe mirror chambers. Normalisation was provided by an ionisation chamber positioned downstream of the micro-probe mirror acceptance slits and air-paths were taken into consideration (Section 5.6).

A small scraping of praseodymium metal was obtained under a high-purity nitrogen atmosphere to prevent oxidation of the metal. This was then loaded into the DAC sample chamber, together with mineral oil that acted as the pressure-transmitting medium and which also prevented oxidation. A few ruby chips were also inserted into the DAC sample chamber to allow for pressure calibration. The diamond-anvils were closed to create the gasket seal, and the starting pressure was measured to be 11 GPa, below the volume-collapse transition, using the well-known shifts of the ruby fluorescence lines (Section 6.1).

The DAC assembly was then transferred to the X13B micro-probe end-station and placed onto the micro-metre sample stage at the x-ray focal point. Accurate sample positioning was obtained by monitoring the incident flux on the Si-pn-photodiode,

placed upstream of the sample position. The resolution of the X13 double-crystal Si(111) monochromator was calculated to be  $\sim 1.1$  eV at the praseodymium  $L_3$  absorption edge, and the monochromator was detuned to approximately half of the peak Bragg reflected intensity to prevent higher-order harmonics emerging from the lower crystal (Section 3.3.4).

In the first experimental run, x-ray fluorescence spectra were recorded by varying the incident photon energy from 5.85 keV to 6.127 keV across the praseodymium  $L_3$  absorption edge, and the  $L\alpha$  emission line was selected using a Nucleus PCA-II<sup>®</sup> multi-channel analyser. The fluorescence photons were captured by an energy dispersive XR-100CR amptek detector, that was placed  $\sim 2$  cm from the sample position, and in the back-scattering geometry. The pre-edge was scanned from 5.85 keV  $\rightarrow$  5.93 keV in 1 eV steps, the “white-line” feature was recorded from 5.930 keV  $\rightarrow$  6.027 keV in steps of  $\sim 0.3$  eV, and the post edge was scanned between 6.027 keV  $\rightarrow$  6.127 keV in steps of 2 eV. Counting times of 10 seconds per energy point were used, and integrated counts of  $\sim 6000$  at positions in the post-edge region were obtained at background-subtracted count-rates of  $\sim 30$  cps. Further fluorescence data were recorded at pressures close to and exceeding the volume-collapse transition at  $\sim 18$  GPa and  $\sim 29$  GPa respectively.

A second experimental run to gain some more pressure data on praseodymium metal was conducted. The only difference in the experimental configuration was that a slightly larger amptek detector of area  $13 \text{ mm}^2$  was used to collect the back-scattered fluorescence photons. For this run, two pressures were measured below and above the volume-collapse transition, corresponding to pressures of  $\sim 10$  GPa and  $\sim 25$  GPa. The incident energy was scanned between 5.8 keV  $\rightarrow$  5.945 keV in steps of  $\sim 10$  eV to cover the pre-edge region, the “white-line” feature was scanned between 5.95 keV  $\rightarrow$  5.999 keV in steps of  $\sim 0.5$  eV, and the post-edge region was scanned between 6 keV  $\rightarrow$  6.09 keV and

6.15 keV  $\rightarrow$  6.4 keV in steps of 2 eV and 5 eV respectively.<sup>†</sup> Counting times of 10 s per energy point were used, and at background-subtracted count-rates of  $\sim 50$  cps.

### 8.1.1 Self-absorption correction of XANES spectra

For back-scattered fluorescence detection, the normalised fluorescence signal is obtained by substituting  $\frac{\sin \theta_i}{\sin \Omega} = 1$  into Equation {6.13} giving,

$$\frac{I_f(E)}{I_o(E)} \propto \frac{\mu_{\text{sub}}(E)}{\mu_{\text{sub}}(E) + \mu_{\text{other}}(E) + \mu_{\text{tot}}(E_f)} + \frac{I_{\text{bac}}(E)}{I_o(E)} \quad \{6.17\}$$

where  $\frac{I_{\text{bac}}(E)}{I_o(E)}$  is the normalised back-ground function and is largely due to Compton scattering from the beryllium gasket material. This can be subtracted from Equation {6.17} by either fitting a smooth function to the pre-edge region to force  $\frac{I_f(E)}{I_o(E)} = 0$ , or by measuring the scattering from the beryllium gasket itself. The latter method was used to obtain the subsequent data.

By rearrangement, and after background subtraction, the true absorption coefficient as a function of energy is given by,

$$\mu_{\text{sub}}(E) = \frac{-I_{\text{norm}}(E) [\mu_{\text{other}}(E) + \mu_{\text{tot}}(E_f)]}{I_{\text{norm}}(E) - \tau} \quad \{6.18\}$$

where  $I_{\text{norm}}(E)$  is the normalised fluorescence intensity and  $\tau$  is a constant of proportionality.

Equation {6.18} can be used to determine  $\tau$  away from the absorption edge, where  $\mu_{\text{sub}}(E)$ ,  $\mu_{\text{other}}(E)$  and  $\mu_{\text{tot}}(E_f)$  are well defined.<sup>‡</sup> A plot of the atomic values for praseodymium are shown in Figure 8-5. These values were obtained from the Henke

<sup>†</sup> The region between 6.09 keV  $\rightarrow$  6.15 keV was not included in the analysis because Bragg reflections emerging from the beryllium gasket were saturating the energy-dispersive amptek detector here.

<sup>‡</sup> To fix the endpoint above the edge to that of the atomic absorption coefficient, it is necessary to extend the incident energy range well above the absorption-edge so that empty continuum states are only probed, and the absorption-coefficient is atomic-like.

tables,<sup>1</sup> and can also be found within the XOP computer package,<sup>84</sup> and an explanation of how this data can be disassembled is described in Section 6.30.

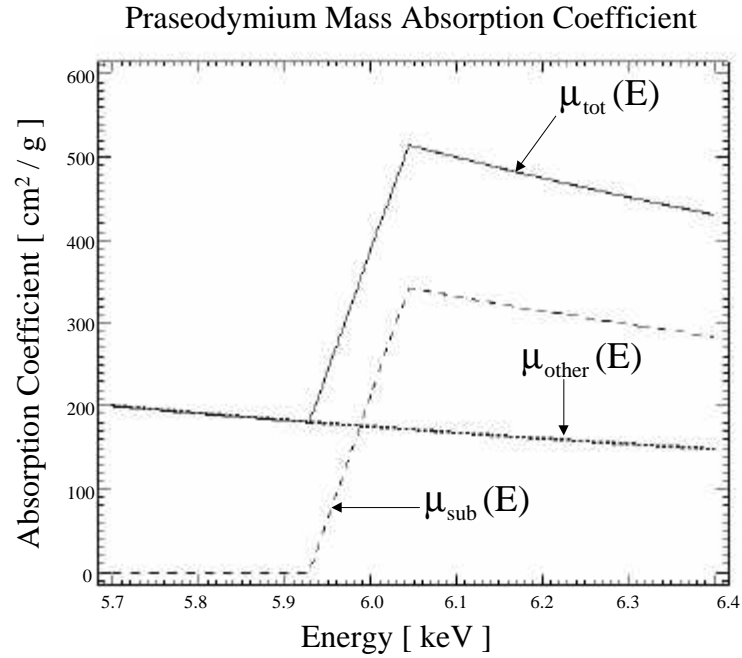


Figure 8-5: Calculation of atomic photo-absorption coefficients using tabulated values.

The error in  $\tau$  is due to counting statistics in measuring the fluorescence intensity.

The relative error in  $\mu_{\text{sub}}(E)$  is then given by,

$$\frac{\Delta\mu_{\text{sub}}(E)}{\mu_{\text{sub}}(E)} = \pm \sqrt{\left(\frac{\Delta I_n(E)}{I_n(E)}\right)^2 + \left(\frac{\Delta I_n(E) + \Delta\tau}{I_n(E) - \tau}\right)^2} \quad \{6.19\}$$

The following plots show the uncorrected and self-absorption corrected data taken during the two experimental runs:

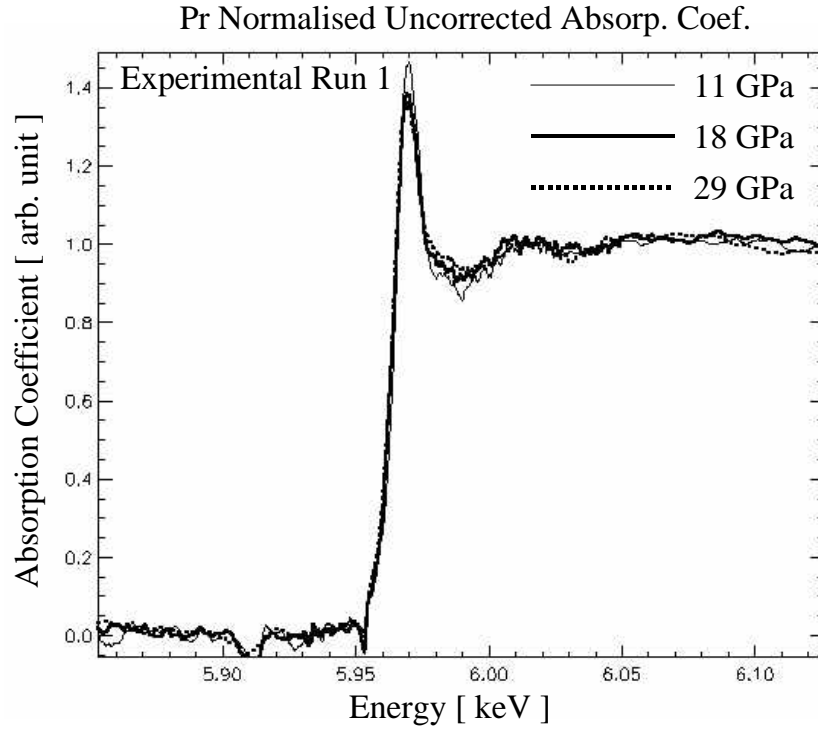


Figure 8-6: Experimental run 1. Normalised back-ground subtracted back-scattered fluorescence spectra collected at the praseodymium  $L_3$  absorption edge at three different pressures.

Figure 8-6 shows the normalised back-ground subtracted fluorescence spectra taken at 11 GPa , 18 GPa and 29 GPa . Notice the intensity drop of the “white-line” feature at the higher pressures.<sup>†</sup> There is a fall at 18 GPa, which is below the praseodymium volume-collapse transition. This is probably due to errors in pressure determination within the sample cell and accuracy of the measurement itself. Due to self-absorption effects, the intensity of the “white-line” is reduced, and corrected spectra are displayed in Figure 8-7. The self-absorption corrected data display large variations in the intensity of the “white-line” feature. This region is magnified in Figure 8-8, and error bars are also displayed. The errors are due to fixing the end-points of the unnormalised spectra to values corresponding to the atomic-like absorption coefficients, within the accuracy determined by counting statistics.

<sup>†</sup> Strictly speaking, the integrated area under the “white-line” feature gives the measurement of the empty  $5d$  states. However, a measurement of the peak-height is justified in this case as the shape of the “white” line remains essentially unaltered across the praseodymium volume-collapse transition.

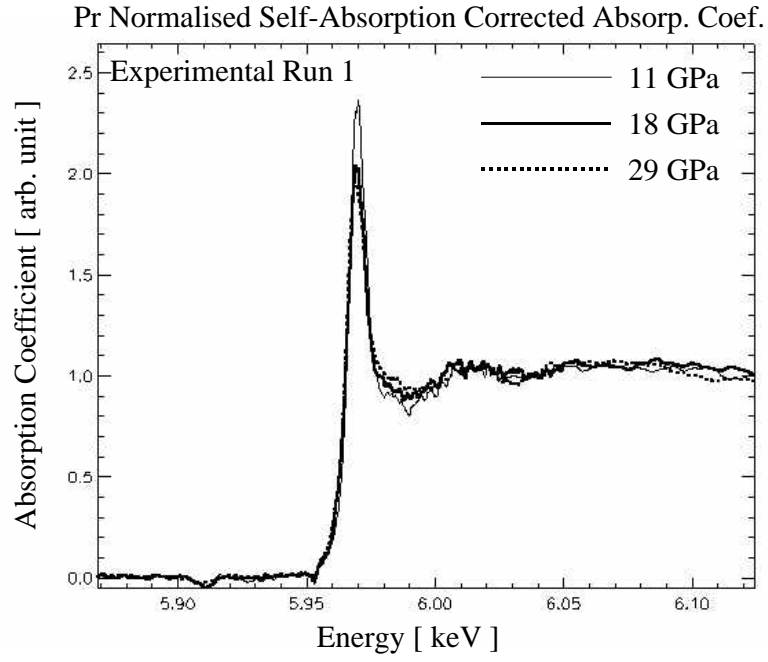


Figure 8-7: Self-absorption corrected fluorescence spectra of Figure 8-6.

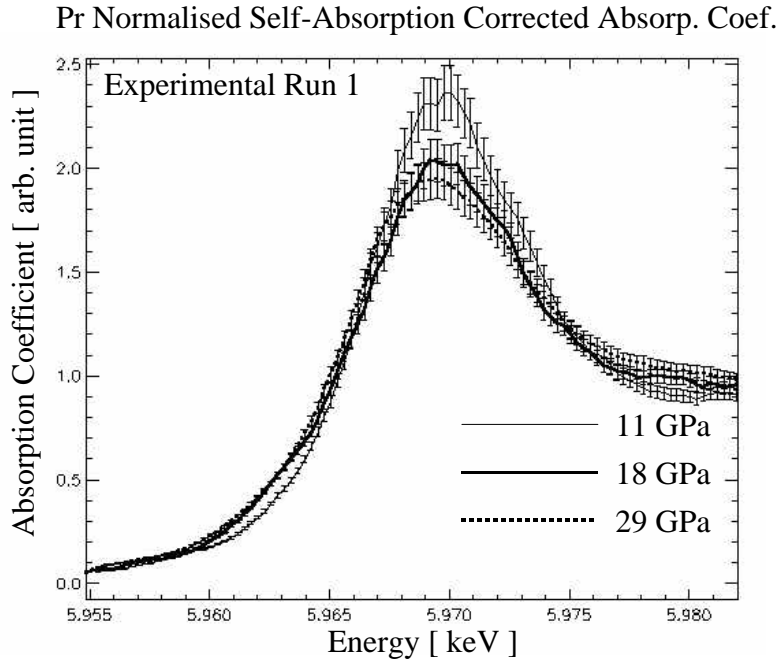


Figure 8-8: Highlighting the pressure-induced intensity variations of the “white line” feature in Figure 8-7.

The same type of plots as described above are shown below for experimental run 2, using the same analysis procedures.



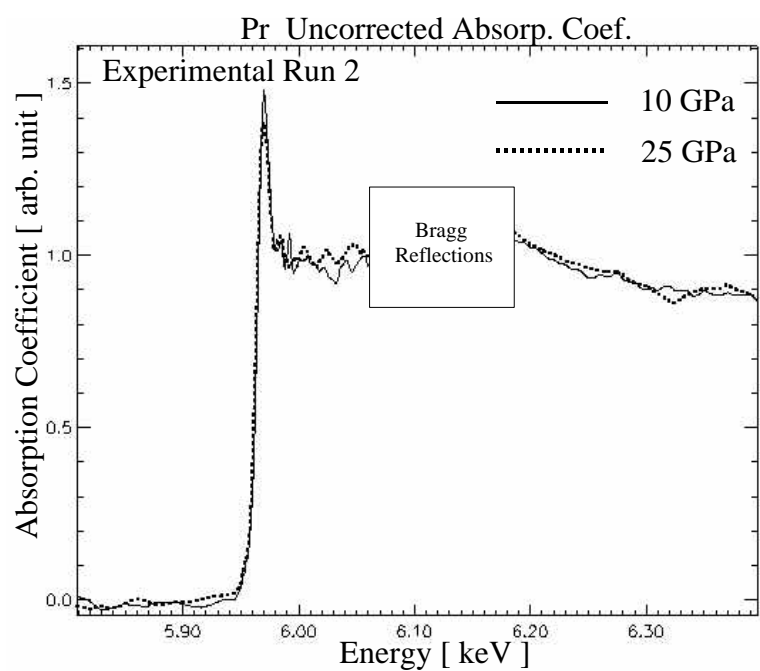


Figure 8-9: Experimental run 2. Normalised back-ground subtracted back-scattered fluorescence spectra collected at the praseodymium  $L_3$  absorption edge at two different pressures.

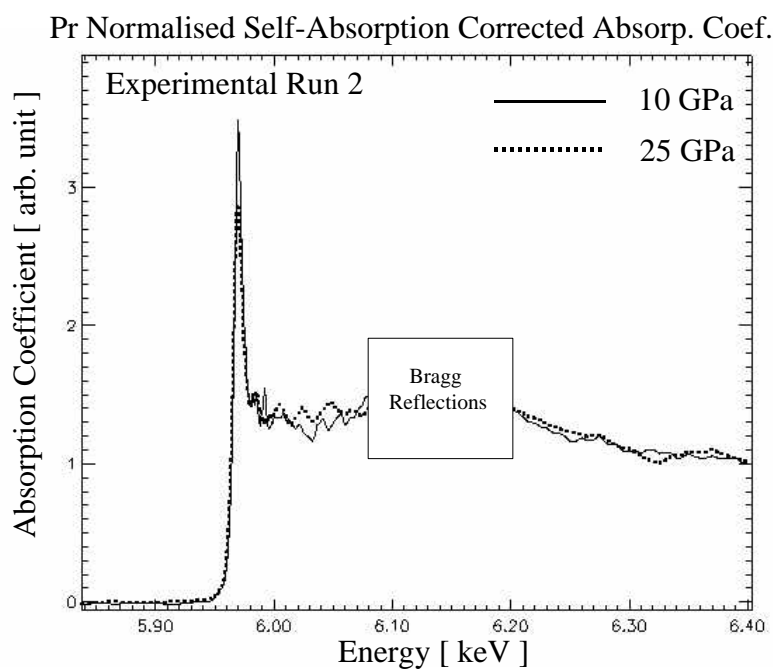


Figure 8-10: Self-absorption corrected fluorescence spectra of Figure 8-9.

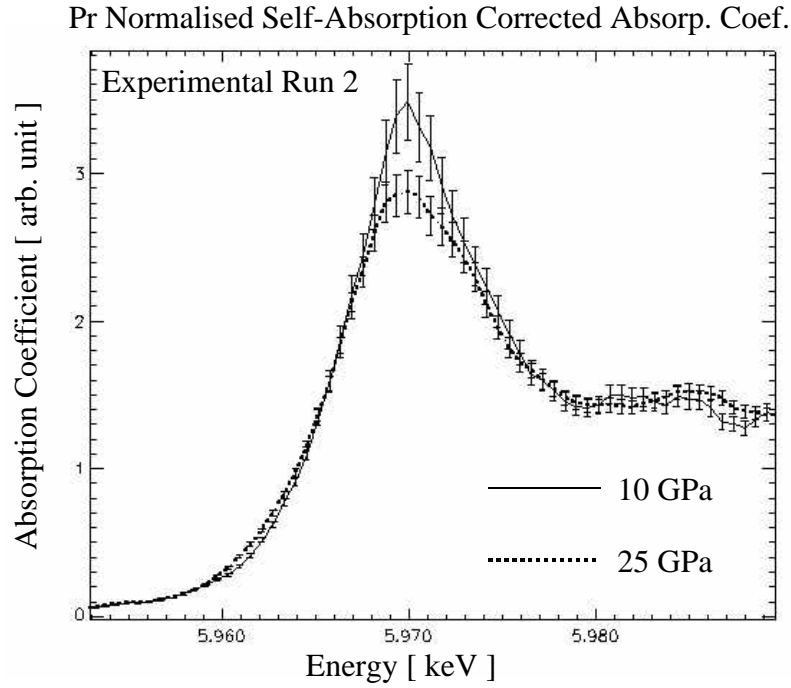


Figure 8-11: Highlighting the pressure-induced intensity variations of the “white line” feature in Figure 8-10.

Comparing the data obtained during the two experimental runs, decreases in the “white-line” feature have been found above the volume-collapse transition pressure. Discrepancies in the peak values between the two sets of data are due to choosing the value of the end-point to correspond to the atomic-like absorption coefficient. However, ratios are not as sensitive and agreement between the two data sets are summarised in Table 8-1.

	Measured Intensity Ratios	Self-Absorption Corrected Intensity Ratios
Experimental 1	$\frac{I_{18 \text{ GPa}}}{I_{10 \text{ GPa}}} = 0.94 \pm 0.01$	$\frac{I_{18 \text{ GPa}}}{I_{10 \text{ GPa}}} = 0.86 \pm 0.06$
	$\frac{I_{29 \text{ GPa}}}{I_{10 \text{ GPa}}} = 0.93 \pm 0.01$	$\frac{I_{29 \text{ GPa}}}{I_{10 \text{ GPa}}} = 0.82 \pm 0.06$
Experimental Run 2	$\frac{I_{25 \text{ GPa}}}{I_{10 \text{ GPa}}} = 0.93 \pm 0.01$	$\frac{I_{25 \text{ GPa}}}{I_{10 \text{ GPa}}} = 0.83 \pm 0.08$

Table 8-1: Variations in the “white-line “ intensities between data taken below the volume-collapse and above the volume collapse in two experimental runs.

## 8.2 Summary

The volume-collapse transition that occurs in praseodymium metal has been studied using the x-ray micro-probe optics to concentrate x-rays onto a small sample under pressure within the diamond-anvil cell. The experiment was arranged to collect back-scattered fluorescence x-rays so that self-absorption effects can be accurately corrected for. This new method of extracting absorption coefficients from thick high-Z materials in the diamond-anvil cell is a significant addition to x-ray diffraction, resistivity and shock-wave measurements that have been the standard tools for investigating high-pressure phase transitions. Self-absorption corrected intensity ratios of the “white-line” feature that occurs near the praseodymium  $L_3$  absorption edge, between data collected below and above the volume-collapse transition, have been quantified. Sets of data obtained during two experimental runs agree well. The intensity ratios of the “white-line” feature above and below the volume-collapse transition were found to be  $\sim 0.83 \pm 0.06$  and  $\sim 0.83 \pm 0.08$ . These measurements may infer  $4f$  delocalisation through mixing of the  $4f$  and conduction electrons due to the decrease in the “white-line” intensity, and more data is envisaged to be collected later to improve upon the experimental accuracy of the measurement.

Finally, to address the issue of if the  $4f$  electrons are delocalised in the high-pressure phase, an x-ray resonant Raman scattering is planned. In this measurement, the  $3d \rightarrow 2p$  fluorescence line is analysed using a high-resolution x-ray crystal spectrometer (with better than 1 eV resolution),<sup>190,191</sup> and the quadrupole transition from Pr  $2p \rightarrow 4f$  can be separated from the  $2p \rightarrow 5d$  dipole transition reported in this chapter. This will then allow the direct investigation of the behaviour of the  $4f$  electronic states.

## Chapter 9 X-ray micro-probe fluorescence calcium mapping of normal and diseased bone

The X13B x-ray micro-focusing mirrors were used to study the calcium content in two bone sections, one normal and the other suffering from osteoarthritis, using fluorescence detection in the back-scattering geometry (Figure 9-2). The sensitivity of x-ray fluorescence<sup>2</sup> and the spatial resolution of x-ray micro-beam imaging as a complementary probe to infrared micro-spectroscopy,<sup>192</sup> opens up many new exciting areas of research in this expanding field of study.

Bone is a fundamental building block of all vertebrate systems. It is both strong and flexible and acts as a mineral-reservoir for the blood supply and a protective casing for the vital internal organs. Bone, as an organ, can dispense or withdraw minerals to maintain the delicate balance between calcium and phosphorus levels in the body.<sup>193</sup> Bone consists of protein-rich collagen fibres, within and around which plate-shaped calcium-phosphate crystals are located.<sup>193,194</sup> The organic and mineral components are the type I collagen, which accounts for ~ 90 % of the total bone protein, and the main hydroxyapatite crystal,  $\text{Ca}_{10}(\text{PO}_4)_6(\text{OH})_2$ .<sup>193</sup> The collagen fibres are typically laid down in sections, producing lamella or circular structures. There are two types of bone: Cortical bone is the outer part of the skeleton that provides the inherent strength and accounts for about 80% of the skeletal mass. Trabecular bone, which consists of a mesh-like pattern of collagen fibres, forms the interior portion and is surrounded by the cortical part.

Deep within the bone, in the trabecular regions and around the growth plates, osteocyte cells can be found whose function is to form and deplete the bone structure. There are two types of osteocyte; osteoblasts and osteoclasts. All types of bone are formed and depleted by these cells which facilitate the exchange of nutrients and waste. Osteoclasts are responsible for bone depletion. These are large multi-nuclear cells that produce enzymes. These enzymes break down and resorb the mineralised bone before delivering it to the blood stream. The osteoclasts consume the protein rich collagen, and

by releasing the bone minerals to the blood supply, the overall result is bone errodement. Osteoblasts build bone by pumping out collagen fibres. These fibres bind together to form a denser bone matrix called osteoid which forms ~ 10 % → 20 % of the total bone mass. In the cortical regions, these new layers of bone appear as concentric circles, commonly referred to as osteons.

Bone is continuously in a state of formation and depletion, through the actions of the osteoblasts and osteoclasts. The rates at which these function depend upon the density of the cells, the levels of calcium and phosphorus, and the hormones which activate them. The overall process of remodelling is simple; the osteoclasts tunnel from the bone surface and into the structure by absorbing the mineralised components. Subsequently, the osteoblasts diffuse into these cavities to deliver the collagen (the osteoid) which in turn is mineralised to form a new layer of bone. To maintain a constant bone mass, these processes exist in equilibrium for a normal healthy adult. However, the actual processes that cause bone mineralisation are not fully understood.

It is known that often in diseased bone, there is an imbalance between the resorption and deposition rate of the skeleton. Three examples of bone disease that are characterised by bone remodelling imbalances are; osteoporosis,<sup>195</sup> osteopetrosis<sup>196</sup> and osteoarthritis.<sup>197</sup> Osteoporosis is characterised by reduced bone mass which may be attributed to a deficiency in the production or function of the osteoblasts. Secondly, osteopetrosis is a net overgrowth of bone due to a reduction in the function or production of osteoclasts that reabsorb the older bone. Thirdly, osteoarthritis results in a splitting or splintering of the articular cartilage, together with a marked thickening of the subchondral bone. A section of a normal and osteoarthritic monkey tibia is shown in Figure 9-1.

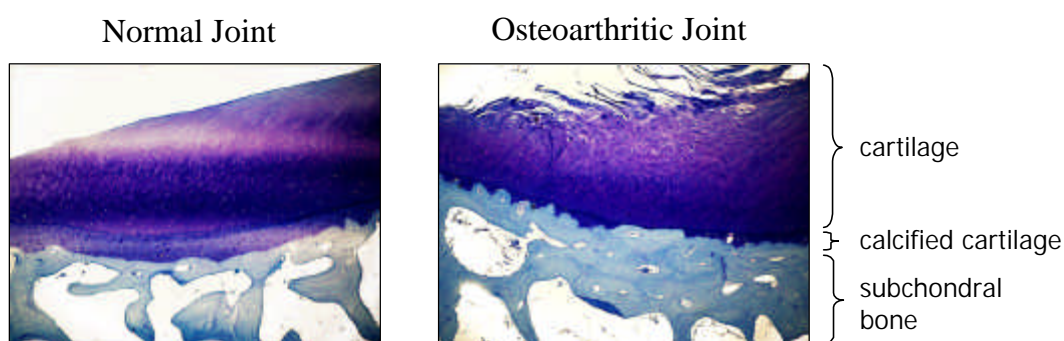


Figure 9-1: Optical images of normal and diseased monkey tibia.

Infrared micro-spectroscopy is an ideal tool to investigate the chemical composition of bone due to its inherent sensitivity to the vibrational modes of the various components. Together with light microscopy, infrared micro-spectroscopy enables the correlation of molecular chemistry with the micro-structure of the sample. The infrared absorption bands of bone proteins are extremely sensitive to the chemical composition of mineral components such as carbonate and phosphate, the mineral crystallinity, and the content of the organic matrix.<sup>192</sup> By analysing various sections of bone, chemical composition can be mapped as a function of age and morphology. Until recently, bone composition was studied using ash-weight analysis (the grinding and heat treatment of bone) which cannot yield spatially-resolved information.

At the NSLS U4-IR beamline, a recent infrared absorption study around the vicinity of an osteon located within a monkey tibia has been performed.<sup>192</sup> The majority of chemical changes in bone occur within  $20\mu\text{m}$  of the osteon centre which are typically  $200\mu\text{m}$  in diameter. As the hydroxyapatite crystals age, a variety of changes can occur. Cations of  $\text{Na}^+$ ,  $\text{K}^+$ ,  $\text{Mg}^{2+}$  and  $\text{Pb}^{2+}$  can be substituted for calcium, and the anions  $(\text{CO}_3)^{2-}$ ,  $(\text{HPO}_4)^{2-}$ ,  $\text{Cl}^-$  and  $\text{F}^-$  can replace the phosphate and hydroxide ions in the hydroxyapatite crystals. These substitutions into the bone crystal are important as they effect the size, density and solubility of the crystals, which are very important in the bone remodelling process. The infrared results demonstrated that the articular cartilage is non-mineralised. In addition, three separate  $(\text{CO}_3)^{2-}$  substitution sites in the hydroxyapatite crystal lattice were discovered, with the most intense peaks

coming from phosphate ( $\text{PO}_4^{3-}$ ) substitution. Infrared micro-spectroscopy can therefore be used to determine not only the mineral content of bone, but also the nature of the local environment. A measure of the relative protein and mineral concentrations were extracted from the infrared data, and a decrease in the amide I/phosphate and amide I/carbonate ratios as a function of distance from the osteon centre was found. This reduction is because young bone (near the osteon centre) contains a higher protein/mineral ratio than older bone, and as it matures, crystallisation occurs in the hydroxyapatite lattice. Also, it was discovered that the phosphate/carbonate ratio decreases from the centre of the osteon. Previous studies suggested that the carbonate molecule,  $(\text{CO}_3)^{2-}$  is substituted into the phosphate  $(\text{PO}_4)^{3-}$  sites and Fourier-transform infrared (FTIR) micro-spectroscopy confirmed this notion. Studying the area of bone around the subchondral section, from the marrow region to the articular cartilage, the infrared micro-probe revealed that the protein/mineral ratio is high in the cartilage and in the regions of new bone growth, but reduced in the older bone. The new bone has a low carbonate/phosphate ratio and as it matures, carbonate substitution into the phosphate sites increase, thus compounding this ratio.

Calcium is an important component of bone that cannot be examined with infrared micro-spectroscopy. With the advent of the X13B micro-focusing optics, calcium fluorescence maps of a normal and osteoarthritic monkey knee joint were undertaken to investigate any anomalies that may occur.

### **9.1 X-ray micro-probe fluorescence calcium mapping of normal bone**

The normal monkey bone sample<sup>†</sup> was thinly sectioned into a  $5\mu\text{m}$  thickness by first embedding the entire knee-joint into methyl-methacrylate/dibutyl-phthalate (a plastic-like material), and slicing with a diamond saw. Using the wiggler insertion device, the X13B crystal monochromator was set to select an energy of  $6.7\text{ keV}$ , above the calcium K absorption-edge ( $\sim 4\text{ keV}$ ). Using this high x-ray energy, the Compton and elastically scattered radiation can easily be discriminated, although the sensitivity is slightly

---

<sup>†</sup> Provided by Dr. Cathy Carlson at the University of Minnesota, department of veterinary medicine. The sample was from a healthy female monkey.

reduced due to higher transmission through the sample. The fluorescence radiation was collected by an amptek XR-100CR energy-dispersive silicon-pin-photodiode with an active area of  $13 \text{ mm}^2$ . The detector was placed  $\sim 2 \text{ cm}$  from the sample surface in an approximate back-scattering geometry. This orientation minimises horizontal beam-spread on the sample and a schematic of the experimental arrangement is shown below.

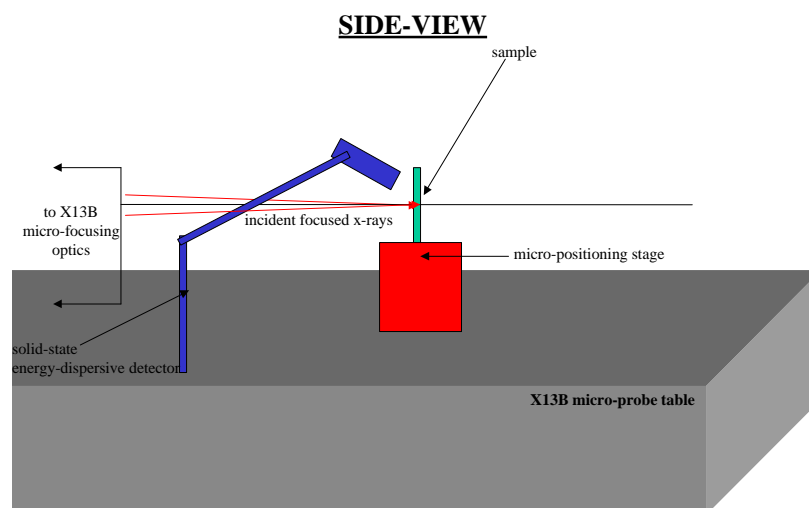


Figure 9-2: Experimental arrangement for X13B calcium fluorescence collection.

The fluorescence line was recorded by selecting energy window around the  $K_{\alpha}$  calcium fluorescence line ( $\sim 3.7 \text{ keV}$ ) on a Nucleus PCA-II<sup>®</sup> multi-channel analyser. Helium was allowed to flow through the mirror chambers, and an additional helium flight-path was inserted before the mirror aperture slits, to increase photon flux on the sample. To compensate for decay of the electron beam current in the NSLS storage ring, normalisation was performed by monitoring the flux through an ionisation chamber (Section 5.6). The sample stage was arranged to enable sub-micron positioning, orthogonal to x-ray beam propagation. An initial wide-area scan of the subchondral bone region with coarse stepping of  $35 \mu\text{m}$  in the horizontal and  $18.5 \mu\text{m}$  in the vertical directions was first performed to select areas for further investigation. A counting time of 1 second per pixel was used, and the map is shown in Figure 9-3. The colour coding is grey-scale, with the lighter areas representing higher calcium content, the black regions are empty space, and the darker areas signify a lower calcium composition. The numbers on the grey-scale bar represent the total pixel counts divided by the mean



intensity for the whole bone section. There is little variation in the intensity profile of the bone region as the sample is normal.

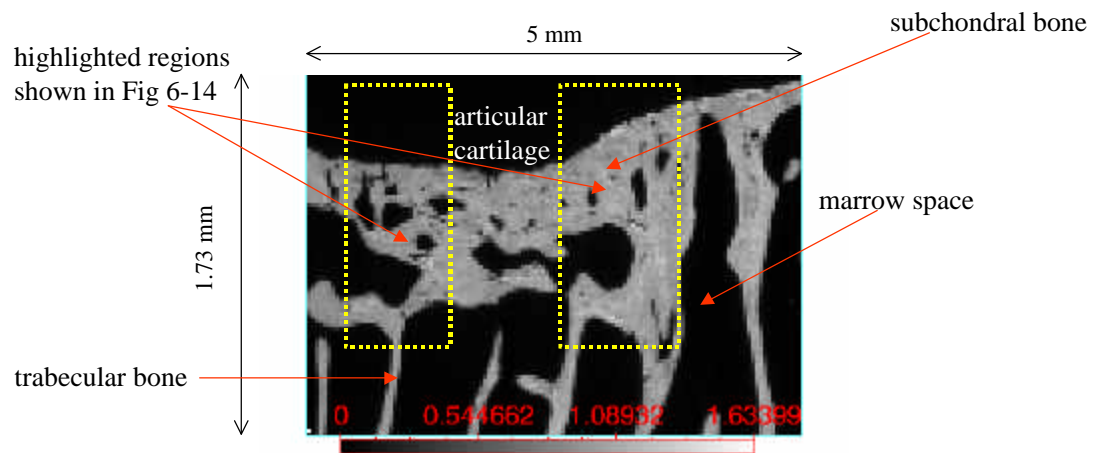


Figure 9-3: Coarse resolution calcium fluorescence map of normal monkey bone (  $35\text{ }\mu\text{m}$  hor. X  $18.5\text{ }\mu\text{m}$  vert. resolution ). Counting time was one second/pixel.

This type of coarse scan is essential for pin-pointing areas for more accurate investigation. The spongy-like region of the inner trabecular bone is clearly visible towards the lower area of Figure 9-3. The bone becomes denser towards the top of the figure, and is referred to as subchondral bone. The articular cartilage, which is joined to the upper part of the subchondral bone is not visible in the calcium map because it is comprised mainly of protein, and contains no mineral.

After the coarse scan had been completed, two smaller regions were selected and mapped. Step sizes of  $15\text{ }\mu\text{m}$  in the horizontal and  $5\text{ }\mu\text{m}$  in the vertical directions were used to collect the images shown in Figure 9-4, each with counting times of 1 second per pixel. These images clearly show the high resolution delivered by the X13B micro-probe optics. Osteons and micro-cracks<sup>198</sup> are visible in the bone structure as regions of low calcium content. These areas of subchondral bone, which join to the articular cartilage, show little sign of high calcification. However, in the right-hand side map of Figure 9-4 there is a small region of the articular cartilage which shows signs of increased calcification. This is the calcified cartilage zone of the joint, which lies between the articular cartilage and subchondral bone. In this particular region, it appears

as though the calcified cartilage region is over-mineralised and may indicate early onset of osteoarthritis in this joint.

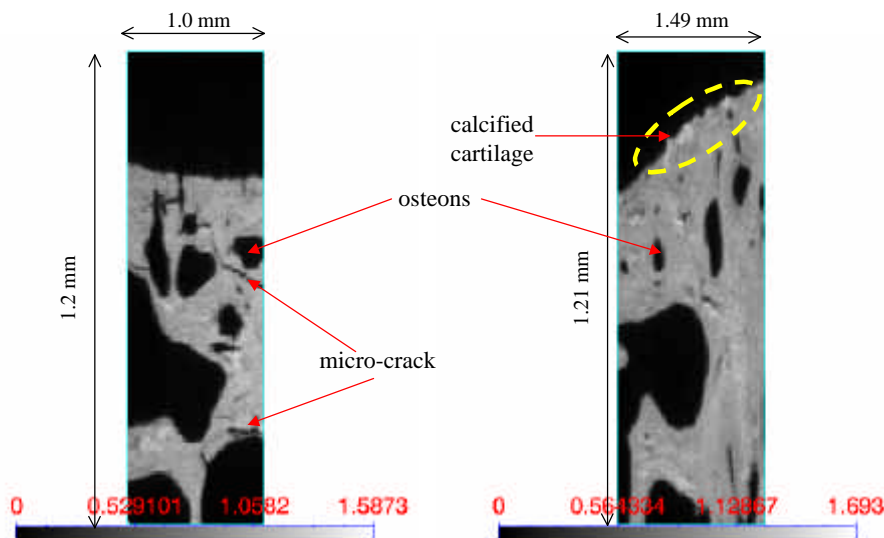


Figure 9-4: High resolution calcium fluorescence map of normal monkey bone (  $15\text{ }\mu\text{m}$  hor. X  $5\text{ }\mu\text{m}$  vert. resolution ) from highlighted regions in Figure 9-3. Counting time = 1 second/pixel.

## 9.2 X-ray micro-probe fluorescence calcium mapping of osteoarthritic bone

The second part of the investigation was the calcium mapping of the subchondral bone of a monkey which had severe osteoarthritis. This was induced by removal of the ovaries in the female specimen.<sup>199</sup> The undulator insertion device ( IVUN ) in the X13 straight-section was the source of x-rays in this experiment. The magnetic gap of the undulator was closed to  $3.7\text{ mm}$ , and the crystal monochromator was set to select the undulator first harmonic at  $\sim 5.6\text{ keV}$ . Helium flow was provided, as in the previous section and the decay of the electron beam in the NSLS storage ring was compensated for by normalising to an ionisation chamber reading (Section 5.6). An amptek XR-100CR Si-pin-photodiode detector of active area  $7\text{ mm}^2$  was used, and the calcium  $K_{\alpha}$  fluorescence photons were selected on a Nucleus PCA-II<sup>®</sup> multi-channel analyser. A large section of the sample of area  $(3.7\text{ mm} \times 3.3\text{ mm})$  was scanned in steps of  $10\text{ }\mu\text{m}$  in the horizontal, and  $5\text{ }\mu\text{m}$  in the vertical directions, and the total counting time per pixel was 1 second. The calcium fluorescence map is shown in Figure 9-5, and the total counting time was  $\sim 68$  hours. Unlike the calcium fluorescence maps of the normal

monkey tibia, there are numerous regions of high calcium concentration in the subchondral bone and several significant micro-cracks. Moreover, repair of these cracks has been implicated in the high rate of bone turnover in the subchondral bone region in osteoarthritis, which may in turn contribute to subchondral bone thickening in the disease.<sup>200-202</sup> Three sections of high calcium concentration have been highlighted in Figure 9-5 and are subsequently displayed in Figure 9-6.

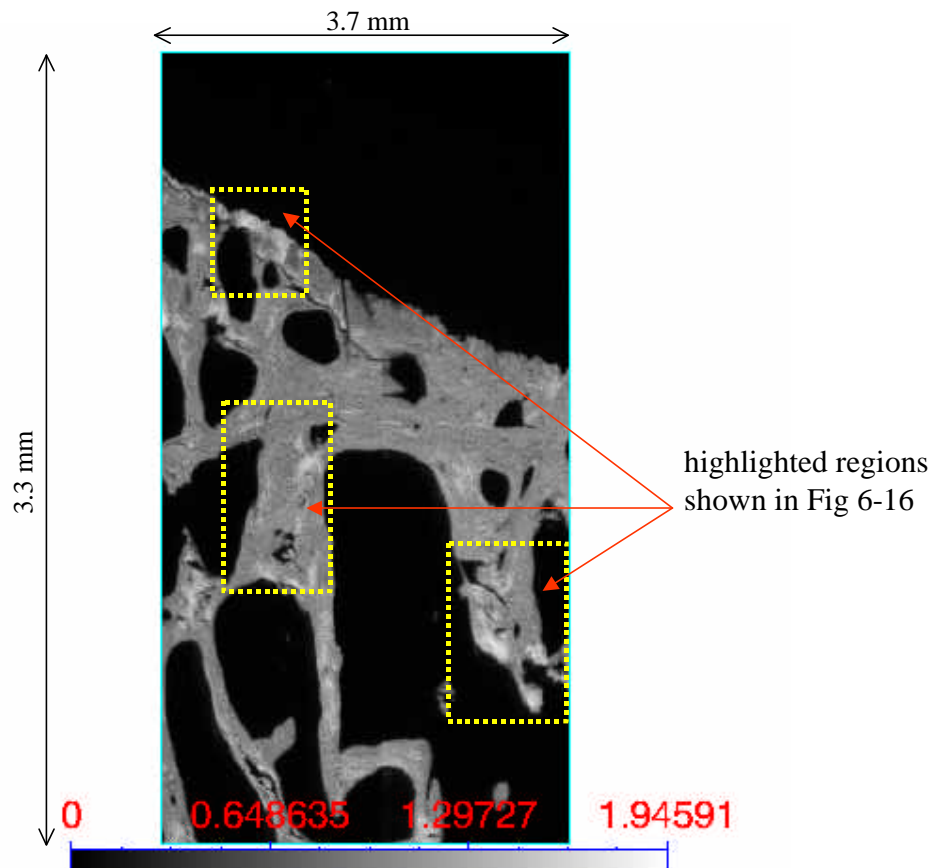


Figure 9-5: High resolution calcium fluorescence map of osteoarthritic monkey bone ( 10  $\mu\text{m}$  hor. X 5  $\mu\text{m}$  vert. resolution ). Counting time = 1 second/pixel. The three highlighted regions depict areas of high calcium concentration.

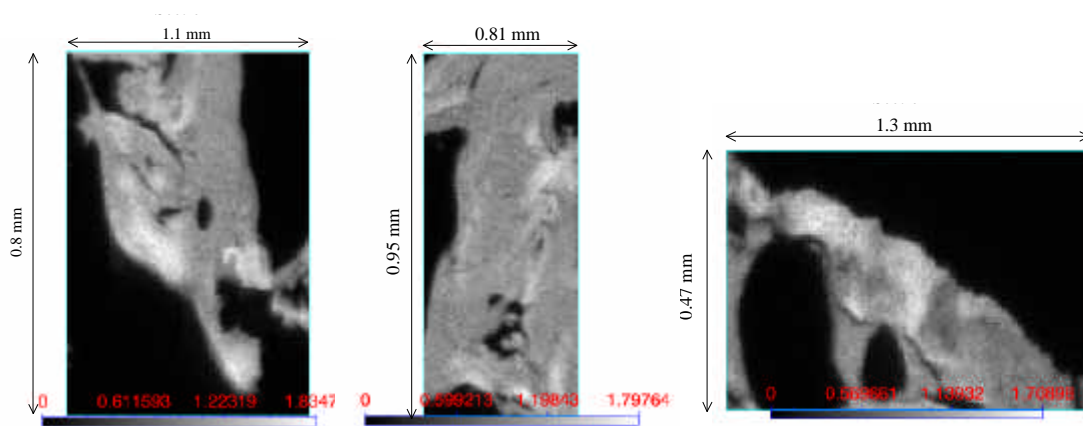


Figure 9-6: Magnified regions as highlighted in Figure 9-5.

The left-hand side map in Figure 9-6 is a section within the trabecular region of the monkey tibia and shows areas of high calcification. An osteon site is clearly visible and there are some micro-cracks. The central map in Figure 9-6 is also taken within the trabecular region and shows areas of elevated calcium concentration. The right-hand side map in Figure 9-6 is taken along the articular cartilage and also displays high calcification, and there are also a number of micro-cracks in this region. In addition, this elevated calcium concentration level could also indicate significant deposits of calcium-rich pyrophosphate that can be associated with osteoarthritis in this region.<sup>203</sup>

In general, it can be seen that osteoarthritic bone is much more non-uniform in calcium content when compared to the normal bone (Section 9.1). A further two high-resolution x-ray maps of the diseased joint were undertaken and shown in Figure 9-7. The right-hand side image was a particularly noteworthy region: The small holes which can be seen are probably small osteons which do not surround blood vessels, or ones which are being filled in by the osteoblasts. In particular, the interesting feature of this section is the very intense thin line of calcification, which runs between two osteon centres. After the x-ray calcium fluorescence map had been completed, the sample was removed from its holder, prior to an infrared study to map the mineral and protein composition of this section (Section 9.3). At the NSLS U10B infrared beamline, an optical investigation of the area revealed that a micro-crack had developed along this line of high calcification. Even though the sample had been handled with care, this

section must have been sufficiently brittle along this fault line for the micro-crack to develop.

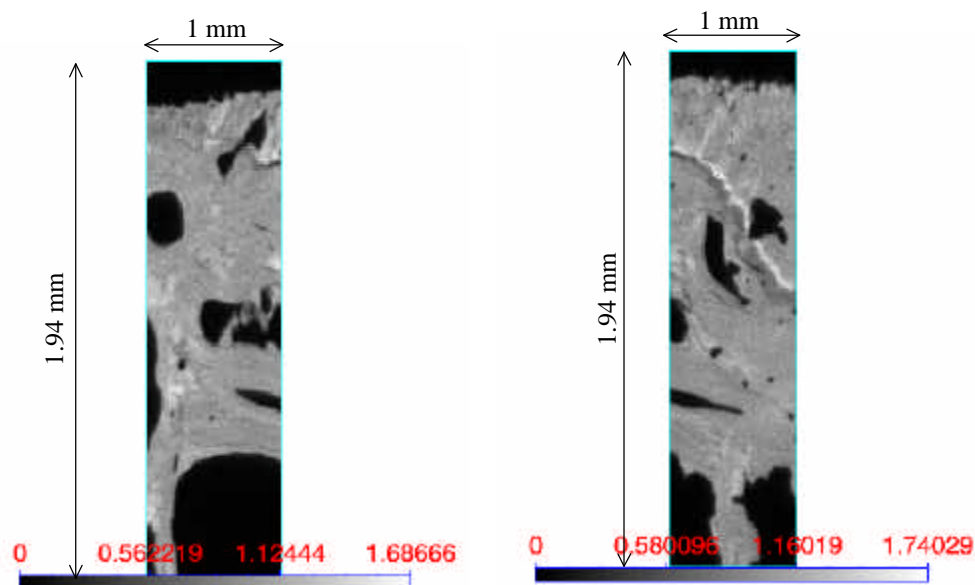


Figure 9-7: High resolution calcium fluorescence map of osteoarthritic monkey bone. (  $10\text{ }\mu\text{m}$  hor. X  $5\text{ }\mu\text{m}$  vert. resolution ). Counting time = 1 second/pixel.

### 9.3 Fourier transform infrared micro-spectroscopy

Infrared micro-spectroscopy can be used to study the protein and mineral contents of the sample. Measurements were performed using the FTIR microscope located at the U10B NSLS beamline. Regions corresponding to the calcium-mapped areas as taken from the x-ray fluorescence data were located using the optical microscope that was integrated into the FTIR equipment. The sample that was scanned was that taken from the normal bone section, part of which is shown in Figure 9-3. A scanning step size of  $50\text{ }\mu\text{m}$  x  $50\text{ }\mu\text{m}$  was used, and transmitted photons were detected using a copper-doped germanium detector. Using deconvolution techniques, carbonate/protein and phosphate/protein ratios maps were produced and are shown in Figure 9-8. In this example, the spatial resolution of the infrared maps was much lower than the x-ray fluorescence calcium maps due to longer integration times needed for IR imaging.<sup>199</sup> In the future, equal spatial resolutions will be used for both IR and x-ray imaging. Also, longer integration times will be needed to obtain a sufficient signal-to-background ratio

for accurate quantification. The important point to make clear is that the potential for correlating the x-ray fluorescence and infrared data is evident.

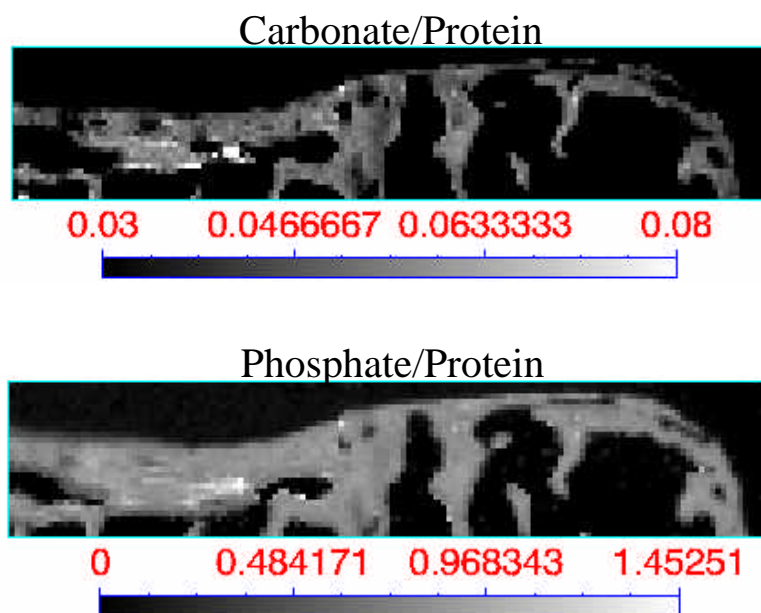


Figure 9-8: Carbonate/Protein and Phosphate/Protein ratios of the normal monkey bone as measured using infrared micro-spectroscopy in transmission at the NSLS UV ring. The numbers on the scale are those obtained through the analysis software using deconvolution techniques.

#### 9.4 Summary

The successful completion of the x-ray calcium mapping of bone had been undertaken on normal and diseased monkey tibia. The sensitivity of x-ray fluorescence imaging is evident,<sup>2</sup> and regions of high contrast are clearly visible in the diseased state. In the future, it would be beneficial to quantify the calcium concentration in these samples. Studies on the heavier elemental substitutions into the hydroxyapatite lattice, such as lead and strontium, are possible and fluorescence NEXAFS experiments could be performed to accurately determine the local environment.<sup>199</sup>

Due to the long counting times involved for the corresponding FTIR study, corresponding data sets at high spatial resolution have not yet been obtained. For comparative maps, using the infrared and x-ray microprobes, it is first necessary to perform the map in the x-ray region. Then, identification of regions of interest and subsequent transfer to the infrared microscope would take place to obtain the protein and mineral content. However, one-to-one correspondence between the x-ray and

infrared data is challenging as optical alignment does not have the mandatory accuracy. However, using reference markers on the sample e.g. an electron-beam burn or a point on the sample itself, would overcome part of the alignment difficulty. Furthermore, exact positioning should be possible if image processing techniques were used.

## Chapter 10 Micro-fluorescence investigation of the selective area growth process

The micro-electronics industry is driven to higher levels of device integration and miniaturisation by cost and increased speed and efficiency. Increased performance requires the development of new materials and processing techniques. X-ray micro-probes are uniquely suited for characterisation of many of these new devices, which are often reduced to sub-micron dimensions and/or buried deep inside materials. Improvements in the design of semiconductor devices relies largely on perfecting the control and growth of these materials. Opto-electronic device integration is one of the key elements in increased bandwidth and speed for telecommunications.

Metal-organic chemical vapour deposition (MOCVD) is currently the preferred choice for growing thin-film semiconductor devices.<sup>204-207</sup> MOCVD growth uses metal-organic precursor gases to deliver the semiconductor species to the substrate. By restricting the semiconductor materials to certain areas of the substrate, various parameters that are essential to the growth process can be varied. This is known as selective area growth (SAG).<sup>207,208</sup> To achieve SAG, a substrate is patterned with unreactive SiO<sub>2</sub> pads that defines the mask. As the metal-organic growth precursors fall on the substrate, they will not stick to the oxide surface, leading to local variations of the reactant concentrations. A schematic of the growth process is shown in Figure 10-1. For each element there is a length scale over which the local concentrations of the elements vary, i.e. an effective diffusion length. The patterning thus perturbs the local growth rate and composition of the semiconductor material. Hence in different regions on the substrate, there will be local variations in strain, thickness and band-gap of the semiconductor species.<sup>207,208</sup> A model for SAG has been developed based on prior descriptions of the growth process.<sup>207</sup> To substantiate the model, a test structure consisting of pairs of oxide pads of varying pad widths were studied.<sup>206</sup>



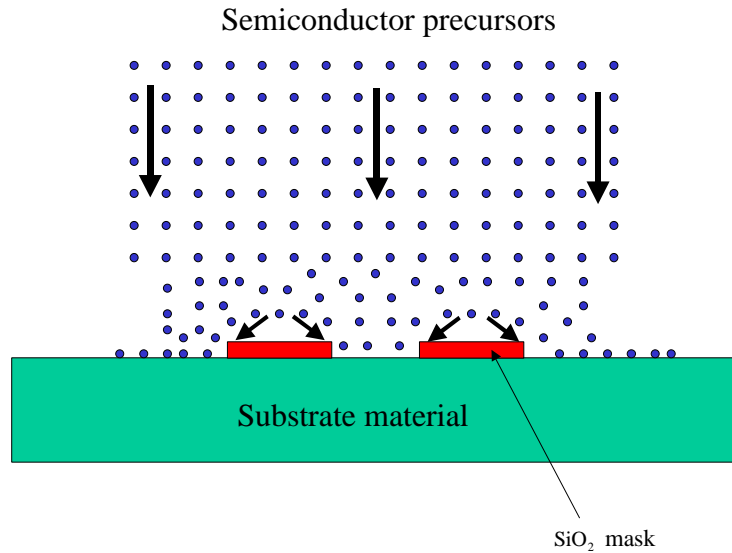


Figure 10-1: Schematic of selective area growth process.

### 10.1 X-ray micro-probe fluorescence investigation of InGaAsP quantum-wells

Selective area growth of quaternary InGaAsP alloys was accomplished by patterning an InP substrate with an oxide mask pattern, and then growing the semiconductor layer in an MOCVD reaction chamber. A schematic of the sample is shown in Figure 10-2. The test pattern comprised of various silicon-oxide pad geometries, and a section of the sample that consisted of seven quantum-well structures was examined. These structures consisted of a constant pad-spacing,  $g = 20\ \mu\text{m}$  and a variable pad width,  $w = 15\ \mu\text{m} \rightarrow 45\ \mu\text{m}$ .

By raster-scanning the sample through the X13B x-ray micro-focused beam, fluorescence intensity profiles of the semiconductor materials were collected in the vicinity of the masked areas. The fluorescence detector was an amptek XR-100CR energy-dispersive silicon pin-diode (active area  $\sim 7\ \text{mm}^2$ ) which was placed  $\sim 2\ \text{cm}$  from the sample surface and in approximately the same geometry as shown in Figure 9-2. The experiment was performed using 2.8 GeV operations, around the second harmonic of IVUN (Figure 3-11). The sample was orientated so that when scanned through the x-ray micro-beam, the vertical beam size was directed across the pad-gap. To compensate for decay of the electron beam current in the NSLS storage ring,

normalisation was performed by monitoring the flux through an ionisation chamber (Section 5.6).

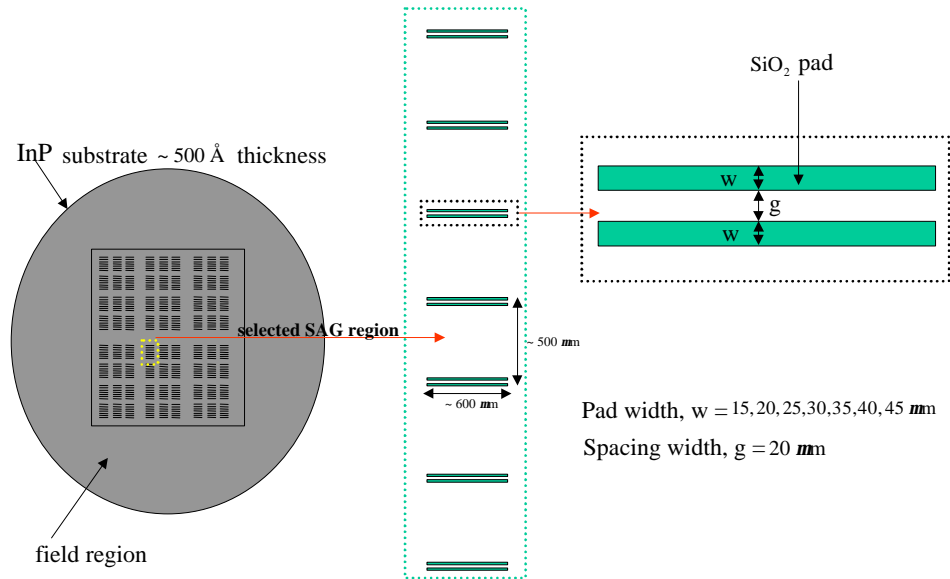


Figure 10-2: Schematic of InGaAsP quantum-well structures grown on a patterned InP substrate.

The gallium and arsenic K -edges, at  $\sim 10.37$  keV and  $12.5$  keV<sup>†</sup> were accessed by tuning the incident photon energy above these edges, and collecting the fluorescent photons with the amptek energy-dispersive detector. Energies corresponding to the  $K_{\alpha}$  lines were selected using a Nucleus PCA-II<sup>®</sup> multi-channel analyser. Counting times of 60 secs/pixel were used to obtain good photon counting statistics, and the sample was scanned in steps of  $< 4 \mu\text{m}$  across the pad-gap.

Figure 10-3 shows the fluorescence intensity for arsenic as a function of position across the masked region. The structure had been previously scanned in the horizontal direction so that the central part of the quantum-well was selected. The two strong dips in the signal correspond to the silicon-oxide pads and there is a clear arsenic increase (i.e. total mass) at the edges of these regions. A similar profile was obtained for gallium composition. The intersecting solid line of the arsenic fluorescence is the theoretical model for the growth process and agrees well with the experimental measurement. To retrieve the relative concentrations of the semiconductor materials, it is necessary to

<sup>†</sup> This energy is far from the undulator second harmonic (Figure 3-11). However, there was still sufficient flux to perform the experiment.

divide by the film thickness, which also varies near the pads. This thickness had been measured previously, using x-ray micro-diffraction techniques on the same sample.<sup>208</sup>

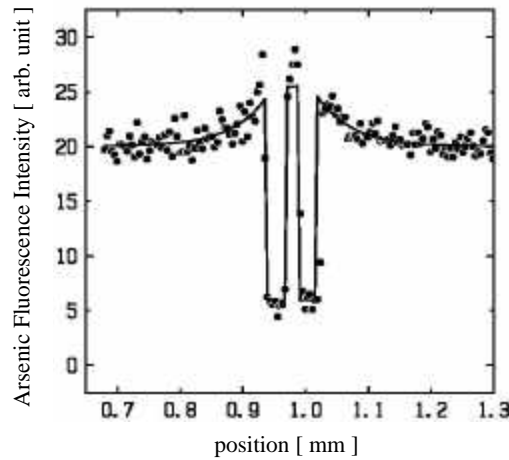


Figure 10-3: Arsenic fluorescence intensity across a silicon-dioxide pad.

By measuring the fluorescence intensity between each pad and knowledge of the film thickness, a plot of the gallium concentration is shown in Figure 10-4. Although the total amount of gallium increases between the silicon-oxide pads, the film thickness also increases, with the effect that the gallium concentration is less than that in the field region. A similar decrease was obtained for arsenic concentration. An increase of the indium and phosphor concentration would be expected, so as to balance the chemical formula  $\text{In}_{1-x}\text{Ga}_x\text{As}_{1-y}\text{P}_y$ . Such measurements were not performed using the current set up as phosphor fluorescence is too low in energy to measure in air, and therefore requires a vacuum environment, and the InP substrate may complicate interpretation around these edges.

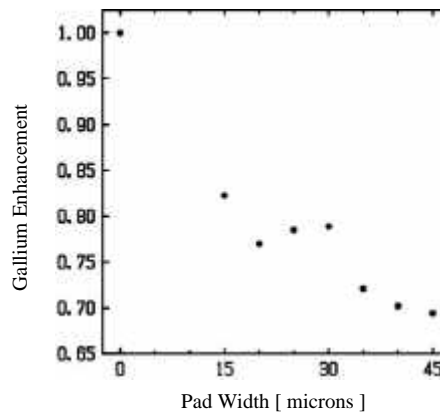


Figure 10-4: Gallium enhancement within an InGaAsP quantum-well, relative to the field region. A pad width of zero corresponds to a point far away from all pads, i.e. many effective diffusion lengths away.

## **10.2 Summary**

It has been demonstrated that the measurement of elemental concentrations within semiconductor thin-films is achievable using x-ray microprobe techniques. Gallium and arsenic concentrations have successfully been extracted in association with previous thickness measurements. These data provide essential information in the further development of theoretical models to describe the whole growth-process. Further investigation of the role of pad-shape and gap-width in growth perturbation are planned for the future.

## Chapter 11 Conclusion and Outlook

The motivation for this thesis was the design and implementation of differentially coated elliptical x-ray optics. There are many areas of research that can benefit from micro-focused x-ray beams, and some are discussed in Chapter 1. Spectroscopic measurements are ideally suited to these achromatic focusing optics, which generally offer larger collection apertures than the other micro-focusing elements that are currently available (Chapter 2). Differentially deposited mirrors are a significant improvement on traditional bendable optics, which are difficult to align, bulky and often do not perform to their design specifications. Using the SHADOW ray-tracing code, an x-ray micro-focusing end-station that was to be installed at the NSLS X13B beamline was successfully designed. The differential deposition profile was calculated using this ray-tracing code, and the overall performance of the system was assessed. Subsequently, the optics were installed at the beamline, and measurements confirmed that they performed to the high-standards necessary for x-ray micro-focusing research. The X13B micro-probe has enhanced the micro-focusing capabilities of the NSLS considerably by providing a focused spot size of  $\sim 3\text{ }\mu\text{m}$  in the vertical and  $\sim 9\text{ }\mu\text{m}$  in the horizontal directions. These dimensions are smaller than those originally estimated for these mirrors, and the low slope-error clearly provides the potential for delivering sub-micron focused beams in the future.

The diamond-anvil cell has enabled x-ray experiments to be performed on materials when they are subjected to extremely high pressures, and in addition, the beryllium gasket has made softer x-ray studies possible. High-pressure studies utilising the X13B micro-probe, and two extremely interesting materials were studied in this thesis:

X-ray transmission measurements on thallium-rhenium oxide directly revealed the pressure-induced electronic changes that occur in this material with applied pressure. EXAFS measurements were also performed on this compound, and the structural changes of the oxygen cage that surrounds the rhenium atom are clearly

shown. X-ray investigations on the high-pressure phase-transition in  $\text{TlREO}_4$  have provided essential information on the understanding of this material, and studies on similar  $\text{ABO}_4$  compounds are envisaged for the future.

In many cases, high-pressure x-ray absorption studies are not feasible in transmission mode due to the thickness and/or high-Z of the material. However, by collecting the fluorescence photons from thick concentrated samples in the back-scattering geometry, absorption coefficients can be successfully extracted. This unique measurement opens up many new areas of study within the field of high-pressure research. Using this technique, the decrease in the white-line intensity of praseodymium metal at the volume-collapse transition has been quantified. Several members of the lanthanide series possess this large volume-collapse at high-pressures, which is often attributed to the delocalisation of the  $4f$  electrons. The decrease in the white-line feature at the Pr  $L_3$  absorption-edge provided evidence for delocalised  $4f$  behaviour, and further studies using x-ray resonant Raman scattering with high-energy resolution are planned for the future to substantiate these results.

Micro-fluorescence x-ray mapping of the calcium content in diseased bone and the investigation of quantum-well structures are two areas where the X13B micro-probe optics are well suited. Measurements have been obtained in the calcium mapping of osteoarthritic bone and correlation with infrared data is conceivable. Further experiments are planned in the future to quantify calcium content and provide one-to-one correspondence with infrared data.

Several upgrades to the micro-probe design are envisaged: First, to increase the number of photons delivered to the sample, all air paths are to be replaced by vacuum or helium environments. This will improve the photon throughput of the system considerably, and especially at low x-ray photon energies. The building of a large area x-ray ring detector to capture back-scattered fluorescence photons during high-pressure studies is currently in progress. This will replace the amptek silicon-pin-photodiodes that were used throughout this thesis, and a hole in the centre will allow focused x-rays

to pass through before reaching the sample. The large collection angles that this detector will provide are clearly advantageous.

As discussed previously, there are very many areas of research which require intense x-ray micro-beams. With the advent of the X13B micro-probe, many exciting new research programs are envisaged, and the experimentalists who have started to benefit from its exceptional capabilities are impressed.

The future is bright for differentially-coated x-ray micro-focusing optics.

## Appendix A: List of abbreviations.

ALS	Advanced Light Source		IDP	Interplanetary Dust Particle
APS	Advanced Photon Source		IVUN	In-Vacuum Undulator
BFL	Bragg Fresnel Lens		KB	Kirkpatrick-Baez
CC	Computer Controlled		LINAC	Linear Accelerator
CHESS	Cornell High Energy Synchrotron Source		LTP	Long Trace Profiler
CRL	Compound Refractive Lens		MOCVD	Metal-Organic Chemical Vapour Deposition
DAC	Diamond-Anvil Cell		NEXAFS	Near Edge X-ray Absorption Fine Structure
EPW	Elliptically Polarised Wiggler		NSLS	National Synchrotron Light Source
ESRF	European Synchrotron Radiation Facility		RF	Radio Frequency
EXAFS	Extended X-ray Absorption Fine Structure		RMS	Root Mean Square
FPZP	Fresnel Phase Zone Plate		SAG	Selective Area Growth
FTIR	Fourier Transform Infra-Red		VUV	Vucuum Ultra Violet
FWHM	Full-Width at Half-Maximum		XANES	X-ray Absorption Near Edge Structure
FZP	Fresnel Zone Plate			



## Appendix B: List of frequently used symbols

### Optical Parameters:

$u$	source-optic distance
$v$	optic-image distance
$\theta$	angle subtended from source-optic
$\theta'$	angle subtended from image-optic
$\sigma$	source size
$\sigma_x, \sigma_z$	horizontal and vertical source size
$\sigma'$	image size
$\sigma'_x, \sigma'_z$	horizontal and vertical image size
$M$	demagnification
$M_x, M_z$	horizontal and vertical demagnification
$\theta_c$	critical angle
$\theta_i$	grazing incidence angle
$\sigma_{\text{rough}}$	RMS mirror roughness
$\sigma_{\text{slope}}$	RMS slope error

### Physical Constants:

$\tilde{n}$	refractive index
$\delta$	refractive index decrement
$\beta$	absorption index
$\mu$	absorption coefficient
$f_1, f_2$	atomic scattering factors

$e$	electronic charge, $1.60217733 \times 10^{-19}$ C
$m_e$	rest mass of electron, $9.1093898 \times 10^{-31}$ kg
$r_e$	classical electron radius, $2.817515 \times 10^{-15}$ m
$c$	speed of light in vacuum, $2.99792458 \times 10^8$ ms <sup>-1</sup>
$h$	Plank constant, $6.6260755 \times 10^{-34}$ Js
$N_A$	Avagadro's number, $6.02214199 \times 10^{23}$ mol <sup>-1</sup>

### Miscellaneous:

$E^*$	Electron beam energy
$E$	X-ray energy
$\lambda$	X-ray wavelength
$\chi$	EXAFS function
$k_e$	photoelectron wave-number

## Appendix C: SHADOW ray-tracing input parameters - X13B x-ray micro-probe design

Source Definition: ( Use make\_id module to create insertion device first ).

Source type	RAN/RAN	Depth	Off
Number of random rays	25000	Sigma x	0.000324
Emittance in x	$9.44 \times 10^{-8}$	Sigma z	$6.4 \times 10^{-6}$
Emittance in z	$1 \times 10^{-10}$	Angle Distribution	Synchro.
Polarisation Component	Total	Horizontal Divergence	$\pm 0.0001$
Spatial Type	Gaussian	Vertical Divergence	$\pm 0.0001$

Optical Configuration:

Mirror Parameters	Internal	
Figures	Elliptical	
Type Of Elements	Reflective	
Concave	Yes	
Cylindrical	Yes	
Incidence Angle	89.78	
Focii and Continuation Planes	Different	
Width (x)	0.005	
Length (y)	0.05	
	<u>Vertical Focusing Mirror</u>	<u>Horizontal Focusing Mirror</u>
Source Plane Distance	25.5 m	0.06 m
Image Plane Distance	0.06 m	0.28 m
Mirror Orientation Angle	0	90
Object Side Focal Distance	25.5 m	25.62 m
Image Side Focal Distance	0.40 m	0.28 m

## Appendix D: List of manufacturers - X13B x-ray micro-probe

Manufacturer	Equipment	Web Address
Newport Corporation	Mirror-Sample Positioning Stages and Controllers	<a href="http://www.newport.com">www.newport.com</a>
Beamline Technologies Corporation	Mirror Substrates and Coatings	<a href="http://www.beamline.com">www.beamline.com</a>
New Focus	Picomotors for Mirror Rotation	<a href="http://www.newfocus.com">www.newfocus.com</a>
Oriel Instruments	Stepper Mikes for Mirror Translation and camera stages	<a href="http://www.oriel.com">www.oriel.com</a>
Advanced Control Systems	Power supply and motor drivers	<a href="http://www.acsmotion.com">www.acsmotion.com</a>
Certified Scientific Software	Beamline Control Software	<a href="http://www.certif.com">www.certif.com</a>
Gateway Inc P5-166	Beamline Computer	<a href="http://www.gateway.com">www.gateway.com</a>
Bergher-Lahr	X13B Monochromator 5-phase driver	<a href="http://www.berger-lahr.de">www.berger-lahr.de</a>
Preciosa Crytur Ltd.	YAG:Ce scintillator crystals	<a href="http://www.crytur.cz">www.crytur.cz</a>
Edmund Scientific	CCD cameras,microscopes, mounts and monitors	<a href="http://www.edsci.com">www.edsci.com</a>
International Radiation Detectors Inc	silicon-pn-photodiode detector	<a href="http://www.ird-inc.com">www.ird-inc.com</a>
Amptek Inc.	Energy-dispersive silicon-pin-photodiode detectors	<a href="http://www.amptek.com">www.amptek.com</a>
*Out of production*-alternative PCA-III from Oxford Instruments	Vibration damped granite table – manufacturer not known. Dimensions of granite=3ftx3ftx1ft(thick)	
	Nucleus PCA-II Multi-channel Analyser®	
	Mirror Chambers	( In-house manufactured )
	Ionisation Chambers	( In-house manufactured )

## Bibliography

- <sup>1</sup>B.L. Henke, E.M. Gullikson, and J.C. Davis, "X-ray interactions: photoabsorption, scattering, transmission and reflection at E=50-30000 eV, Z=1-92," Atomic Data and Nuclear Data Tables 54 (2), 181-342 (1993).
- <sup>2</sup>C.J. Sparks, "X-Ray Fluorescence Microprobe for Chemical Analysis," in *Synchrotron Radiation Research*, edited by H. Winick and S. Doniach (Plenum Press, 1973), pp. 459-512.
- <sup>3</sup>B.E. Warren, *X-Ray Diffraction* (Dover Publications, New York, 1990).
- <sup>4</sup>P.-C. Wang, G.S. III Cargill, I.C. Noyan *et al.*, "Electromigration-induced stress in aluminum conductor lines measured by x-ray diffraction," Applied Physics Letters 72 (11), 1296-1298 (1998).
- <sup>5</sup>H.H. Solak, Y. Vladimirovsky, F. Cerrina *et al.*, "Measurement of strain in Al-Cu interconnect lines with x-ray microdiffraction," Journal Of Applied Physics 86 (2), 884-890 (1999).
- <sup>6</sup>X. Zhang, H. Solak, F. Cerrina *et al.*, "X-ray microdiffraction study of Cu interconnects," Applied Physics Letters 76 (3), 315-317 (2000).
- <sup>7</sup>I.C. Noyan, S.K. Kaldor, P.-C. Wang *et al.*, "A cost-effective method for minimising the sphere-of-confusion error of x-ray microdiffractometers," Review of Scientific Instruments 70 (2), 1300-1304 (1999).
- <sup>8</sup>S.-J. Chung and G.E. Ice, "Automated indexing for texture and strain measurement with broad-bandpass x-ray microbeams," Journal Of Applied Physics 85 (9), 5249-5255 (1999).
- <sup>9</sup>G.E. Ice, J.-S. Chung, and W. Lowe, "Small-displacement monochromator for microdiffraction experiments," Review of Scientific Instruments 71 (5), 2001-2006 (2000).
- <sup>10</sup>Apollo, P.Y. Wong, and P. Wiltzius, "Dynamic light scattering with a ccd camera," Review of Scientific Instruments 64 (9), 2547-2549 (1993).
- <sup>11</sup>J. Wang, A.K. Sood, P.V. Satyman *et al.*, "X-ray Fluorescence Correlation Spectroscopy: A method for studying particle dynamics in condensed matter," Physical Review Letters 80 (5), 1110-1113 (1998).
- <sup>12</sup>S.B. Dierker, R. Pindak, R.M. Fleming *et al.*, "X-Ray Photon Correlation Spectroscopy Study of Brownian Motion of Gold Colloids in Glycerol," Physical Review Letters 75 (3), 449-452 (1995).
- <sup>13</sup>Z.H. Cai, B. Lai, W.B. Yun *et al.*, "Observation of X-ray Speckle by Coherent Scattering at Grazing Incidence," Physical Review Letters 73 (1), 82-85 (1994).
- <sup>14</sup>S.R. Sutton, S. Bajt, J. Delaney *et al.*, "Synchrotron x-ray fluorescence microprobe: Quantification and mapping of mixed valence state samples using micro-XANES," Review of Scientific Instruments 66 (2), 1464-1467 (1995).
- <sup>15</sup>L.P. Keller, G.J. Flynn, J.P. Bradley *et al.*, "Synchrotron Measurements of Interplanetary Dust Particles," National Synchrotron Light Source News Letter (July), 8-10 (2000).
- <sup>16</sup>P. Strange, P.J. Durham, and B.L. Gyorffy, "Dichroic X-Ray Fluorescence," Physical Review Letters 67 (25), 3590-3593 (1991).
- <sup>17</sup>J. Pollmann, G. Srajer, J. Maser *et al.*, "Characterization of a microfocused circularly polarized x-ray probe," Review of Scientific Instruments 71 (6), 2386-2390 (2000).
- <sup>18</sup>G. Schmahl, P. Guttman, D. Raasch *et al.*, "Imaging of Magnetic Domains at BESSY," Synchrotron Radiation News 9 (6), 35-39 (1996).
- <sup>19</sup>T. Eimüller, R. Kalchauer, P. Fischer *et al.*, "Quantitative imaging of magnetization reversal in FeGd multilayers by magnetic transmission x-ray microscopy," Journal Of Applied Physics 87 (9), 6478-6480 (2000).
- <sup>20</sup>S. Lagomarsino, A. Cedola, P. Cloetens *et al.*, "Phase contrast hard x-ray microscopy with submicron resolution," Applied Physics Letters 71 (8) (1997).
- <sup>21</sup>A. Pogany, D. Gao, and S.W. Wilkins, "Contrast and resolution in imaging with a microfocus x-ray source," Review of Scientific Instruments 68 (7), 2774-2782 (1997).
- <sup>22</sup>Y. Moritomo, K. Hirota, H. Nakao *et al.*, "Pressure-induced insulator-metal transition in a bilayer manganite: Pressure control of orbital stability," Physical Review B 62 (1), 17-20 (2000).
- <sup>23</sup>M.P. Pasternak, R.D. Taylor, A. Chen *et al.*, "Pressure-induced metallization and the magnetic state in the antiferromagnetic insulator NiI<sub>2</sub>," Physical Review Letters 65 (6), 790-793 (1990).

- <sup>24</sup>M.M. Abd-Elmeguid and H. Micklitz, "Observation of a pressure-induced collapse of the Fe magnetic moment in the strong itinerant ferromagnet Fe<sub>72</sub>Pt<sub>28</sub>," *Physical Review B* 40 (10), 7395-7398 (1989).
- <sup>25</sup>J. Ye, Z. Zou, A. Matsushita *et al.*, "Unusually large T<sub>c</sub> enhancement in superconducting PrBa<sub>2</sub>Cu<sub>3</sub>O<sub>x</sub> under pressure," *Physical Review B* 58 (2), R619-R622 (1998).
- <sup>26</sup>X.J. Chen, C.D. Gong, and Y.B. Yu, "Pressure effect on T<sub>c</sub> for the rare-earth series R Ba<sub>2</sub>Cu<sub>3</sub>O<sub>7-d</sub>," *Physical Review B* 61 (5), 3691-3698 (2000).
- <sup>27</sup>G. Serghiou, G. Miehe, O. Tschauner *et al.*, "Synthesis of a cubic Ge<sub>3</sub>N<sub>4</sub> phase at high pressures and temperatures," *Journal of Chemical Physics* 111 (10), 4659-4662 (1999).
- <sup>28</sup>A.E. Carlsson and N.W. Ashcroft, "Approaches for reducing the insulator-metal transition pressure in hydrogen," *Physical Review Letters* 50 (17), 1305-1308 (1983).
- <sup>29</sup>W.J. Nellis, "Making metallic hydrogen," *Scientific American*, 84-90 May (2000).
- <sup>30</sup>P. Dhez, P. Chevallier, T.B. Lucatorto *et al.*, "Instrumental aspects of x-ray microbeams in the range above 1 keV," *Review of Scientific Instruments* 70 (4), 1907-1920 (1999).
- <sup>31</sup>G.E. Ice, "Microbeam-Forming Methods for Synchrotron Radiation," *X-Ray Spectrometry* 26, 315-326 (1997).
- <sup>32</sup>H.A. Padmore, G. Ackerman, R. Celestre *et al.*, "Sub-micron white-beam focusing using elliptically bent mirrors," *Synchrotron Radiation News* 10 (6), 18-26 (1997).
- <sup>33</sup>J. Hrdý, "A double-crystal x-ray monochromator in antiparallel position with a sagittally bent crystal," *Review of Scientific Instruments* 64 (8), 2207-2210 (1993).
- <sup>34</sup>G.M. Lamble and S.M. Heald, "Operation of a dynamically bent sagittally focusing double crystal monochromator for XAFS studies," *Review of Scientific Instruments* 63 (1), 880-884 (1992).
- <sup>35</sup>C. Schulze, U. Lienert, M. Hanfland *et al.*, "Microfocusing of Hard X-Rays with Cylindrically Bent Crystal Monochromators," *Journal of Synchrotron Radiation* 5, 77-81 (1997).
- <sup>36</sup>J. Pellicer-Porres, A. San Miguel, and A. Fontaine, "High-Focusing Bragg-Crystal Polychromator Design for Energy-Dispersive X-ray Absorption Spectroscopy," *Journal of Synchrotron Radiation* 5, 1250-1257 (1998).
- <sup>37</sup>P. Kirkpatrick and A.V. Baez, "Formation of Optical Images by X-Rays," *Journal of The Optical Society of America* 38 (9), 766-774 (1948).
- <sup>38</sup>M.R. Howells, D. Cambie, R.M. Duarte *et al.*, "Theory and Practice of elliptically bent x-ray mirrors," *Optical Engineering* 39 (10), 2748-2761 (2000).
- <sup>39</sup>H.A. Padmore, M.R. Howells, S. Irick *et al.*, "Some new Schemes For Producing High-Accuracy Elliptical X-Ray Mirrors by Elastic Bending," presented at the Optics For High Brightness Synchrotron Radiation Beamlines II, Denver, 1996 (unpublished).
- <sup>40</sup>B.X. Yang, M. Rivers, W. Schildkamp *et al.*, "GeoCARS microfocusing Kirkpatrick-Baez mirror bender development," *Review of Scientific Instruments* 66 (2), 2278-280 (1995).
- <sup>41</sup>Ch. Morawe, P. Pecci, J. Ch. Peffen *et al.*, "Design and performance of graded multilayers as focusing elements for x-ray optics," *Review of Scientific Instruments* 70 (8), 3227-3232 (1999).
- <sup>42</sup>G.E. Ice, J-S. Chung, and J.Z. Tischler, "Elliptical x-ray microprobe mirrors by differential deposition," *Review of Scientific Instruments* 71 (7), 2635-2639 (2000).
- <sup>43</sup>A.G. Michette and C.J. Buckley, *X-Ray Science And Technology* (Institute of Physics Publishing, 1993).
- <sup>44</sup>W.B. Yun, P.J. Viccaro, B. Lai *et al.*, "Coherent hard x-ray focusing optics and applications," *Review of Scientific Instruments* 63 (1), 582-585 (1992).
- <sup>45</sup>J. Kirz, "Phase Zone Plates for X-rays and the Extreme UV," *Journal of The Optical Society of America* 64 (301) (1974).
- <sup>46</sup>B. Lai, W.B. Yun, D. Legnini *et al.*, "Hard x-ray phase zone plate fabricated by lithographic techniques," *Applied Physics Letters* 61 (16), 1877-1879 (1992).
- <sup>47</sup>W. Yun, B. Lai, A.A. Krasnoperova *et al.*, "Development of zone plates with a blazed profile for hard x-ray applications," *Review of Scientific Instruments* 70 (9), 3537-3541 (1999).
- <sup>48</sup>R. Medenwaldt, J. Abraham-peskir, and E. Uggerhøj, "X-ray Microscopy in Aarhus with 30nm resolution," *Synchrotron Radiation News* 11 (4), 38-41 (1998).

- 49 S.J. Spector, C.J. Jacobsen, and D.M. Tennant, "Process optimization for production of sub-20 nm soft x-ray zone plates," *Journal of Vacuum and Scientific Technology B* 15 (6), 2872-2876 (1997).
- 50 E. Di Fabrizio, M. Gentili, M. Kiskinova *et al.*, "Recent Developments and Applications of Microfocus X-ray Zone Plates," *Synchrotron Radiation News* 12 (1), 37-46 (1999).
- 51 N. Kamijo, S. Tamura, Y. Suzuki *et al.*, "Fabrication of a hard x-ray sputtered-sliced Fresnel phase zone plate," *Review of Scientific Instruments* 68 (1), 14-16 (1997).
- 52 B. Lai, W. Yun, Y. Xiao *et al.*, "Development of a hard x-ray imaging microscope," *Review of Scientific Instruments* 66 (2), 2287-2289 (1995).
- 53 W. Yun, B. Lai, Z. Cai *et al.*, "Nanometer focusing of hard x rays by phase zone plates," *Review of Scientific Instruments* 70 (5), 2238-2241 (1999).
- 54 V.V. Aristov, A.A. Snigirev, Y.A. Basov *et al.*, presented at the AIP Conference Proc., 1986 (unpublished).
- 55 V.V. Aristov, Y.A. Basov, G.N. Kulipanov *et al.*, "Focusing Properties of a Bragg-Fresnel Lens in the White Spectrum of Synchrotron Radiation," *Nuclear Instruments & Methods in Physics Research A* 274, 390-393 (1989).
- 56 V.V. Aristov, Y.A. Basov, A.A. Snigirev *et al.*, "Optical Properties of a phase linear Bragg-Fresnel lens," *Nuclear Instruments & Methods in Physics Research A* 308, 413-415 (1991).
- 57 U. Bonse, C. Riekel, and A.A. Snigirev, "Kirkpatrick-Baez microprobe on the basis of two linear single crystal Bragg-Fresnel lenses," *Review of Scientific Instruments* 63 (1), 622-624 (1992).
- 58 Y.A. Basov, T.L. Pravdivtseva, A.A. Snigirev *et al.*, "Two-dimensional focusing of hard X-rays by a phase circular Bragg-Fresnel lens in the case of Bragg backscattering," *Nuclear Instruments & Methods in Physics Research A* 308, 363-366 (1991).
- 59 A. Snigirev, "The recent development of Bragg-Fresnel crystal optics. Experiments and applications at the ESRF ( invited )," *Review of Scientific Instruments* 66 (2), 2053-2058 (1995).
- 60 A. Snigirev, I. Snigireva, P. Engström *et al.*, "Testing of submicrometer fluorescence microprobe based on Bragg-Fresnel crystal optics at the ESRF," *Review of Scientific Instruments* 66 (2), 1461-1463 (1995).
- 61 V.A. Sharov, Q.-F. Xiao, I.Y. Ponomarev *et al.*, "Cold neutron microprobe for materials analysis using tapered capillary optics," *Review of Scientific Instruments* 71 (9), 3247-3253 (2000).
- 62 E.A. Stern, Z. Kalman, A. Lewis *et al.*, "Simple method for focusing x rays using tapered capillaries," *Applied Optics* 27 (24), 5135-5139 (1988).
- 63 D.H. Bilderback and D.J. Thiel, "Microbeam generation with capillary optics (invited)," *Review of Scientific Instruments* 66 (2), 2059-2063 (1995).
- 64 A. Attalmanan, P. Voglis, A. Rindby *et al.*, "Improved capillary optics applied to microbeam x-ray fluorescence: Resolution and sensitivity," *Review of Scientific Instruments* 66 (1), 24-27 (1995).
- 65 D.J. Thiel, D.H. Bilderback, A. Lewis *et al.*, "Submicron concentration and confinement of hard X-rays," *Nuclear Instruments & Methods in Physics Research A* 317, 597-600 (1992).
- 66 D.H. Bilderback, S.A. Hoffman, and D.J. Thiel, "Nanometer Spatial Resolution Achieved in Hard X-ray Imaging and Laue Diffraction Experiments," *Science* 263, 201-203 (1994).
- 67 I.C. Noyan, P.-C. Wang, S.K. Kaldor *et al.*, "Divergence effects in monochromatic x-ray microdiffraction using tapered capillary optics," *Review of Scientific Instruments* 71 (5), 1991-2000 (2000).
- 68 Y.P. Feng, S.K. Sinha, E.E. Fullerton *et al.*, "X-ray Fraunhofer diffraction patterns from a thin-film waveguide," *Applied Physics Letters* 67 (24), 3647-3649 (1995).
- 69 Y.P. Feng, S.K. Sinha, H.W. Deckman *et al.*, "X-Ray Flux Enhancement in Thin-Film Waveguides Using Resonant Beam Couplers," *Physical Review Letters* 71 (4), 537-540 (1993).
- 70 W. Jark, S. Di Fonzo, S. Lagomarsino *et al.*, "Properties of a submicrometer x-ray beam at the exit of a waveguide," *Journal Of Applied Physics* 80 (9), 4831-4836 (1996).
- 71 Y.P. Feng, H.W. Deckman, and S.K. Sinha, "Mode-mixing in an x-ray thin-film waveguide.," *Applied Physics Letters* 64 (7), 930-933 (1994).
- 72 A. Cedola, S. Lagomarsino, S. Di Fonzo *et al.*, "Submicrometre Beams from a Hard X-ray Waveguide at a Third-Generation Synchrotron Radiation Source," *Journal of Synchrotron Radiation* 5 (1), 17-22 (1998).

- <sup>73</sup>M. Montagna, M. Ferrari, F. Rossi *et al.*, “Brillouin scattering in planar waveguides,” *Physical Review B* 58 (2), 547-550 (1998).
- <sup>74</sup>L. Dobrzynski, A. Akjouj, B. Djafari-Rouhani *et al.*, “Giant gaps in photonic band structures,” *Physical Review B* 57 (16), 9388-9391 (1998).
- <sup>75</sup>R.E. De Wames and S.K. Sinha, “Possibility of Guided-Neutron-Wave Propagation in Thin Films,” *Physical Review B* 7 (3), 917-921 (1973).
- <sup>76</sup>R. Gähler, J. Kalus, and W. Mampe, “An optical instrument for the search of a neutron charge,” *Journal of Physics E* 13, 546-548 (1980).
- <sup>77</sup>A. Snigirev, V. Kohn, I. Snigireva *et al.*, “A compound refractive lens for focusing high-energy X-rays,” *Nature* 384, 49-51 (1996).
- <sup>78</sup>B. Lengeler, J. Tümmler, A. Snigirev *et al.*, “Transmission and gain of singly and doubly focusing refractive x-ray lenses,” *Journal Of Applied Physics* 84 (11), 5855-5861 (1998).
- <sup>79</sup>J.T. Cremer, M.A. Piestrup, H.R. Beguiristain *et al.*, “Cylindrical compound refractive x-ray lenses using plastic substrates,” *Review of Scientific Instruments* 70 (9), 3545-3548 (1999).
- <sup>80</sup>A. Snigirev, V. Kohn, I. Snigireva *et al.*, “Focusing high-energy x-rays by compound refractive lenses,” *Applied Optics* 37 (4), 653-662 (1998).
- <sup>81</sup>P. Elleaume, “Two-Plane Focusing of 30 keV Undulator Radiation,” *Journal of Synchrotron Radiation* 5 (1), 1-5 (1998).
- <sup>82</sup>B. Lengeler, C.G. Schroer, M. Richwin *et al.*, “A microscope for hard x rays based on parabolic refractive lenses,” *Applied Physics Letters* 74 (26), 3924-3926 (1999).
- <sup>83</sup>B. Lengeler, C. Schroer, J. Tümmler *et al.*, “Imaging by parabolic refractive lenses in the hard X-ray range,” *Journal of Synchrotron Radiation* 6, 1153-1167 (1999).
- <sup>84</sup>M. Sanchez del Rio and R.J. Dejus, “XOP: Recent Developments,” *SPIE* 3448, 340-345 (1998).
- <sup>85</sup>A. Thompson, *X-ray Data Booklet* (Lawrence Berkeley Laboratory, 2001).
- <sup>86</sup>H.R. Beguiristain . Personal Communication. (2000)
- <sup>87</sup>A.Q.R. Baron, Y. Kohmura, Y. Ohishi *et al.*, “A refractive collimator for synchrotron radiation,” *Applied Physics Letters* 74 (10), 1492-1494 (1999).
- <sup>88</sup>A.I. Chumakov, R. Rüffer, O. Leupold *et al.*, “High-energy-resolution x-ray optics with refractive collimators,” *Applied Physics Letters* 77 (1), 31-33 (2000).
- <sup>89</sup>A.Q.R. Baron, Y. Kohmura, V.V. Krishnamurthy *et al.*, “Beryllium and aluminium refractive collimators for synchrotron radiation,” *Journal of Synchrotron Radiation* 6, 953-956 (1999).
- <sup>90</sup>B. Cederström, R.N. Cahn, M. Danielsson *et al.*, “Focusing hard X-rays with old LPs,” *Nature* 404, 951 (2000).
- <sup>91</sup>G. Margaritondo, *Introduction to Synchrotron Radiation* (Oxford University Press, 1988).
- <sup>92</sup>F. Wuilleumier and Y. Farge, *Synchrotron Radiation Instrumentation And New Developments* (North-Holland Publishing Company, 1978).
- <sup>93</sup>F.R. Elder, A.M. Gurewitsch, R.V. Langmuir *et al.*, “Radiation from electrons in a synchrotron,” *Physics Review* 71 (11), 829-830 (1947).
- <sup>94</sup>G.K. Green, “Spectra and Optics of Synchrotron Radiation; in: Proposal for National Synchrotron Light Source, Brookhaven National Laboratory, Upton, New York,” Brookhaven National Laboratory Report BNL-50595 (1977).
- <sup>95</sup>P.M. Stefan, “In-Vacuum Undulator Commissioned in the NSLS X-ray Ring,” *Synchrotron Radiation News* 11 (1), 22-24 (1998).
- <sup>96</sup>P.M. Stefan, S. Krinsky, G. Rakowsky *et al.*, “Small-gap undulator research at the NSLS: concepts and results,” *Nuclear Instruments & Methods in Physics Research A* (412), 161-173 (1998).
- <sup>97</sup>A. Friedman, X. Zhang, S. Krinsky *et al.*, “Polarized Wiggler for NSLS X-ray Ring,” Brookhaven National Laboratory Report (BNL-49175) (1993).
- <sup>98</sup>A. Friedman, S. Krinsky, and E. Blum, “Polarized Wiggler for NSLS X-ray Ring Design Consideration,” Brookhaven National Laboratory Report (BNL-47317) (1992).

- <sup>99</sup>S. Krinsky and C.C. Kao, "Time Varying Elliptically Polarized Wiggler at the NSLS," *Synchrotron Radiation News* 8 (5), 38-39 (1995).
- <sup>100</sup>K.J. Randall, Z. Xu, E. Gluskin *et al.*, "Characterization of a Novel Elliptically Polarized Wiggler," Brookhaven National Laboratory Report (BNL-65091) (1998).
- <sup>101</sup>P. Gürtler, "Installation and Test of a Multipole Wiggler in DORIS II," *Nuclear Instruments & Methods in Physics Research A* 246, 91-93 (1986).
- <sup>102</sup>C. Welnak, P. Anderson, M. Khan *et al.*, "Recent developments in SHADOW," *Review of Scientific Instruments* 63 (1), 865-868 (1992).
- <sup>103</sup>R.P. Walker and B. Diviacco, "URGENT- A computer program for calculating undulator radiation spectral, angular, polarization, and power density properties," *Review of Scientific Instruments* 63 (1), 392-395 (1992).
- <sup>104</sup>S. Sugiyama, H. Ohgaki, T. Mikado *et al.*, "Design and manufacture of a 10-T superconducting wiggler magnet at TERAS," *Review of Scientific Instruments* 66 (2), 1960-1963 (1995).
- <sup>105</sup>Z. Xu, I. McNulty, K.J. Randall *et al.*, "X13A: A versatile soft x-ray undulator beamline," *Review of Scientific Instruments* 66 (2), 1827-1829 (1995).
- <sup>106</sup>P. Loeffen, J.M. Tingay, T.M. Gill *et al.*, "Commercial developments in synchrotron optical components: A novel coolant for high heat load optics," presented at the Crystal and Multilayer Optics, San Diego, California, 1998 (unpublished).
- <sup>107</sup>C.S. Rogers and L. Assoufid, "Design and thermal stress analysis of high-power x-ray monochromators cooled with liquid nitrogen," *Review of Scientific Instruments* 66 (2), 2200-2202 (1995).
- <sup>108</sup>M. Deutsch and M. Hart, "Noninterferometric measurement of the x-ray refractive index of beryllium," *Physical Review B* 30 (2), 643-646 (1984).
- <sup>109</sup>M. Sánchez del Río and A. Marcelli, "Waviness effects in ray-tracing of "real" optical surfaces," *Nuclear Instruments & Methods in Physics Research A* (319), 170-177 (1992).
- <sup>110</sup>S.C. Irick, W.R. McKinney, D.L.J. Lunt *et al.*, "Using a straightness reference in obtaining more accurate surface profiles from a long trace profiler," *Review of Scientific Instruments* 63 (1), 1436-1438 (1992).
- <sup>111</sup>C. Bresloff and D.M. Mills, "The Advanced Photon Source Metrology Laboratory," *Review of Scientific Instruments* 67 (9), 3369 (1996).
- <sup>112</sup>P.Z. Takacs, E.L. Church, C.J. Bresloff *et al.*, "Improvements in the accuracy and the repeatability of long trace profiler measurements," *Applied Optics* 38 (25), 5468-5479 (1999).
- <sup>113</sup>E. Johnson, "One view of the NSLS from the perspective of SRI 2000," *NSLS newsletter* , 8 (2000).
- <sup>114</sup>J.S. Schilling and R.N. Shelton, *Physics of Solids Under High Pressure* (North-Holland Publishing Company, 1981).
- <sup>115</sup>R. Ingalls, G.A. Garcia, and E.A. Stern, "X-Ray absorption at High Pressure," *Physical Review Letters* 40 (5), 334-336 (1978).
- <sup>116</sup>D. Greenberg, "Mimicking Conditions at the Center of the Earth," *Brookhaven National Laboratory Bulletin* (Januray 2001).
- <sup>117</sup>H.K. Mao and P.M. Bell, "Absolute pressure measurements and analysis of diamond subjected to maximum static pressures of 1.3-1.7 Mbar," *Review of Scientific Instruments* 50 (8), 1002-1009 (1979).
- <sup>118</sup>H.K. Mao and P. M. Bell, "High-Pressure Physics: Sustained Static generation of 1.36 to 1.72 Megabars," *Science* 200 (9), 1145-1147 (1978).
- <sup>119</sup>K.A. Goettel, H.K. Mao, and P.M. Bell, "Generation of static pressures above 2.5 megabars in a diamond-anvil pressure cell," *Review of Scientific Instruments* 56 (7), 1420-1427 (1985).
- <sup>120</sup>K. Brister, "X-ray diffraction and absorption at extreme pressures," *Review of Scientific Instruments* 68 (4), 1629-1647 (1997).
- <sup>121</sup>W.C. Moss, J.O. Hallquist, R. Reichlin *et al.*, "Finite element analysis of the diamond anvil cell: Achieving 4.6 Mbar," *Applied Physics Letters* 48 (19), 1258-1260 (1986).
- <sup>122</sup>D. Andrault and G. Fiquet, "Synchrotron radiation and laser heating in a diamond anvil cell," *Review of Scientific Instruments* 72 (2), 1283-1297 (2001).



- 123G. Shen, M.L. Rivers, Y. Wang *et al.*, "Laser heated diamond cell system at the Advanced Photon Source for in situ x-ray measurements at high pressure and temperature," *Review of Scientific Instruments* 72 (2), 1273-1282 (2001).
- 124W. Bassett, "The birth and development of laser heating in diamond anvil cells," *Review of Scientific Instruments* 72 (2), 1270-1272 (2001).
- 125D.L. Heinz, J.S. Sweeney, and P. Miller, "A laser heating system that stabilizes and controls the temperature: Diamond anvil cell applications," *Review of Scientific Instruments* 62 (6), 1568-1575 (1991).
- 126T. Yagi, T. Kondo, T. Watanuki *et al.*, "Laser heated diamond anvil apparatus at the Photon Factory and SPring-8: Problems and improvements," *Review of Scientific Instruments* 72 (2), 1293-1297 (2001).
- 127N.W.A. van Uden and D.J. Dunstan, "Zen diamond-anvil low-pressure cell," *Review of Scientific Instruments* 71 (11), 4174-4176 (2000).
- 128G.J. Piermarini and S. Block, "Ultrahigh pressure diamond-anvil cell and several semiconductor phase transition pressures in relation to the fixed point pressure scale," *Review of Scientific Instruments* 46 (8), 973-979 (1975).
- 129C-M. Sung, C. Goetze, and H.-K. Mao, "Pressure Distribution in the diamond anvil press and the shear strength of fayalite," *Review of Scientific Instruments* 48 (11), 1386-1391 (1977).
- 130J.D. Barnett, S. Block, and G.J. Piermrini, "An Optical Fluorescence System for Quantitative Pressure Measurement in the Diamond-Anvil Cell," *Review of Scientific Instruments* 44 (1), 1-9 (1973).
- 131J.S. Schilling and R.N. Shelton, *Physics of Solids Under High Pressure* (North-Holland Publishing Company, 1981).
- 132H. Launois, M. Rawiso, E. Holland-Moritz *et al.*, "X-Ray Absorption Study of Mixed-Valence TmSe," *Physical Review Letters* 44 (19), 1271-1278 (1980).
- 133U. Staub, L. Soderholm, S.R. Wasserman *et al.*, "Valence determination as a function of doping in PrBa<sub>2</sub>Cu<sub>3</sub>O<sub>7</sub>," *Physical Review B* 61 (2), 1548-1554 (2000).
- 134J.J. Rehr, R.C. Albers, and S.I. Zabinsky, "High-order multiple-scattering calculations of X-ray-absorption fine structure," *Physical Review Letters* 69 (23), 3397-3400 (1992).
- 135J.J. Rehr and R.C. albers, "Theoretical approaches to x-ray absorption fine structure," *Reviews of Modern Physics* 72 (3), 621-652 (2000).
- 136E.A. Stern, "Theory of the extended x-ray absorption fine structure," *Physical Review B* 10 (8), 3027-3037 (1974).
- 137F.W. Lytle, D.E. Sayers, and E.A Stern, "Extended x-ray-absorption fine-structure technique. II. Experimental practice and selected results," *Physical Review B* 11 (12), 4825-4835 (1975).
- 138E.A. Stern, D.E. Sayers, and F.W. Lytle, "Extended x-ray-absorption fine-structure technique. III. Determination of physical parameters," *Physical Review B* 11 (12), 4836-4846 (1975).
- 139D.E. Sayers and E.A. Stern, "New Technique for Investigating Noncrystalline Structures: Fourier Analysis of the Extended X-Ray-Absorption Fine Structure," *Physical Review Letters* 27 (18), 1204-1207 (1971).
- 140G.G. Li, F. Bridges, and C.H. Booth, "X-ray-absorption fine-structure standards: A comparison of experiment and theory," *Physical Review B* 52 (9), 6332-6348 (1995).
- 141B. Houser and R. Ingalls, "X-ray-absorption fine structure determination of pressure-induced bond-angle changes in ReO<sub>3</sub>," *Physical Review B* 61 (10), 6515-6520 (2000).
- 142J. Jaklevic, J.A. Kirby, M.P. Klein *et al.*, "Fluorescence Detection of EXAFS: Sensitivity Enhancement for Dilute Species and Thin Films," *Solid State Communications* 23, 679-682 (1977).
- 143S. Hayakawa, Y. Goshi, A. Iida *et al.*, "Fluorescence x-ray absorption fine structure measurements using a synchrotron radiation x-ray microprobe," *Review of Scientific Instruments* 62 (11), 2545-2549 (1991).
- 144D.M. Pease, D.L. Brews, Z. Tan *et al.*, "Accurate X-Ray Absorption Spectra Obtained From Concentrated Bulk Samples By Fluorescence Detection," *Physics Letters A* 138 (4,5), 230-234 (1989).
- 145S. Eisebitt, T. Böske, J.-E. Rubensson *et al.*, "Determination of absorption coefficients for concentrated samples by fluorescence detection," *Physical Review B* 47 (21), 14103-14109 (1993).
- 146L. Tröger, D. Arvanitis, K. Baberschke *et al.*, "Full correction of the self-absorption in soft-fluorescence extended x-ray-absorption fine structure," *Physical Review B* 46 (6), 3283-3289 (1992).

- 147P. Pfalzer, J.-P. Urbach, M. Klemm *et al.*, "Elimination of self-absorption in fluorescence hard x-ray absorption spectra," *Physical Review B* 60 (13), 9335-9339 (1999).
- 148M.O. Krause, "Atomic Radiative and Radiationless Yields for K and L Shells," *Journal of Physics and Chemistry Reference Data* 8 (2), 307-322 (1979).
- 149J.A. Victoreen, "The calculation of X-Ray Mass absorption Coefficients," *Journal Of Applied Physics* 20, 1141-1147 (1949).
- 150O. Fukunaga and S. Yamaoka, "Phase Transformations in  $\text{ABO}_4$  Type Compounds Under High Pressure," *Physics And Chemistry Of Minerals* 5, 167-177 (1979).
- 151Y. Abraham, N. A. Holzwarth, and R. T. Williams, "Electronic structure and optical properties of  $\text{CdMoO}_4$  and  $\text{CdWO}_4$ ," *Physical Review B* 62 (3), 1733-1741 (2000).
- 152M. Itoh and M. Fujita, "Optical properties of scheelite and raspite  $\text{PbWO}_4$  crystals," *Physical Review B* 62 (19), 12825-12830 (2000).
- 153A. Jayaraman, B. Batlogg, and L.G. VanUitert, "Effect of high pressure on the Raman and electronic absorption spectra of  $\text{PbMoO}_4$  and  $\text{PbWO}_4$ ," *Physical Review B* 31 (8), 5423-5427 (1985).
- 154J.M. Moreau, Ph. Galez, J.P. Peigneux *et al.*, "Structural characterization of  $\text{PbWO}_4$  and related new phase  $\text{Pb}_7\text{W}_8\text{O}_{(32-x)}$ ," *Journal of Alloys and Compounds* 238, 46-48 (1996).
- 155J.M. Moreau, R.E. Gladyshevskii, Ph. Galez *et al.*, "A new structural model for Pb-deficient  $\text{PbWO}_4$ ," *Journal of Alloys and Compounds* 284, 104-107 (1999).
- 156Y. Zhang, A.W. Holzwarth, and R.T. Williams, "Electronic band structures of the scheelite materials  $\text{CaMoO}_4$ ,  $\text{CaWO}_4$ ,  $\text{PbMoO}_4$  and  $\text{PbWO}_4$ ," *Physical Review B* 57 (20), 12738-12750 (1998).
- 157N.W. Ashcroft and N.D. Mermin, *Solid State Physics* (Saunders College Publishing, 1976).
- 158N. Chandrabhas and A.K. Sood, "Raman study of pressure-induced phase transitions in  $\text{RbIO}_4$ ," *Physical Review B* 51 (14), 8795-8800 (1995).
- 159A. Jayaraman, G.A. Kourouklis, L.G. Van Uitert *et al.*, "A High-Pressure Raman study of  $\text{KReO}_4$ ,  $\text{RbReO}_4$ , and  $\text{CsReO}_4$  to 25 GPa and pressure-induced phase transitions," *Physica A* 156, 325-340 (1988).
- 160J.W. Otto, J.K. Vassiliou, R.F. Porter *et al.*, "Raman study of  $\text{AgReO}_4$  in the scheelite structure under pressure," *Physical Review B* 44 (17), 9223-9227 (1991).
- 161I. Kawada, K. Kato, and T. Fujita, " $\text{BaWO}_4$ -II ( A High Pressure Form )," *Acta Crystallographica B* 30 (8), 2069-2071 (1974).
- 162A. Jayaraman, B. Batlogg, and L.G. VanUitert, "High-pressure Raman study of alkaline-earth tungstates and a new pressure-induced phase transition in  $\text{BaWO}_4$ ," *Physical Review B* 28 (8), 4774-4777 (1983).
- 163N. Chandrabhas, D. Victor, S. Muthu *et al.*, "Raman Study of Pressure-Induced Structural Transitions in  $\text{CsIO}_4$  to 12 GPa," *Journal of Physics and Chemistry of Solids* 53 (7), 959-965 (1992).
- 164L.C. Ming, A. Jayaraman, S.R. Shieh *et al.*, "*In situ* high-pressure x-ray-diffraction study of  $\text{TlReO}_4$  to 14.5 GPa: Pressure-induced phase transformations and the equation of state," *Physical Review B* 51 (18), 12100-12106 (1995).
- 165A. Jayaraman, G.A. Kourouklis, R.M. Fleming *et al.*, "Temperature-induced phase transition in  $\text{TlReO}_4$ : A Raman spectroscopic and x-ray diffraction study," *Physical Review B* 37 (1), 664-667 (1988).
- 166A. Jayaraman, G.A. Kourouklis, and L.G. VanUitert, "Pressure-induced structural transitions and valence change in  $\text{TlReO}_4$ : A high-pressure Raman study," *Physical Review B* 36 (16), 8547-8551 (1987).
- 167E. Sarantopoulou, Y.S. Raptis, E. Zouboulis *et al.*, "Pressure and temperature-dependent Raman study of  $\text{YLiF}_4$ ," *Physical Review B* 59 (6), 4154-4162 (1999).
- 168A. Jayaraman, S.Y. Wang, and S.K. Sharma, "High-pressure Raman investigation on  $\text{CdMoO}_4$  and pressure-induced phase transformations," *Physical Review B* 52 (14), 9886-9889 (1995).

- 169Y. Hasegawa, Y. Ueji, K. Okitsu *et al.*, "Transmission-type X-ray linear polarizer with perfect crystals," *Journal of Synchrotron Radiation* 5, 738-740 (1998).
- 170Y. Hasegawa, Y. Ueji, K. Okitsu *et al.*, "Tunable X-ray polarization reflector with perfect crystals," *Acta Crystallographica A* 55, 955-962 (1999).
- 171M. Newville, P. Livins, Y. Yacoby *et al.*, "Near-edge x-ray-absorption fine structure of Pb: A comparison of theory and experiment," *Physical Review B* 47 (21), 14126-14131 (1993).
- 172T. Ressler, "WinXAS: a Program for X-ray Absorption Spectroscopy Data Analysis under MS-Windows," *Journal of Synchrotron Radiation* 5, 118-122 (1998).
- 173W.H. Gust and E.B. Royce, "New Electronic Interactions in Rare-Earth Metals at High Pressure," *Physical Review B* 8 (6), 3595-3609 (1973).
- 174B. Johansson and A. Rosengren, "Generalized phase diagram for the rare-earth elements: Calculations and correlations of bulk properties," *Physical Review B* 11 (8), 2836-2857 (1975).
- 175W.B. Holzapfel, "Structural systematics of 4f and 5f elements under pressure," *Journal of Alloys and Compounds* 223 (2), 170-173 (1995).
- 176J.C. Duthie and D.G. Pettifor, "Correlation between d-Band Occupancy and Crystal Structure in the Rare Earths," *Physical Review Letters* 38 (10), 564-567 (1977).
- 177H.L. Skriver, "Crystal structure from one-electron theory," *Physical Review B* 31 (4), 1909-1922 (1985).
- 178A.K. McMahan, C. Huscroft, R.T. Scalettar *et al.*, "Volume-collapse transitions in the rare earth metals," *Journal of Computer-Aided Materials Design* 5, 131-162 (1998).
- 179B. Johansson, "The a-g transition in cerium is a Mott transition," *Philosophical Magazine* 30, 469-482 (1974).
- 180J.W. Allen and R.M. Martin, "Kondo Volume Collapse and the g@a Transition in Cerium," *Physical Review Letters* 49 (15), 1106-1110 (1982).
- 181C. Huscroft, A.K. McMahan, and R.T. Scalettar, "Magnetic and Thermodynamic Properties of the Three-Dimensional Periodic Anderson Hamiltonian," *Physical Review Letters* 82 (11), 2342-2345 (1999).
- 182W.J. Carter, J.N. Fritz, S.P. Marsh *et al.*, "Hugoniot Equation of State of the Lanthanides," *Journal of Physics and Chemistry of Solids* 36, 741-752 (1975).
- 183J. Wittig, "Pressure-induced valence instability in praseodymium metal and dilute La Pr and Y Pr alloys: A counterpart of the cerium case?," in *Physics of Solids Under High Pressure*, edited by J.S. Schilling and R.N. Shelton (North-Holland Publishing Company, 1981), pp. 283-293.
- 184Y.C. Zhao, F. Porsch, and W.B. Holzapfel, "Determination of triple points in the phase diagram of praseodymium," *Physical Review B* 52 (1), 134-137 (1995).
- 185G.N. Chesnut and Y.K. Vohra, "Phase transformations and equation of state of praseodymium metal to 103 GPa," *Physical Review B* 62 (5), 2965-2968 (2000).
- 186W.A. Grosshans, Y.K. Vohra, and W.B. Holzapfel, "F-bonding in praseodymium under high pressure," *Journal of Physics F* 13, L147-L149 (1983).
- 187W.A. Grosshans, Y.K. Vohra, and W.B. Holzapfel, "Evidence for a Soft Phonon Mode and a New Structure in Rare-Earth Metals Under Pressure," *Physical Review Letters* 49 (21), 1572-1575 (1982).
- 188G.S. Smith and J. Akella, "Reexamination of the crystal structure of a high-pressure phase in praseodymium metal," *Journal Of Applied Physics* 53 (12), 9212-9213 (1982).
- 189H.K. Mao, R.M. Hazen, and P.M. Bell, "Evidence for 4f-shell delocalization in praseodymium under pressure," *Journal Of Applied Physics* 52 (7), 4572-4574 (1981).
- 190F. Bartolome, J. Tonnerre, M., L. Seve *et al.*, "Identification of Quadrupolar Excitation Channels at the L<sub>III</sub> Edge of Rare Earth Compounds," *Physical Review Letters* 79, 3775 (1997).
- 191M.H. Krisch, C.-C. Kao, F. Sette *et al.*, "Evidence for Quadrupolar Contribution to the Absorption Cross Section at the L<sub>III</sub> Edge of Gadolinium in Gadolinium Gallium Garnet," *Physical Review Letters* 74, 4931 (1995).
- 192L.M. Miller, C.S. Carlson, G.L. Carr *et al.*, "A method for examining the chemical basis for bone disease: synchrotron infrared microspectroscopy," *Cellular and Molecular Biology* 44 (1), 117-127 (1998).

- 193 M.J. Glimcher, *The Nature of the Mineral Phase in Bone: Biological and Clinical Implications* (Academic Press, 1998).
- 194 R.E. Baron, *Anatomy and ultrastructure of bone* (Lippincott-Raven, 1996).
- 195 H.M. Frost, *The Bone Dynamics in Osteoporosis and Osteomalacia* (1966).
- 196 L. Lichtenstein, *Diseases of bones and joints* (1975).
- 197 H.L. Muncie and R.W. Moskowitz, *Current Management of Osteoarthritis* (1988).
- 198 R. Huiskes, R. Ruimerman, and E. Tanck, "Architectural consequences of microcrack-related stimuli for osteoclastic resorption in trabecular bone," presented at the 12th Conference of the European Society of Biomechanics, Dublin, Ireland, 2000 (unpublished).
- 199 C.J. Buckley, N. Khaleque, S.J. Bellamy *et al.*, "Mapping the Organic and Inorganic Components of Tissue using NEXAFS," *Journal De Physique IV* 7 (C2), 83-90 (1997).
- 200 D.B. Burr and M.B. Schaffler, "The involvement of subchondral mineralized tissues in osteoarthritis: quantitative microscopic evidence," *Microsc. Res. Tech* 37 (4), 343-57 (1997).
- 201 D.B. Burr, "The importance of subchondral bone in osteoarthritis," *Curr. Opin. Rheumatol.* 10 (3), 256-62 (1998).
- 202 T.E. Wenzel, M.B. Schaffler, and D.P. Fyhrie, "In vivo trabecular microcracks in human vertebral bone," *Bone* 19, 89-95 (1996).
- 203 C.J. Buckley, R.E. Burge, G.F. Foster *et al.*, "X-ray imaging of calcium deposits in human cartilage," presented at the SPIE Soft X-Ray Microscopy Conference, San Diego, California, 1992 (unpublished).
- 204 B.R. Bennett and J.A. del Alamo, "Optimal epilayer thickness for  $\text{In}_x\text{Ga}_{1-x}\text{As}$  and  $\text{In}_y\text{Al}_{1-y}\text{As}$  composition measurement by high-resolution x-ray diffraction," *Journal Of Applied Physics* 73 (12), 8304-8308 (1993).
- 205 A. Krost, J. Böhrer, A. Dadgar *et al.*, "High-resolution x-ray analysis of compressively strained 1.55 mm  $\text{GaIn/AlGaInAs}$  multiquantum well structures near the critical thickness," *Applied Physics Letters* 67 (22), 3325-3327 (1995).
- 206 J. Ablett, C.C. Kao, K. Evans-Lutterodt *et al.*, "Micro-fluorescence Studies of Selective Area Growth in  $\text{InGaAsP}$  thin films," NSLS abstract (2001).
- 207 M.A. Alam, R. People, E. Isaacs *et al.*, "Simulation and characterization of the selective area growth process," *Applied Physics Letters* 74 (18), 2617-2619 (1999).
- 208 Z.H. Cai, W. Rodrigues, P. Ilinski *et al.*, "Synchrotron x-ray microdiffraction diagnostics of multilayer optoelectronic devices," *Applied Physics Letters* 75 (1), 100-102 (1999).

## Acknowledgement

I would like to thank all of the staff of the National Synchrotron Light Source for providing me with the opportunity to complete this thesis. The excellent facilities and dedicated personal enabled the successful installation of a dedicated x-ray micro-focusing end-station possible. I would also like to thank the United States Department of Energy for providing me with the opportunity to perform my research.

Special praise goes to my scientific advisor, Dr. Chi-Chang Kao who taught me everything there is to know about x-rays. His expertise in x-ray physics and dedication to the NSLS were invaluable. He introduced me to many researchers who were interested in using x-ray micro-beams and I enjoyed working with all of them. In particular, Dr. Trevor Tyson (New Jersey Institute of Technology) and Dr. Ken Evans-Lutterodt (Lucent Technologies) were very interested in the X13B micro-probe, and I took immense pride in helping them to conduct their research using this instrument. In fact, as I am writing this concluding part of this thesis in England, Trevor is conducting high-pressure experiments at X13B with his student, and I hope all is going well for them.

I have also designed a micro-probe end-station for IBM at the NSLS X20A beamline. As I write, these optics are currently being installed, which I hope will provide as much success as those at X13B. I also wish to thank Andy Lundt, at 'Beamline Technologies Corporation' for manufacturing the differentially deposited mirrors, without which, this thesis would not have been possible.

The building of the micro-probe could only have been possible with the brilliant technicians of the experimental systems group. Whenever I needed specially machined-parts, or holes drilling in aluminium, they were always extremely kind and helpful. Anthony Leonard was superb in helping me to design the mirror stages, and always offered me his help when I ran into difficulties. Rick Green put a lot of time and effort into machining many of the micro-probe parts, and also introduced me to 'tree-felling.'

Gary Nitnzal is an expert in vacuum systems, and took care of X13B whenever there was a leak. I wish them all the best for the future.

As a member of the experimental systems group at the NSLS, I have made many friends. There were some people who deserve a special mention and made my time at the light source highly enjoyable. Wolfgang Caliebe, Elio Vesuvco, Cecilia Hanke-Sanchez, In-Gyu Baek, Zhong-Zhong and Dieter Lott were all very good friends.

I would also like to thank Dr. Jerry Hastings and Dr. Peter Siddons for their deep knowledge of x-ray physics and friendly advice during my time at the NSLS. I also did some baby-sitting for Jerry and enjoyed playing with his son, Daniel who often beat me at soccer. The barbeques and dinners that Pete often prepared at his house with his wife, Liz will be sadly missed. The many times I spent at Chi-Chang's house playing games with his lovely children, Thomas and Theresa will be cherished as will the warm and friendly hospitality of his wife, Grace.

Finally, this thesis could not have been completed without the help of my parents, Alan and Elaine. They have always given me the encouragement to persevere in my studies and the financial help to keep my head above water. I cannot thank them enough and hope I have made them very proud.